AN EMPIRICAL STUDY OF THE PLANETARY BOUNDARY LAYER IN THE VICINITY OF THE INTERTROPICAL CONVERGENCE ZONE

by

PAUL JANOTA

A.B. Butler University (1957)

S.M. St. Louis University (1959)

SUBMITTED IN
PARTIAL FULFILLMENT
OF THE REQUIREMENTS FOR THE
DEGREE OF DOCTOR OF PHILOSOPHY

at the

MASSACHUSETTS INSTITUTE OF TECHNOLOGY

September, 1971

Signature of Author: _____
Department of Meteorology, September 10, 1971

Certified By: _____
Thesis Supervisor

Accepted By: _____
Chairman, Departmental Committee on
Graduate Students

AN EMPIRICAL STUDY OF THE PLANETARY BOUNDARY LAYER IN THE VICINITY OF THE INTERTROPICAL CONVERGENCE ZONE

by

PAUL JANOTA

Submitted to the Department of Meteorology on September 10, 1971
in partial fulfillment of the requirements
for the degree of Doctor of Philosophy

ABSTRACT

Marshall Islands data for May 1956 are used to evaluate the balance of forces in the equatorial tropics. Flow is balanced north of the ITC, while south to the equator various inertial and Reynolds stress terms are important. Friction is important in the first 2km at all latitudes.

Composite profiles of wind, humidity and temperature in the boundary layer near the ITC are derived from the Line Islands Experiment and BOMEX Fourth Phase as well as the Marshalls data. On the average, an Ekman layer north of the ITC accounts for the equatoward flux. The layer is 2-3km deep but 50 percent of the transport is below 750m. The poleward flux south of the ITC is much deeper and winds back with height above a shallow veering layer below the clouds. The boundary layer on the equator is on the order of 2km deep and winds either turn very little or back with height.

Daily case studies from BOMEX using aircraft and satellite-derived winds reveal excellent correlation between ITC cloud bands and meso-scale patterns of cyclonic vorticity and convergence in the boundary layer. These data support the hypothesis that CISK maintains the ITC.

Characteristics of tropical waves and an easterly jet at 700mb are also shown in the case study. The jet forms in the temperature gradient established by intrusions of African air and may be unstable in the manner of an internal jet.

Thesis Supervisor: Jule G. Charney
Title: Sloan Professor of Meteorology

DEDICATED WITH DEEPEST LOVE AND AFFECTION

to

MY WIFE CAROL

and my children

JIM, DAN, DAVE, MIKE and MOLLIE

TABLE OF CONTENTS

CHAPTER 1

INTRODUCTION

1.1. Background

In the oceanic equatorial tropics, the most commonly observed meteorological feature is the narrow belt of cloudiness associated with the Intertropical Convergence Zone (ITC). The previous statement is oversimplified in the extreme, and one's reaction to it depends on one's perspective.

Climatologically, the ITC is nearly always found 5^{o} to 15^{o} away from the equator and primarily in the Northern Hemisphere, at least in the Atlantic and eastern Pacific. In the western Pacific and Indian Ocean, the ITC, the monsoon, and the frequent tropical disturbances are combined and the maximum mean cloudiness is found in the summer hemisphere along with convergence in the mean low level winds. This traditional picture has varied little over the years (Riehl, 1954; Atkinson and Sadler, 1970). The weather satellites have more recently shown that during March, April and May there are two cloud bands symmetric about the equator in the Pacific east of 180^{o}W (Kornfield and Hasler, 1969).

Synoptically, the ITC is much more complex. If one leafs through a catalog of daily global satellite images (e.g. ATS-III, 1969), the previous conclusion is quickly reached. The ITC can be linear, single-banded and extend for thousands of miles on one day; and on the next, it can be broken, multi-banded and have a wavy

appearance. It is seen to interact with passing tropical waves to the north (Frank, 1969), or it may be ruptured by gusts of air from the Southern Hemisphere (Fujita et al., 1969). It does, however, avoid the equator, except perhaps in the western Pacific and Indian Ocean.

We can get a misleading picture of the structure of the ITC cloud bands from satellite imagery. Large cumulonimbus can generate enormous anvils which mask the true dimension of the significant cloud lines. Figure 1.1 illustrates the point. Scalloped lines denote cloud outlines derived from an ESSA-9 photograph on 13 July 1969. The small shaded patches are from an APS-20 radar flown in the boundary layer on board a Research Flight Facility (RFF) aircraft. Winds are from a companion RFF flight. This section is along segment M-N in Fig. 5.1b. The dimensional contrast is obvious and is probably representative of many cloud bands viewed by satellites.

Wind shear and convergence values are functions of the differencing increment and exceed 10^{-4} s^{-1} in the vicinity of individual clouds. At the meso-scale, values of vorticity and divergence near the ITC tend to be multiples of 10^{-5} s^{-1}; thus the wind perturbations related to these very narrow cloud lines are reflected in meso-scale analyses with a resolution of $\sim$100 km.

Riehl and Malkus (1958) have shown that penetrative cumulus in the equatorial trough (essentially the ITC) supply most of the heat energy that drives the tropical circulation; and Gray (1968) has surveyed the origin of tropical storms and states that most form equatorward of 20^{o}N on the poleward side of "doldrum Equatorial Troughs"

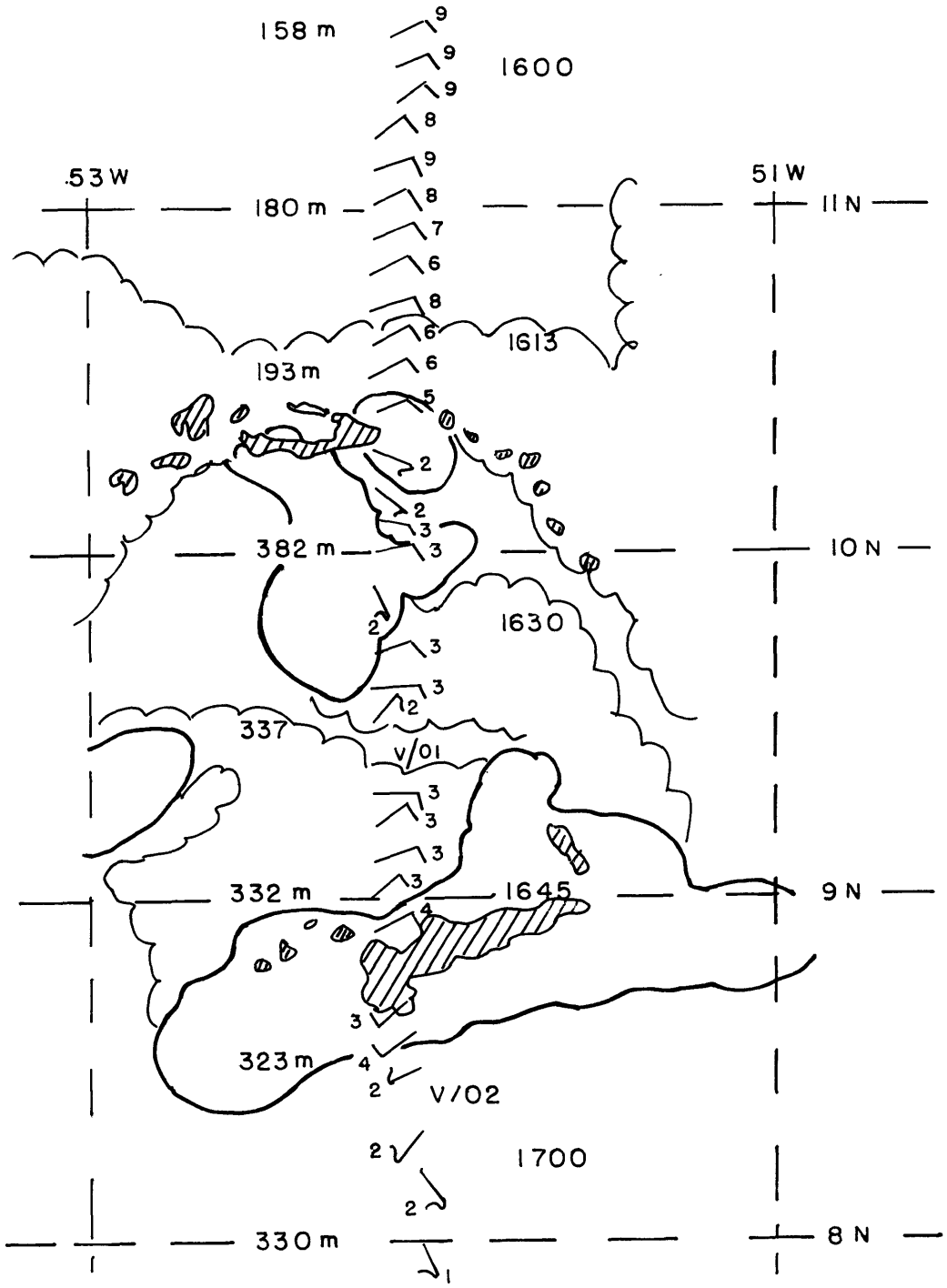

Fig. 1.1. Dimensions of ITC cloud bands as seen by ESSA-9 (scalloped thin and bold lines) and APS-20 radar (shaded), 13 July 1969. Winds are from the RFF A-Plane (see Ch. 2) in m/s. Flight altitude in meters to the left and time (GMT) to the right. Bold cloud outlines were brightest on ESSA-9 photos.

(or ITC in this context). Thus the ITC plays a fundamental role in the general circulation and as a breeding ground for many destructive storms.

Early theories concerning equatorial trough meteorology were sorted by Palmer (1951) into the Climatological, Air-Mass, and Perturbation Schools of Thought. Each school contributed refinements to the descriptive aspects of the ITC, such as: the ITC undergoes seasonal migrations which essentially follow the sun; ITC cloud bands lie in confluence axes in the streamlines; and easterly waves are important features of the tropical circulation. However, no viable dynamical basis for the ITC was formed during those years.

Many current studies of tropical systems belong to what Zipser (1970) has termed the "Fourth School of Thought"; this is the scale-interaction school. For example, Zipser's own work (1969) shows how organized downdrafts from a small convective disturbance can modify a much larger area. Also, Charney and Eliassen (1964) related cumulus-scale heating in a conditionally unstable synoptic scale disturbance to the pumping of moisture out of the planetary boundary layer and showed that such a system was unstable with a linear growth rate nearly independent of the scale of the perturbation in the sub-synoptic and meso-scale range. The growth rate rapidly decays to zero for scales above $\sim$1000 km. This mechanism was called "conditional instability of the second kind" (CISK) by Charney and Eliassen, and its utility depends on an in-phase relationship between cyclonic vorticity and convergence as is found with an Ekman layer.

A theory of the general circulation in the tropics must account for the ITC and explain the narrowness of the cloud zone (rarely in excess of 5^{o} lat.), its characteristic position away from the equator, and its capacity to spawn occasional warm-core disturbances.

Charney (1968) used a zonally symmetric model incorporating the CISK mechanism in his study of the ITC and the tropical Hadley cell. The ITC was 400 km wide or less and formed away from the equator when condensation heating was allowed to overcome cooling due to adiabatic expansion. The width of the ITC was bounded above because CISK favors small disturbances (though not catastrophically), and bounded below principally by the grid mesh.

Gravitational instability of the air for moist processes increases toward the equator in Charney's model, but the efficiency of Ekman pumping increases away from the equator, thus the ITC was invariably found at a compromise latitude near 10^{o}. In a non-linear, time dependent version of the model, Charney found that the steady state circulation was degenerate in his "strong ITC" cases, and that the position of the ITC was sensitive to sea surface temperature anomalies because they locally enhanced horizontal wind shear and associated boundary layer pumping.

Bates (1969) added the x-dimension to Charney's model in order to study disturbances in the ITC. These derived their initial energy at the expense of the mean flow through Reynolds stress conversion (a mechanism studied by Nitta and Yanai, 1969). Eventually, the direct conversion of condensationally produced eddy available potential

energy dominated the barotropic mechanism. The preferred length scale was $\sim$2000 km, the disturbances were warm core, and they propagated westward at about 13 knots.

Although other parameterizations of convective heating are in the literature (e.g. Kuo, 1965, or Manabe et al., 1965), the CISK mechanism has, in a simpler fashion, captured the essence of the more involved physical processes and highlights the important role of the planetary boundary layer in the tropics.

1.2. Objective

Normally, theoretical work such as that described in the previous section, follows in the wake of empirical study. However, little empirical data has actually been published on the character of the planetary boundary layer in the equatorial tropics, especially south of the ITC. Gray (1968) has found statistical evidence for an Ekman layer, but most of his data are 10^{o} or more from the equator. Estoque (1971) does not find an Ekman layer at Christmas Island (2^{o}N), but a boundary layer character is noted in the shear of the mean wind. Anawalt (1971), using BOMEX Fourth Phase data, finds evidence of a 2 km boundary layer with characteristics that support CISK. His data are essentially north of the ITC at 10^{o}N; hence, they corroborate Gray's statistics but shed little light on the near equatorial behavior.

Because this subject is controversial, the objective of this paper is to use data gathered near the ITC during the last 15 years

and describe the structure of the planetary boundary layer (if it exists) in the equatorial tropics. Hopefully, theoreticians will use the results of this research to help guide their investigations.

1.3. Outline

Chapter 2 describes the data bases from the Marshall Islands, the Line Islands Experiment and BOMEX, and the various problems encountered by the author in utilizing these data.

Chapter 3 discusses the results of an empirical scale analysis based on Marshall Islands data, and an experiment in which the winds north of the ITC were modeled rather well with the Ekman expressions.

Chapter 4 compares composited data from the three regions and shows that when data are stratified as north or south of the ITC, the character of the boundary layer changes from an Ekman layer in the north to something significantly different south of the ITC. Boundary layer depth and the correlation between vorticity and divergence are also discussed.

Chapter 5 discusses in detail a 9-day case study based on BOMEX Fourth Phase data. The study covers a period of growth and decay of the ITC and compares the 500 m and 700 mb flow patterns with the cloud bands and traveling disturbances. Although Ekman theory is not appropriate at all latitudes, it is shown that the necessary boundary layer support for CISK is present in virtually all significant features. The 700 mb analyses describe several tropical waves and

a strong jet in the easterlies.

Chapter 6 is a summary and gives some recommendations for further empirical and theoretical studies.

CHAPTER 2

DATA SOURCES AND PROCESSING

2.1. Marshall Islands - Redwing, 1956

During the period 15 April through July 1956, a series of nuclear tests were conducted in and around the Marshall Islands under the code name "Operation Redwing" (Joint Task Force Seven, 1956). These tests were supported by an augmented net of meteorological sounding stations operating from the islands, and by reconnaissance aircraft. The stations used are described in Table 2.1. and shown in Figure 2.1.

STATION	BY	LAT.	LONG.	ELEV.[d]	EQUIP.
Marcus[a]	W	24.3N	154.0E	55 ft	G
Wake	W	19.3N	166.6E	13	G
Bikini[b]	N	11.5N	165.5E	10[c]	F
Eniwetok	A	11.3N	162.3E	11	G
Rongerik[b]	A	11.3N	167.4E	10[c]	G
Kwajalein	N	9.0N	167.3E	10[c]	G
Truk	W	7.5N	151.8E	8	S
Majuro	W	7.1N	171.3E	10[c]	G
Ponape	W	6.6N	158.3E	151	G
Kusaie[b]	A	5.0N	163.0E	10[c]	G
Tarawa[b]	A	1.5N	173.0E	10	G
Kapingamarangi[b]	A	1.0N	155.0E	10	G

Table 2.1. Sounding stations used in this study. The column labeled "BY" shows agency that operated the station: Air Force (A), Navy (N), US Weather Bureau (W). In the equipment column (EQUIP) the code is: AN/GMD-1A (G), AN/SCR-658 (S), AN/FMQ-2 (F). Also: ([a]) USWB data, not from the Redwing volumes; ([b]) Stations added to support the bomb tests; ([c]) Estimates, reasonably accurate since the locations are atolls; ([d]) Elevations from H.O. Publication No. 207, 1958.

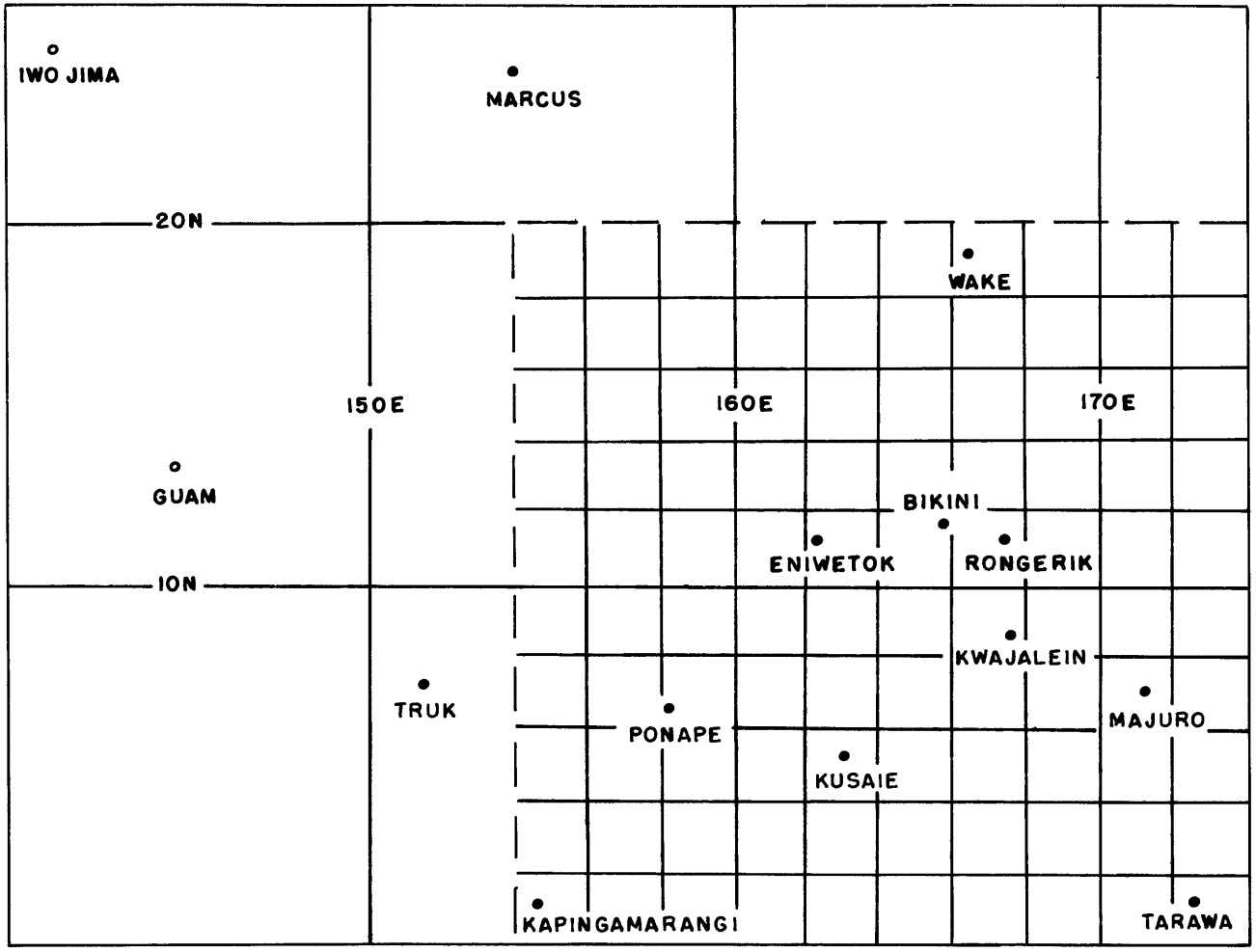

Fig. 2.1. Map showing the stations used in Redwing study (solid circles), and the analysis grid for numerical computations.

The map also shows the analysis grid. Grid points are at even two degree intersections of latitude and longitude.

2.1.1. Data Reporting Information

Data were available at a mix of three, six, nine and twelve hour increments depending on station and date. The soundings were in a standard format and included both mandatory and significant levels. Winds were recorded to the nearest ten degrees and whole knot. Winds were reported at the surface, at 1000 foot increments up to 10,000 feet, 2000 foot increments up to 20,000 feet, and then 5000 foot increments above 20,000 feet.

Air reconnaissance data were available from a variety of tracks at fixed levels and mainly during daylight hours. Dropsondes were not employed. This study used reconnaissance data taken only at 700 mb and within three hours of the chosen synoptic time, 0300Z. The mandatory synoptic times in 1956 were 0300Z plus six or 12 hour increments. The three hour increments were available mainly during the test periods which normally appeared to last for a few days to a week.

2.1.2. Selection of the Data

Although data from other sources and times are occasionally referenced, the basic study is based upon the collection period 1-30 May 1956. This choice is a compromise between two objectives, namely: to maintain homogeneity in the flow patterns and the position of the ITC, and to insure reasonable reliability in the estimation of the pressure gradient terms in the equations of motion. The first objective

argues for a short sampling period, while the latter requires that uncertainty be reduced by a fairly long averaging of the reports.

From an examination of US Weather Bureau Daily Historical Maps for the period of "Operation Redwing", it was noted that the area of interest seemed particularly undisturbed by major storminess during May 1956. Thus, relatively homogeneous zonal flow patterns could be found each day and May was chosen as the working month. The initial study employed only data from 0300Z which eliminated the time varying aspect of the diurnal pressure wave and took advantage of the air reconnaissance data. Finally, the use of a 30-day average reduced the probable error in measurement of height of constant pressure surfaces used in the study. The latter point is discussed further in the next section.

2.1.3. Further Effects from Averaging the Data

Early in the research, the writer tried to study daily situations in depth in order to evaluate individual terms in the equations of motion and to isolate viscous effects as residues required to balance the equations. But the winds are only reported to tens of degrees and whole knots and probable errors in the heights of pressure surfaces are intolerable for daily analysis in the tropics.

Table 2.2 shows probable error (PE = 0.67 standard deviation) of measurement of heights of various pressure surfaces based on statistics from a wide variety of locales and equipment. The reference assumed no error at 1000 mb.

PRESSURE	PROBABLE ERROR	REDUCED HEIGHT ERROR
1000 mb	0 ft	0 ft
700	23	4.2
500	45	8.2
300	80	14.5
200	108	19.7
100	153	27.8

Table 2.2. Probable error in deriving the height of a given pressure surface using typical sounding equipment of the mid-1950's. Values are in feet. Reduced probable errors using a 30-day mean are shown in the right-hand column. (Air Weather Service Technical Report 105-133, 1955).

Since typical height variability on a constant pressure surface over the entire grid shown in Figure 2.1 is only on the order of 150 feet, Table 2.2 shows that daily high-altitude pressure analyses are futile. However, assuming that the instruments and operators are unbiased, an n-day sample mean will reduce the probable error values by a factor of $1/\sqrt{n}$. The reduction for n=30 is shown in the right-hand column of Table 2.2. It appears that analyses of 30-day mean maps are feasible, at least in the lower troposphere.

The analysis process adds a certain amount of subjective smoothing and further suppresses the effects of errors at a station if the collective trend of surrounding stations suggests that an adjustment must be made. This same process removes part of the artificial truncation present in the wind data. The drawback is that the analysis process is difficult to quantify, and major adjustments are not justified in regions of sparse data. In this study, the analyses of time-mean data are drawn to fit the reports as closely as possible without introducing

features which are small relative to the grid spacing.

Another benefit of time averaging is the fact that terms like $\partial u/\partial t$ approach zero in the limit of very long time. This is a welcome trait since local time derivatives are not particularly reliable even though some observations were available every three hours and centered differences could have been used. Unfortunately, averaging creates terms involving the products of fluctuation quantities (Reynolds stress terms), but these are tractable with the aid of a digital computer.

2.1.4 The Question of Accuracy

No doubt, one could dwell at length upon the subject of data reliability and perhaps even "prove" that detailed equatorial analyses of pressure/wind relationships are not yet possible. However, the investigation went ahead subject to the following conditions:

1. Although great accuracy is probably beyond reach, the results will not be considered spurious unless individual quantities to be evaluated (such as $u\partial u/\partial x$ etc.) and/or the area analyses of such quantities seem meteorologically unlikely. That is, either the expected orders of magnitude are unreasonable, or analyzed fields seem random and inconsistent.

2. One of the objectives of this paper is to determine whether or not a quasi-geostrophic model with a parameterized boundary layer can be used to advantage in studying near-equatorial behavior. Hence the scale

analysis portion will be phrased in terms of orders of magnitude, not decimal point accuracy. Any more precise conclusions that seem to be justified will be considered bonuses and will be pointed out as we proceed.

2.1.5. Systematic Barometry Correction

First attempts at constant pressure analyses for April and May 1956 turned up evident barometry errors at a majority of the reporting stations. The most obvious clue appeared when one compared the surface pressure value from a sounding with the sea-level pressure from the corresponding surface synoptic report. In several cases, the surface pressure came in higher than the sea-level pressure by as much as a millibar. A more subtle problem appeared first in the Ponape reports. Their 1000 mb heights were generally lower than those of neighboring stations, and even an analysis of mean data for the entire May sample demanded a small but deep low pressure cell over the island. However, no such feature was evident in the surface pressure analyses. An example of such a situation is demonstrated in Figures 2.2 a,b. The listed station elevation for Ponape is 151 feet (see Table 2.1); however, it appeared that their observers were using an elevation of about 120 feet in building their soundings. Because of the lack of a perturbation at sea level, the persistent appearance of such a feature at 1000 mb seemed quite impossible.

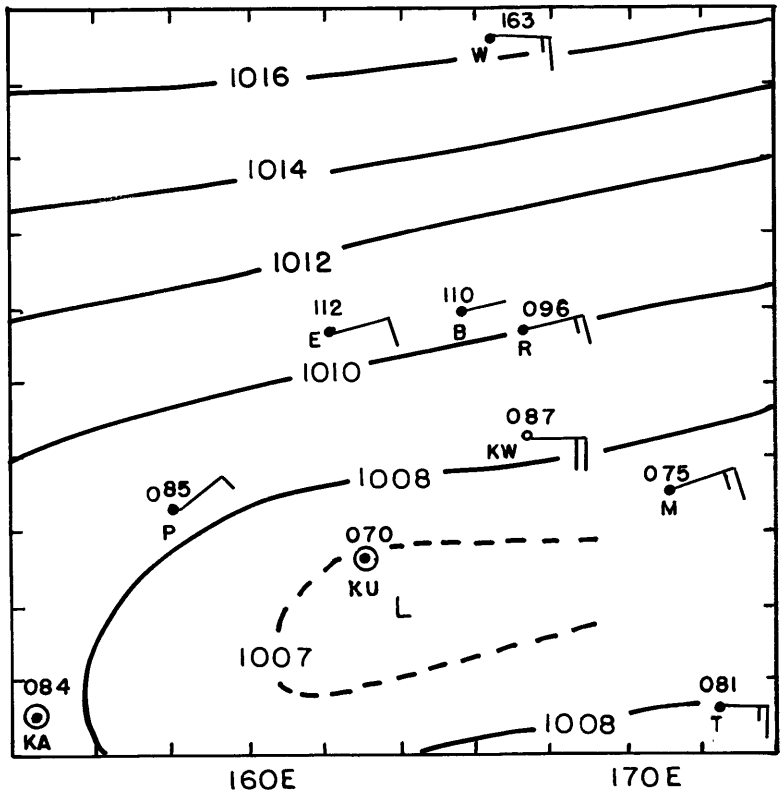

Fig. 2.2a. Surface chart for 0300Z, 26 May 1956. The pattern is simple, and Ponape's report (P) fits without difficulty.

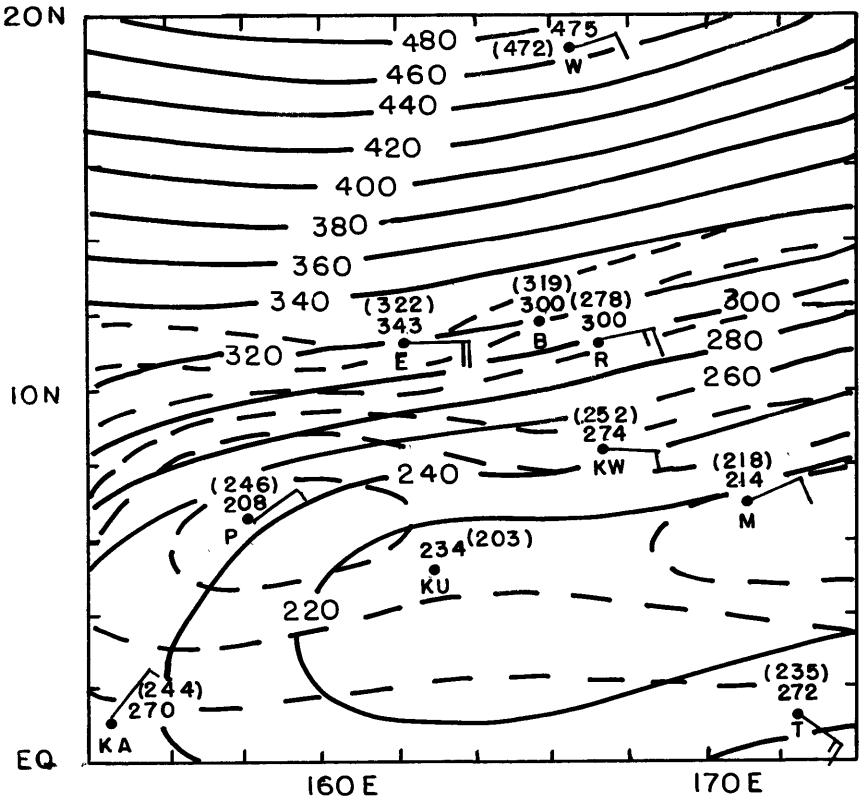

Fig. 2.2b. 1000 mb chart for 0300Z, 26 May 1956. Dashed contours are uncorrected. Note the small low cell at Ponape (P) in the uncorrected field, and the tight gradient between Ponape and Eniwetok (E). Values in parentheses are corrected heights from equation 2.1. Solid contours show the corrected field.

Time sections of surface pressure and sea-level pressure were then drawn for other stations over the May period and a picture began to emerge. There were initialization errors in the building of the soundings due to one or more of the following problems: improper elevation information, bad station pressure readings, and/or bad sea-level pressure adjustment. The following simple procedure was used to eliminate the error. Assume that sea-level pressure (SLP) values were accurate since these were presumably read from Mercury barometers in a favorable environment. Subtract the 1000 mb height from all heights on a given sounding thus preserving thickness between pressure levels while discarding initialization errors. Then generate a ficticious 1000 mb height from the formula

$$Z_{1000} = (\text{SLP}-1000) \times 29 \text{ feet} \qquad (2.1)$$

and add this back into all other heights from the sounding. At Wake Island, 28 feet was used in (2.1) due to the cooler and drier climatology.

Even though this procedure may sound too rigid, reanalysis at 1000 mb using the "corrected" data showed that the micro-low at Ponape was removed, yet the overall patterns were only slightly different and somewhat smoother. See Figure 2.2b for an example of a 1000 mb analysis before and after correction. This procedure appeared to create perturbations at Rongerik, and it was decided by comparison with values from Kwajalein and Eniwetok that Rongerik's upper-air heights were better left alone.

It was encouraging to note that thickness computations were very well behaved. Sixty-seven soundings from all stations during April and May 1956 at 0300Z and 1500Z were sampled and the 1000-700 mb thickness fields were computed from given temperature and humidity data. Computations were performed in increments of 25 mbs. Comparison with thickness fields derived from the given height data showed that there was agreement to within 25 feet in 60 of the cases. The largest difference was -125 feet at Kapingamarangi at 0300Z on 5 May 1956 (the book value was higher), and this sounding was then reconstructed, but the next highest difference was only -34 feet. Further reconstruction of May data was deemed uneconomical and the book values of thickness were accepted. However, during the process of punching data cards from the printed soundings, any suspicious looking height values were reconstructed, and, on a few occasions, minor thickness adjustments were made. Certainly, this phase of the sounding construction had been well handled prior to publication of the Redwing data.

Finally, it should be noted that corrected soundings from Truk had lower 1000-700 mb thicknesses than either Ponape or Kusaie on 26 of the May cases. The heights and temperatures were consistent since Truk's mean air column between 1000 mb and 700 mb averaged about 1.5^{o}K cooler than those of Ponape and Kusaie. Although this is probably real, note from Table 2.1 that only Truk and Bikini used other than AN/GMD-1A tracking gear; perhaps Truk used a different sonde as well. There is an uncertainty here which must be considered in subsequent analyses.

2.1.6. The Diurnal Pressure Wave

The temporal variations of the diurnal wave (semi-diurnal near the surface) are not generally a problem in this study because the basic data are taken at 24-hour intervals. However the spatial height variation was investigated and found to be not inconsiderable. Riehl (1947) had published results from a two-month test series in which careful analysis of the diurnal wave was based on soundings taken at three-hour intervals in the eastern Caribbean. Daily amplitudes varied between 1 and 1.5 mb; maxima occurred near 1000L and 2200L while minima were at 0400L and 1600L. In the Redwing area, 0300Z corresponds to 1400L at 165°E. Data were extracted from Riehl's curves at half-hour intervals from 1300L to and including 1430L, and at the heights shown in Table 2.3.

LEVEL (FT)	150°E 1300L	157.5°E 1330L	165°E 1400L	172.5°E 1430L
0	0 ft	10.2 ft	16.0 ft	18.8 ft
5000	0	16.0	25.6	30.4
10,000	0	10.8	21.6	28.8
15,000	0	7.8	19.5	31.2
20,000	0	9.8	22.0	34.3
32,800	0	12.3	32.8	49.2
42,600	0	19.2	44.8	70.4
46,500	0	20.0	48.0	76.0
52,500	0	20.3	50.7	81.1

Table 2.3. Spatial and vertical variation of the diurnal pressure wave for 0300Z in the Redwing analysis region. Values are in feet converted from millibars. Local times are converted to longitude for ease of interpretation.

In the table, local times have been converted to longitude which locates the synoptic diurnal wave position at 0300Z in the area of interest. One notes that spatial variations as large as 50 feet occur in the upper troposphere; hence, this systematic effect has been subtracted out of the final pressure analyses.

2.1.7. Analysis of Air Reconnaissance Data

The data were included at 700 mb within plus or minus three hours of 0300Z on 25 of the 30 days. Since the aircraft were never on the same track from day to day, it was not possible to first time-average the data at fixed points and then construct one mean analysis. Rather, 30 charts using all conventional and aircraft data were analyzed, gridded and averaged to generate the mean 700 mb field. Examples of these daily maps are shown as Figures 2.3 and 2.4.

There are problems in the height analyses at 700 mb. For example, the Ponape, Kusaie and Kwajalein heights look reasonable enough on 1 May 1956 (Fig. 2.3), although Kusaie is the main support for a small low, and the gradient near 10^{o}N calls for geostrophic speeds of 40 knots or more. But the analysis for 5 May (Fig. 2.4) looks even more suspect and shows a height distribution characteristic of the mean charts (Section 2.1.8). Truk seemed a bit low in a biased fashion (Section 2.1.5.). The author reluctantly drew for the corrected height data at these stations simply because they are strategically located near the mean ITC position for the month. To pick "good" days and disregard "bad" or to leave them out of the height analysis entirely are both forms of prejudging the data; hence they were preserved.

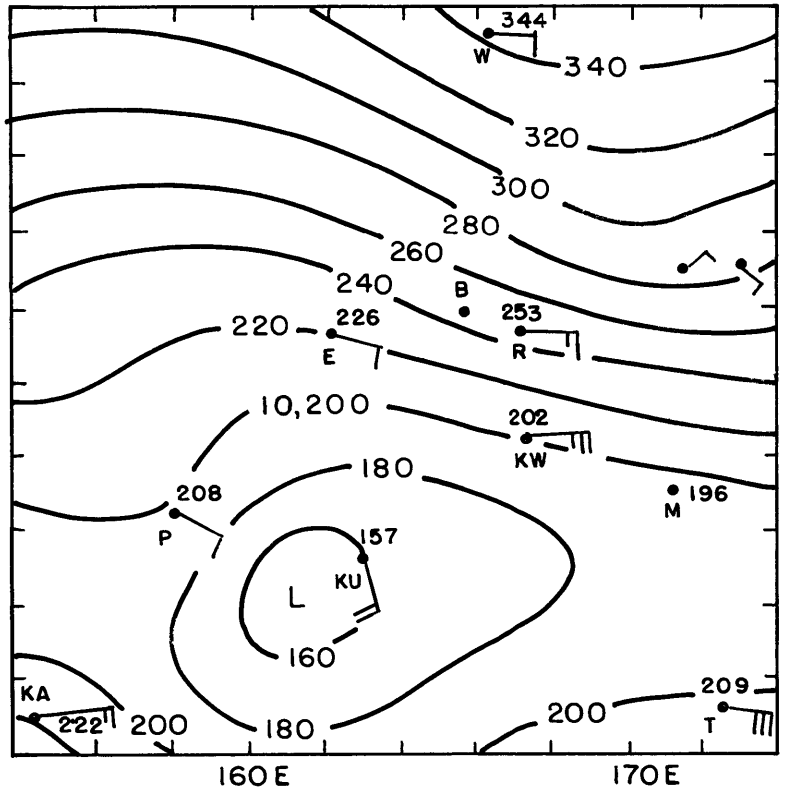

Fig. 2.3. 700 mb analysis for 1 May 1956. Heights in feet, speed in knots.

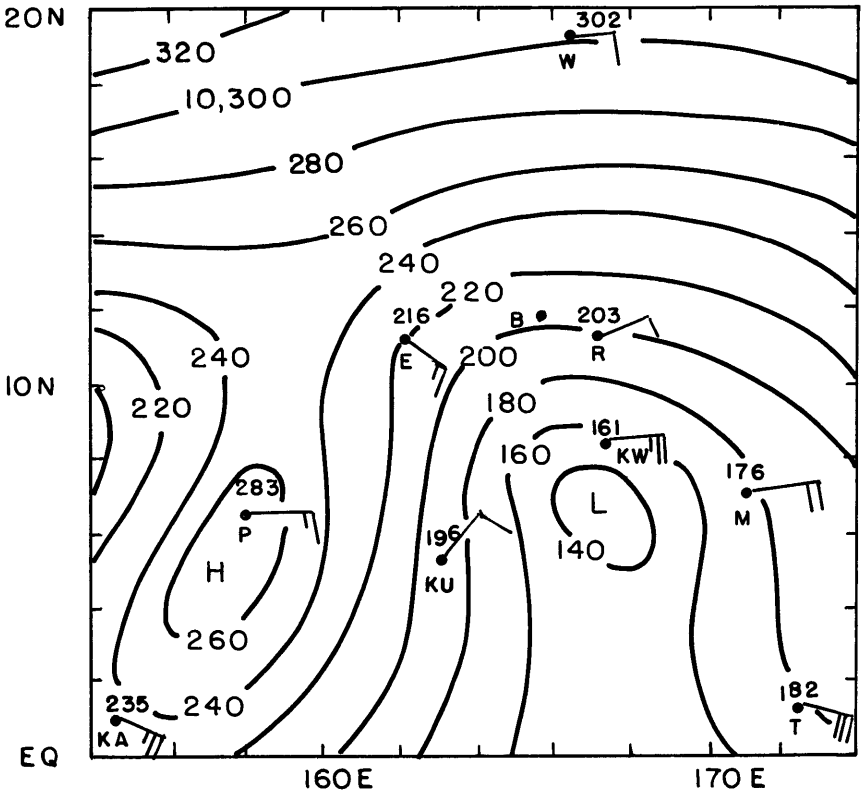

Fig. 2.4. Same as Fig. 2.3 for 5 May 1956.

2.1.8. Final Analysis of the Mean Constant Pressure Charts

Because of the importance of the reconnaissance winds and pressure gradients (absolute aircraft derived heights were rarely drawn for), the 700 mb mean chart became the "keystone" for up-and-down stacking of the remaining mean constant pressure charts. For the latter, the station data were first time-averaged, and then one mean chart was drawn for each level. The process was to first draw mean thickness analyses and then employ graphical addition (subtraction) above (below) the 700 mb chart.

As a final step, diurnal pressure wave charts were drawn using the data from Table 2.3. Actually, all one needs to do is to assume no latitudinal variation in these values, and then simply relabel the appropriate meridians in terms of feet. For example, one such chart is shown as Fig. 2.5. Then graphical subtraction is performed to generate the final fields. Final pressure and streamline analyses at selected mandatory levels from the surface to 100 mb are shown as Figs. 2.6 through 2.10. At the surface the mean pressure field has the appearance of a very weak wave south of 14^{o}N. The closed 1007 isobar depends mainly on Kusaie and the downstacking from the slightly more data rich 700 mb chart. The confluence axis varies from 4^{o} to 5^{o}N. Winds north of this line cut the isobars toward lower pressure (except for Ponape). South of the confluence zone the flow is apparently down the pressure gradient into a weak trough south of the confluence axis.

The pressure gradients weaken with increasing height. The confluence axis is visible at 1000 and 850 mb but gives way to difluence

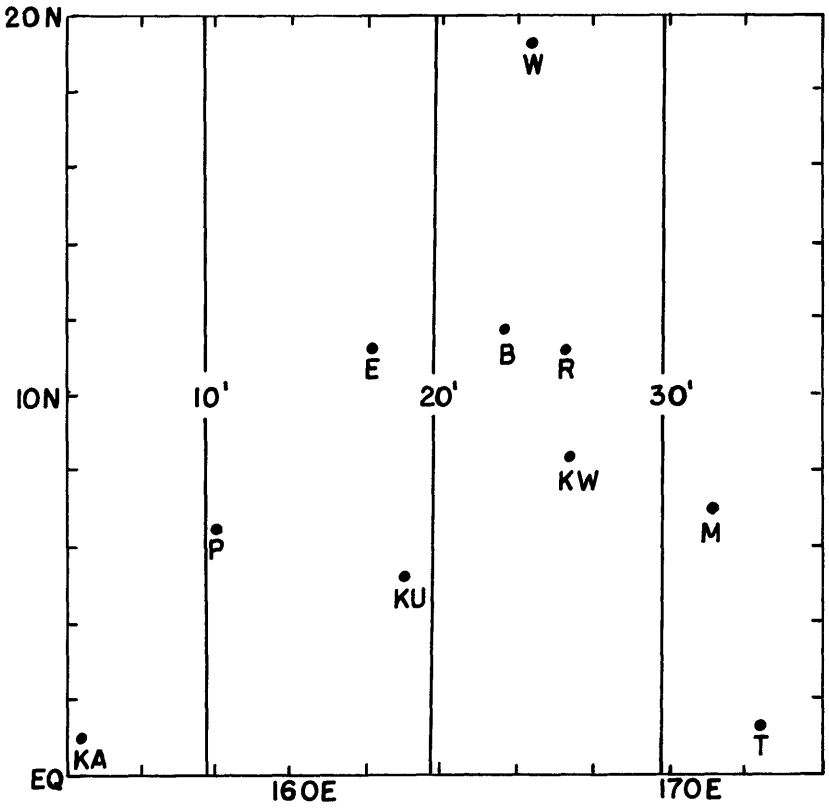

Fig. 2.5. Diurnal pressure wave chart for 0300Z at 500 mb in the Redwing area. Contours are labeled in feet.

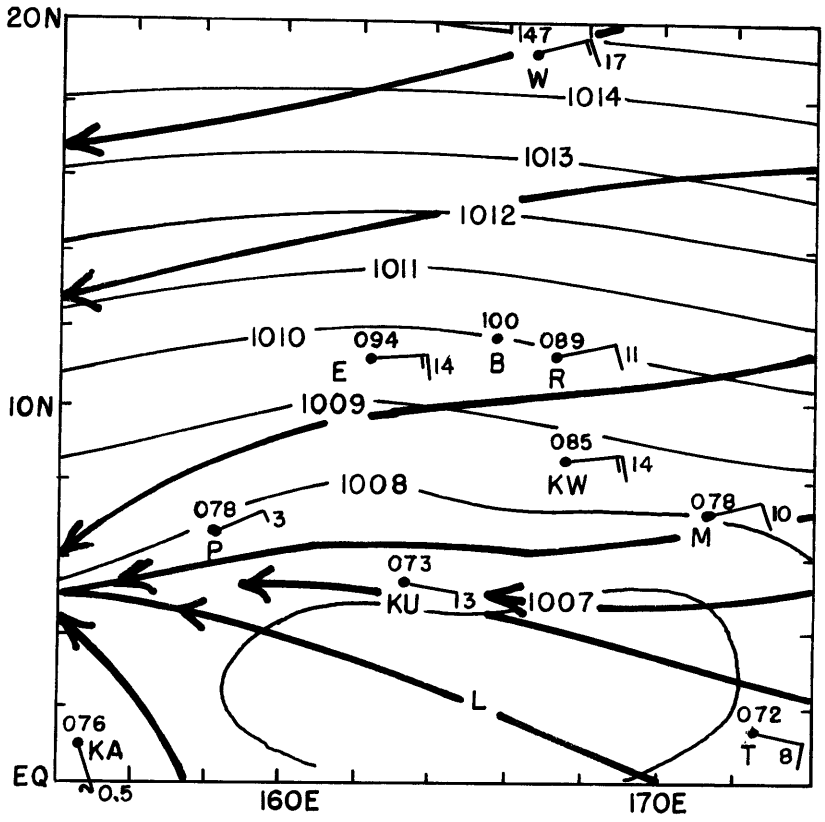

Fig. 2.6. Mean surface chart for May 1956. Heavy lines are streamlines, light lines isobars. Wind speeds are in knots.

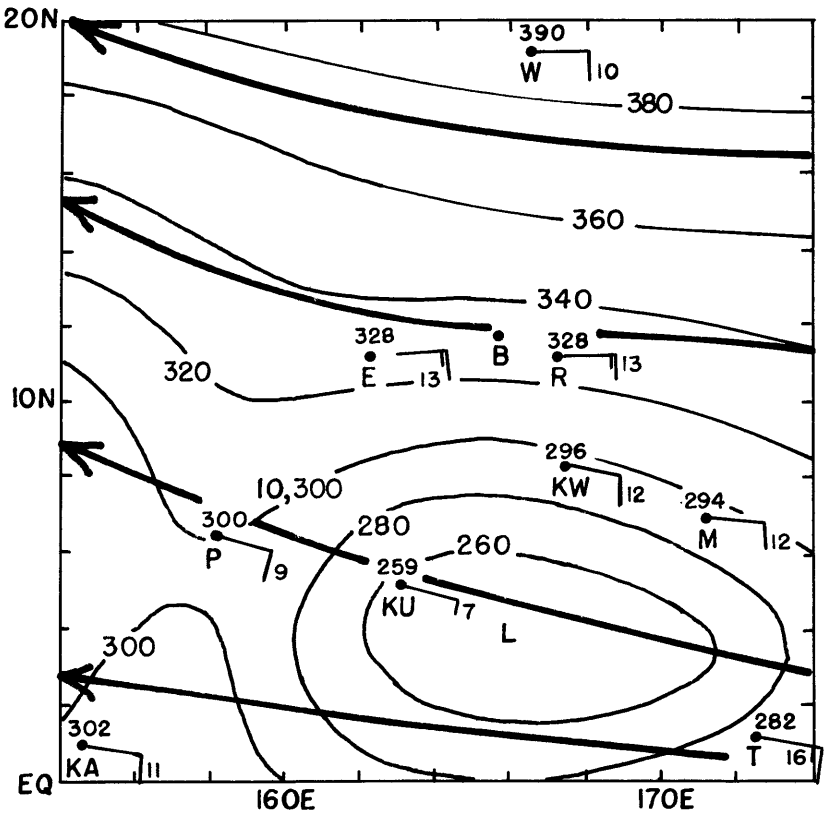

Fig. 2.7. Mean 700 mb chart for May 1956. Heavy lines are streamlines, light lines are contours, heights are in feet.

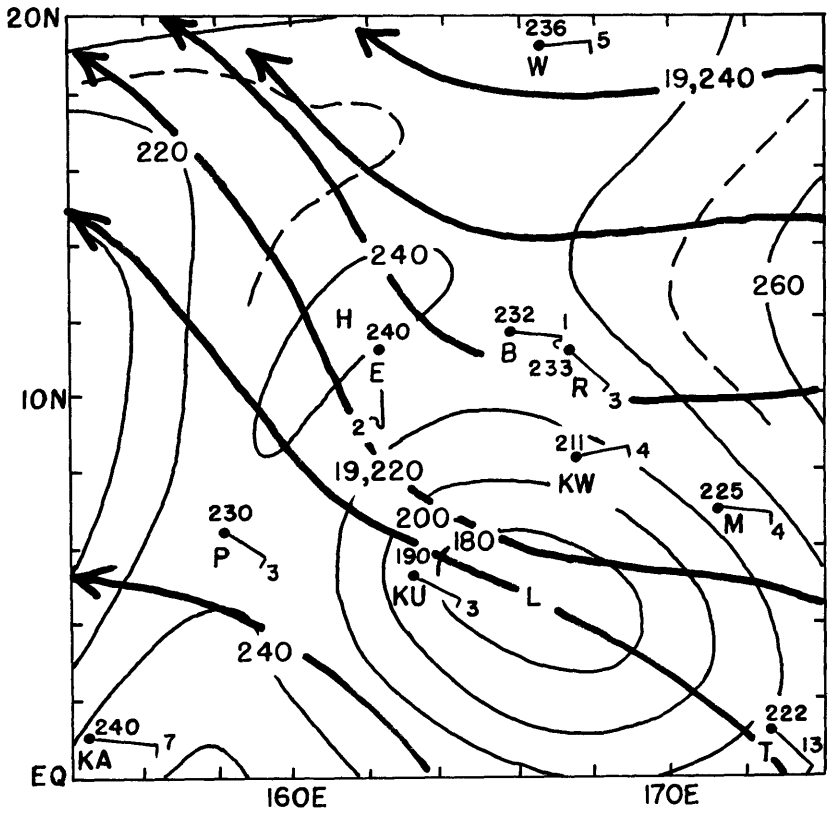

Fig. 2.8. Mean 500 mb chart for May 1956. See Fig. 2.7 for details.

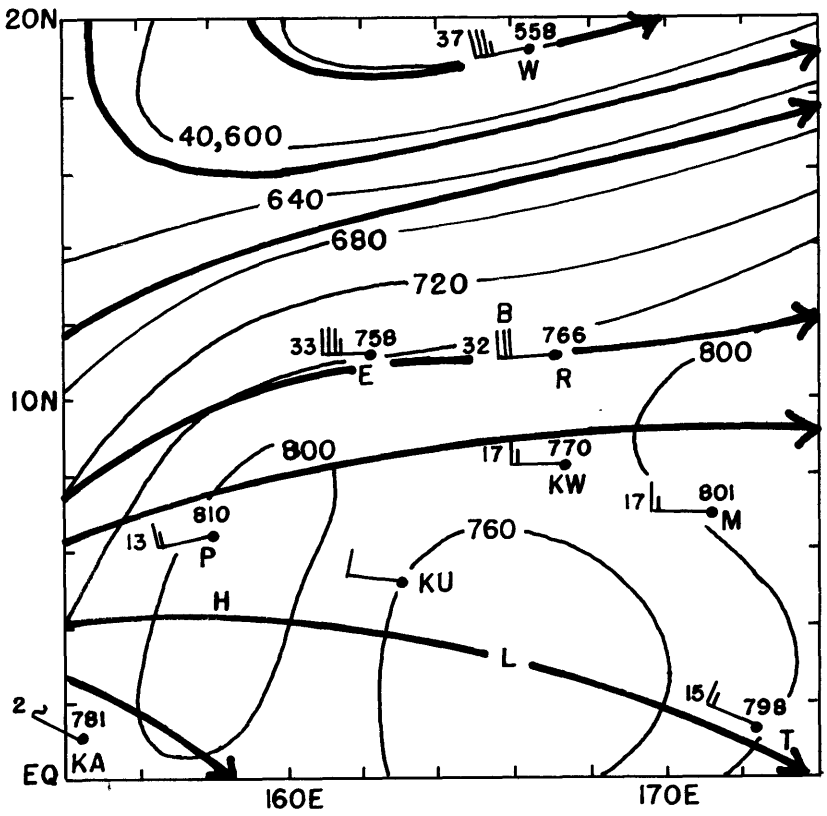

Fig. 2.9. Mean 200 mb chart for May 1956. Note change to 40 ft height increments. See Fig. 2.7 for details.

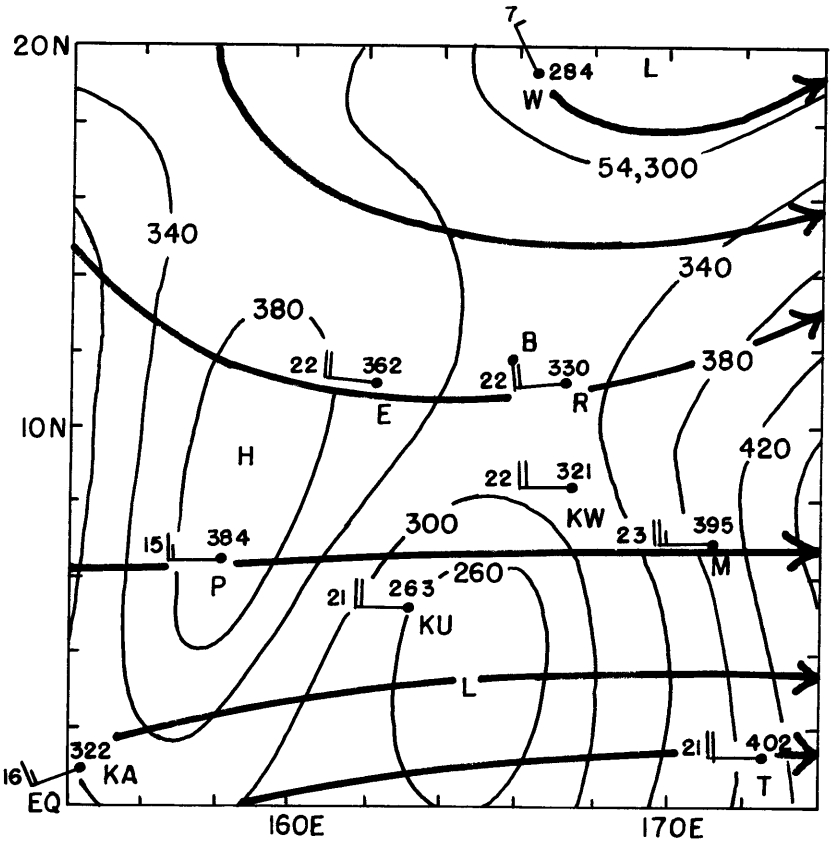

Fig. 2.10. Mean 100 mb chart for May 1956. See Fig. 2.9 for details.

at 700 mb. By 700 mb, the strong trough begins to look more unrealistic vis a vis the winds which exhibit particularly simple streamlines. Winds north of the surface confluence axis veer with height; also note the gentle drift to the north, especially south of 10^{o}N.

The 500 (and 300 mb) surfaces are levels of transition and reversal of the zonal wind. As at other levels, the closed 500 mb low is supported mainly by Kusaie, but even without the latter's value, a trough would be forced by the other stations, though not as deep. At 300 mb (not shown) a weak poleward drift meets stronger westerlies near 10^{o}N. Pressure and wind are well adjusted north of 10^{o}N. A surprisingly sharp trough (for a monthly mean) shows up north of 18^{o}N.

The transition to westerlies is complete by 200 mb. The flow at 200 (and 150 mb) is difluent south of 10^{o}N with substantial anticyclonic shear at that latitude. The low-thickness bias at Truk (off western edge of grid) and Kusaie's influence continue to produce a perturbed height field in the face of a very simple streamline pattern.

The height gradients weaken again at 100 mb as the thermal wind reverses with the transition to the stratosphere. The height analysis looks quite hopeless at this point.

2.1.9. Analyses of Wind Data

Mean horizontal wind depictions were generated in the following manner. At 700 mb, daily wind analyses were made using the sounding, PIBAL and air reconnaissance data; then an average chart of isogons and isotachs was produced. These were also converted to gridded components of u (west to east) and v (south to north) winds. At the other

levels, mean direction and speed data were analyzed and decomposed into u and v components. Figure 2.11 is an example of the analysis of mean u and v fields at 200 mb. Winds and pressures were analyzed separately so that the scale analysis is unbiased.

2.1.10. Summary

We have described the source, time span, and reliability of the Marshall Islands data sample, and discussed the processing and reduction of barometry errors, air reconnaissance data and the diurnal pressure wave. The methods of constructing mean fields of height and wind were described.

In Chapter 3 this data base will be used to construct various fields, profiles and wind roses in order to investigate the balance of forces, the validity of the quasi-geostrophic assumptions and the structure of the boundary layer near the equator. Alghough the constant pressure analyses appear to degenerate hopelessly with altitude, Chapter 3 will show that when these fields are averaged over longitude the geostrophic and thermal winds derived from them will correspond reasonably well with the real mean winds, at least as far south as the mean ITC axis.

2.2. BOMEX, Fourth Phase – 11-28 July, 1969.

Figure 2.12 shows the fixed stations used in this portion of the thesis.

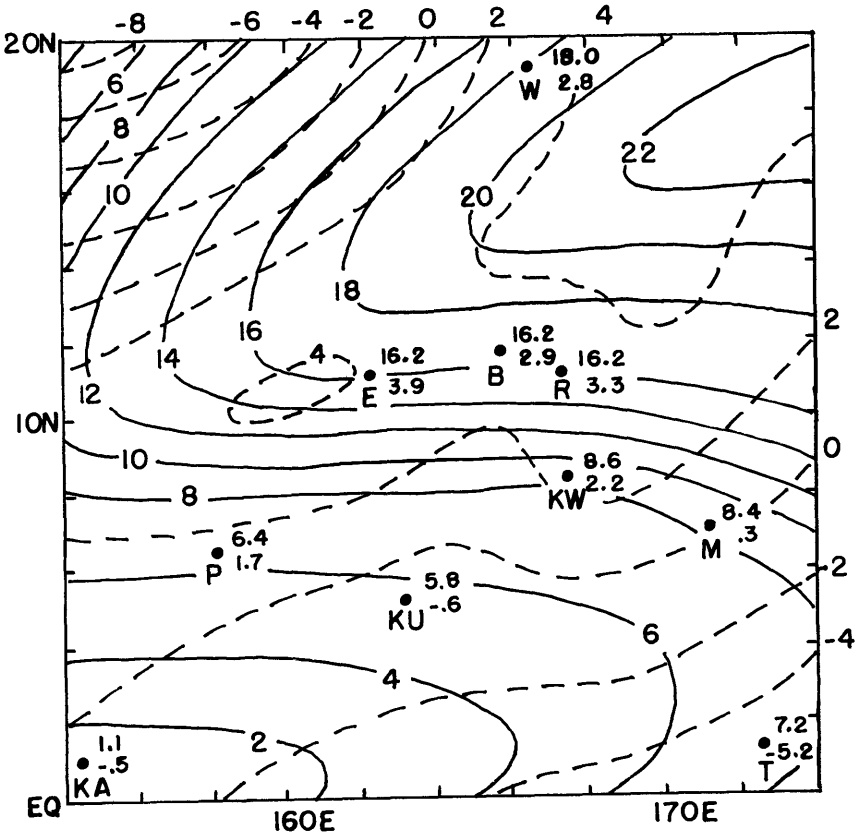

Fig. 2.11. Analysis of mean u (solid) and v (dashed) fields for 0300Z, May 1956 at 200 mb. Units are meters per second.

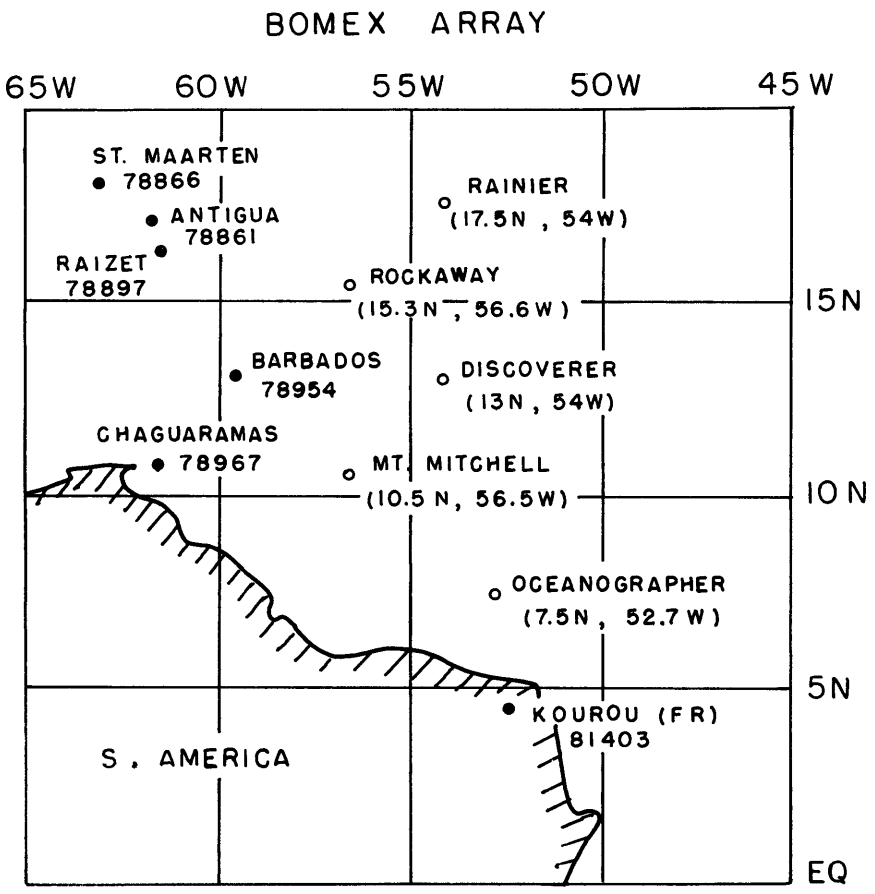

Fig. 2.12. Islands (solid circles) and ships (open circles) that formed the fixed data base during BOMEX Fourth Phase. Block station numbers shown for the islands, location for the ships.

2.2.1. Summary of Data Types

As opposed to the Marshall Islands investigation which considers the entire troposphere as well as the boundary layer, the BOMEX sections are concerned with the layer from the surface to 4500 m (~600 mb). Therefore, only data applying to this range have been used.

Conventional surface reports and Rawinsondes at islands are from the Northern Hemisphere Data Tabs (NHDT). Rawinsondes from Kourou (81403 in Fr. Guiana) were supplied in conventional message form by the Environmental Technical Applications Center (ETAC) of the United States Air Force.

Fixed ship surface synoptic reports and Rawinsondes were from the BOMEX temporary archive (BOMEX Bulletin No. 9, 1971). The rawinsonde data were reduced by NASA's Mississippi Test Facility (NASA/MTF), and are called intermediate or "A_o" data. These data consist of height, pressure, temperature, relative humidity, specific humidity and u, v wind components displayed at five second intervals.

A variety of aircraft-derived data were provided through the BOMAP archives and through personal cooperation between participating institutions. BOMAP provided data from the Navy WC-121 and the USAF WC-130 aircraft in the form of standard RECCO code format (BOMAP, 1971). Woods Hole Oceanographic Institution supplied computer tabulations of meteorological variables at one minute intervals taken from their C-54Q aircraft. For additional details on these flights see Bunker and Chaffee (1970). The National Hurricane Research Laboratory

provided tabulations of the meteorological variables gathered under the NOAA Research Flight Facility (RFF) Airborne Data Collection Program in support of BOMEX. Variables from two DC-6 and one DC-4 aircraft were displayed at 10-sec intervals (Friedman and McFadden, 1970). RECCO coded data from the routine GULL HOTEL flights of the USAF Reconnaissance Program were also available except on 14 July 1969. These data were supplied by USAF/ETAC.

Satellite data were used in two ways: as an observational tool for description of case studies, and as a basis for wind computations. Gridded ESSA-9 glossy prints of the BOMEX area were provided by USAF/ETAC and ATS-III negatives were acquired from the archives at Asheville, N.C. (ATS-III, 1969). Dr. Tetsuya Fujita of the University of Chicago provided low and high level cloud motion vectors for 13, 14 and 25 July, 1969 based on film loop studies using ATS-III imagery. See Fujita (1970) for details on the technique and a BOMEX case study which was also used in this paper (Chapter 5). The Meteorological Satellite Laboratory (MSL/NOAA) provided low, middle and high cloud motion vectors derived from ATS-III imagery on their CBS TV recorder and playback device (Hubert and Whitney, 1971) on 13-15, 22-24 and 26-28 July. The author was privileged to learn the technique at MSL and was able to generate low cloud motion vectors for 17, 18, 20 and 21 July using the MSL device. Suitable ATS-III pictures were not available on 16, 19 and 25 July.

Sections 2.2.2-4 describe these data bases in more detail and point out problems that were correctable and uncertainties that remain.

2.2.2. Surface Synoptic and Rawinsonde Data

Ship Synoptic Data posed no problems in terms of data reduction; however, sea level pressures were probably in need of calibration (see Section 4.1.2). Island Rawinsonde data from the NHDT were assumed to have no correctable errors; however, the fixed ship A_o Rawinsonde data were another matter. A_o winds were not corrected for ship's motion because all ships kept station by alternately drifting and steaming due to the failure of their sea anchors (BOMAP, 1971). Winds from Rockaway are missing below ~1800 m on most days. Three other uncorrected errors can exist in the A_o records: bad temperatures or humidities whenever a radiometersonde is flown along with the normal sonde (Applied to Discoverer and Rainier only in this paper); bad wind components due to loss of the 0^o-azimuth reference (Rainier only); and bad relative (and specific) humidities due to frequency doubling and the recently discovered diurnal humidity bias in American sondes (Teweles, 1970). These errors will be investigated and eventually corrected by the BOMAP Office as one of the steps in producing the final data archives. The author received from the BOMAP Office copies of the sounding logs which were kept by the observers for the flight of each sonde. Thus it was possible to know when a radiometersonde was flown, when relative humidity frequencies doubled and what azimuth value to use to correct the Rainier winds. The radiometersonde interference would generate abnormal spikes in the detailed plots of either temperature or humidity. These are easy to spot and can be avoided by "drawing through" the gap. Unfortunately, virtual temperatures containing spikes were used to

generate the A_o pressure height values. Since the author chose to work with constant height surfaces this meant that pressure values at these heights were off (by as much as 5-10 mb) and this showed up in the author's potential temperature computations. It was therefore necessary to recompute thicknesses from the corrected soundings for approximately 50% of the Discoverer and Rainier flights, a rather unexpected and time consuming nuisance factor.

Frequency doubling was corrected by using the accompanying graph (Fig. 2.13) also supplied by the BOMAP Office. Clearly, from the example on the graph this correction can easily raise the relative humidity by 20 percent or more.

The diurnal relative humidity bias is due to solar radiation reflecting into the ventilation duct on the body of the sonde. An uncorrected time section analysis of relative humidity for Mt. Mitchell demonstrated that the diurnal bias can completely dominate all but the most intense humidity variations. Recent work by Ostapoff who compared flights of biased and unbiased sondes resulted in the correction curve shown in Fig. 2.14.* BOMAP suggested that this be used on all daylight soundings regardless of time of day or cloud cover even though this is an oversimplification of the problem. Subsequent time sections using the correction on 12-21Z soundings showed only a trace of the diurnal error. Chapter 4 discusses these time sections in more detail. An example of a time section set is shown in Appendix II.

*Data supplied by Mr. S. Williams at BOMAP.

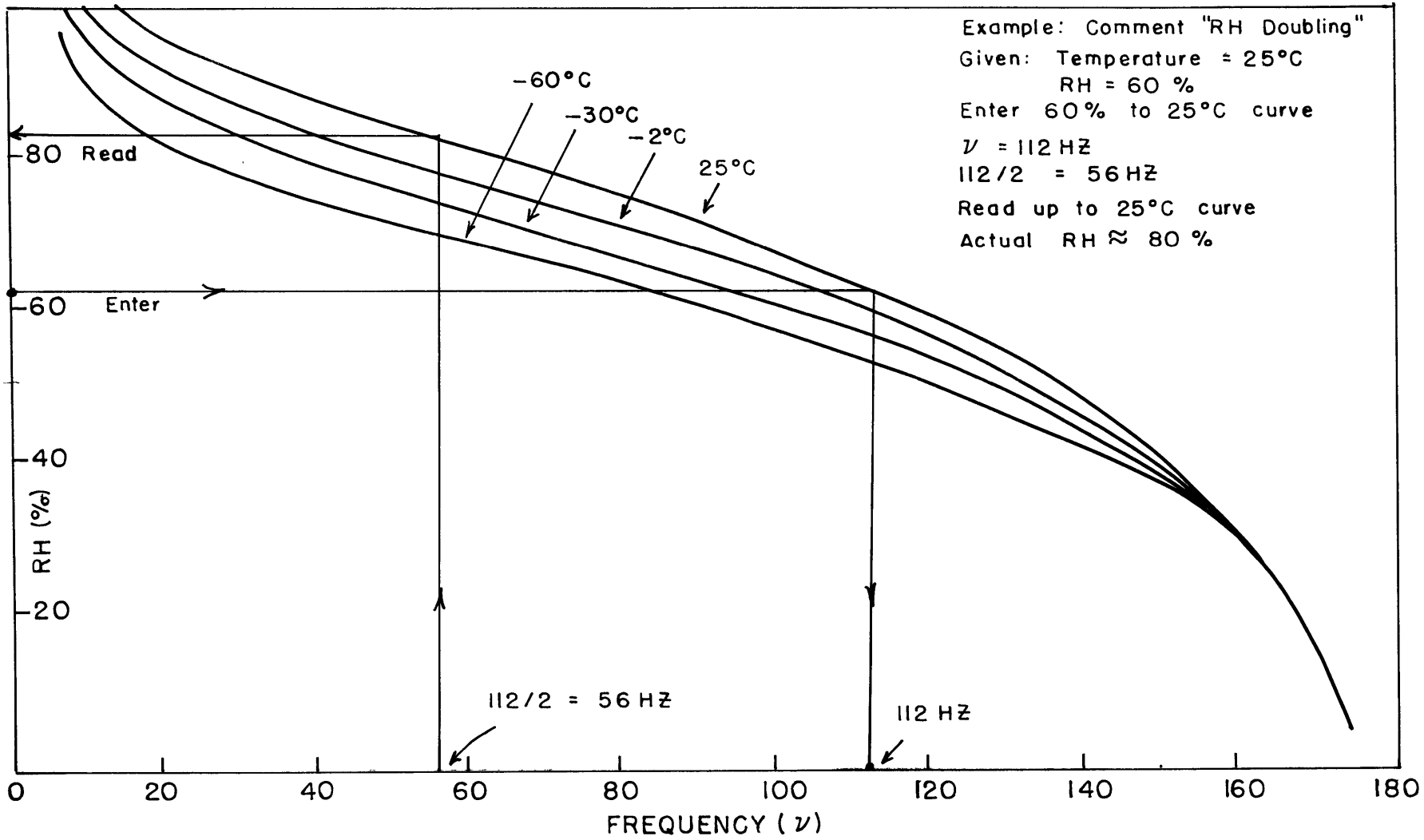

Fig. 2.13. Graph used to correct A_o rawinsonde relative humidity values for "frequency doubling".

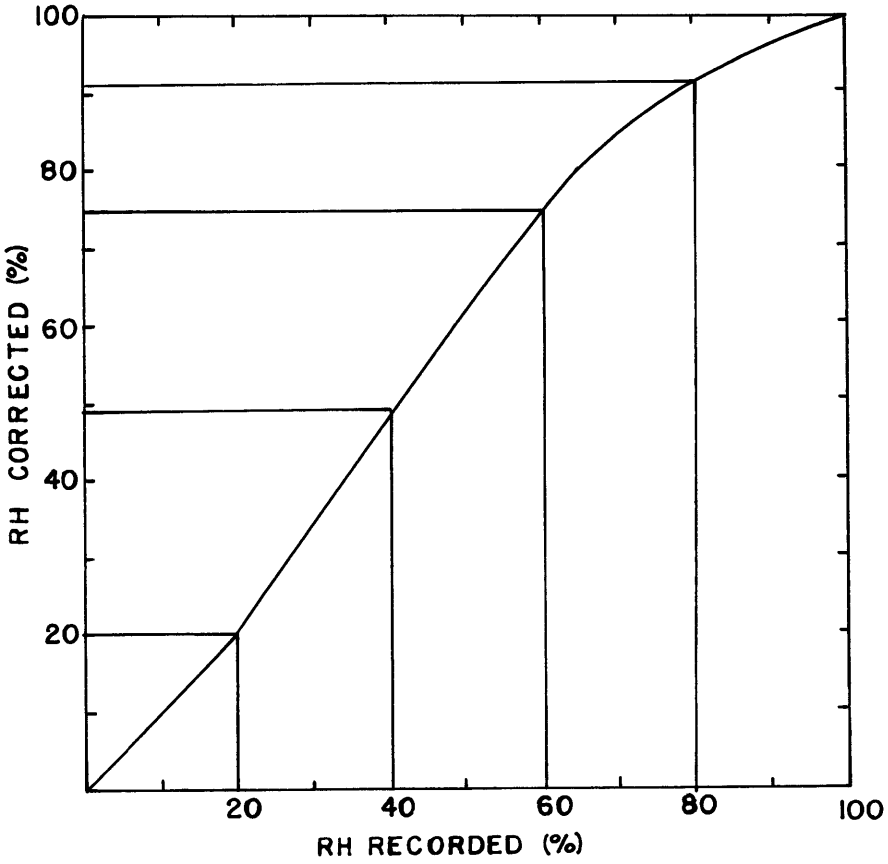

Fig. 2.14. Correction curve for diurnal relative humidity bias. Use only in daylight hours.

The wind direction problem at Rainier was resolved by convert- the given u,v components to direction and speed and subtracting from the original direction a value given on the log forms of either 140 or 220 degrees.

The author checked, corrected and punched the complete Fourth Phase A_o Rawinsonde series at 250 m increments up to 2 KM and at 500 m increments from 2.5 KM through 4.5 KM for the three low latitude ships Discoverer, Mt. Mitchell and Oceanographer. Specific humidities were not corrected on the cards when adjustments to either temperature or relative humidity were made and should not be used. However, specific humidity can be generated in a users program with standard formulas. Appendix III shows how to use these punched cards.

It was found by considerable sampling and cross-checking that the A_o wind values at Discoverer were in poor agreement with the transmitted teletype messages. This was based on a subjective estimate of how well the total soundings agreed to within $\pm$ 10° and/or $\pm$ 1 m/s at the levels in common. On a subjective scale of "Poor, Fair, Good and Excellent", only about 50 percent of Discoverer's A_o winds were judged at least "Good". On advice from the BOMAP staff member in charge of the Rawinsonde processing*, it was assumed that the professional shipboard observers would make all known corrections (including ship motion); hence, teletype winds were substituted for A_o winds in the Discoverer deck. It was necessary to use linear interpolation of the u,v components

*Mr. Scott Williams, BOMAP, personal communication

to transform the pressure level data from the messages into the metric levels previously noted.

The ship motion problem was not successfully solved. The author tried to derive corrections from the hourly Fixed-Ship Operations Data (which contains a mix of either the course and speed averaged over the previous hour or, if there were significant course changes, the instantaneous course and speed on the hour) and the Boom Surface Meteorological Measurements which contain gyro-heading data at 30 sec intervals but no ship speed data (BOMAP 1971). After considerable effort and several consultations with the BOMAP Office, no systematic correction technique was deduced*. The primary difficulty lies in the fact that "heading" and "course" information rarely correlated. Because tabulated ship speeds were nearly always small (0-2 knots) at Mt. Mitchell and Oceanographer, and on the assumption that Discoverer's teletype winds included the correction, the punched data were not corrected for this uncertainty. Also, when Rockaway and Rainier winds were needed, they were taken from the teletype messages unless only A_o values were available. After many frustrating reanalyses, the author recommends that Rockaway A_o wind data should never be used.

Any investigators who choose to work with BOMEX data of any form should become familiar with the qualifications and exceptions discussed in the archive documentation (BOMAP, 1971).

---

*Mr. Delver at BOMAP has had modest success in eliminating ship motion errors. Watch BOMAP Weekly Progress Reports for developments.

2.2.3. Aircraft Data

RFF aircraft data available to the author had been thoroughly processed at NHRL, so that in theory no further modification of these data would be necessary. The only exception is in the wind reporting. Two different Doppler systems were employed, the APN-153 and APN-82 were both on the two DC-6's (known as the A and B planes) but only the APN-153 was on the DC-4 (known as the E plane). Often, simultaneous winds reported by the two different systems would conflict by tens of degrees and several meters per second. Also, both instruments exhibited a substantial high frequency noise component even though eleven one-second values are averaged to form the 10-sec data. The APN-82 generally showed less noise than the APN-153 and seemed to correlate better with the fixed ship wind reports in the immediate vicinity of the aircraft. For day-to-day consistency, and because they were less noisy, the APN-82 data were chosen as the primary source of winds from the A and B planes. The APN-153 was the only source on the E-plane. For plotting purposes, 10-sec spot winds were used if a subjective estimate of the variability of the winds within $\pm$ 90-sec was small. If the estimated vector deviation in this three minute period was greater than $\sim$ 1-2 m/s, then an estimate of a representative wind was plotted. Three minutes at cruising speed corresponds to about 18 KM; thus the extra smoothing filters out minor perturbations on a thunderstorm scale but not on a cloud cluster or organized ITC cloud band scale.

The Doppler winds from the WHOI C-54 flights appeared to pose no problems for meso-scale analysis purposes.

RECCO winds in their original form from the WC-121 and WC-130 aircraft data supplied by BOMAP required considerable correction. In most missions when the aircraft changed course to another flight leg the wind vector changed, often through several tens of degrees and a few meters per second. By assuming an aircraft speed error (either in true air speed (TAS) or groundspeed (GS)) it is possible to solve for the error vectorially using the reported winds just before and after the turn. The computed error can then be checked against errors determined at other corners. Also, the complete navigation logs were available to the author and these had data from "calibration boxes" flown at the corners of the flight paths. A calibration box is a closed rectangular path which provides a chance to form the line integral of the wind components tangent and normal to the path. Assuming that the box encloses a field of equal wind vectors, the residual from the line integrals will give the speed (tangential) and drift (normal) errors in the aircraft instruments. Also, the flights generally overflew one or more fixed ships, often near in time to a Rawinsonde flight; thus another calibration was possible. The author also noted that when the sea was reported as calm, the Doppler winds were more suspect due to the lack of specular reflection from the sea surface. For example, on 14 July, the first calibration box yielded a speed "error" of 1.1 m/s (TAS reads too high) at 12^{o}N, 46^{o}W with surface winds 080^{o}/7.5 m/s (waves present). But the second box at 7^{o}N, 49^{o}W yielded a speed error of 3.8 m/s with light and variable surface winds and a comment in the navigation logs an hour before the

box stating, "8-10 sec intermittent Doppler". Also, a 1.1 m/s reduction in TAS made a better correction to the WC-121 wind as it overflew Discoverer than would the 3.8 m/s correction. Thus the author chose 1.1 m/s for use in his renavigation of all winds for this flight. Similar judgments were made for each WC-121 and WC-130 flight during the period chosen for meso scale analyses to be discussed in Chapter 5. The largest TAS "error" was 2.5 m/s for the WC-121 flight of 17 July.

The Gull Hotel reconnaissance flight winds seemed satisfactory when compared to the overall synoptic situations with one exception. On 19 July, calibration against the synoptic continuity for 18 and 20 July and the Rainier soundings for 19 July indicated a TAS error of 4 m/s! This correction was applied and, in the author's opinion, significantly improved the analysis.

2.2.4. Satellite Data

The ESSA-9 polar orbiting satellite carries the Advanced Vidicon Camera System (AVCS) with resolution of nearly one mile at nadir. Gridded glossy prints were used to study the meso-scale structure of cloud systems and as a basis for the neph analyses shown in Chapter 5. It is clear from landmarks and from comparisons with aircraft penetrations that significant cloud features have been located to within a tolerance of order 15 nm. It is generally possible to distinguish between cirriform and cumuliform clouds by observing brightness variations, fine structure (soft vs. hard outlines, filaments etc.) and frequent shadows cast by the penetrative towers. Also, the aircraft and synoptic observations provide ground truth background data.

Occasional middle clouds are difficult to define without the aid of corroborating conventional data. However, middle clouds are mainly associated with the traveling, mid-tropospheric disturbances north of the ITC (e.g. see Fernandez-Partagas and Estoque, 1970; Burpee, 1971; and Carlson, 1969 for examples of current studies of the structure of disturbances in the trades), but middle clouds can produce an uncertainty near the equator in the surround of mature ITC cloud bands and cumulus clusters. ESSA-9 imagery should be capable of resolving some individual cumulus congestus ($C_L 2$) and cumulonimbus ($C_L 3$ and $C_L 9$), and organized patches of most other cloud types with the exception of thin cirriform clouds.

ATS-III was moved temporarily to a sub-satellite point (SSP) of approximately 46^{o}W longitude for the Fourth Phase activities. Low cloud motion vectors derived from ATS-III imagery may suffer from several possible error inputs: registration errors, image quality and distortion, improper designation of cloud type, effects of vertical wind shear on cloud propagation, and the inability to separate cloud advection from cloud generation over a period of several hours. Each of these is briefly discussed as follows.

Registration is defined here as the act of fitting an ATS-III image to a geographic grid and then consistently fitting the remaining images of a sequence to the same grid. For analysis purposes, it is more critical to minimize the relative errors from image to image than it is to place the entire set accurately on the globe. The most important registration occurs between the first and last images since

the intermediates are used mainly for continuity. A ten mile registration error over a three-hour period amounts to a vector error of about three knots. Given a distortion-free sequence of images and consistent landmarks, the author feels that a three knot vector error is a reasonable estimate. This is the figure also quoted by Fujita (1970) concerning a study using 14 July BOMEX ATS-III data. Hemispheric grids provided by NASA never quite fit the dimensions and landmarks of the images (partially due to drift of the SSP); hence, even with great care, placement error of the entire vector field is probably on the order of 20 nm. From the author's experience working with the TV device at MSL, this placement error is more likely to be in an east-west direction. North-south errors will be near zero at the equator and remain small (although increasing) with increasing latitude through the BOMEX region. Thus, the latitudinal placement of east-west shear zones may be substantially more accurate than location of, say, the axis of a traveling disturbance.

The ATS-III image quality is degraded by poorer resolution (about 2 miles at nadir, Warnecke and Sunderlin, 1968) and by electronic distortion in forming the image (shows up as wavyness in the earth's outline). The first constraint removes most C_L2 and C_L3 targets unless they are in clumps or bands and makes detection of cirrus more difficult. Large C_L3 and C_L9 can be individually resolved but most of the sharp detail is missing. The electronic distortion is not the same from image to image, and when it is present, great care must be taken in interpreting results. Specifically, it appears as an east-west shift

in individual or groups of scan lines. If large scanline displacements occur in either or both of the end images in a sequence, these shifts can add a spurious zonal wind component to targets on the displaced scan lines. At MSL, the first and last images were selected (with the aid of a stereo comparator) to minimize electronic distortion. The process of selection and registration of images can absorb the better part of a working day.

Cloud type definition is easier in the Tropics due to the preponderance of convective activity and/or cirrus of various types. Characteristic shapes and climatology play a role. Also, the author used ESSA-9 photos to aid in the identification process for the cases of 15, 17, 18, 20 and 21 July 1969. Small, bright dot-like targets are most suggestive of cumulus and are very desirable, but they may not survive for the full three hour sequence and are not plentiful in ATS-III images. Cloud bands, clusters or patches can usually be tracked over the full period either by following the edges or internal elements which have persistent signatures. Large shears between low level clouds in the trades and upper level cirrus are important confidence factors. Island cumulus are often quasi-stationary and will not be representative. Trade cumulus and strato-cumulus are also easily identified from their typically "scaly" appearance, and individual clusters (scales) are quite persistent and easily tracked. Also, see Fujita (1969) for a review of the state-of-the-art of cloud motion computation.

Separating cloud development from displacement is not trivial. A cumulus cloud is not an object, rather it is a manifestation of organized, small-scale vertical motion and is composed of a nearly balanced aggregate of eddies made visible by condensation. By definition, the "same" cloud or cloud family cannot be tracked for a period of a few hours, yet ATS-III film and TV loops give the distinct impression that the opposite is true. Frequently, cloud elements form and/or die during an image sequence; however, those that survive throughout are treated as entities and tracked accordingly.

Given that all of the above problems are surmountable, there still remains the fundamental problem of assigning the low cloud motion to the proper level so that these vectors can be blended with conventional ones. In the 9-day case study to be discussed in Chapter 5, 500 meters was chosen to represent the low level flow, thus some rule of thumb is required for adjusting the ATS-III-derived vectors to the 500 m level. Pioneers in this area have found two rough characteristics, namely, clouds move slightly to the right of the "low level" flow and are faster*. The first observation fits in with the notion of Ekman theory since a cumulus large enough to be seen having a typical base at 600 m is probably steered by a vertically averaged wind vector at least part of which is above the active boundary layer. Furthermore, if "low level" flow refers to flow beneath the cloud bases, vertical wind shear could account for the second observation. Currently, A. Timchalk of

---

*Personal communications with Dr. T.T. Fujita, University of Chicago.

MSL is looking at this problem with great care using BOMEX ship soundings and has found several cases where known wind vectors within the trade cloud layer ($\sim$1500 m) fit the ATS-III winds with little error*.

For this thesis, the following empirical approach was used to establish a link to the 500 m level. During the 9-day period of my case study, six days of ATS-III low cloud vector fields were available from Dr. Fujita (13, 14 July) and MSL (13, 14, 15, 18, 20, 21 July). Except for the fact that Fujita's vectors were more plentiful, there was no essential difference in the characteristics of the fields from different sources. Vectors were translated at an east-west rate of 15K to establish a common map time (18Z), then conventional and ATS-III data were compared if they were within a radius of 100 KM. Conventional data includes aircraft winds which were considered to be at 500 m if their altitude was between 250 and 750 m. Whenever several conventional reports clustered within the 100 KM radius, a single mean value was chosen for comparison with the ATS-III vector in the vicinity. Two error quantities were then computed, namely:

$$\Delta\theta = \theta_c - \theta_s \quad \text{and} \quad P_s = 100 \times (S_c - S_s)/S_c ,$$

where θ_c, θ_s, S_c and S_s are the conventional and satellite-derived directions and speeds. Forty-eight comparisons were made and a contingency plot having five degree ($\Delta\theta$) by ten percent (PS) intervals was generated. This was then treated as a two-dimensional probability density field and contoured rather crudely as shown in Fig. 2.15.

*Personal communication

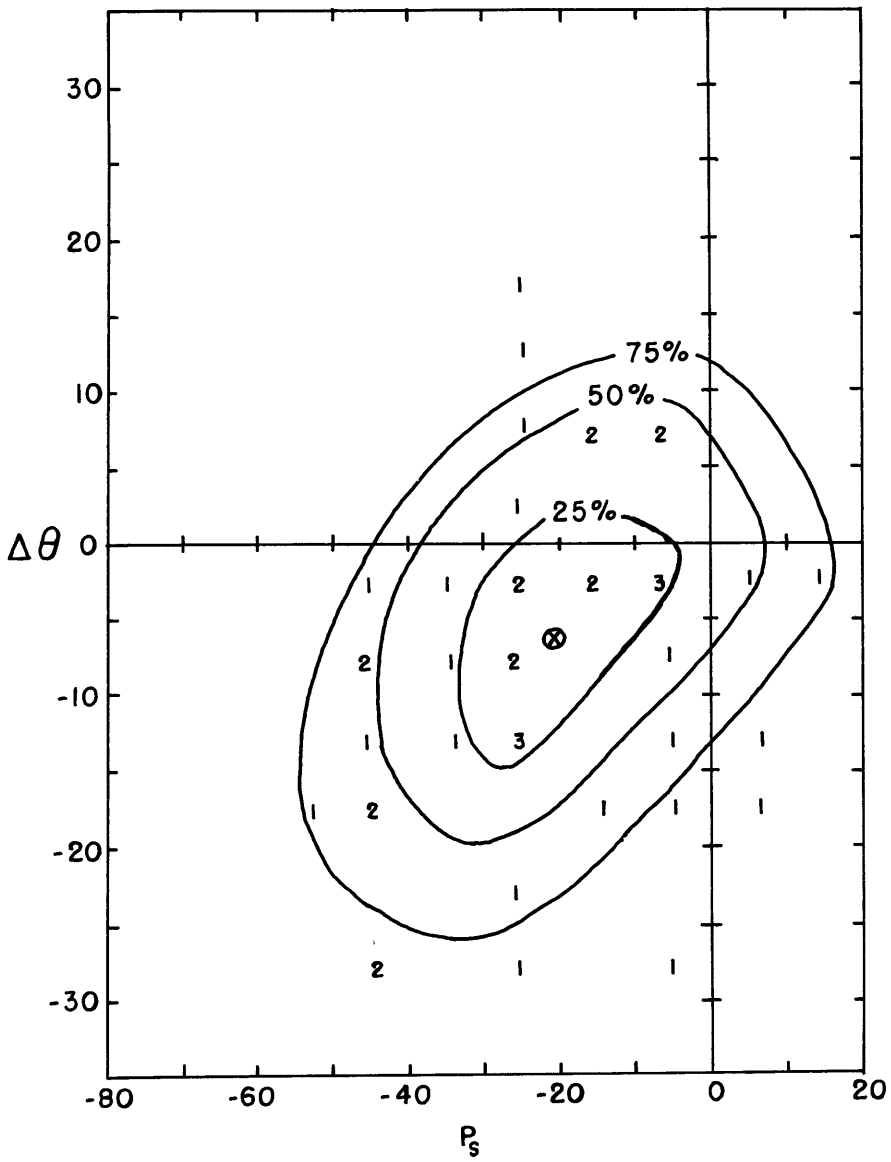

Fig. 2.15. A comparison between ATS-III low level winds and conventional 500 m winds. Axes are normalized speed difference in percent (P_s) and difference in direction in degrees ($\triangle\Theta$). Numbers are cases in each ten percent by five degree category. Contours are interpreted as probability.

The scatter is quite large but it was later noted that this is often due to the light ATS-III winds ($\leq$ 6 m/s). From the centroid of this figure we derive the following formulas to adjust ATS-III winds to fit the 500 m surface:

$$\Theta_A \cong \Theta_S - 7^\circ$$
$$S_A \cong .8 \times S_S \qquad (2.2)$$

Where subscript "A" means "adjusted". Re-examination of the data indicated that light wind directions should be left alone and their speeds adjusted by the following rule:

$$S_A \cong \begin{cases} 4\ m\,s^{-1} & \text{if } 5 \leq S_S \leq 6 \\ 2\ m\,s^{-1} & \text{if } 3 \leq S_S < 5 \\ S_S & \text{if } S_S < 3 \end{cases} \qquad (2.3)$$

The results from Fig. 2.15 corroborate the general characteristics of earlier studies, mainly because the working level is below the cloud base in a layer of vertical speed shear and veering with height, quite characteristic of Ekman behavior.

Aside from an evident mistake on 14 July wherein middle clouds were identified as low clouds (discussed in Chapter 5) the adjusted ATS-III winds proved to be extremely useful for meso-scale analysis in the boundary layer.

2.2.5. Summary of BOMEX Data Processing

The analysis of the planetary boundary layer discussed in Chapter 5 is based in part on BOMEX data of various types, namely: land-and-ship-based rawinsondes, aircraft reports and satellite derived wind vectors and nephanalyses. A_o records from the ships had several problems including uncorrected ship motion, erroneous A_o winds from Discoverer and Rainier, missing low level winds at Rockaway, bad temperatures or relative humidities due to radiometersonde interference at Discoverer and Rockaway, and relative humidity frequency doubling and diurnal trend at each ship. All but ship motion were correctable. Discoverer's winds were taken from teletype messages rather than from the A_o data. The problem at Rainier along with radiometersonde interference and frequency doubling were corrected by referring to the rawinsonde operators logs and appropriate correction curve. The diurnal humidity error was partially overcome using Ostapoff's correction.

Aircraft winds from the RFF and WHOI flights were fairly reliable; however, the Gull Hotel, WC-121 and WC-130 winds were all checked for speed bias and nearly all had to be corrected or recomputed using navigation logs when available.

ESSA 9 imagery was used for nephanalyses and ATS-III provided low cloud motion data. The latter were supplied by Dr. Fujita and/or MSL. The author used MSL's TV device for four of the case study days. An empirical adjustment formula was used to transform ATS-III-derived vectors into 500-meter winds.

Table 2.5 shows the Fourth Phase data types and quantity as applicable to this paper. This represents only a fraction of the total variety of data that were obtained during the Fourth Phase. The low data coverage on 16 and 24 July was due to scheduled rest breaks. The low number of wind soundings at Discoverer (57/100) was due to the use of 6-hr synoptic message winds in place of the more plentiful A_o data. On two of the three days when ATS-III winds were missing (17, 19 July), the WC-121 and WC-130 aircraft flew low latitude missions in the boundary layer and at 700 mb; this was a very fortunate circumstance.

2.3. Line Islands Experiement (LIE).

The Line Islands are located near the equator and some 3000 KM to the east of the Redwing area (see map Fig. 2.16). The LIE was conducted from late February through late April 1967. Soundings of excellent quality were taken every 3 or 6 hours at each island during the period. For specific details as to data content and processing see Zipser and Taylor (1968) and Madden et. al. (1971). Wind and humidity data from the LIE will be used in Chapter 4 for comparison with Redwing and BOMEX boundary layer characteristics. Because of the care exercised by the NCAR group in processing these data, the author could find only two qualifications to be considered. First, the diurnal Relative Humidity bias exists in these data as it did in BOMEX. Fortunately, NCAR provided separate statistical summaries for each 6-hourly synoptic time so only night-time humidity values (06 and

JULY 1969 - FOURTH PHASE DATES

SOURCE	REMARKS	← THESIS CASE STUDY →																TOT.
		13	14	15	16	17	18	19	20	21	22	23	24	25	26	27	28	
Island RWS*	NUMBER	8	8	8	8	8	8	8	8	8	8	8	8	8	8	8	8	128
Kourou RWS	PER	2	1	0	2	1	0	2	1	1	2	1	1	2	1	0	1	18
Rainier RWS		7	5	3	0	4	6	6	7	4	5	6	2	4	5	4	7	75
Rockaway RWS	DAY	7	4	7	0	2	8	8	8	8	6	8	3	7	3	5	7	91
Discover. RWS	(T/W)	8/4	5/4	6/4	0/0	4/4	7/4	7/4	8/4	9/4	6/4	10/4	4/3	8/2	4/4	4/4	10/4	100/57
Mt. Mit. RWS	(T/W)	7/5	5/4	7/6	0/0	3/0	8/8	7/7	7/7	5/2	6/3	6/5	2/1	6/6	4/4	5/4	6/6	84/68
Oceanog. RWS	(T/W)	6/5	4/4	2/2	0/0	3/3	8/8	8/8	7/4	6/6	6/4	8/7	3/3	7/7	4/3	5/5	6/6	80/75
Gull Hotel	X = FLEW	X		X	X	X	X	X	X	X	X	X	X	X	X	X	X	15
RFF A-Plane	HOURS	10.8	11.1				9.4		7.1			11.1		12.3	11.6		9.8	83.2
RFF B-Plane	FLOWN	10.7	11.0				10.7		7.5			10.1			10.3	0.6		60.9
RFF E-Plane	PER	5.3		5.7			10.7			5.0		11.2			11.2	3.6		52.7
WHOI C-54	MISSION	6.2		5.2			5.5			5.8		6.5		4.5			5.3	39.0
NAVY WC-121			10.8			10.1		11.6		5.1	9.0				10.8			57.4
USAF WC-130		8	8			10		10			8	6			7	7	3	67.0
ESSA-9 PICS	X = AVAIL.	X	X	X	X	X	X	X	X	X	X	X	X	X	X	X	X	16
ATS-III Wind:																		
FUJITA		X	X												X			3
MSL		X	X	A			A		A	A	X	X			X	X	X	11
		← THESIS CASE STUDY →																

*Refers to St. Marteen, Antigua, Raizet, Barbados, Chaguramas data from NHDT, totals only.

T = No. of thermodynamic soundings /W = No. of wind soundings used in time cross-sections.

A = Computed by author

Table 2.5. Summary of data availability as applied to this thesis. Beyond 21 July, only the three ships with (T/W) were used for time sections and statistics.

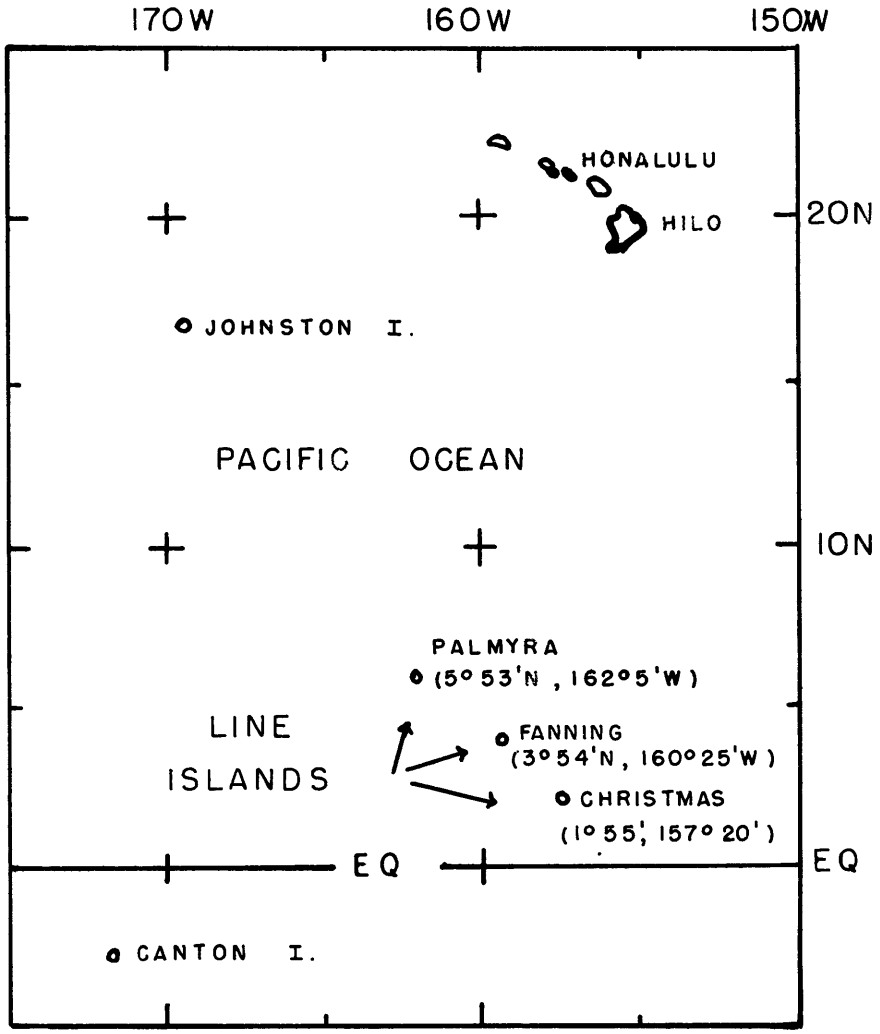

Fig. 2.16. Map of the general area surrounding the Line Islands, and the three islands used in this paper (arrows).

12Z) are used and should be more representative. Second, as pointed out by Estoque (1971), at Christmas Island there is an unresolved directional bias of about 10^{o} between the mean winds taken with the rawindsonde equipment (which form the basis for my LIE study) and the double theodolite winds (PIBALS) taken for Estoque's project during the same period in March and April 1967. The mean hodographs are virtually identical except that up to 2 km the PIBAL winds are from ESE and from 500 m to 2 km the RAWINS are from ENE.

The stratification of the LIE wind statistics was provided by NCAR at the author's request. Their cooperation is greatly appreciated.

CHAPTER 3

CHARACTERIZATION OF THE TROPOSPHERIC FLOW AND PLANETARY BOUNDARY LAYER IN THE MARSHALL ISLANDS - MAY 1956

3.1. General

This chapter primarily emphasizes the kinematics of the tropical troposphere and especially the near-equatorial boundary layer. Although the data are used to form a composite for a particular month (May 1956), the brevity of the sample and the relative quiescence of this particular period give the analysis the flavor of a "case study". An empirical scale analysis is used to test the validity of quasi-geostrophic theory at very low latitudes through the entire troposphere, then we shall look in detail at the lowest three kilometers for evidence of Ekman-like boundary layering and how this changes as the equator is approached. In subsequent chapters, these data will be compared with LIE and BOMEX results.

3.2. Scale Analysis of Terms in the Horizontal Equations of Motion

3.2.1. The Basic Equations.

In an x, y, z system, the horizontal equations of motion are written:

$$\frac{du}{dt} - (uv\tan\phi)/a + uw/a - fv + jw - P_x = 0 \qquad (3.1)$$

$$\frac{dv}{dt} + (u^2\tan\phi)/a + vw/a + fu - P_y = 0 \qquad (3.2)$$

Here, x and y are coordinate in the directions of east and north respectively; u and v are the corresponding horizontal velocity components, and w is vertical velocity normal to a hypothetical sea surface and positive upward. Also, "a" is the mean radius of the earth and P_x and P_y are the horizontal components of the pressure-gradient force per unit mass. We further define: Ω = angular rotation of the earth, $f = 2\Omega\sin\phi$, $j = 2\Omega\cos\phi$, and the operator $\frac{d}{dt} \equiv \frac{\partial}{\partial t} + u\frac{\partial}{\partial x} + v\frac{\partial}{\partial y} + w\frac{\partial}{\partial z}$

Comparing $\frac{uv}{a}\tan\phi$ with $2\Omega v \sin\phi$ from (3.1), we find that where $v \neq 0$, the former term is important only when

$u/a \sim 2\Omega = 14.58 \times 10^{-5} s^{-1}$ or $u \sim 14.58 \times 6.3 \times 10 = 900\ ms^{-1}$.

Since u-max at these latitudes is on the order of 25 ms^{-1}, the $\tan\phi/a$ term will be dropped. Similarly, the $u^2 \tan\phi/a$ term may be compared with fu and dropped from (3.2). Terms uw/a and vw/a are dropped due to their small absolute magnitude. The jw term gains in importance very near the equator. For example, if $v \sim 1 ms^{-1}$ and $w \sim 10^{-2}\ ms^{-1}$, then $jw \sim fv$ near $1^{o}N$ and this term will be retained. With these changes, (3.1) and (3.2) are written:

$$du/dt - fv + jw - P_x = 0 \qquad (3.1a)$$

$$dv/dt + fu - P_y = 0 \qquad (3.2a)$$

3.2.2. Time-Space Averaging

In many studies of tropical phenomena, meridional cross-sections of pertinent variables are constructed. If these sections are derived by zonal averaging around the entire earth's circumference relatively

narrow features such as the ITC, or the sub-tropical jet may be "smeared" out due to their north-south variability with longitude. Since May 1956 was reasonably quiescent and the longitudinal extent of the analysis region is relatively small, meridional cross-sections produced by zonal averaging of data from the horizontal analyses will combine the virtues of smoothing of analysis errors with the detail of a single-meridian cross-section. Of course, longitudinal averaging creates an additional set of eddy stress terms, but these are easily evaluated once the data are in the digital computer.

We define time and space mean operations on any variable as:

$$\bar{\phi} = \frac{1}{T}\int_0^T \phi \, dt \tag{3.3}$$

$$[\phi] = \frac{1}{L}\int_0^L \phi \, dx \tag{3.4}$$

Also, variables are separated into mean and perturbation quantities:

$$\phi = \bar{\phi} + \phi' \tag{3.5}$$

where a prime denotes a deviation from the time average, and:

$$\bar{\phi} = [\bar{\phi}] + \bar{\phi}^* \tag{3.6}$$

where an asterisk denotes a deviation from the space average. We substitute (3.5) into (3.1a) and (3.2a) and apply (3.3) and then substitute (3.6) and apply (3.4) in that order to derive the desired form of the equations of motion:

$$[\bar{u}](\bar{u}_L-\bar{u}_o)/L+[\bar{v}]\partial[\bar{u}]/\partial y+[\bar{w}]\partial[\bar{u}]/\partial z-f[\bar{v}]+$$

$$j[\bar{w}]+(1/\rho_s)(\bar{p}_L-\bar{p}_o)/L+(\bar{u}^{*2}_L-\bar{u}^{*2}_o)/L+(\overline{u'^2_L}-\overline{u'^2_o})/L+$$

$$\partial/\partial y[\bar{u}^*\bar{v}^*+\overline{u'v'}]=-(1/\rho_s)\partial/\partial z[\rho_s\overline{u'w'}+\rho_s\bar{w}^*\bar{u}^*] \qquad (3.7)$$

$$[\bar{u}](\bar{v}_L-\bar{v}_o)/L+[\bar{v}]\partial[\bar{v}]/\partial y+[\bar{w}]\partial[\bar{v}]/\partial z+f[\bar{u}]+$$

$$(1/\rho_s)\partial[\bar{p}]/\partial y+(\bar{u}^*\bar{v}^*_L-\bar{u}^*\bar{v}^*_o)/L+(\overline{u'v'_L}-\overline{u'v'_o})/L+$$

$$\partial/\partial y[\bar{v}^{*2}+\overline{v'^2}]=-(1/\rho_s)\partial/\partial z[\rho_s\overline{v'w'}+\rho_s\bar{v}^*\bar{w}^*] \qquad (3.8)$$

In the above derivation, it is assumed that the density (ρ_s) is a "standard" function of z only; hence, the continuity equation takes the form:

$$\rho_s\left(\frac{\partial u}{\partial x}+\frac{\partial v}{\partial y}\right)+\frac{\partial \rho_s w}{\partial z}=0 \qquad (3.9)$$

In the tropics this is quite satisfactory. Note also that the pressure gradient terms on a z-surface are given explicitly; however, in actual practice, the approximations

$$\frac{1}{\rho_s}\left[\frac{\partial\bar{p}}{\partial x}\right]_z\cong g\left[\frac{\partial\bar{z}}{\partial x}\right]_p=g(z_L-z_o)/L \qquad (3.10)$$

$$\frac{1}{\rho_s}\left[\frac{\partial\bar{p}}{\partial y}\right]_z\cong g\left[\frac{\partial\bar{z}}{\partial y}\right]_p=g\frac{\partial}{\partial y}[\bar{z}] \qquad (3.11)$$

were used for evaluation purposes. The time and space mean local time derivatives take the form $\left[\frac{u_T-u_o}{T}\right]$ and $\left[\frac{v_T-v_o}{T}\right]$ and were dropped

because their maximum magnitude would be of order $10\ ms^{-1}/30 \times 86{,}400\ sec \sim 4 \times 10^{-6}\ ms^{-2}$ versus anticipated Coriolis terms of order 10^{-5} or greater. A few spot checks of $\overline{\frac{\partial u}{\partial t}}$ and $\overline{\frac{\partial v}{\partial t}}$ at stations near the more variable ITC region verified this assumption at both low and high levels, but this is a weakness at the equator where these terms should be considered.

3.2.3. Computation of Vertical Motion

Applying the time-space perturbation integration procedure to the equation of continuity (3.9), we have:

$$\rho_s\left(\frac{\bar{u}_L - \bar{u}_o}{L} + \frac{\partial}{\partial y}[\bar{v}]\right) + \frac{\partial}{\partial z}\left(\rho_s[\bar{w}]\right) = 0 \qquad (3.12)$$

Note that we have neglected the small effect of possible correlations of ρ_s and w. In order to evaluate vertical motion, the first term in parenthesis was manually picked off of the $\bar{u}$, $\bar{v}$ analyses (described in the previous chapter) at even latitudes, and the second term was taken from the $[\bar{v}]$ cross-section, Fig. 3.1, using centered differences. These terms were combined to from a cross-section of the quasi-horizontal velocity divergence. The analysis of this field is shown as Fig. 3.2.

If we divide both sides of (3.12) by ρ_o, a constant sea level value of the density, and integrate vertically we have at height h:

$$\int_0^h \frac{\rho_s}{\rho_o}\left[\overline{\nabla_2 \cdot \mathbf{V}}\right] dz = -\frac{\rho_s(h)}{\rho_o}[\bar{w}]_h \qquad (3.13)$$

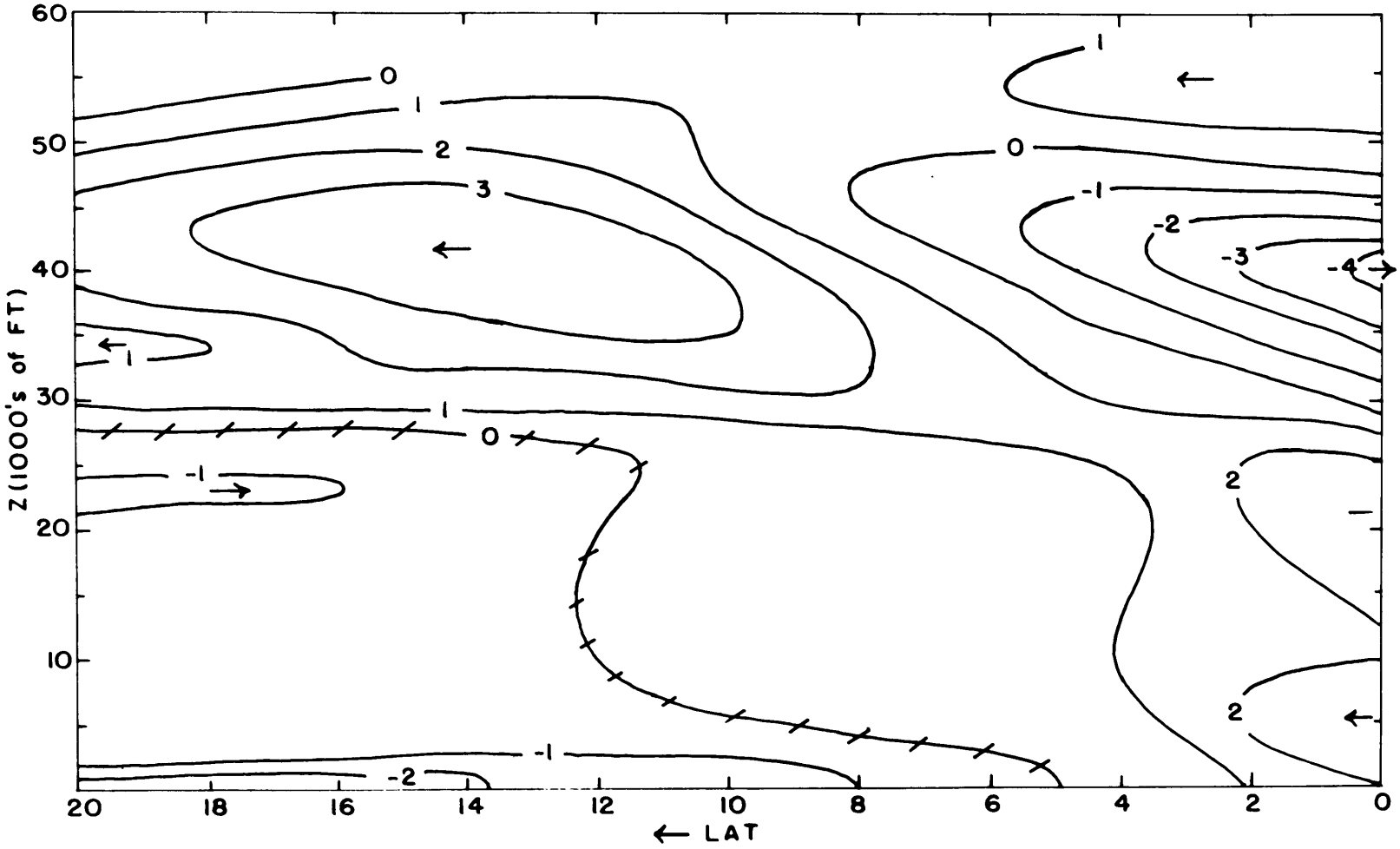

Fig. 3.1. Cross-section of $[\overline{v}]$ for 0300Z, May 1956 Redwing data. Units are m s^{-1}.

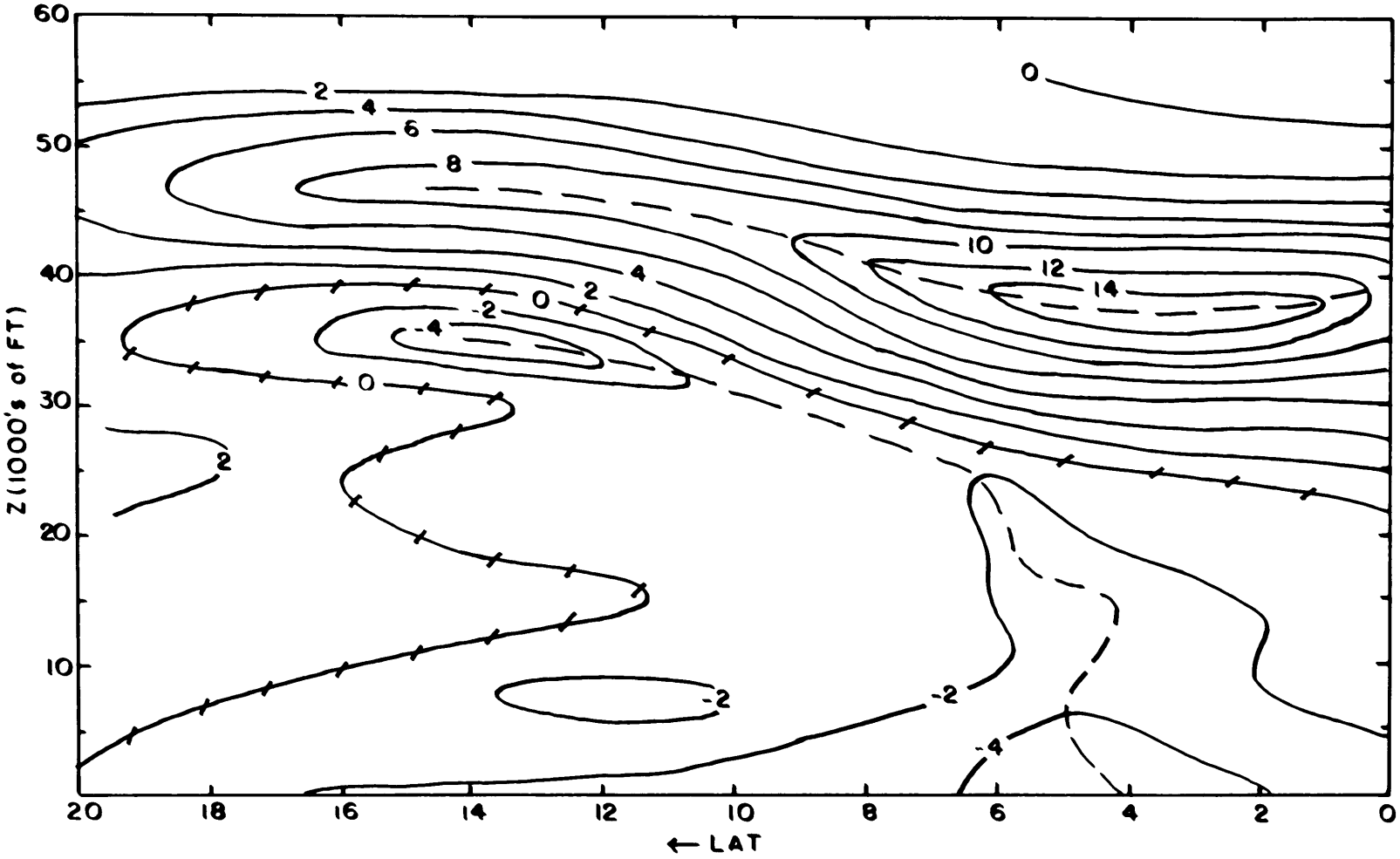

Fig. 3.2. Cross-section of horizontal velocity divergence for 0300Z, May 1956 Redwing data. Units are multiples of 10^{-6} s^{-1}.

where $[\overline{\nabla_2 \cdot V}]$ represents the mean horizontal velocity divergence and $[\bar{w}] = 0$ at the surface.

Inspection of mean temperature profiles for the various stations reveals that they are quasi-linear up to about 50,000 feet which is near the mean tropopause found near 110 mb. A lapse rate value of $-2^{o}C$ per 1000 feet gives a good enough fit to compute the mean density for evaluation of $[\bar{w}]$ from (3.13). We combine the equation of state and the hydrostatic relationship, integrate, and form the following expression for the density ratio.

$$\frac{\rho_s}{\rho_o} = \left(1 + \frac{\Gamma z}{T_o}\right)^{-(1+g/\Gamma R)} \tag{3.14}$$

Here Γ = the (linear) temperature lapse rate, g = acceleration of gravity, R = the gas constant for dry air, and T_o is the sea-level temperature. With $\Gamma = -2^{o}C/1000$ ft $= -6.56^{o}C/1000$ m, R = 287 m.t.s. units, g = 9.8 ms^{-2}, and $T_o = 300^{o}K$, (3.14) becomes:

$$\frac{\rho_s}{\rho_o} = \left(1 - .67 \times 10^{-5} z\right)^{4.2} \tag{3.15}$$

Solve (3.13) for $[\bar{w}]$ by integrating the left-hand side with the trapezoidal rule using fixed density ratios from (3.15) at increments of 5000 feet up to 50,000 feet.

3.2.4. Adjustment of the Divergence Field

The first solutions for $[\bar{w}]$ using the above determinations yielded positive (upward) values as large as 3 cm/s just under the tropopause. Since the basic vertical structure of the divergence field is a simple change from convergence (negative divergence) below to divergence aloft, it is possible to scale the positive areas only so as to zero out the vertical motion at the tropopause. A scale factor (k) is derived at a given latitude by setting

$$\int_0^{Z_{ND}} \frac{\rho_s}{\rho_0} [\overline{\nabla_2 \cdot \vec{v}}]\, dz = -k \int_{Z_{ND}}^{Z_{TROP}} \frac{\rho_s}{\rho_0} [\overline{\nabla_2 \cdot \vec{v}}]\, dz$$

where Z_{ND} = level of non-divergence.

As an example, the application of k at 10^{o}N to each term in the trapezoidal integration of the positive divergence area gives the adjusted values shown in Table 3.1. It is unfortunate that such an adjustment needs to be made; however, others using this approach generally find that the vertical integration to the tropopause of the mass divergence is significantly different from zero*. In a similar study using June 1956 Redwing data, a direct adjustment of the vertical motion was made for the same purpose (Ballif, et. al., 1958). The accuracy of wind observations decreases with height, thus the need for correction should be at higher levels where, in this study, positive divergence exists. Any more sophisticated corrections are probably not justified.

---

*Personal discussion of this point with Prof. F. Sanders, Dept. of Meteorology, M.I.T.

z	ρ_s/ρ_o	$D \times 10^6$	$\frac{\rho_s}{\rho_o} D$	$k\frac{\rho_s}{\rho_o} D$	kD	$\frac{\rho_s}{\rho_o}[\bar{w}]$ m s^{-1}		$[\bar{w}]$ cm s^{-1}	
0	1.0	-1.91	-1.91			0.0		0.0	
5	.87	-.98	-.85			.00211		.243	
10	.75	-1.55	-1.16			.00364		.485	
15	.649	-.25	-.16			.00469		.723	
20	.554	-1.20	-.67			.00531		.960	
25	.473	-1.47	-.70			.00635		1.34	
30	.397	-.90	-.36			.00716		1.81	
35	.332	1.10	.36	.476	1.44	.0072	ADJ. .0071	2.16	ADJ. 2.13
40	.278	5.15	1.43	1.89	6.80	.0058	.0053	2.08	1.90
45	.227	7.20	1.63	2.15	9.50	.0035	.0022	1.52	.96
50	.185	3.20	.59	.77	4.23	.0018	0.0	.96	0.0

$$-\int_0^{z_{ND}} \frac{\rho_s}{\rho_o}[\overline{\nabla_2 \cdot v}]\,dz = 4.68\,, \quad \int_{z_{ND}}^{z_{TROP}} \frac{\rho_s}{\rho_o}[\overline{\nabla_2 \cdot v}]\,dz = 3.54\,, \quad k = \frac{4.68}{3.54} = 1.32$$

Table 3.1. An example at 10°N of the computation and adjustment of $[\bar{w}]$. D is velocity divergence. The term kD is the scaled positive divergence after area adjustment of the mass divergence. The last two columns show the original and adjusted density-weighted vertical motion and $[\bar{w}]$ respectively.

If no adjustment had been made, a defense for the existence of large mean vertical motions at the tropopause would be needed, and this seems less plausible than the indicated adjustments. Figure 3.3 shows a cross-section of $[\bar{w}]$ in cm/s after adjustment. The strong upward values will mean that inertial terms involving $[\bar{w}]$ can be significant in the equations of motion at low latitudes.

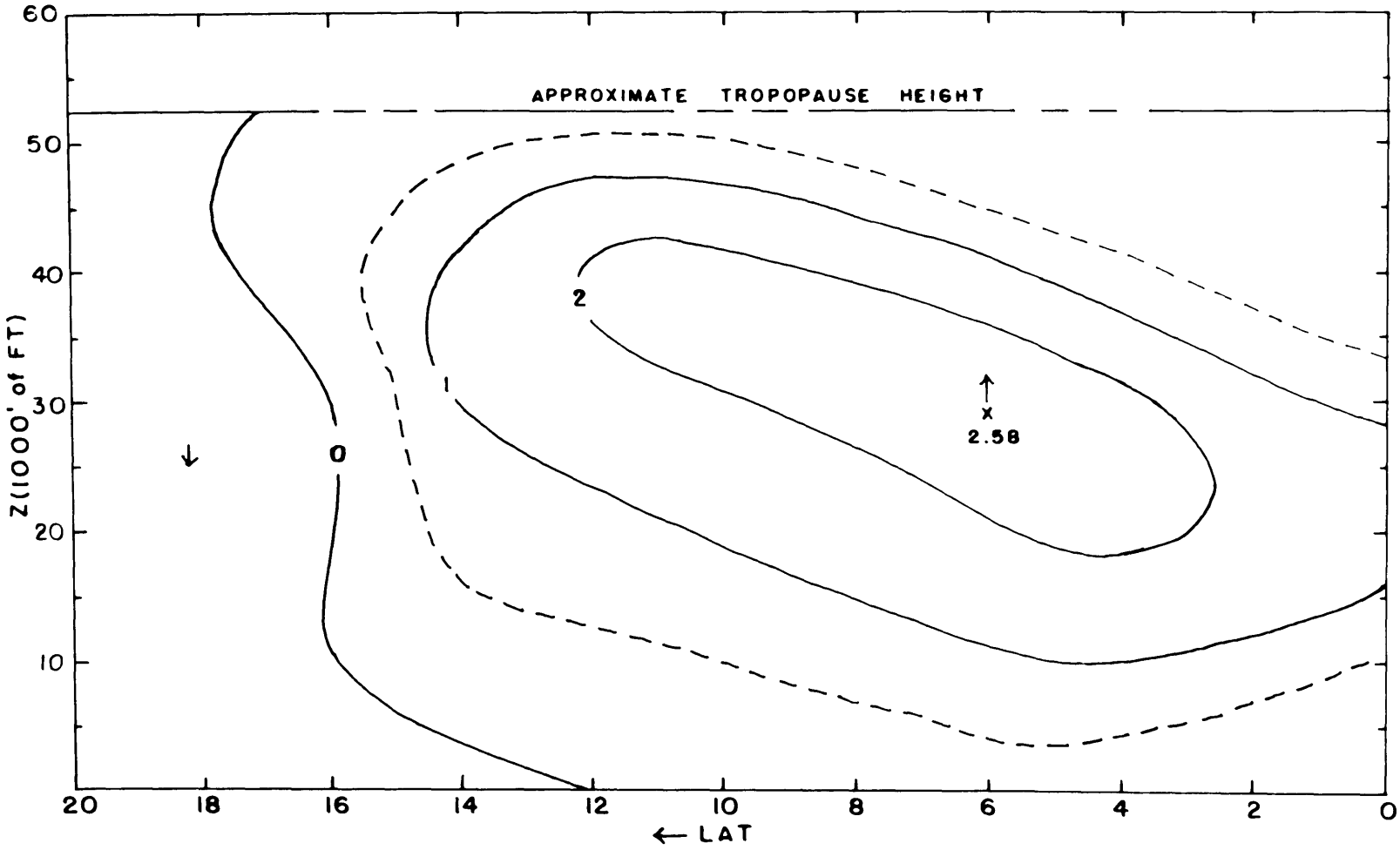

Fig. 3.3. Cross-section of $[\overline{w}]$ for 0300Z, May 1956. Units are in cm s^{-1}.

3.2.5. The Fluctuation Terms

Terms on the left-hand side of (3.7) and (3.8) involving primes were determined in three steps as follows. The values of $\overline{u'v'}$, $\overline{u'^2}$ and $\overline{v'^2}$ were computed for each station by processing the daily wind data on the digital computer. Next, the fields were analyzed at each mandatory level. Finally, the gridded data at each level were used to form the required derivatives by centered differencing over four degrees latitude.

The spatial fluctuations were computed from the gridded analyses of the time-mean wind components discussed in Chapter 2.

Fluctuation terms on the right-hand side of (3.7) and (3.8) which represent the vertical divergence of momentum flux due mainly to small-scale eddies cannot be determined directly, and are derived as a residue when all other terms have been computed.

Figures 3.4, 3.5, and 3.6 are analyses of $\overline{u'v'}$ for 850, 500, and 200 mb. Even though the May 1956 sample is relatively short and the 24-hour period between observations tends to act as a low-pass filter, the indicated analyses are reasonably coherent. Thus, the signs, and orders of magnitude if not the exact values of the smaller stress terms are probably correct.

3.2.6. Final Evaluation of Terms

The remaining terms on the left-hand side of (3.7) and (3.8) involve mean quantities only and can be computed from the gridded analyses of mean wind components and pressure heights. As before, centered

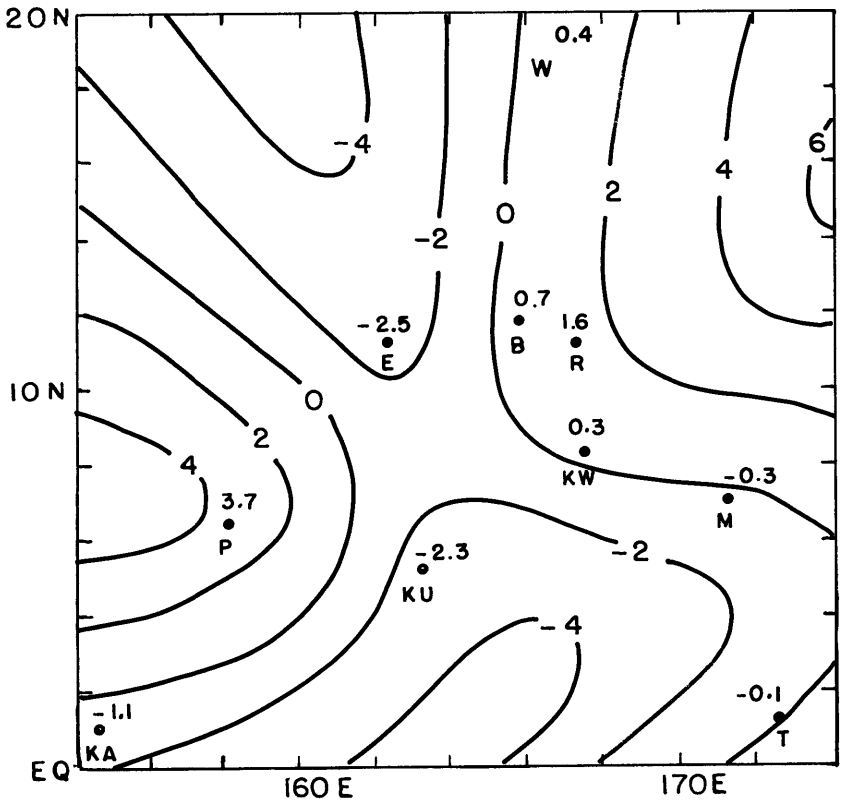

Fig. 3.4. Analysis of $\overline{u'v'}$ at 850 mb, 0300Z, May 1956. Units are m^2/s^2.

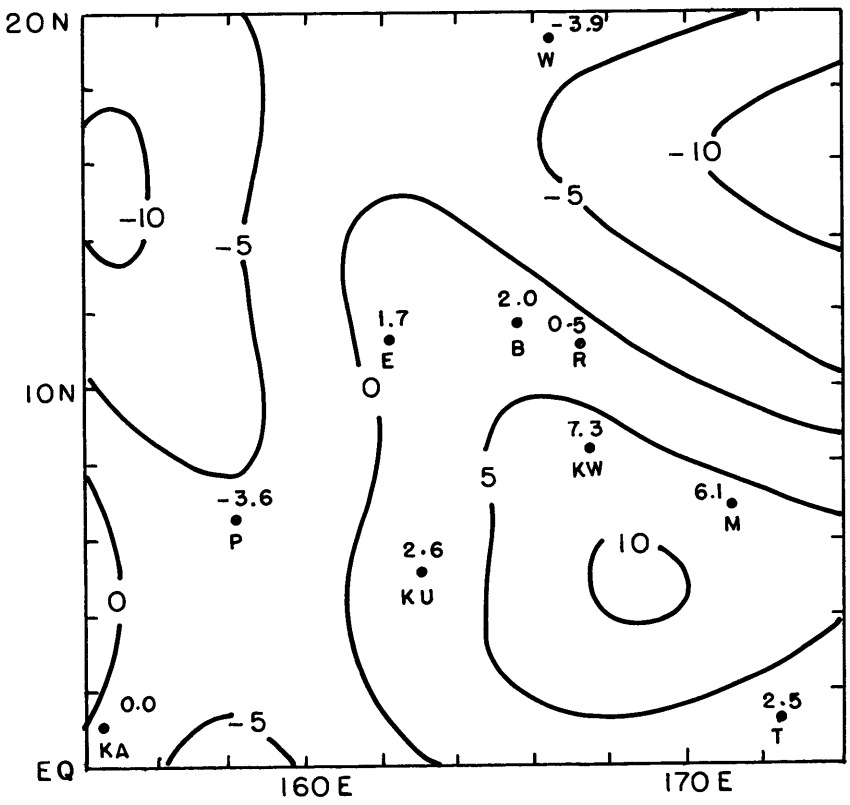

Fig. 3.5. Analysis of $\overline{u'v'}$ at 500 mb, 0300Z, May 1956. Units are m^2/s^2.

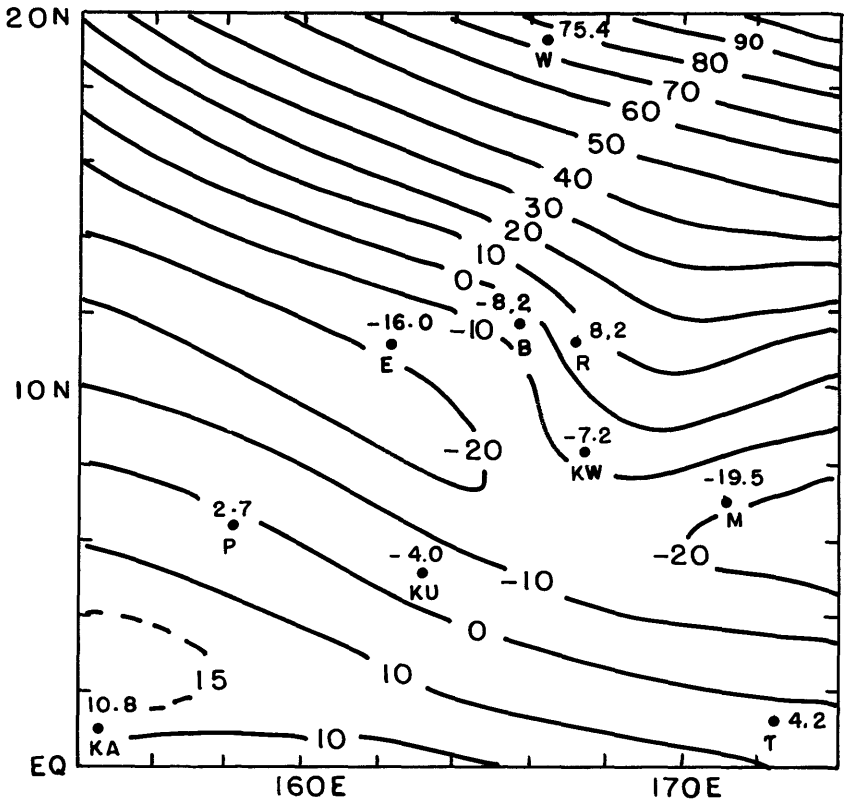

Fig. 3.6. Analysis of u'v' at 200 mb, 0300Z, May 1956. Units are m^2/s^2.

differences over four degrees latitude were used for all calculations. Tables 3.2 through 3.9 show values at the various pressure levels of the forces per unit mass in (3.7) and (3.8) in units of 10^{-5} ms^{-2}, and as a function of latitude. In order to simplify these tables, the following terms have been defined:

DEFINITION OF TERMS USED IN THE SCALE TABLE

$$U_x = [\bar{u}]\,(\bar{u}_L - \bar{u}_o)/L \qquad V_x = [\bar{u}]\,(\bar{v}_L - \bar{v}_o)/L$$

$$U_y = [\bar{v}]\,\partial[\bar{u}]/\partial y \qquad V_y = [\bar{v}]\,\partial[\bar{v}]/\partial y$$

$$U_z = [\bar{w}]\,\partial[\bar{u}]/\partial z \qquad V_z = [\bar{w}]\,\partial[\bar{v}]/\partial z$$

$$-FV = -f[\bar{v}] \qquad FU = f[\bar{u}]$$

$$JW = j[\bar{w}]$$

$$P_x = \frac{1}{L\rho_s}(\bar{p}_L - \bar{p}_o) \cong \frac{g}{L}(\bar{z}_L - \bar{z}_o) \qquad P_y = \frac{1}{\rho_s}\partial[\bar{p}]/\partial y \equiv g\,\partial[\bar{z}]/\partial y$$

$$S_1 = (\bar{u}_L^{*2} - \bar{u}_o^{*2})/L \qquad T_1 = (\bar{u}^*\bar{v}_L^* - \bar{u}^*\bar{v}_o^*)/L$$

$$S_2 = (\overline{u'^2_L} - \overline{u'^2_o})/L \qquad T_2 = (\overline{u'v'_L} - \overline{u'v'_o})/L$$

$$S_3 = \partial/\partial y\,[\bar{\bar{u}}^*\bar{\bar{v}}^*] \qquad T_3 = \partial/\partial y\,[\bar{\bar{v}}^{*2}]$$

$$S_4 = \partial/\partial y\,[\overline{u'v'}] \qquad T_4 = \partial/\partial y\,[\overline{v'^2}]$$

$$F_x = -\frac{1}{\rho_s}\frac{\partial}{\partial z}\left[\rho_s\left(\overline{u'w'} + \bar{u}^*\bar{w}^*\right)\right] \qquad F_y = -\frac{1}{\rho_s}\frac{\partial}{\partial z}\left[\rho_s\left(\overline{v'w'} + \bar{v}^*\bar{w}^*\right)\right]$$

Before drawing conclusions from the terms in the preceding tables, it will be helpful to look at comparisons of the real and geostrophic winds as functions of height and latitude.

X-Direction

Lat.	U_x	U_y	U_z	-FV	JW	P_x	S_1	S_2	S_3	S_4	F_x
2	.44	-.09	0.0	-.59	0.0	4.41	-.10	V	.04	V	4.11
4	.56	-.11		-.47		3.07	-.14		.04		2.95
6	.66	.18		.61		2.50	-.22		.03		3.77
8	.59	.53		2.13		2.51	-.24		V		5.53
10	.04	.65		3.26		3.89	V		-.05		7.79
12	V	.90		5.11		4.31	V		V		10.3
14	.11	.60		7.72		4.15	-.02		.07		12.6
16	.44	-.01		10.3		3.00	-.10		.09		13.7
18	.77	-.54		12.1		2.82	-.15		.01		15.0

Y-Direction

Lat.	V_x	V_y	V_z	FU	P_y	T_1	T_2	T_3	T_4	F_y
2	V	-.30	0.0	-1.26	-4.87	.06	V	-.01	V	-6.37
4	.05	-.13		-2.86	13.4	.06		.01		10.6
6	.11	.01		-5.41	26.8	.05		.02		21.7
8	.31	.17		-9.77	36.3	-.04		.06		27.0
10	.64	.20		-14.6	42.3	-.02		.09		28.6
12	1.07	.35		-21.4	47.2	-.01		.07		27.3
14	1.35	.42		-28.7	49.4	-.11		.09		22.4
16	1.61	.27		-33.3	48.3	-.18		.12		16.8
18	1.75	V		-36.6	44.8	-.18		.02		9.76

Table 3.2. Terms from (3.7) and (3.8) at the surface in units of 10^{-5} m/s^{-2}. Definitions on page 77 ; v means very small.

X-Direction

Lat.	U_x	U_y	U_z	-FV	JW	P_x	S_1	S_2	S_3	S_4	F_x
2	1.10	.06	-.53	-1.13	.06	3.64	-.17	.22	.06	.74	4.05
4	1.19	-.09	-.34	-1.68	.08	2.69	-.10	.23	-.02	.50	2.46
6	.73	-.22	-.22	-1.42	.08	2.12	-.05	.32	-.05	.49	1.79
8	.17	-.06	-.04	-.34	.05	3.10	-.02	.27	-.02	.22	3.32
10	-.25	.05	.04	.44	.03	4.28	.05	.18	-.02	-.02	4.77
12	-.26	.01	.11	.87	.02	4.90	.06	.09	..01	-.14	5.66
14	-.13	-.05	.04	1.54	.01	4.94	.04	0.0	.02	-.23	6.16
16	-.25	-.02	-.06	1.94	-.01	3.99	.09	.09	.05	-.23	5.59
18	.06	-.04	-.11	1.63	-.02	3.63	-.02	.14	.08	-.16	5.19

Y-Direction

Lat.	V_x	V_y	V_z	FU	P_y	T_1	T_2	T_3	T_4	F_y
2	.65	-.34	.13	-3.98	-14.9	..03	V	-.04	.32	-18.2
4	.50	-.46	.22	-7.88	6.72	..03	-.11	-.05	-.17	-1.2
6	.36	-.30	.22	-12.3	27.5	-.01	-.18	-.01	-.36	14.9
8	.40	-.09	.25	-17.8	35.1	-.03	-.16	.08	-.37	17.3
10	1.00	.01	.12	-24.3	35.1	-.08	V	.15	-.36	11.5
12	1.52	.02	.10	-30.4	33.8	-.18	.12	.13	-.26	4.81
14	1.80	.02	.02	-34.3	33.1	-.26	.26	.06	-.22	.55
16	1.84	-.01	-.02	-38.2	30.1	-.32	.30	-.02	-.21	-5.85
18	1.73	-.02	-.06	-42.9	26.4	-.30	.36	-.08	-.11	-15.0

Table 3.3. Terms from (3.7) and (3.8) at 850 mb in units of 10^{-5} ms^{-2}. Definitions on p. 77; v means very small.

X-Direction

Lat.	U_x	U_y	U_z	-FV	JW	P_x	S_1	S_2	S_3	S_4	F_x
2	1.16	.60	.98	-1.00	.10	.96	-.20	.58	.01	.02	3.23
4	1.01	.30	1.54	-1.54	.15	.19	-.18	.50	.02	.05	2.04
6	1.02	-.12	1.47	-1.53	.14	1.54	-.31	.18	.06	-.04	2.41
8	.55	-.25	1.19	-1.54	.10	2.32	-.24	-.04	.02	-.21	1.92
10	..38	-.06	.87	-1.37	.07	2.33	-.18	-.09	-.02	-.22	1.72
12	.09	.01	.65	-.16	.04	2.55	-.04	-.09	-.04	-.19	2.82
14	-.12	-.09	.29	1.43	.02	2.57	.05	.05	-.07	-.18	3.95
16	-.24	V	V	2.35	V	2.59	.12	.33	V	-.14	5.00
18	-.13	-.02	-.30	2.01	-.02	2.62	.07	.43	.04	-.11	4.59

Y-Direction

Lat.	V_x	V_y	V_z	FU	P_y	T_1	T_2	T_3	T_4	F_y
2	.34	-.18	-.07	-3.42	-20.8	.08	.07	V	1.6	-22.4
4	.23	-.32	-.20	-6.15	2.94	.08	.11	V	.91	-2.39
6	.26	-.19	-.10	-8.93	26.6	.06	.14	.04	-.27	17.7
8	.76	-.08	.08	-13.3	30.3	-.14	.17	.13	-.97	17.0
10	1.19	-.06	.10	-18.5	25.9	-.28	.18	.14	-1.41	7.22
12	1.29	-.01	V	-21.3	22.0	-.26	.18	.03	-.60	1.33
14	1.17	.04	V	-22.2	19.5	-.24	.18	.02	.54	-1.0
16	1.25	V	V	-24.3	18.1	-.29	.19	-.02	.41	-4.67
18	1.10	-.04	.02	-28.3	19.3	-.28	.19	-.06	.44	-7.52

Table 3.4. Terms from (3.7) and (3.8) at 700 mb in units of 10^{-5} ms^{-2}. Definitions on page 77 ; v means very small.

X-Direction

Lat.	U_x	U_y	U_z	-FV	JW	P_x	S_1	S_2	S_3	S_4	F_x
2	-.04	.34	2.09	- .97	.27	-1.15	.01	.27	.02	.94	1.69
4	.11	.10	1.04	-1.35	.30	V	-.02	V	.04	.26	.48
6	.20	.01	1.52	-1.17	.27	2.31	-.05	-.23	.07	- .59	2.34
8	.21	.02	1.85	- .55	.19	3.68	-.14	-.32	.04	-1.08	3.91
10	.14	.03	2.02	- .42	.14	3.70	-.16	-.41	-.03	-1.00	4.00
12	.04	.01	2.03	- .36	.12	4.90	-.06	-.32	-.02	- .90	5.45
14	.08	.02	1.38	.71	.10	6.12	-.08	-.32	-.02	- .92	7.07
16	-.07	.07	V	1.50	V	5.98	.07	-.52	-.06	- .20	6.79
18	-.13	.13	-.75	2.00	-.06	3.63	.10	-.71	-.04	.72	4.88

Y-Direction

Lat.	V_x	V_y	V_z	FU	P_y	T_1	T_2	T_3	T_4	F_y
2	.04	-.44	-.19	-1.38	-21.2	-.01	V	V	1.55	-21.6
4	.06	-.34	-.21	-2.45	- 2.77	V		V	1.28	- 4.43
6	.11	-.19	.19	-3.62	17.0	V		.02	.63	14.1
8	.12	-.06	V	-4.76	22.3	-.02		.06	-.02	17.6
10	.15	-.01	.11	-5.29	15.1	-.06		.08	-.49	9.62
12	.16	V	.09	-4.93	3.27	-.10		.02	-.20	- 1.69
14	.21	.01	.14	-5.91	- 4.62	-.09		.04	.90	- 9.00
16	.33	.02	V	-8.26	- 4.62	-.18		.11	1.71	-10.9
18	.50	V	-.09	-12.4	.504	-.20		.08	2.02	- 9.57

Table 3.5. Terms from (3.7) and (3.8) at 500 mb in units of $10^{-5}ms^{-2}$. Definitions on page 77 ; v means very small.

X-Direction

Lat.	U_x	U_y	U_z	-FV	JW	P_x	S_1	S_2	S_3	S_4	F_x
2	.05	-.20	1.23	-.15	.18	2.30	.61	1.12	.12	2.04	7.29
4	-.07	-.08	2.87	-.91	.31	V	.23	1.04	.17	1.04	4.60
6	.01	.76	3.70	-2.19	.37	2.12	-.06	.81	.21	.02	5.75
8	-.16	2.04	3.68	-3.42	.32	4.64	-.18	.54	.24	-.31	7.42
10	-.59	2.48	4.65	-3.85	.26	9.53	-.01	-.14	.08	.19	12.7
12	-.82	1.55	5.82	-4.63	.24	12.1	.14	-.60	-.23	.82	14.4
14	1.09	-.31	3.90	-5.34	.15	14.2	-.12	-1.48	-.17	.96	12.9
16	1.44	-1.43	V	-6.50	V	14.0	.03	-2.34	.10	.45	6.19
18	.93	-1.62	V	-7.64	-.06	11.5	.09	-3.22	.18	-.26	-1.61

Y-Direction

Lat.	V_x	V_y	V_z	FU	P_y	T_1	T_2	T_3	T_4	F_y
2	-.02	.08	-1.35	.10	-11.6	-.19	-.45	.02	-2.92	-16.3
4	.08	.22	-.44	-.76	9.32	-.15	-.09	.04	.04	8.25
6	.03	.23	-.53	-.34	23.3	-.12	.45	.20	2.85	26.1
8	-.29	.03	.92	3.29	15.1	-.14	1.04	.28	3.26	23.5
10	-1.01	-.06	1.30	13.1	-7.31	.06	1.55	V	3.69	11.3
12	-1.22	V	1.41	26.9	-31.0	.19	2.07	-.22	4.16	2.32
14	-.70	.03	.95	34.2	-48.0	-.07	2.46	-.14	4.52	-6.80
16	.05	.07	V	32.0	-51.8	-.17	2.57	V	4.97	-11.3
18	.50	.04	-.31	25.8	-46.6	-.11	2.46	.19	4.79	-13.2

Table 3.6. Terms from (3.7) and (3.8) at 300 mb, units of $10^{-5}ms^{-2}$
Definitions on page 77 ; v means very small.

X-Direction

Lat.	U_x	U_y	U_z	-FV	JW	P_x	S_1	S_2	S_3	S_4	F_x
2	1.53	-.01	.62	1.57	.06	4.41	.12	.45	.41	-1.72	7.43
4	1.20	-.68	1.16	1.54	.08	2.30	.18	.86	.24	-3.78	3.11
6	1.33	V	2.69	-.01	.15	1.93	.24	.63	-.04	-2.59	4.38
8	2.82	2.88	5.42	-3.35	.27	4.64	.62	.23	.02	-.12	13.44
10	2.96	5.82	8.35	-7.19	.34	10.1	-.04	-.41	.28	1.86	22.1
12	1.83	4.34	6.15	-10.7	.31	13.7	-.26	-.88	.38	4.70	19.6
14	3.99	1.55	4.45	-13.5	.20	16.0	-.84	-1.48	.86	7.17	18.4
16	7.90	-.64	1.12	-13.3	.05	16.3	-1.85	-2.11	1.68	8.56	17.7
18	12.0	-1.99	-.80	-11.8	-.04	13.7	-2.30	-2.90	1.92	8.97	16.7

Y-Direction

Lat.	V_x	V_y	V_z	FU	P_y	T_1	T_2	T_3	T_4	F_y
2	-1.09	-1.99	.04	2.48	-6.80	-.16	-.81	-.26	-3.44	-12.0
4	-1.03	-1.06	-.35	5.60	10.2	-.19	-1.40	-.13	-1.98	9.70
6	-1.15	.05	-.62	10.5	21.2	-.20	-1.63	-.02	1.89	30.0
8	-1.72	.91	-1.36	19.2	7.14	-.35	-.68	.01	5.24	28.4
10	-2.68	1.10	-1.72	37.1	-26.1	-.07	.32	-.09	6.83	14.7
12	-1.46	.73	.22	56.3	-53.7	.03	1.61	.08	8.34	12.1
14	1.60	-.18	.32	71.0	-69.3	-.47	2.55	.78	10.1	16.4
16	5.72	-.87	.08	81.9	-74.6	-1.37	3.14	1.55	11.4	27.1
18	9.62	-.73	V	86.8	-69.1	-2.05	3.74	2.10	11.1	41.5

Table 3.7. Terms from (3.7) and (3.8) at 200 mb, units of 10^{-5} ms^{-2}. Definitions on page 77 ; v means very small.

X-Direction

Lat.	U_x	U_y	U_z	-FV	JW	P_x	S_1	S_2	S_3	S_4	F_x
2	3.21	-.26	.29	.43	.02	9.20	..06	1.17	.35	-1.91	12.6
4	3.64	-.76	.54	.96	.06	9.41	..47	1.26	.41	-2.04	13.9
6	3.42	-.97	.66	1.28	.06	10.4	..24	1.08	.37	-.29	16.2
8	3.24	-.53	1.23	.62	.11	8.32	..04	.77	.10	.76	14.7
10	1.74	1.79	-.11	-2.35	.15	6.03	-.20	.68	-.12	1.30	10.2
12	1.50	2.86	-.98	-6.80	.17	3.33	-.30	.41	.45	4.97	5.62
14	7.84	.36	-.92	-10.7	.11	1.58	-2.22	.05	1.08	6.59	3.79
16	10.9	-2.90	-.25	-12.2	.02	1.79	-3.12	-.47	.76	6.74	1.28
18	10.4	-3.53	V	-11.6	V	-1.21	-3.24	-.71	.39	8.50	-1.06

Y-Direction

Lat.	V_x	V_y	V_z	FU	P_y	T_1	T_2	T_3	T_4	F_y
2	-.54	.07	.20	3.92	-7.73	.45	-.27	-.05	-4.27	-8.22
4	-.24	V	.31	9.29	8.48	.40	-.86	-.03	.61	17.8
6	.44	-.09	.04	17.2	14.7	.30	-.59	.07	4.70	36.8
8	1.76	.02	-.31	29.0	-1.34	.14	V	.14	6.16	35.6
10	3.22	.56	-.43	48.1	-31.6	-.18	.82	.08	7.04	27.6
12	4.49	.93	-1.35	69.1	-54.1	-.48	1.66	.22	7.62	28.1
14	7.03	.47	-.77	87.2	-65.5	-1.24	1.90	.77	7.89	37.7
16	10.1	-.28	-.09	93.8	-72.0	-1.96	2.48	.80	7.98	40.8
18	10.2	-.63	V	92.2	-66.5	-1.94	3.27	.44	9.19	46.3

Table 3.8. Terms from (3.7) and (3.8) at 150 mb, units of 10^{-5} ms^{-2}. Definitions on page 77; v means very small.

X-Direction

Lat.	U_x	U_y	U_z	-FV	JW	P_x	S_1	S_2	S_3	S_4	F_x
2	2.22	-.03	0.0	-.76	0.0	27.4	-.38	-.14	.12	V	28.5
4	1.91	.78	↓	-1.26	↓	24.4	-.65	1.00	.11	↓	26.3
6	1.92	.68	↓	-1.52	↓	20.6	-.65	1.22	.13	↓	22.4
8	1.98	.40	↓	-1.65	↓	16.4	-.60	1.54	.29	↓	18.4
10	2.66	.05	↓	-1.81	↓	12.6	-.80	1.00	.36	↓	14.1
12	2.50	-.23	↓	-1.80	↓	5.68	-1.03	.41	.26	↓	5.79
14	2.12	-.26	↓	-1.25	↓	.99	-1.08	-.28	.12	↓	.37
16	1.94	-.02	↓	-.07	↓	-2.79	-1.06	-1.26	.05	↓	-3.22
18	1.82	.42	↓	1.42	↓	-7.05	-1.30	-2.7	.05	↓	-7.34

Y-Direction

Lat.	V_x	V_y	V_z	FU	P_y	T_1	T_2	T_3	T_4	F_y
2	-.52	-.20	0.0	4.63	2.77	.23	V	-.07	1.33	8.16
4	.13	-.14	↓	10.4	19.3	.12	↓	-.02	1.28	31.1
6	.84	-.10	↓	18.2	28.0	-.02	↓	.12	.79	47.8
8	1.81	-.05	↓	26.9	20.0	-.16	↓	.21	.52	49.2
10	2.66	-.04	↓	35.6	-.34	-.32	↓	.19	1.03	38.8
12	3.12	-.04	↓	41.2	-16.5	-.61	↓	.18	1.57	28.9
14	3.26	-.04	↓	43.5	-22.8	-.84	↓	.12	1.62	24.9
16	2.90	V	↓	41.6	-24.9	-.82	↓	.04	1.57	20.4
18	2.17	.04	↓	33.7	-21.4	-.81	↓	-.04	2.40	16.0

Table 3.9. Terms from (3.7) and (3.8) at 100 mb, units of 10-5 ms^{-2}. Definitions on page 77 ; v means very small.

3.2.7. Profiles of Geostrophic vs. Real Winds and Balance in the Y-Direction

Figures 3.7 through 3.16 show profiles of $[\bar{u}]$, $[\bar{v}]$ and their geostrophic counterparts $[\bar{u}_G]$ and $[\bar{v}_G]$ where:

$$[\bar{u}_G] = -g/f \frac{\partial}{\partial y}[\bar{z}] \tag{3.16}$$

$$[\bar{v}_G] = g/f (\bar{z}_L - \bar{z}_o)/L \tag{3.17}$$

Values are plotted at 2^o latitude intervals except that no geostrophic components are available at the equator. In addition, wind components from indicated stations near the appropriate latitude are shown to indicate that longitudinal averaging has not caused an inordinate amount of smoothing.

One persistent feature of these profiles is the simple structure of the zonal wind component $[\bar{u}]$. Positive (west to east) vertical wind shear is obvious at all latitudes between the easterly and westerly maxima. This characteristic can be illustrated in the $[\bar{u}]$ cross-section Fig. 3.17. Inspection of monthly and seasonal climatologies reveals that the lower tropospheric easterlies are to be expected at all latitudes (Atkinson and Sadler, 1970); however, the rather strong westerlies aloft may be somewhat anomalous (Atkinson, 1971, pg. 4-18; Sadler and Harris, 1970, pg. 16). May is a transition month for upper tropospheric flow at these longitudes and is subject to vagaries of the position of the subtropical ridge position at 200 mb. The magnitude of the mean zonal vertical shear doubles gradually from

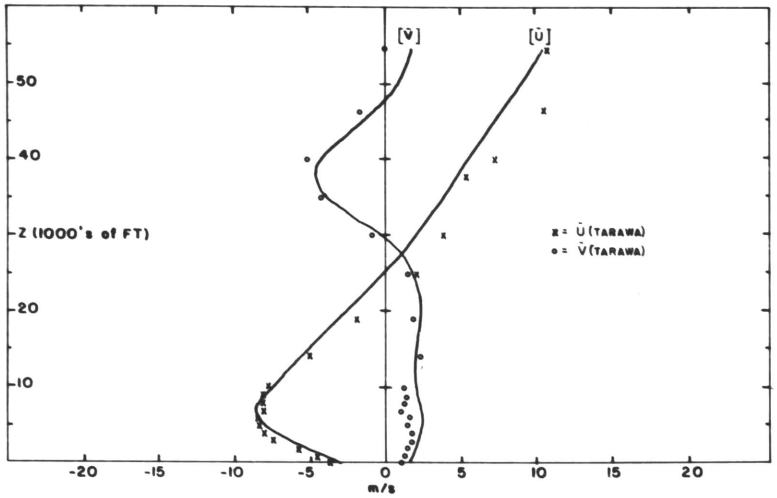

Fig. 3.7. Profiles of $[\bar{u}]$ and $[\bar{v}]$ for 0300Z, May 1956 at 0°N. No geostrophic. Tarawa data plotted as shown.

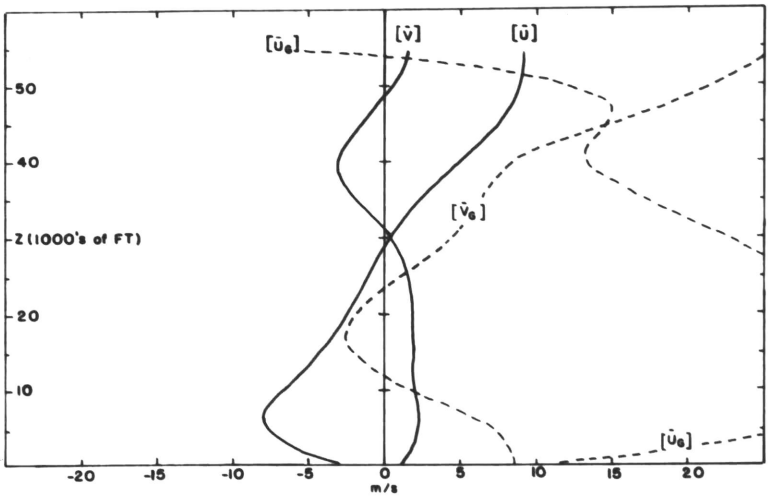

Fig. 3.8. Profiles of $[\bar{u}]$, $[\bar{v}]$, $[\bar{u}_G]$ and $[\bar{v}_G]$ for 0300Z, May 1956 at 2°N.

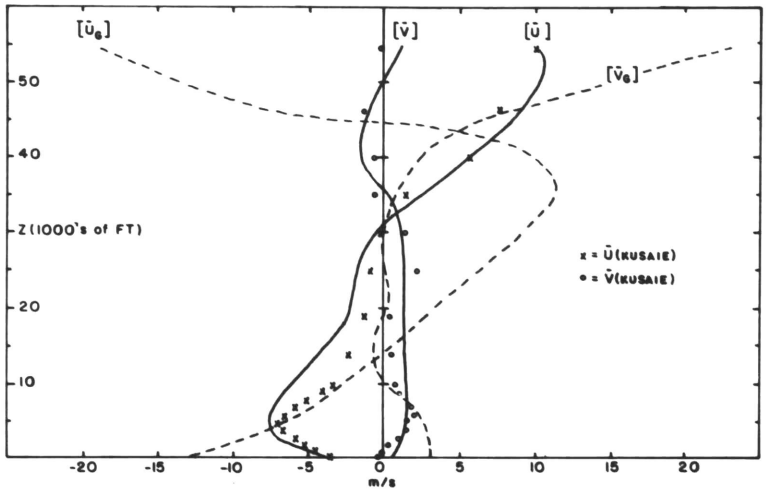

Fig. 3.9. Profiles of $[\bar{u}]$, $[\bar{v}]$, $[\bar{u}_G]$ and $[\bar{v}_G]$ for 0300Z, May 1956 at 4°N. Kusaie data plotted as shown.

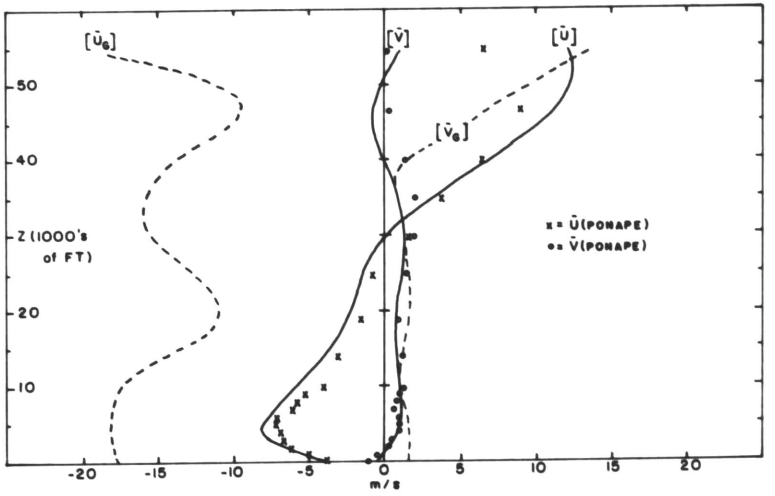

Fig. 3.10. Profiles of $[\bar{u}]$, $[\bar{v}]$, $[\bar{u}_G]$ and $[\bar{v}_G]$ for 0300Z, May 1956 at 6°N. Ponape data plotted as shown.

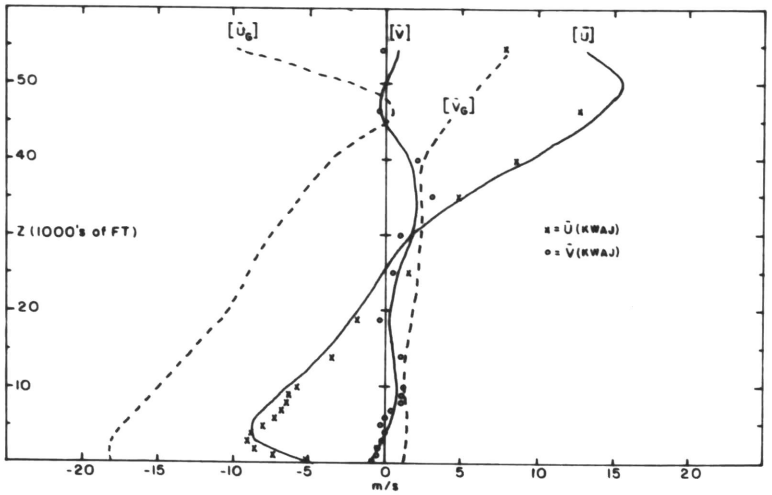

Fig. **3.11.** Profiles of $[\bar{u}]$, $[\bar{v}]$, $[\bar{u}_G]$ and $[\bar{v}_G]$ for 0300Z, May 1956 at 8°N. Kwajalein data plotted as shown.

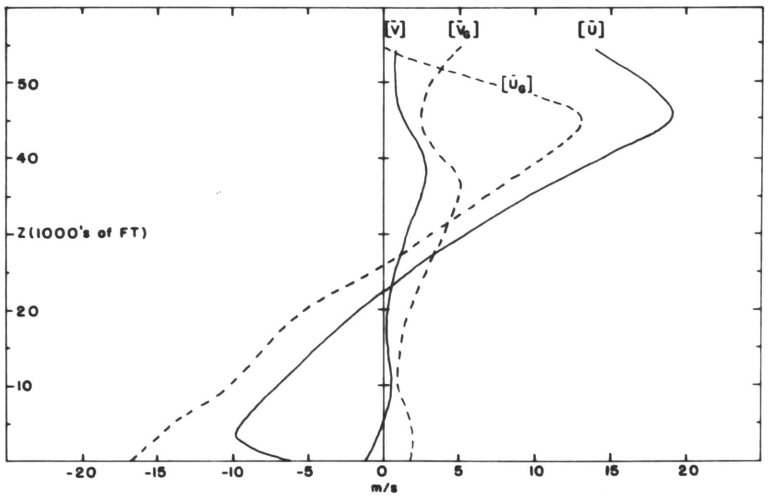

Fig. **3.12.** Profiles of $[\bar{u}]$, $[\bar{v}]$, $[\bar{u}_G]$ and $[\bar{v}_G]$ for 0300Z, May 1956 at 10°N.

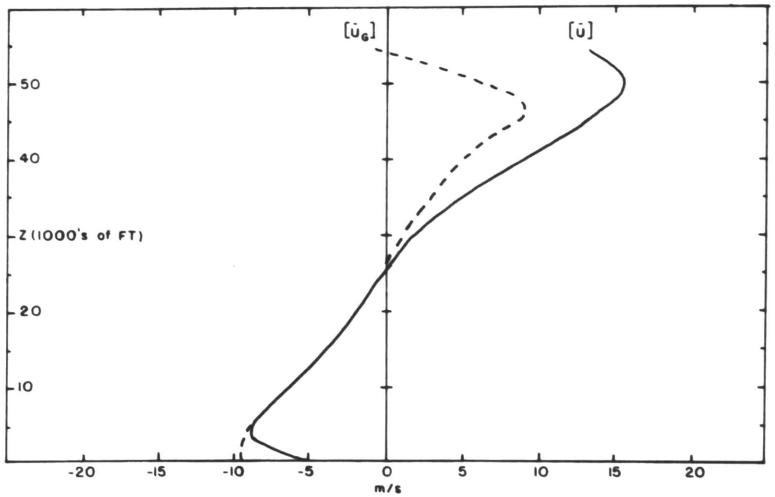

Fig. **3.11a.** Profiles of $[\bar{u}]$ and $[\bar{u}_G]$ superimposed to show the strong dependence of the real wind shear on the thermal wind. 0300Z, May 1956 at 8°N.

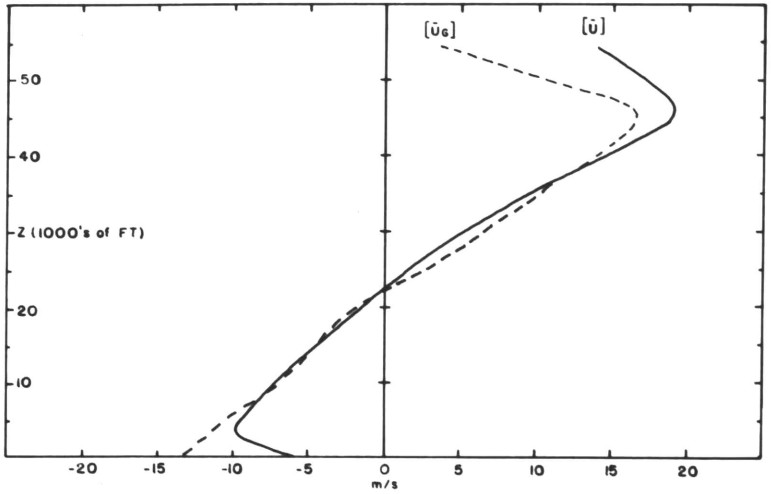

Fig. **3.12a.** Profiles of $[\bar{u}]$ and $[\bar{u}_G]$ superimposed to show the strong dependence of the real wind shear on the thermal wind. 0300Z, May 1956 at 10°N.

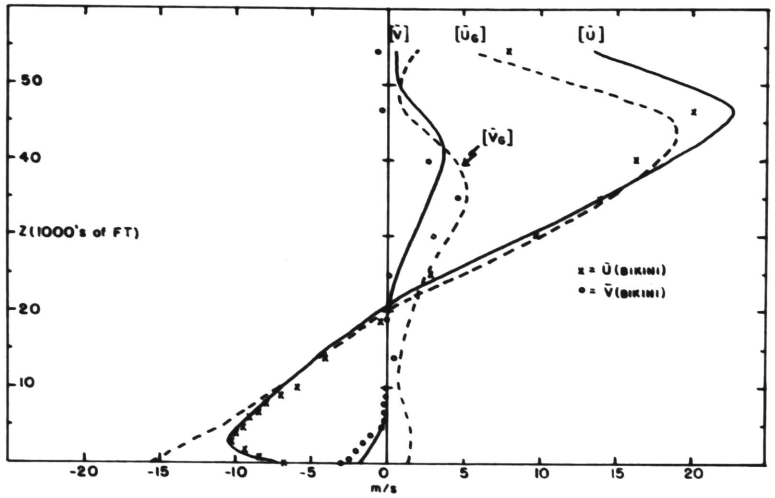

Fig. 3.13. Profiles of $[\bar{u}]$, $[\bar{v}]$, $[\bar{u}_G]$ and $[\bar{v}_G]$ for 0300Z, May 1956 at 12°N. Bikini data plotted as shown.

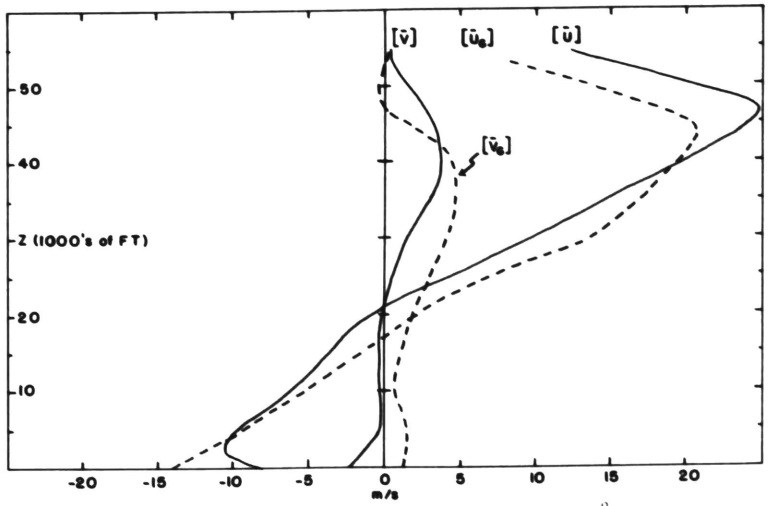

Fig. 3.14. Profiles of $[\bar{u}]$, $[\bar{v}]$, $[\bar{u}_G]$ and $[\bar{v}_G]$ for 0300Z, May 1956 at 14°N.

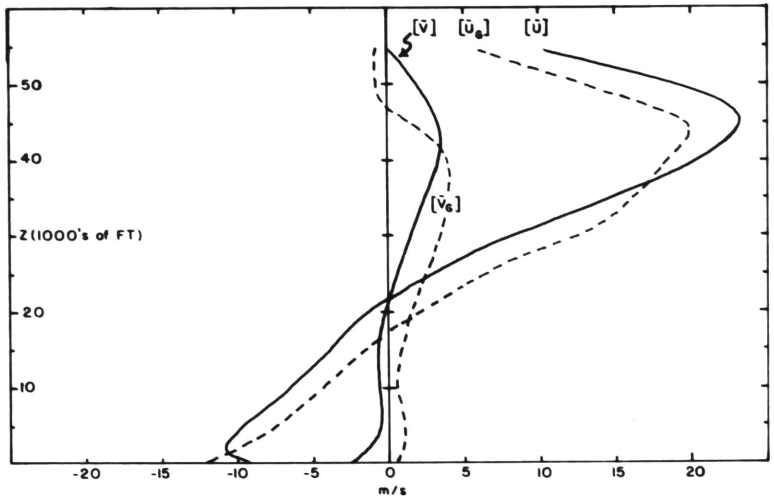

Fig. 3.15. Profiles of $[\bar{u}]$, $[\bar{v}]$, $[\bar{u}_G]$ and $[\bar{v}_G]$ for 0300Z, May 1956 at 16°N.

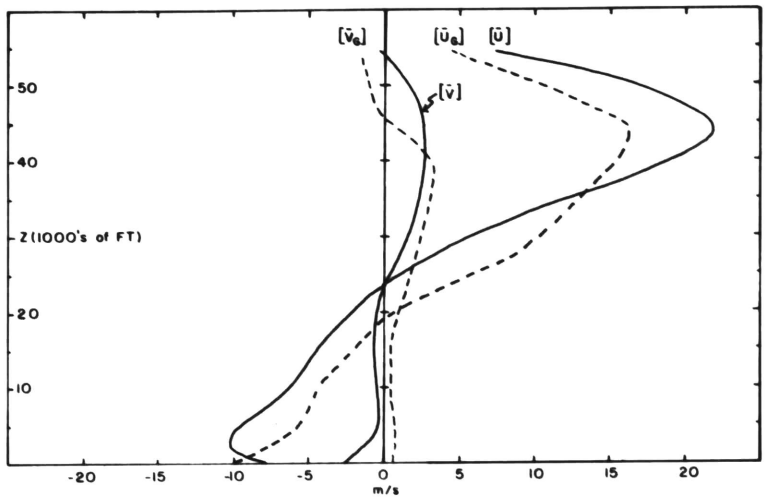

Fig. 3.16. Profiles of $[\bar{u}]$, $[\bar{v}]$, $[\bar{u}_G]$ and $[\bar{v}_G]$ for 0300Z, May 1956 at 18°N.

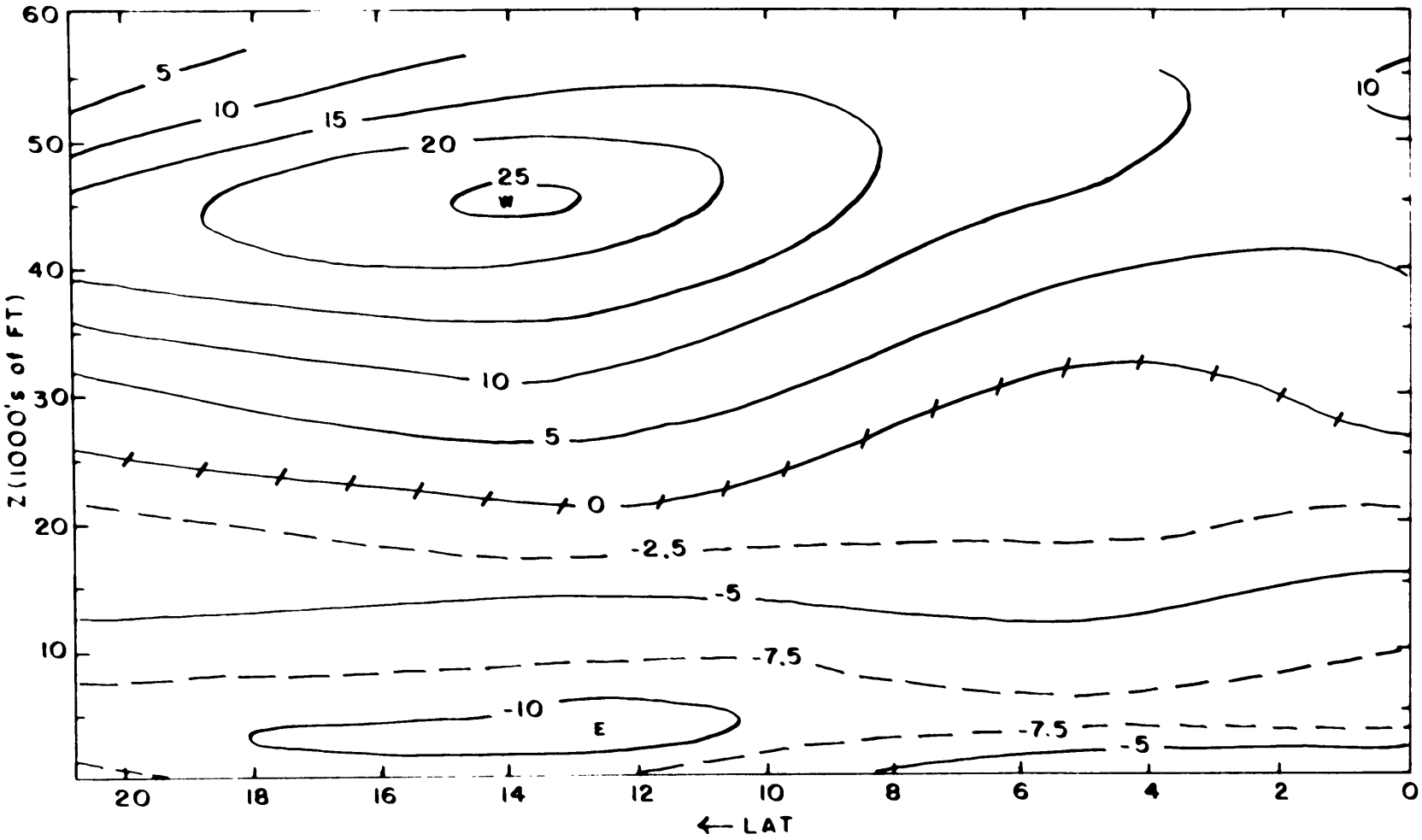

Fig. 3.17. Cross-section of $[\bar{u}]$ for 0300Z, May 1956 Redwing data. Units are m s^{-1}.

$1.4 \times 10^{-3} s^{-1}$ at the equator to $2.8 \times 10^{-3} s^{-1}$ at $18^{o}N$. At these latitudes, these represent horizontal temperature differences of $\sim 0.1^{o}C$ per degree latitude. At and above $8^{o}N$, the meridional component $[\bar{v}]$ has the classical Hadley structure (e.g., see Palmen et al., 1958), i.e., an equatorward branch at the surface, and a poleward branch centered near 40,000 feet. South of $8^{o}N$ there is a portion of a strong reverse cell. Whether or not this is due to encroachment by a complete Southern Hemisphere Hadley cell cannot be determined from these data. At any rate, there is substantial flux across the equator.

At $2^{o}N$, there appears to be little correspondence between the geostrophic and real winds. At $4^{o}N$ and below about 36,000 feet, the shapes of the corresponding profiles begin to resemble one another, but there are considerable absolute differences. Beginning at $5^{o}N$ and progressing northward, one notes that the thermal wind increasingly resembles the shear of the real winds even though large absolute differences still occur at most latitudes. This is especially true in the zonal components. Excellent examples of the latter condition may be seen at $8^{o}N$ and $10^{o}N$.

Figures 3.11a and 3.12a show the results of simple translations of the computed $[\bar{u}_G]$ profiles such that they are brought into coincidence with the lower portions of the $[\bar{u}]$ profiles. Appendix I demonstrates that biased sea level pressure errors of the order fraction of one millibar can account for the principal geostrophic departures at latitudes north of about $4^{o}N$. Further shaping of the $[\bar{u}_G]$ profile can be accounted for by errors in thickness estimates due to

temperature differencing errors on the order of .1°C over 4° latitude especially south of about 4°N. Even with the barometry corrections discussed in section 2.1, it appears that accurate geostrophic departures based on 30-day means are not feasible without partial adjustment at these low latitudes.

Inspection of Tables 3.2 through 3.9 show that north of about 4°-5°N, the only term in the y-equation that is large enough to maintain the unadjusted geostrophic departures seen in the previous profiles is the vertical frictional force per unit mass, the residual F_y. We may write $\rho_s F_y$ approximately as

$$\rho_s F_y \cong -\frac{\partial}{\partial z}\left[\rho_s \overline{w'v'}\right] \tag{3.18}$$

At 8°N, the product $\rho_s F_y$ may be taken as a slowly varying function of z with a value of about 10^{-7}. Thus if we integrate (3.18) from the surface to 200 mb (12 km) and assume $\left[\overline{w'v'}\right] = 0$ at the surface we have $-\left[\rho_s \overline{w'v'}\right]_{12\ km} \simeq 12\times10^{-4}$ or since ρ_s (12 km) = 3×10^{-4}, the vertical eddy flux of meridional momentum must approach -4 $m^2 s^{-2}$ at 200 mb. This enormous value would require vertical motion perturbations around 1 ms^{-1} assuming <u>perfect</u> correlation between w and v. This might be remotely feasible in deep convective activity sustained for the entire month but this quantitative estimate argues for the more plausible explanation that the deep-layer geostrophic departures are due to small errors in sea level pressure and thickness determination. On the other hand, even if the deep troposphere geostrophic departures were eliminated by translation of the $\left[\bar{u}_G\right]$ profile, there would

remain F_y values of essentially 10^{-4} ms^{-1} near the surface dropping to negligible amounts near about 2 km where $[\bar{u}]$ and the adjusted $[\bar{u}_G]$ profiles blend together. This frictional residue is well within realistic bounds as subsequent sections of this chapter will show.

The lack of any substantial inertial or perturbation terms in the y-equation of motion (except where the flow is weak or very near the equator), and the fact that the zonal thermal wind is in reasonable agreement with the slopes of the $[\bar{u}]$ profiles north of $6^{o}N$, leads to the conclusion that the time and space-mean zonal wind component is in quasi-geostrophic balance down to perhaps $4^{o}N$ in the lower troposphere and to 6^{o}-$8^{o}N$ at levels above the zonal wind reversal layer near 300 mb. In addition, the vertical friction term is important below about 2 km.

3.2.8 Balance in the X-Direction

Examination of Tables 3.2-3.9 permit the following generalizations:

1. Pronounced zonality keeps the Coriolis term (-FV) near order 10^{-5} except in the horizontal branches of the Hadley cell toward higher latitudes where $-FV \sim 10^{-4}$.

2. The inertial terms (U_x, U_y, U_z) are generally of order 10^{-5} and tend to dominate the fluctuation terms (S_1, S_2, S_3, S_4) except near 500 mb where only U_z is dominant from 700 mb through 200 mb between $4^{o}N$ and $14^{o}N$, approaches order 10^{-4}, and is often larger than the Coriolis term.

3. The time fluctuation terms, S_2 and S_4 are generally larger than the space fluctuations, S_1 and S_3. S_4 is especially important North of 10^{o}N at 200 and 150 mb where it approaches 10^{-4} and indicates eddy interaction with extra-tropical latitudes.

4. P_x is always significant and attains order 10^{-4} at levels above 500 mb. Below 500 mb in ENE flow ($v < 0$), P_x and -FV tend not to cancel.

5. It is likely that the unbalanced relationship between P_x and -FV near the surface may be explained as follows. The mean geostrophic wind is ESE but the real wind is ENE and cuts the isobars toward lower pressure. Clearly, this is in line with simple Ekman theory. The lack of any other important terms in the region reinforces this conclusion.

6. Based on the above, the frictional residue terms (F_x) near the surface are probably of the correct sign and order of magnitude. To emphasize this, we use the diffusion form of the frictional term and let

$$F_x = K_e \, \partial^2 u / \partial z^2 \sim 5 \times 10^{-5} \text{ ms}^{-2}$$

a typical value from the tables. From the $[\bar{u}]$ profiles (Figs. 3.7-3.16), $\partial^2 u/\partial z^2 = 3 \times 10^{-6}$ near 4000 feet; hence, K_e, the coefficient of eddy viscosity is ~ 10 m^2/s which is quite compatible with values suggested by other workers (e.g., Priestly, 1959 and Byers 1944).

The evidence to this point suggests that the mean zonal flow is quasi-geostrophic with surface friction to within 4^{o} to 6^{o} of the equator and that there are both traveling disturbances and a pronounced meridional cell which generate the inertial and stress terms of relative importance in the x-equation of motion. Since time-space means were employed, this picture could be misleading. At low latitudes, the geostrophic adjustment between wind and pressure requires $\frac{\pi}{f} \sim 2$ days; thus if large, short-period wind fluctuations are the rule throughout the region, geostrophy may be a useless concept at a given instant. Certainly, if the winds had been very steady in both direction and magnitude, we could expect geostrophy on a daily as well as an average basis. Steadiness values will be examined in the next section of this chapter. In any event, if large fluctuations in the wind were prevalent, and uncorrelated with u_G, we would expect to see other than geostrophic terms play an important role in the y-equation; yet these are of little consequence north of 4^{o}N and below 500 mb.

The ultimate test would be to measure and compare real and geostrophic winds on a synoptic basis, but without improved sounding gear and a more dense reporting network this will not be particularly rewarding today at very low latitudes.

In order to have a better grasp of the degree of fluctuation in this predominantly zonal wind-regime, the next section quantifies the "steadiness" of the wind and the distribution of kinetic energy between the mean and perturbation portions of the flow.

3.3. Wind Variability During Redwing, May 1956

3.3.1. Steadiness

Under certain conditions, a useful concept for investigations in the tropics is the steadiness of the winds (S). This is defined as the ratio of the magnitude of the mean wind vector to the mean magnitude expressed in percent.

$$S = \frac{|\bar{V}|}{\overline{|V|}} \times 100 \tag{3.19}$$

This is primarily a measure of directional variability and equals zero for winds which shift randomly and have a zero resultant speed, and equals one for winds which always blow in one direction. A large value of S does not insure a stationary wind regime, that is, large speed variability is still possible, but a large value of S does enhance the credibility of quasi-geostrophic balance as an instantaneous characteristic of at least the zonal component when combined with the fact that the mean wind is nearly zonal.

The reader can get a feel for the utility of steadiness values by considering some idealized cases, for example:

1. If wind magnitude is constant and winds are equally distributed through 90°. S = 90%.

2. If wind magnitude is constant and winds are equally distributed through 180°. S = 64%.

3. If wind magnitude is constant and winds are either from

45^{o} or 135^{o} (bimodal model), $S = \sqrt{2}/2 = .707$ for the combination of two perfectly steady regimes.

4. If wind magnitude varies from 0 to 10 m/s as a linear function of direction, and winds are equally distributed over 90^{o}, S = 93%. The large speed change had the effect of increasing S slightly over case 1 which had a constant magnitude.

5. If winds with easterly components have twice the speed of winds with westerly components and they are equally distributed through 360^{o}, S = 21%. This also shows that the speed variations do play a small role in increasing steadiness when speed and direction are correlated, for without the easterly bias in this last case, S = 0.

Very low values of S (0-20%) suggest randomness in direction with some speed bias, and very high values (90-100%) suggest a direction envelope less than 90^{o} or a slightly larger envelope with speeds correlated with direction. Values from 20-90% are not very descriptive.

Figure 3.18 is a vertical cross-section of S through Wake, Eniwetok, Ponape and Kapingamarangi derived from the 03Z observations for May 1956. The largest values approach 95% and are associated with the strongest easterlies near the surface, and westerlies aloft. The smaller values are found where winds are weakest, principally along the level of zonal wind reversal and also south of 6^{o}N in general.

3.3.2. Kinetic Energy Distribution

The time mean kinetic energy per unit mass may be written

$$\bar{K} = \overline{u^2+v^2} = \bar{u}^2+\bar{v}^2+\overline{u'^2}+\overline{v'^2} = \bar{K}_m + \bar{K}_p \qquad (3.20)$$

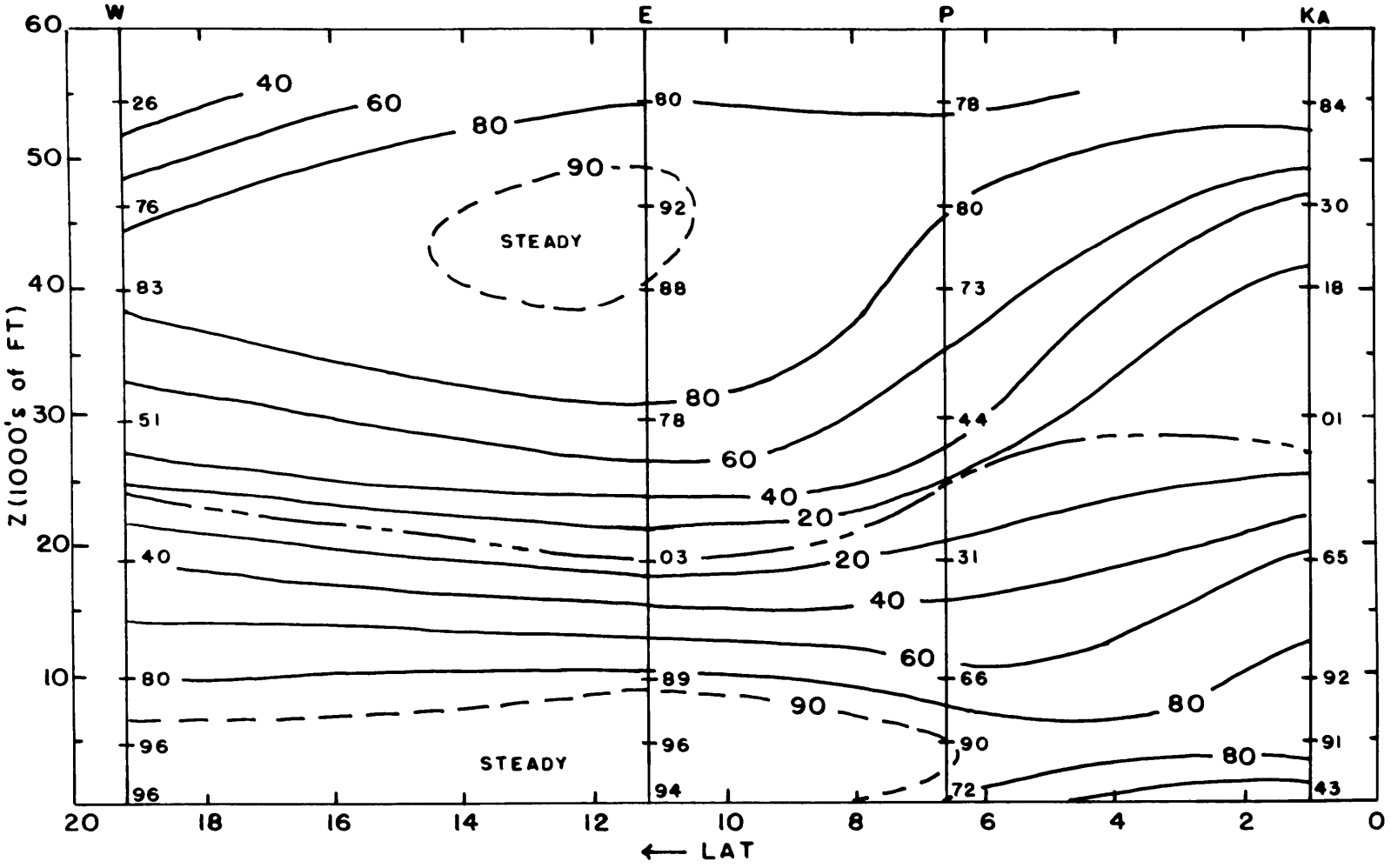

Fig. 3.18. Cross-section of wind steadiness for 0300Z, May 1956 Redwing data. Units are percent.

where $\bar{K}_m$ = the kinetic energy per unit mass of the mean flow and $\bar{K}_p$ = the mean perturbation kinetic energy per unit mass. The ratio $\bar{K}_m/\bar{K}$ may be written as

$$R_K = \frac{\bar{K}_m}{\bar{K}} = \frac{(\Sigma u)^2 + (\Sigma v)^2}{N \Sigma V^2} \qquad (3.21)$$

where N = number of reports and $V^2 = u^2 + v^2$. R_K is related to S the steadiness (note the numerators of each) as

$$R_K = \frac{(\Sigma V)^2}{N \Sigma V^2} S^2 \qquad (3.22)$$

And we see that if V = constant, $R_K = S^2$ and, in this special case, is essentially a measure of steadiness. On the other hand, if the flow is pure easterly with a variable magnitude, R_K will be < 1 while S = 1. Figure 3.19 is a cross-section of R_K using the same stations as in Figure 3.18. Evidently the two zones of steadiest winds do undergo substantial longitudinal pumping since $R_K = .75$ when $S \sim 1$.

It appears that deviations from the mean state near the two belts of zonal wind maxima north of about 6^{o}N are not so large as to invalidata the instantaneous application of quasi-geostrophic theory in these zones. This may be conservative since probable sounding errors force us to speculate about, rather than measure, the pressure gradient terms nearer the equator. On the other hand, May 1956 was chosen because of its relatively undisturbed nature and this should not be disregarded when considering the preceding remarks. Obviously, since the Coriolis

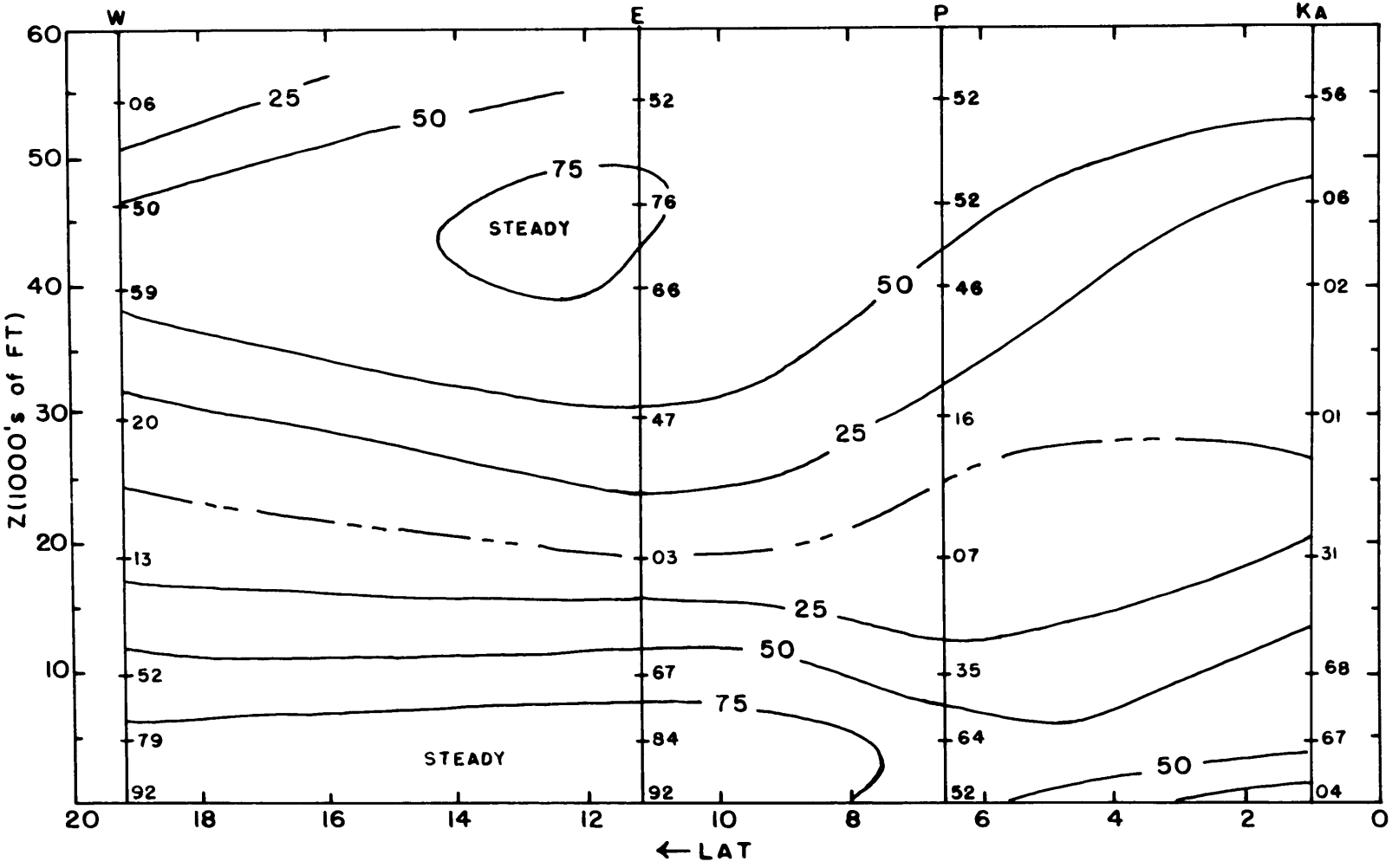

Fig. 3.19. Cross-section of percent of kinetic energy per unit mass due to the mean flow for 0300Z, May 1956 Redwing data.

effect is quite small near the equator, well developed disturbances cannot be geostrophic.

It seems realistic, for this investigation, to consider that incipient disturbances in the ITC can be described, mathematically, as small perturbations upon a geostrophic zonal current. Also, when friction is included in the balance, the simplest mechanism that can explain the equatorward branch of the Hadley cell north of the ITC at about $4^{o}N$ is an Ekman-like boundary layer.

3.4. Structure of the Flow near the Surface

It has been shown that the principal forces per unit mass in the y-equation of motion in the two layers of maximum zonal wind north of about $4^{o}N$-$6^{o}N$ are the pressure gradient and Coriolis terms, plus friction in the surface easterlies.

We will now look in more detail at the wind structure in the lowest 10,000 feet, using reports for each 1000 foot interval, plus the 1000 mb observations which are normally recorded at 200-300 feet dependent upon latitude. The primary objective will be to determine the utility of Ekman theory in describing behavior in the planetary boundary layer at very low latitudes.

Wind direction is reported to the nearest 10 degrees; thus, the maximum reporting error is $\pm$ 5 degrees. It will be assumed that below 10,000 feet, other measurement errors are no larger than this order of magnitude. If we use the May 1956 mean data, the averaging process should reduce directional error below this amount. However,

since it is difficult to apply a simple reduction due to averaging, ±5 degrees will be considered a convervative estimate of the mean wind direction error.

3.4.1. Turning of the Wind with Height

Hodographs of the monthly mean wind through 10,000 feet were constructed at each of the reporting stations and are shown as Figs. 3.20 through 3.25. All stations, except for Tarawa and Kapingamarangi which are near 1^{o}N, show significant clockwise turning (veering) with height. Most of this is accomplished within the first 5000 feet except at Kwajalein (9.0^{0}N) and Eniwetok (11.3^{o}N) where, at this height, the veering is only about half complete. It is interesting that Ponape and Truk (both near 7^{o}N) show the largest direction envelopes; however, these islands are not atolls, and terrain features may have had a pronounced influence here. Turning angles through 10,000 feet vary from 16^{o} at Bikini (11.5^{o}N) and Rongerik (11.3^{o}N) to 42^{o} at Ponape (6.6^{o}N) with the remainder near 20^{o}. These are not necessarily the same as the important cross-isobar angles, but they emphasize the fact that the turning values are safely out of the probable range of errors of measurement and reporting.

The fact that winds this close to the equator turn with height near the surface is important in itself since there is divided opinion on this point. Taylor (1915) found reasonable agreement between real winds and the Ekman Spiral at higher latitudes; however, apparently there are oceanic regions where an Ekman-like effect is either poorly

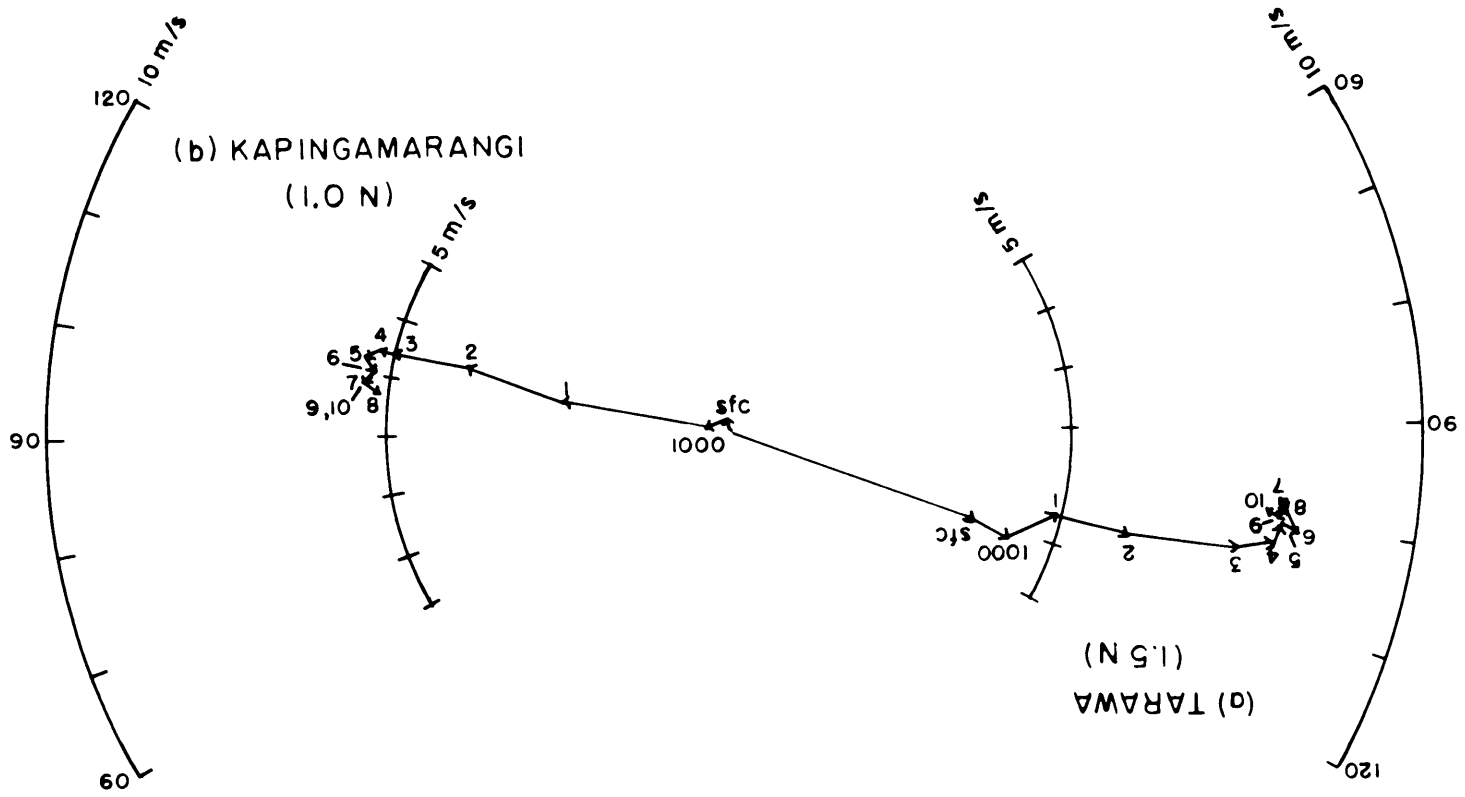

Fig. 3.20a,b. Hodographs from 0300Z, May 1956 Redwing data. Units are m s^{-1} and heights are 1000's of feet except for "1000" which means 1000 mb.

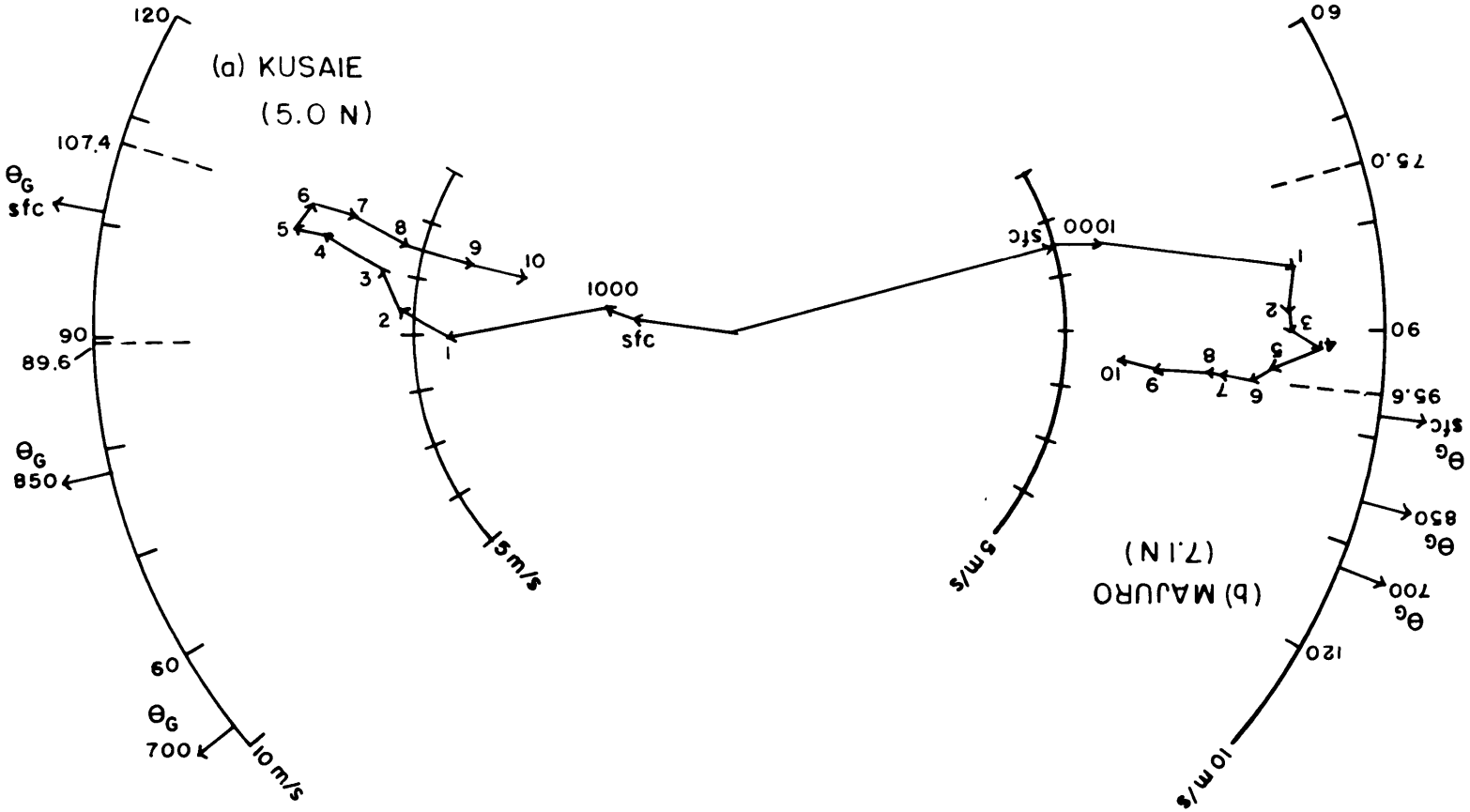

Fig. 3.21a,b. See Fig. 3.20. Also, turning angle range indicated by dashed lines, and geostrophic directions indicated by Θ_G .

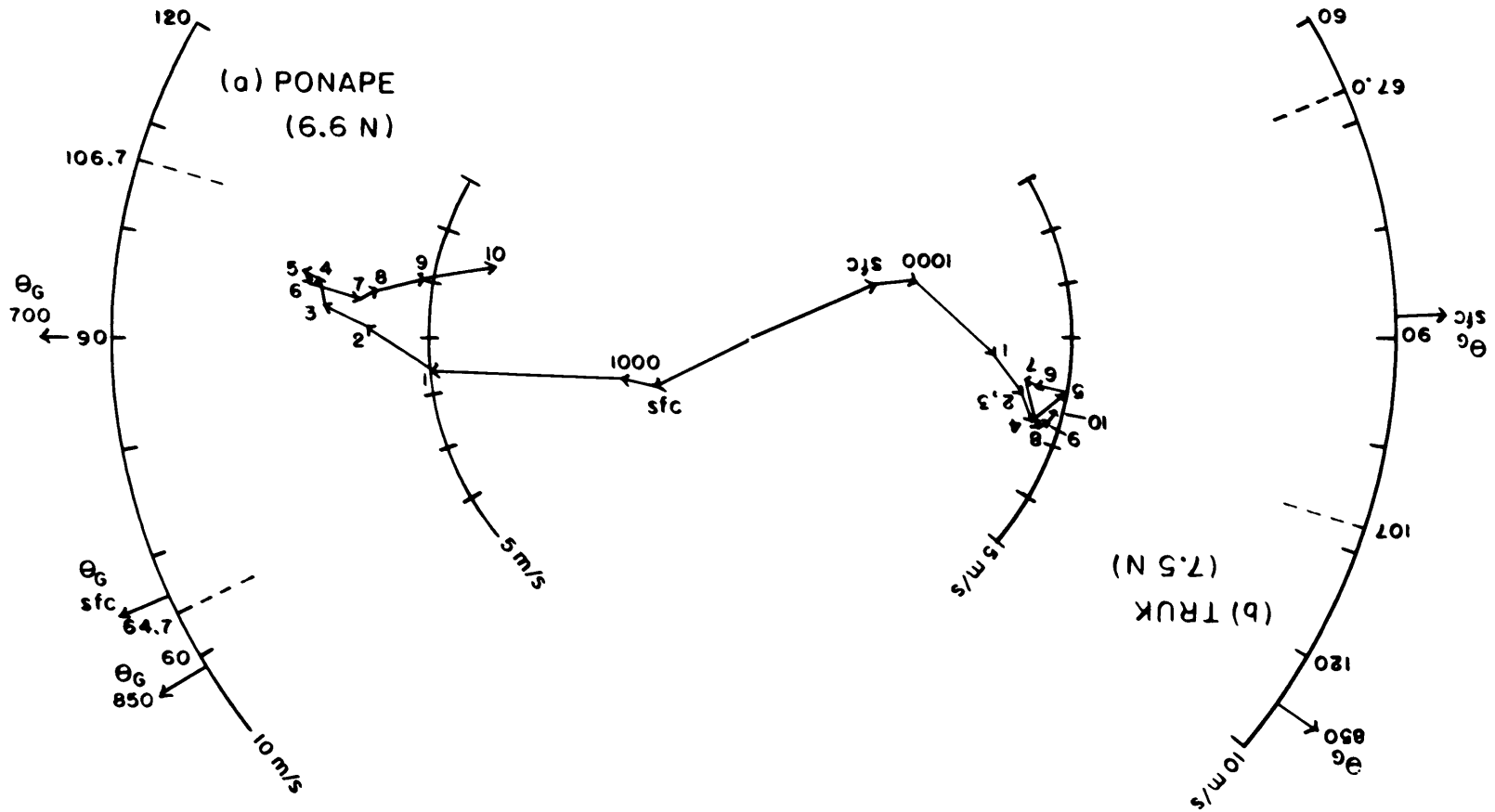

Fig. 3.22a,b. See Fig. 3.21

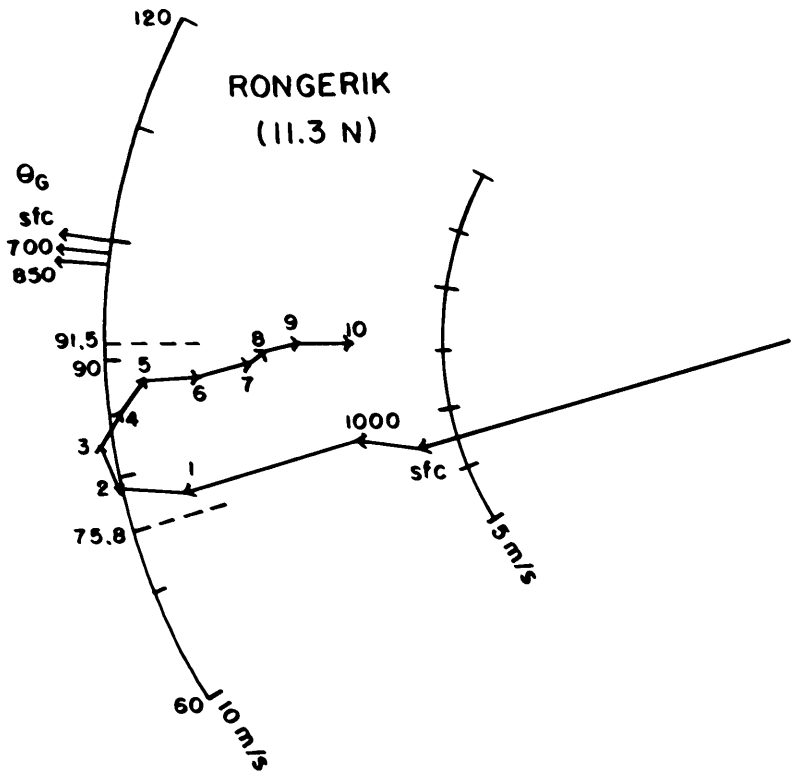

Fig. 3.23. See Fig. 3.21

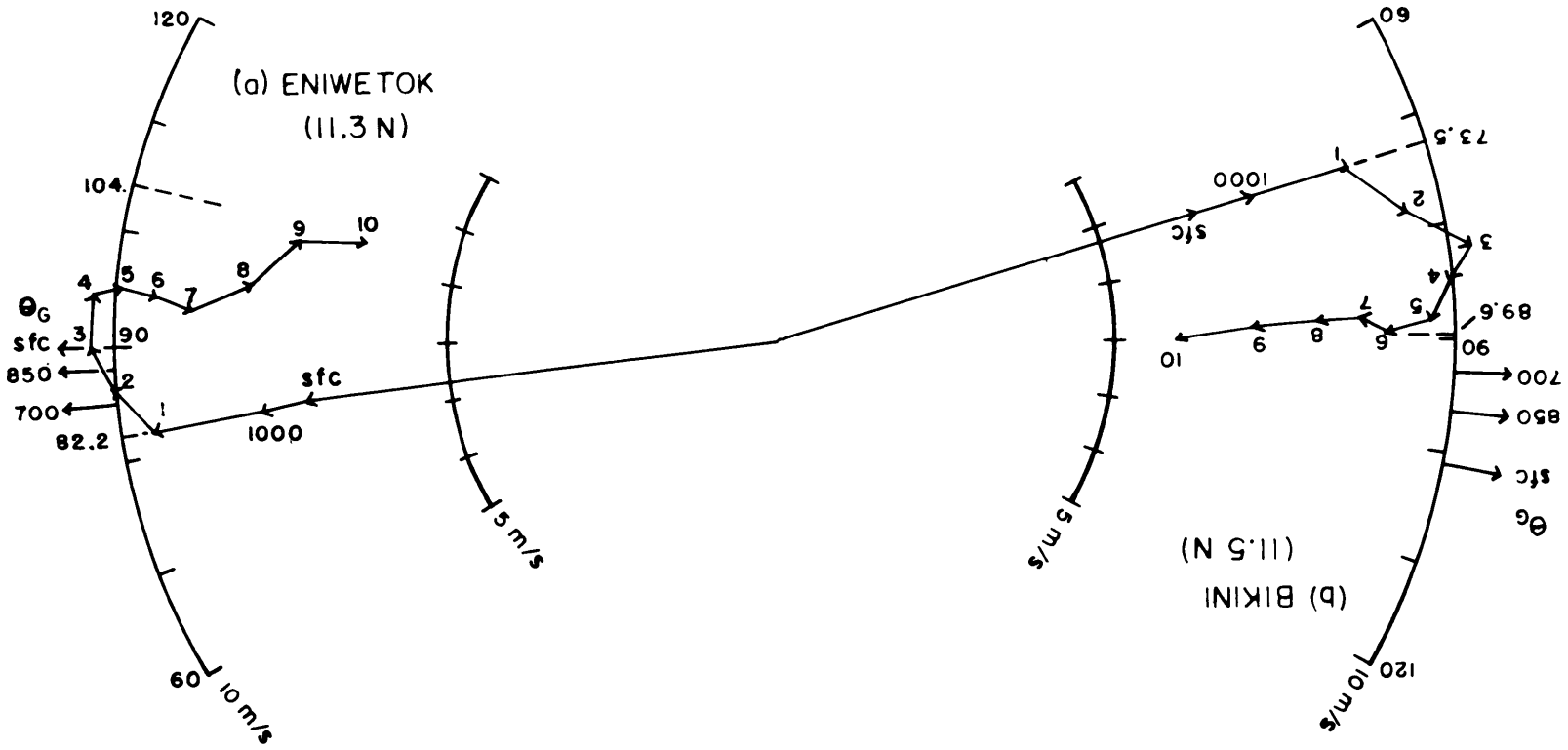

Fig. 3.24a,b. See Fig. 3.21.

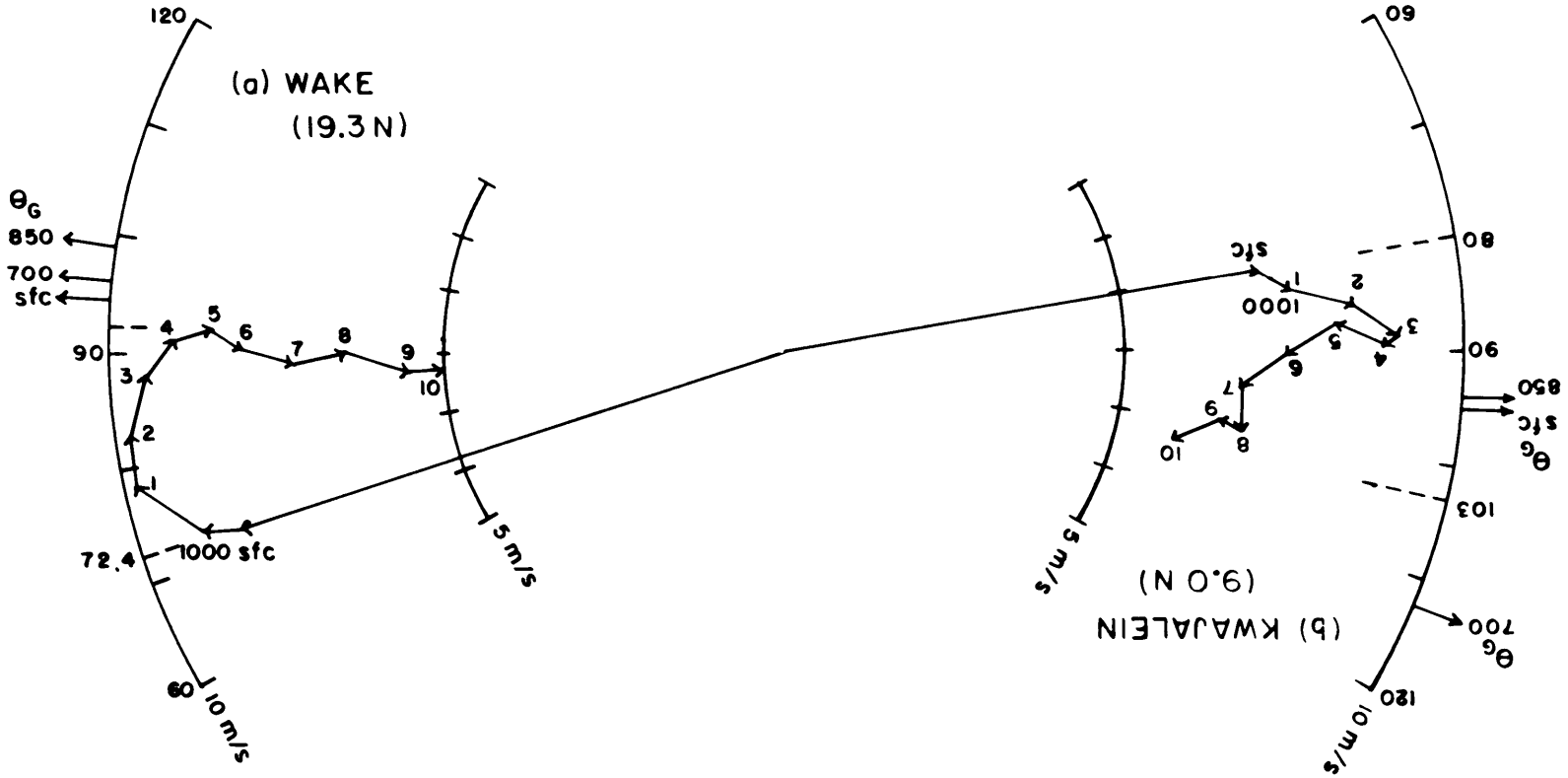

Fig. 3.25a,b. See Fig. 3.21.

defined or non-existent. Sheppard, et al. (1952) found no significant Ekman regime in strongly baroclinic winter wind profiles of the mid-latitude North Atlantic. Riehl and collaborators (1951) studied a restricted branch of the north-east Pacific trade between 20^{o}N and 30^{o}N east of the Hawaiian Islands, and found so little turning of the wind with height that they considered the flow to be two-dimensional along the trajectory. However, they measured a downstream pressure drop at the surface which diminished with height and disappeared at 3 km; consequently, the geostrophic wind had to rotate counterclockwise with height as the real winds maintained their direction. Using the same data base, Riehl and Malkus (1957) proposed that such a condition may be characteristic of a "driving" member of the general circulation. The latter is defined as a circulation that maintains itself and exports energy. In the study of June 1956 Redwing data by Ballif, et al. (1958), it is stated in C.E. Palmer's chapter that tropical winds show little change in direction with height and that this has long been known.

More recently, Gray (1968) in a broad survey of over 10,000 rawin reports from surface vessels between 30^{o}N and 30^{o}S has shown that veering through the first km is about 12^{o} with additional veering of 2^{o}-3^{o} through the second km. It should be noted also that these data principally come from the Northern Hemisphere between 10^{o} and 30^{o}. There are only minor variations (about 2^{o}-3^{o}) due to location or source of data in these composites.

3.4.2. Thermal Wind Effect

One of the principal causes for large disparities between theory and observation is the presence of marked baroclinity and corresponding geostrophic wind shear (thermal wind). The latter can take one of two forms: (a) speed shear with little or no rotation, and (b) rotation with or without speed shear. An infinite variety of models in which Coriolis, pressure gradient, and frictional forces are dominant could be constructed from class (b). One of these might be made to resemble the turning pressure field described by Riehl et al. (1951), and, indeed, an empirical model including friction was constructed for these data by Malkus (1956) based on stress and heating distributions. The rotation of the isobars was explained without any a priori assumptions about the pressure field or its relation with the wind field. Thus, this model did not use the standard approach to the Ekman solution and its associated assumptions (e.g., Petterssen, 1956).

In Figures 3.21 through 3.25, the directions of the geostrophic winds for the surface, 850 mb and 700 mb levels have been indicated on the hodographs. This was achieved by taking contour directions at the various stations from the mean pressure charts described in Chapter 2.

It should be emphasized that pressure and wind analyses were independently derived as discussed in Chapter 2. Stations north of 9^{o}N (Wake, Eniwetok, Bikini, and Rongerik) show little geostrophic turning through 10,000 feet with a range of 2^{o} (Rongerik) to 8^{o} (Bikini). The real winds at the same stations turn from 16^{o} to 21^{o} through

10,000 feet. The geostrophic turning envelopes for Kwajalein and Majuro are as large as those of the real winds, while those of the remaining stations (all south of 8^{o}N) may not even be representative since pressure measurements are most suspect in this region. An examination of the component pressure gradient forces from the study of the June 1956 Redwing data (Ballif, et al., 1958) reveals that geostrophic turning through 10,000 feet amounts to about 10^{o} down through 7^{o}N, and this increases significantly further south. North of 7^{o}N, however, this turning is only a few degrees in the first 5000 feet.

The evidence from these two Redwing studies strongly suggest that the wind regime north of 8^{o} or 9^{o}N is associated with class (a), i.e., geostrophic shear without turning. Further south, the possibility of major pressure errors makes it difficult to confirm or deny the reality of the increase in geostrophic turning; however, it should be noted that hodographs of the real winds do not show marked change with decreasing latitude as far south as Kusaie near 5^{o}N.

The author feels that pressure errors at these lower latitudes are significant, and that the combination of the scale analysis, thermal wind argument, and the appearance of the real wind hodographs favors a fairly simply relationship between wind, pressure, and friction to within 4^{o}-5^{o} of the equator as long as the flow pattern is relatively undisturbed.

As a final illustration of the behavior of the wind direction fields, Fig. 3.26 shows vertical mean cross-sections of the directions of the real winds (θ_R), geostrophic winds (θ_G) and the difference

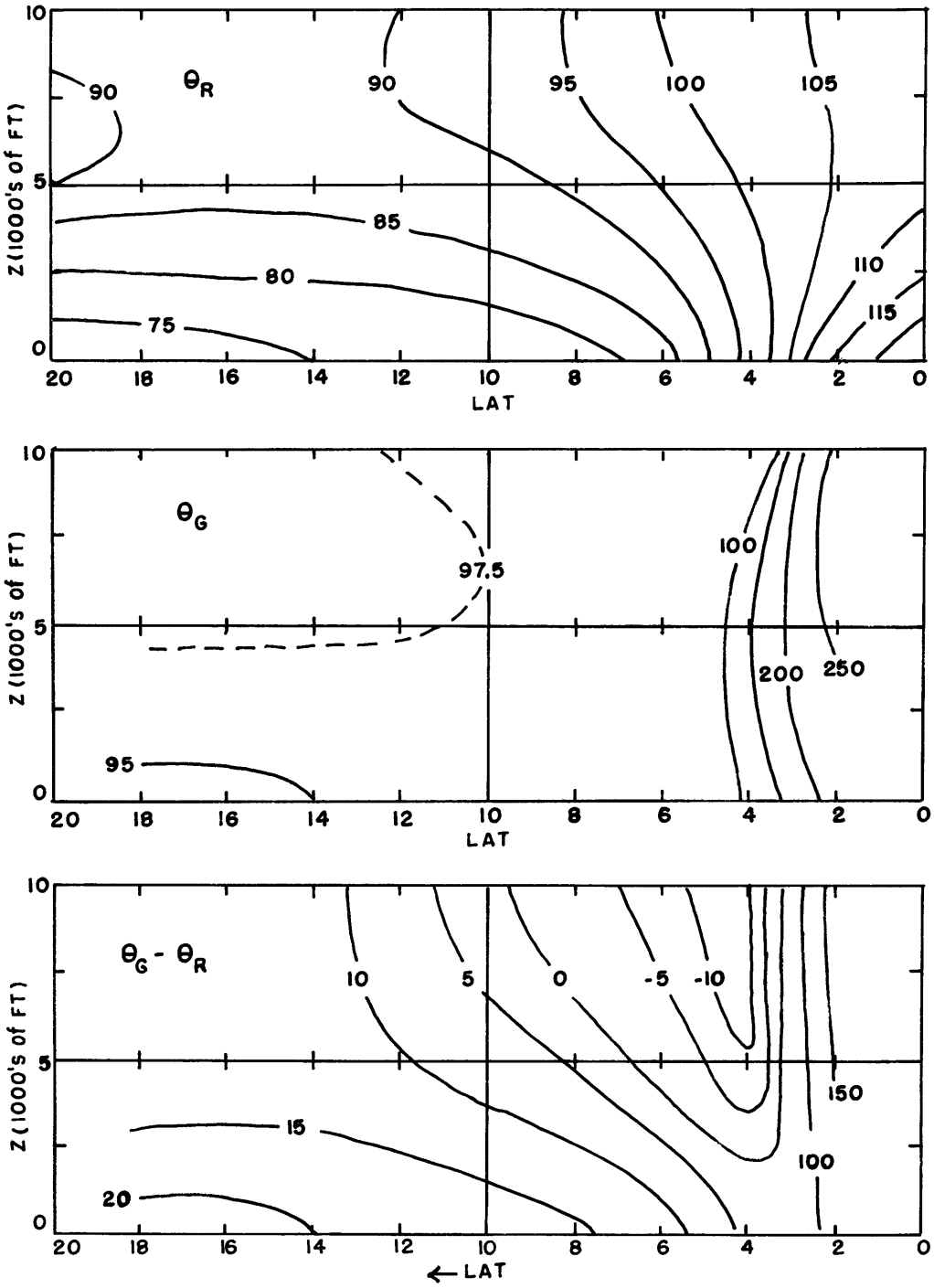

Fig. 3.26. Cross-sections of the mean real wind direction (Θ_R), geostrophic wind direction (Θ_G), and cross-isobar direction (Θ_G-Θ_R) for 0300Z, May 1956.

($\theta_G - \theta_R$) through 10,000 feet as a function of latitude. The values have been derived from the time-space means of u,v, $\frac{\partial z}{\partial x}$ and $\frac{\partial z}{\partial y}$. The effects of longitudinal averaging should be emphasized. The veering of θ_R is generally more conservative than in many of the individual hodographs, and, north of 4^{o}N, most turning is accomplished within 5000 feet, which is consistent with Gray's 1968) results. Winds back with height south of 4^{o}N which cannot be explained by simple Ekman theory. This latter characteristic shows up again in BOMEX and LIE studies discussed in Chapter 4. The large individual variations of θ_G with height near 6^{o}N (Truk, Ponape, and Kusaie) have tended to cancel in this mean cross-section so that, north of 4^{o}N, θ_G is nearly invariant with height. Thus, in the mean, the class (a) thermal wind regime extends down to 4^{o}N. The rapid reversal of θ_G south of 4^{o}N has necessitated a scale change on the figure. The significant cross-isobar flow ($\theta_G - \theta_R$) toward low pressure occurs below 5000 feet and north of 4^{o}-5^{o}N.

It appears that a simple approach may be justified to explain the basic dynamics of the boundary layer north of about 4^{o}N. This will be developed in the next section.

3.5. Ekman Theory Applied to a Special Baroclinic Regime

3.5.1. Model

In regions where the geostrophic components are quasi-linear in z, we can modify the Ekman solution and compare it with actual data. Also, certain constraints on the relationship between real

and geostrophic winds will be derived and used to adjust the latter profiles.

We begin with the equations of non-accelerated motion with friction, in which the "natural" x-coordinate is along the real surface wind, and the y-coordinate is positive to the left.

$$-f(v-v_G) = K_e \frac{d^2u}{dz^2} \tag{3.23}$$

$$f(u-u_G) = K_e \frac{d^2v}{dz^2} \tag{3.24}$$

Here we have used the diffusion form of the friction terms and assumed that the coefficient of eddy viscosity (K_e) is constant. The dependent variables u and v are assumed invariant in x, y and t. We will further specify a class (a) thermal wind region in which the geostrophic shear is constant with height. When referred to the natural coordinates, we find that this restriction generates geostrophic components which are also linear and which may be written

$$u_G = u_{G_0} + \ell z \,, \quad v_G = v_{G_0} + m z \tag{3.25}$$

Figure 3.27 illustrates the "natural" coordinate system and ψ the constant angle between the surface wind ($\mathbb{V}_0$) and geostrophic wind ($\mathbb{V}_G$).

If $G = |\mathbb{V}_G|$, it is clear that

$$u_G = G\cos\psi = (G_0 + Mz)\cos\psi \tag{3.26}$$

$$v_G = G\sin\psi = (G_0 + Mz)\sin\psi \tag{3.27}$$

where: G_o is the surface geostrophic speed, and M is the slope of G. Thus, from (3.25), (3.26) and (3.27), we have

$$u_{G_o} = G_o \cos\psi \quad , \quad v_{G_o} = G_o \sin\psi \tag{3.28}$$

$$\ell = M\cos\psi \quad , \quad m = M\sin\psi \tag{3.29}$$

If we had required only that the geostrophic components be linear, in general v_G would rotate with height. Since part of the analysis region falls nearly into class (a), we will use this constraint, then the constancy of ψ permits (3.29) and the special relationship $m = \ell \tan\psi$.

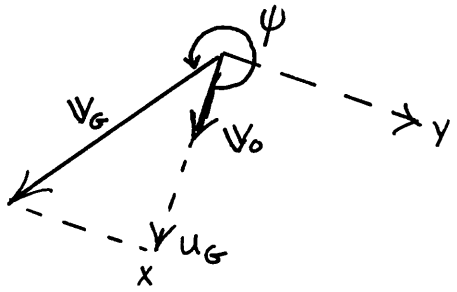

Fig. 3.27. The "Natural" coordinates used in the Ekman analysis.

Because of (3.25), (3.23) and (3.24) may be written

$$-f(v - v_G) = K_e \frac{d^2}{dz^2}(u - u_G) \tag{3.30}$$

$$f(u - u_G) = K_e \frac{d^2}{dz^2}(v - v_G) \tag{3.31}$$

which take the form of the first steps in the standard solution to this problem with a constant geostrophic wind. Multiply (3.31) by

$i = \sqrt{-1}$, then combine (3.30) and (3.31) by defining $w = u + iv$ and $w' = u - u_G + i(v - v_G)$ to give

$$\frac{d^2w'}{dz^2} - \frac{if}{K_e}w' = 0 \tag{3.32}$$

to be solved with the boundary conditions

$$w' = u_o - u_{Go} - i v_{Go} \quad \text{at } z = 0$$

$$w' \to 0 \quad \text{as } z \to \infty$$

Equation (3.32) is an ordinary D. E. with the solution in the form:

$$w' = A e^{(1+i)\alpha z} + B e^{-(1+i)\alpha z} \tag{3.33}$$

where $\alpha = \sqrt{f/2K_e}$ and A and B may be complex. Use of the second boundary condition shows that A = 0; then, the first boundary condition gives $B = u_o - u_{Go}$, and the final solution becomes:

$$u - u_G = e^{-\alpha z}\left[(u_o - u_{Go})\cos\alpha z - v_{Go}\sin\alpha z\right] \tag{3.34}$$

$$v - v_G = -e^{-\alpha z}\left[(u_o - u_{Go})\sin\alpha z + v_{Go}\cos\alpha z\right] \tag{3.35}$$

The expansion of u_G and v_G from (3.25) can be substituted into (3.34) and (3.35) if required. The solutions are the geostrophic departures, and do not explicitly depend on l and m the slopes of u_G and v_G.

If we define the "top" of the friction layer as the first level where the real and geostrophic winds are parallel, then we have the condition $(v - v_G)/(u - u_G) = \tan\psi$.

From (3.34) and (3.35) we have:

$$\frac{v-v_G}{u-u_G} = \tan\psi = \frac{[(u_o-u_{Go})\sin\alpha z + v_{Go}\cos\alpha z]}{[v_{Go}\sin\alpha z - (u_o-u_{Go})\cos\alpha z]}$$

With $v_{Go} = u_{Go}\tan\psi$, the real and geostrophic winds will be parallel when:

$$\tan\alpha z = \frac{u_o}{v_{Go} - (u_o-u_{Go})\cot\psi} \tag{3.36}$$

The first value of z satisfying (3.36) is the top of the friction layer by this definition.

In this particular class (a) thermal wind regime, the cross-isobar flow at any level is given by the expression

$$V_I(z) = -u(z)\sin\psi + v(z)\cos\psi \tag{3.37}$$

Thus, assuming a relatively constant density $\tilde{\rho}$ in the lower few kilometers, the mass transport across isobars as a function of height is:

$$T_I(z) = \tilde{\rho}\int_0^z V_I(z)\,dz \tag{3.38}$$

Substitution of (3.37) (with (3.34) and (3.35)) into (3.38) yields:

$$T_I(z) = \frac{\tilde{\rho}}{2\alpha}\left\{(G_o - u_o\cos\psi)\left[1-e^{-\alpha z}(\sin\alpha z+\cos\alpha z)\right]\right.$$

$$\left. -u_o\sin\psi\left[1-e^{-\alpha z}(\cos\alpha z-\sin\alpha z)\right]\right\} \tag{3.39}$$

In (3.39), G_o is the magnitude of the surface geostrophic wind vector. From classical Ekman theory (e.g. Sutton 1960) the real surface wind would be zero and ψ would be 315^o; if we put either of these conditions into (3.39) and let $z \to \infty$ we achieve the appropriate result

$$T_I(\infty) = \tilde{\rho} \frac{G_o}{2\alpha} \tag{3.40}$$

compared with

$$T_I(\infty) = \frac{\tilde{\rho}}{2\alpha}\left[G_o - u_o(\cos\psi + \sin\psi)\right] \tag{3.41}$$

derived directly from (3.39). Thus, the magnitude and vertical distribution of $T_I(z)$ can depart significantly from the classical model when the surface (or deck level) wind does not vanish.

3.5.2. The Surface Stress and a Constraint on u and u_G.

Write (3.23) and (3.24) in a more general form as:

$$-f(v - v_G) = \frac{1}{\rho}\frac{\partial \tau_x}{\partial z} \cong \frac{1}{\rho}\frac{\partial}{\partial z}\left(\mu_e \frac{\partial u}{\partial z}\right) \tag{3.42}$$

$$f(u - u_G) = \frac{1}{\rho}\frac{\partial \tau_y}{\partial z} \cong \frac{1}{\rho}\frac{\partial}{\partial z}\left(\mu_e \frac{\partial v}{\partial z}\right) \tag{3.43}$$

where τ_x and τ_y are the virtual stress components due to vertical turbulent momentum exchange in the x- and y-directions, and μ_e is the horizontally invariant dynamic coefficient of eddy viscosity (Sutton, 1960). Since ρ varies slowly with z in the friction layer, we write $K_e \cong \frac{\mu_e}{\rho}$ and integrate (3.42) and (3.43) to give:

$$-f\int_0^H (v-v_G)\,dz \cong K_e\left(\frac{\partial u}{\partial z}\Big|_H - \frac{\partial u}{\partial z}\Big|_0\right) \tag{3.44}$$

$$f\int_0^h (u-u_G)\,dz \cong K_e\left(\frac{\partial v}{\partial z}\Big|_h - \frac{\partial v}{\partial z}\Big|_0\right) \tag{3.45}$$

In the Redwing data, wind profiles in the natural coordinate system tend to resemble the idealized profiles of Fig. 3.28. If we choose H at the level where $\frac{\partial u}{\partial z} = 0$, and h at the level where $\frac{\partial v}{\partial z} = 0$, then (3.44) and (3.45) become:

$$-f\int_0^H (v-v_G)\,dz \cong -K_e \frac{\partial u}{\partial z}\Big|_0 \cong -\frac{1}{\rho}\tau_x\Big|_0 \tag{3.46}$$

$$f\int_0^h (u-u_G)\,dz \cong -K_e \frac{\partial v}{\partial z}\Big|_0 \cong -\frac{1}{\rho}\tau_y\Big|_0 = 0 \tag{3.47}$$

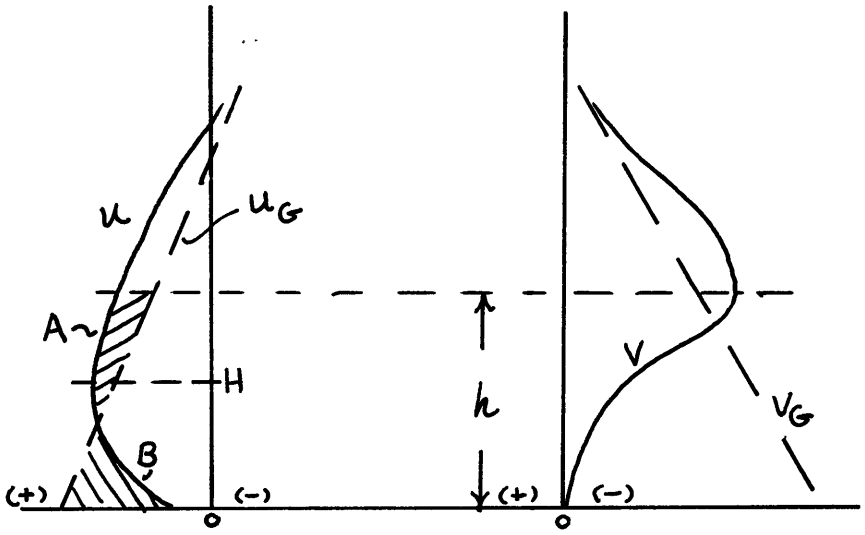

Fig. 3.28. Idealized tropical wind profiles in natural coordinates.

Thus (3.46) provides a means of solving for the surface stress, while the second constraint (3.47) requires area A to equal area B in Fig. 3.28. The zero result in (3.47) is due to the following argument.

Since we are using natural coordinates, the wind at z = 0 is along x only. Furthermore, in the near-surface Prandtl layer the stress is directed along the surface wind (e.g. see Petterseen, 1956); hence, the stress component normal to the surface wind equals zero.

One valid criticism of this technique is due to the fact that the eddy shearing stresses are actually proportional to $\overline{u'w'}$ and $\overline{v'w'}$ (see derivation of equations (3.7) and (3.8). We approximate these stresses by using the molecular analogy which makes them proportional to the slopes of the mean wind component profiles. Thus the approximate stresses must vanish at component extrema, but the real stresses may, in fact, be non-zero (Priestly, 1959). Chances are very good that stresses are small at these velocity extrema, especially if the profiles are symmetric. This may be good enough for certain types of engineering studies using real data which probably contain errors of larger magnitude. Malkus (1956) accepted the vanishing of the stress at a velocity maximum based on conclusions by Charnock, et al. (1956) who developed (3.46) and (3.47) in their study of the trades. The latter group used careful PIBAL observations to determine that the shearing stress was actually quite small near velocity extrema.

Examples can be drawn from the May 1956 data which show quite reasonable agreement with Ekman theory modified for characteristics of class (a) geostrophic winds. The next section describes one of the better cases.

3.5.3. The Friction Layer at Rongerik, May 1956

The hodograph for Rongerik (Fig. 3.23) shows that $\theta_R = 76^\circ$ at the surface, and $\theta_G \cong 99^\circ$ through 10,000 feet; hence, angle $\psi \cong 337^\circ$. The geostrophic magnitude G derived from the mean contour analyses for the surface, 850, and 700 mb levels is linear in z when differencing is taken over 4° latitude and centered on Rongerik. Components of the real and geostrophic winds are expressed in natural coordinates along and to the left of $\bar{u}_o$, and are shown plotted through 10,000 feet in Fig. 3.29.

On this plot, $\frac{\partial \bar{v}}{\partial z}$ first equals zero at 5000 feet. We choose h = 5000 since the next extreme is in a less well defined zone near 8000 feet. H is easily seen to be near 2700 feet on the u-curve. It is obvious that the integral (3.47) will not equal zero unless the $\bar{u}_G$ curve is adjusted since the original $\bar{u}_G$ profile never intersects $\bar{u}$.

Previously we have noted that the thermal wind appears to be more reliable than the geostrophic wind; therefore, the $\bar{u}_G$ curve will be translated to the right in such a way as to satisfy (3.47) without changing the slope. Then, by using $\bar{v}_G = \bar{u}_G \tan\psi$, $\bar{v}_G$ will be adjusted so that ψ remains the same as before because there is no valid reason to change its value. We write (3.47) as:

$$\int_o^h (\bar{u} - \bar{u}_G - \ell z)\, dz = \int_o^h \bar{u}\, dz - \frac{\ell h^2}{2} - \bar{u}_G h = 0 \qquad (3.48)$$

by substituting from (3.25). Thus we can solve for the required $\bar{u}_G$ by using the unadjusted value of the slope l, that is:

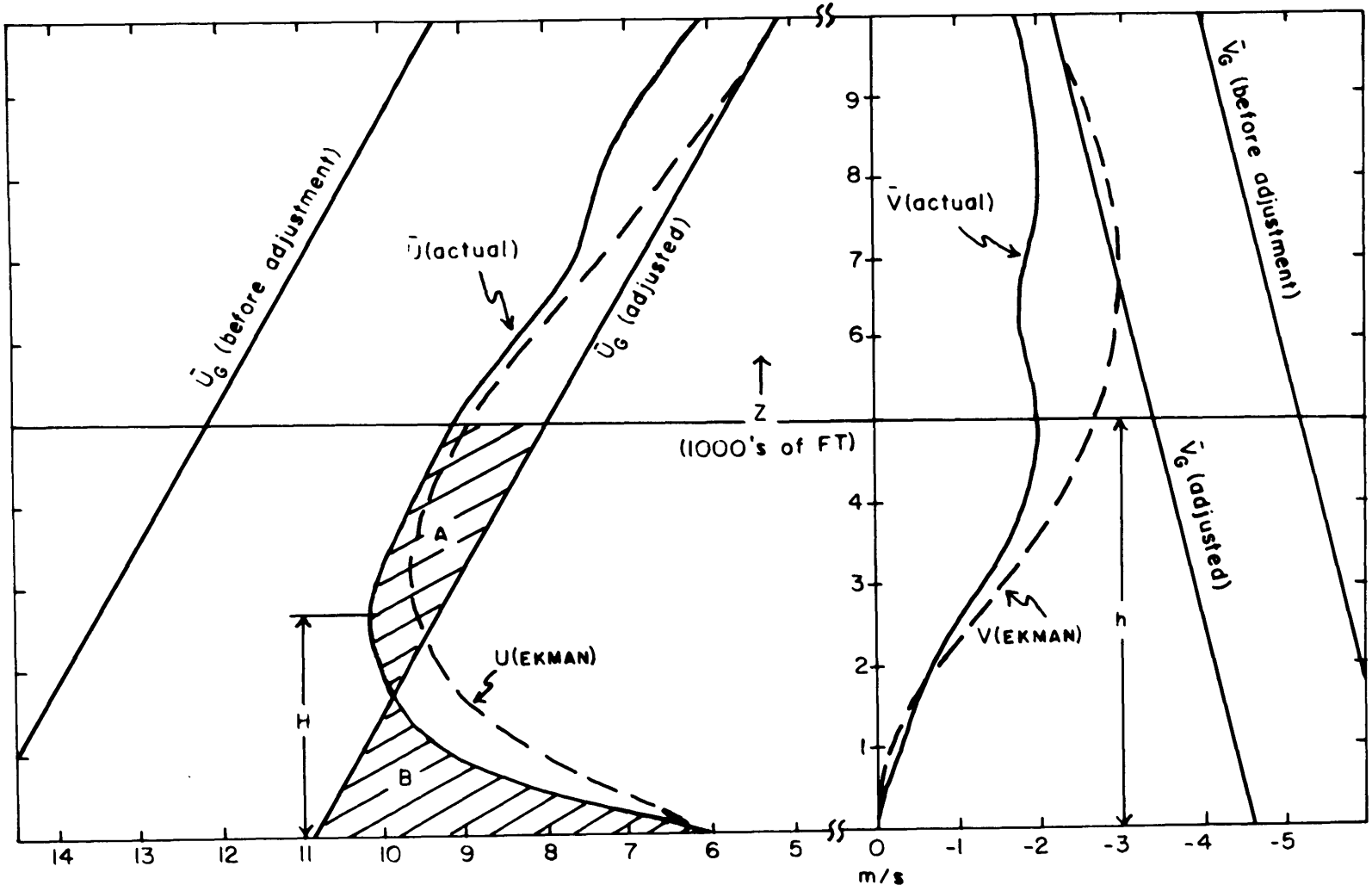

Fig. 3.29. Rongerik (11°N) mean wind components plotted in "natural" coordinates (curved solid lines). Unadjusted and adjusted geostrophic wind components shown as sloping straight lines. Dashed lines show Ekman solution. H and h are heights used in expressions (3.46) and (3.47). Note suppressed zero.

$$u_{G_0} = \frac{1}{h}\int_0^h \bar{u}\,dz - \frac{\ell h}{2} \tag{3.49}$$

The integral in (3.49) was solved directly from the original figure by "counting squares". The adjusted curves for $\bar{u}_G$ and $\bar{v}_G$ are shown in Fig. 3.29 along with the equal areas A and B. Next the integration of (3.46) yields a value of the surface stress of

$$\tau_x\big|_0 = 1.06 \times 10^{-4} \text{ ton } m^{-1}s^{-2} = 1.06 \text{ dyne } cm^{-2}.$$

This is seen to compare quite favorably with values from other sources (e.g., Charnock et al., 1956, and Sutton, 1960), but is about twice the value found by Estoque (1971) at Christmas Island near $2^{o}N$.

In order to draw the theoretical wind profiles from (3.34) and (3.35), we must specify a constant value for K_e the coefficient of eddy viscosity. This could be done arbitrarily by picking a typical value of order 10 m^2s^{-1}. Or by using (3.23) and (3.24), we may solve for a variable $K_e(z)$, since the winds are given. This method will, in general, generate a $K_e(z)$ for each equation independently, and these will also be functions of the choice of coordinate system (i.e. natural vs. earth-oriented). If we use the more general form for the frictional terms suggested by equations (3.42) and (3.43), a K_e may be derived which is only a function of z. Then an average value can be substituted into (3.34) and (3.35). We write (3.42) and (3.43) as:

$$-f(v-v_G) \cong \frac{\partial}{\partial z}\left(K_e \frac{\partial u}{\partial z}\right) = F_x \tag{3.50}$$

$$f(u-u_G) \cong \frac{\partial}{\partial z}\left(K_e \frac{\partial v}{\partial z}\right) = F_y \tag{3.51}$$

where F_x and F_y are derived at any level by knowing u and u_G. Thus we have:

$$\frac{\partial K_e}{\partial z}\frac{\partial u}{\partial z} + K_e \frac{\partial^2 u}{\partial z^2} = F_x$$

$$\frac{\partial K_e}{\partial z}\frac{\partial v}{\partial z} + K_e \frac{\partial^2 v}{\partial z^2} = F_y$$

and elimination of $\frac{\partial K_e}{\partial z}$ gives the following formula for $K_e(z)$.

$$K_e(z) = \frac{F_y \partial u/\partial z - F_x \partial v/\partial z}{\frac{\partial^2 v}{\partial z^2}\frac{\partial u}{\partial z} - \frac{\partial^2 u}{\partial z^2}\frac{\partial v}{\partial z}} \tag{3.52}$$

Finite differences were used with a 1000 foot spacing to solve (3.52). Table 3.10 gives $K_e(z)$ at Rongerik for each 1000 foot level to 10,000 feet from (3.52). The geostrophic components are adjusted by using (3.47) and the constancy of ψ, and f = 2.83 x 10^{-5} s^{-1}.

Except for the two negative values at 6000 and 7000 feet, K_e is rather well behaved, especially in the first 5000 feet. The minor u-minimum and v-maximum near 7000 feet cause curvature and slope variations which do not relate properly to the signs of the friction terms, and cause the negative results. Considering the sensitivity of (3.52), and the limited utility of the concept of the eddy coefficient where

z	u	u_G	v	v_G	F_x	F_y	K_e
0	5.68	10.85	0.0	-4.60	-13.0	-14.65	---
1	9.13	10.28	-0.25	-4.36	-11.61	-3.26	8.7
2	10.06	9.71	-0.66	-4.12	-9.78	0.99	7.7
3	10.12	9.14	-1.27	-3.88	-7.38	2.78	13.4
4	9.62	8.57	-1.82	-3.64	-5.15	2.98	15.3
5	9.15	8.00	-2.01	-3.40	-3.94	3.26	8.5
6	8.36	7.43	-1.84	-3.16	-3.74	2.63	-10.9
7	7.62	6.86	-1.87	-2.92	-2.97	2.15	-19.3
8	7.39	6.29	-1.96	-2.68	-2.04	3.11	20.9
9	6.84	5.72	-1.93	-2.44	-1.44	3.17	17.7
10	6.10	5.15	-1.71	-2.20	-1.39	2.69	---

Table 3.10. Parameters used in (3.53) to derive the coefficient of eddy viscosity (K_e) at Rongerik as a function of height (z). Winds are in m/s, F_x and F_y are in units of 10^{-5} ms^{-2}, and K_e is in m^2s^{-1}.

strong curvature in the wind profile is absent, even the positive values at 8000 and 9000 feet are probably spurious. Thus an average of the values of K_e through only the first 5000 feet will be used and subtituted into equations (3.34) and (3.35). We find $K_e = 10.7\ m^2s^{-1}$, then $\alpha = \sqrt{f/2K_e} = 1.15 \times 10^{-3}\ m^{-1}$; the theoretical profiles are shown in Fig. 3.29. The "top" of the friction layer is, from (3.36):

$$z_T = \frac{1}{\alpha} \tan^{-1}\left(\frac{5.68}{-4.6+5.17 \cot 337^\circ}\right)$$

$$= 2450 \text{ m} = 8030 \text{ ft.}$$

It is apparent from the figure that, considering the assumptions and simplifications, the real and theoretical profiles show good agreement through 5000 feet in the y-direction , and through 7000 feet in the x-direction.

From (3.39) with $\tilde{\rho} \sim 10^{-3}$ ton m^{-3}, the cross-isobar mass transports integrated to three different heights at Rongerik are given in Table 3.11 below.

Z	870 m	1740 m	∞
$T_I(Z)$	2.49	3.77	3.82
% Total	65	99	100

Table 3.11. Cross-isobar mass transport from the Rongerik Ekman solution at heights corresponding to $1/\alpha$, $2/\alpha$ and ∞ . Units of $T_I(Z)$ are ton $m^{-1}s^{-1}$.

From classical theory (zero surface wind) the percentages of total cross-isobar transport would be 49% and 92% at the first two e-folding depths. The point is simply that even though the model Ekman solution in the tropics suggests a gradient level at 2-3 km using reasonable parameters, at least 50% of the cross-isobar transport should occur in roughly the first kilometer. Furthermore this percentage increases to 65% when a non-zero surface wind is used in the model.

The previous point lends credence to the CISK hypothesis of Charney and Eliassen (1964) which explicitly depends for its relevance

on reasonably shallow, cross-isobar, boundary layer mass and moisture transport.

3.5.4. Sensitivity of the Model to Variations in K_e

The model profiles of u and v are quite sensitive to the choice of K_e. Figure 3.30 shows this graphically as K_e varies from 1 to 30 mts units by approximate one-half order of magnitude steps ($\log_{10}$). Modest enhancement of the mixing process in cumulus-rich regions should be capable of affecting both the depth and mass transport of the boundary layer by changing the effective value of K_e. Cloud bases in the tropics are usually at 2000 feet, thus, following this reasoning, the monthly mean K_e should increase above this point. In Table 3.10, K_e at 3-4000 feet is approximately double the 2000 foot value. The use of a vertically averaged K_e in the model could have been avoided by matching two Ekman solutions at 2000 feet using K_e's of 8 $m^2 s^{-1}$ and 14 $m^2 s^{-1}$. In fact this was done and the profiles actually looked a little better. The author is well aware that eddy coefficients, Ekman layers and single station case studies taken together can tempt one to stretch a good thing too far. Also, the role of cumulus convection in the vertical transport of momentum is not in the province of this paper; therefore, no further attempt to "fine tune" the model is justified herein.

In this example, four important factors must be considered: (1) mean monthly data were employed, (2) the geostrophic winds did not rotate with height while the speed shear was linear, (3) the geostrophic winds were adjusted to fit (3.47) the constraint imposed by stress

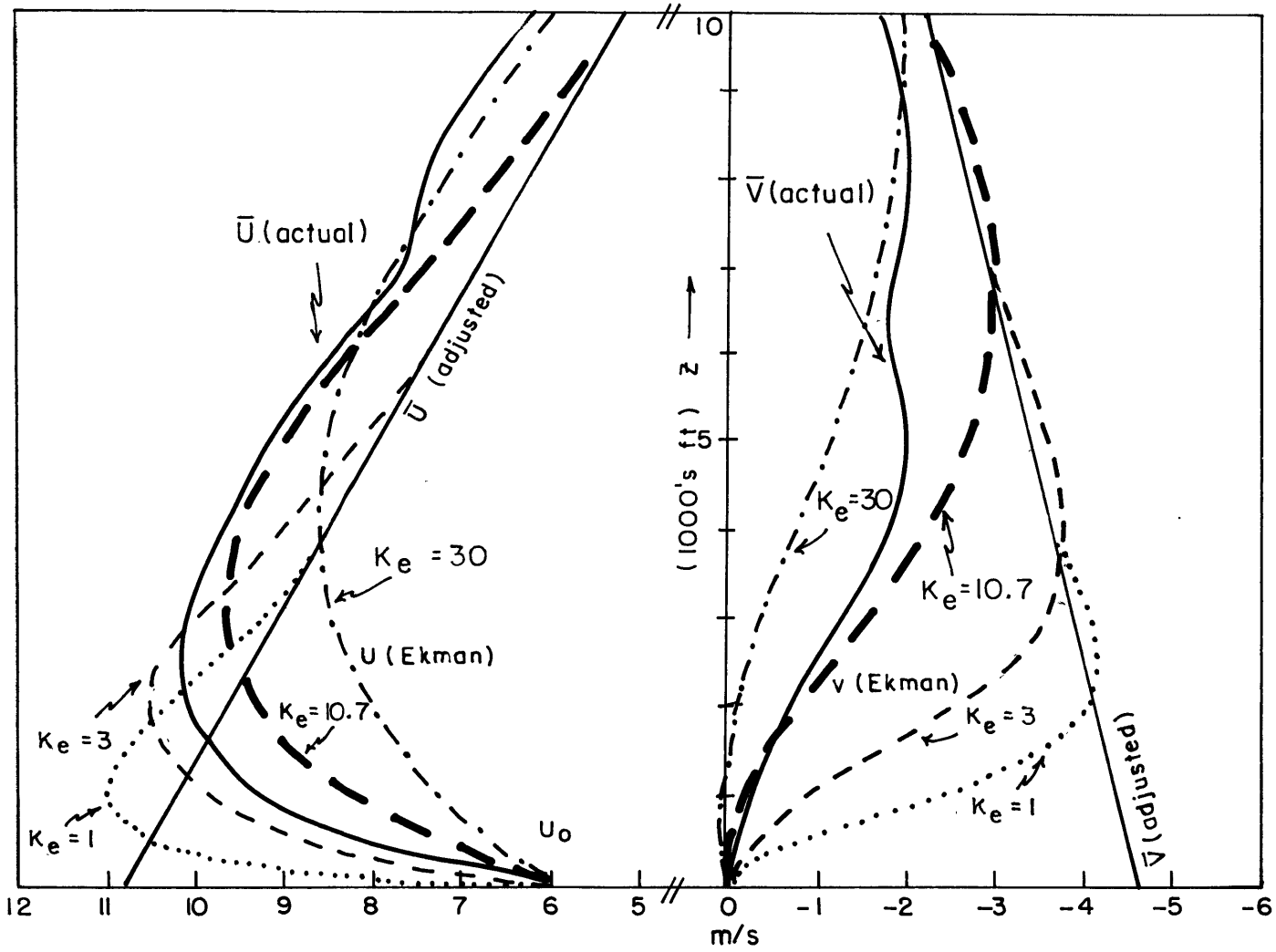

Fig. 3.30. Sensitivity of the Ekman model to variations in K_e shown along with the solution for K_e = 10.7.

considerations, and (4) the simplicity of Ekman theory itself.

In regard to the first consideration, steadiness values at Rongerik ranged between 0.88 at 10,000 feet to 0.98 at the surface. Values of $1 - R_K$, which represents the fraction of perturbation kinetic energy, vary between .33 and 0.185 at the same levels. Thus, daily characteristics of the real wind must not have departed too much from the mean. Figure 3.31 shows four daily 0300Z hodographs at Rongerik which represent the general range of extreme inputs to the mean hodograph for May 1956.

One problem in plotting Fig. 3.31 was that synoptic wind reports are given in units of tens of degrees. The 11 May case shows simple veering with height; the 13th was a case of little turning; the 17th is an extreme case of veering; and the 18th is quite anomalous due to the considerable backing with height.

Clearly, there is a variety of possible daily patterns, many having substantial turning with height, even if this is occasionally in the "wrong" direction for simple Ekman theory to explain. Some of the more extreme cases are probably dominated by relatively strong baroclinicity and turning of the pressure field. Table 3.12 puts the sixty 0300Z and 1500Z May Rongerik reports into categories of backing, veering, and no turning (turning through 10^{o} or less) through 5000 and 10,000 feet.

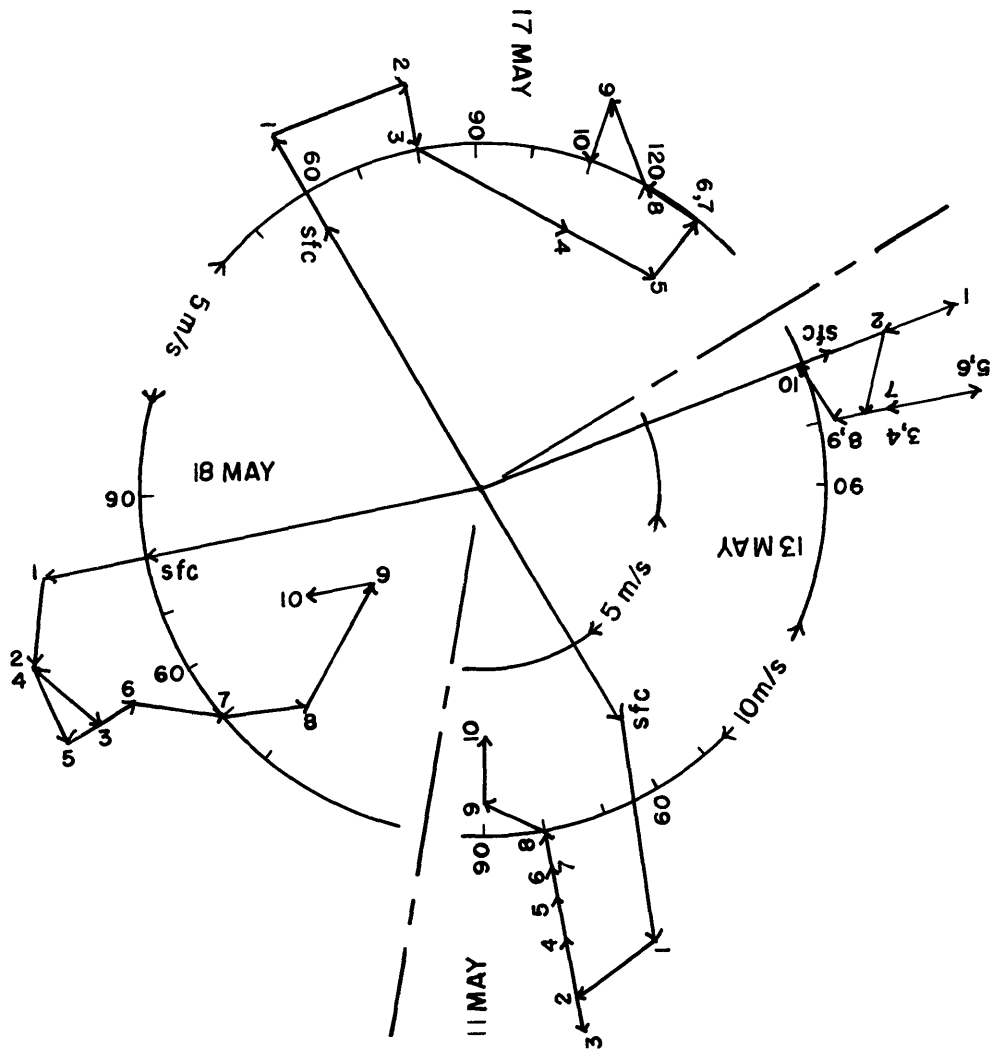

Fig. 3.31. Some Rongerik hodographs for 0300Z, May 1956, showing the general range of daily, low-level wind behavior. Note change of speed scale on the 17th and 18th.

z	BACKING		VEERING		NO TURN	
	03Z	15Z	03Z	15Z	03Z	15Z
5000 ft	5	2	13	17	12	11
10,000 ft	5	9	21	14	4	7

Table 3.12. Categories of Rongerik wind direction change through 5000 feet and 10,000 feet for sixty 0300Z and 1500Z cases in May 1956. NO TURN means turning through 10^{o} or less. The numerals show the number of cases in each category.

Unless there was a systematic tendency toward veering in the daily geostrophic wind, the effect of an Ekman-like behavior is seen in Table 3.12, especially through the first 5000 feet. As a test for bias in the geostrophic turning for May, Table 3.13 shows the same categories and times for the period 16 June through 14 July 1956. There was a different distribution of veering and no turn cases in this latter sample compared to the May data, especially at 1500Z. But the number of backing cases is similar in the two periods, and only comprises about 10 percent of the total number of observations.

If we tentatively assume that there were an equal number of backing and veering geostrophic wind cases (with the restriction that the component profiles were quasi-linear), then an Ekman effect from (3.41) would: exaggerate those cases that veered, partially compensate for many that backed (giving cases with veering or little turning), and be overcome by only those cases that backed excessively. Obviously, in this idealized picture, real winds that backed with height would be in the minority. Significantly, this is the kind of distribution shown

in Tables 3.12 and 3.13, and this supports an Ekman-like wind regime in the daily as well as the mean situations.

z	BACKING		VEERING		NO TURN	
	03Z	15Z	03Z	15Z	03Z	15Z
5000 ft	4	2	15	9	11	19
10,000 ft	4	7	13	11	13	12

Table 3.13. Same as Table 3.12 for the period 15 June through 14 July 1956.

The second and third considerations remain somewhat speculative due to their dependence on the accuracy of sounding data. Essentially, in the Rongerik example, we preserved the direction of the height contours and the integrity of the thickness fields (thermal winds), but changed the absolute slope of each pressure surface by adjusting the "constant of integration" (the surface geostrophic wind). At Rongerik's latitude (11^{o}N) the inertial and fluctuation terms in the y-equation are all small below 10,000 feet; thus, the constraints of (3.46) and (3.47) must approximately hold if we accept the structure of the Prandtl layer and the vanishing of stress at velocity extrema. Otherwise, the scale analysis showed that a nearly constant frictional force due to vertical momentum exchange would have been operating through the depth of the troposphere in order to explain the difference between the $\bar{u}$ and $\bar{u}_G$ curves north of about 4^{o}N. This may be an exciting discovery and it deserves further investigation using very accurate sounding data; however, the author feels that the circumstantial evidence, presented to this point, suggests that modest

errors in the construction of the soundings are the more likely cause.

All applications of Ekman theory are subject to the fourth consideration, that of simplicity. Under ideal conditions, such as those found in the laboratory (e.g., Holton 1965, Hide 1963, Faller 1963) the Ekman solution is nearly exact. Charney and Eliassen (1949) used the theory in deriving the surface vertical motion term for numerical atmospheric modelling and various modifications of this technique are still in use. However, strong baroclinicity and turning of the geostrophic wind with height can mask the Ekman effect. The Rongerik case demonstrates that, where turning of the mean geostrophic wind is absent, the theoretical wind profile is a reasonable representation of the real wind, even at these low latitudes.

No other station fit the idealized geostrophic departure pattern as closely as did Rongerik, mainly due to turning of the pressure gradient with height or some other complications in the geostrophic fields. But characteristics of the real wind do not vary a great deal over the map except for the two stations near $1^{o}N$ – Kapingamarangi and Tarawa. This was noted in the discussion of the hodographs, and may be seen in profile as well. For example, Fig. 3.32 has natural coordinate plots of Wake, Kwajalein, Rongerik, and Kusaie winds which have basic similarities through the first 4000 to 5000 feet, even though their latitudes vary between $5^{o}N$ and $19^{o}N$. Kusaie's $\bar{v}$-profile is like the others from 1000 to 5000 feet only.

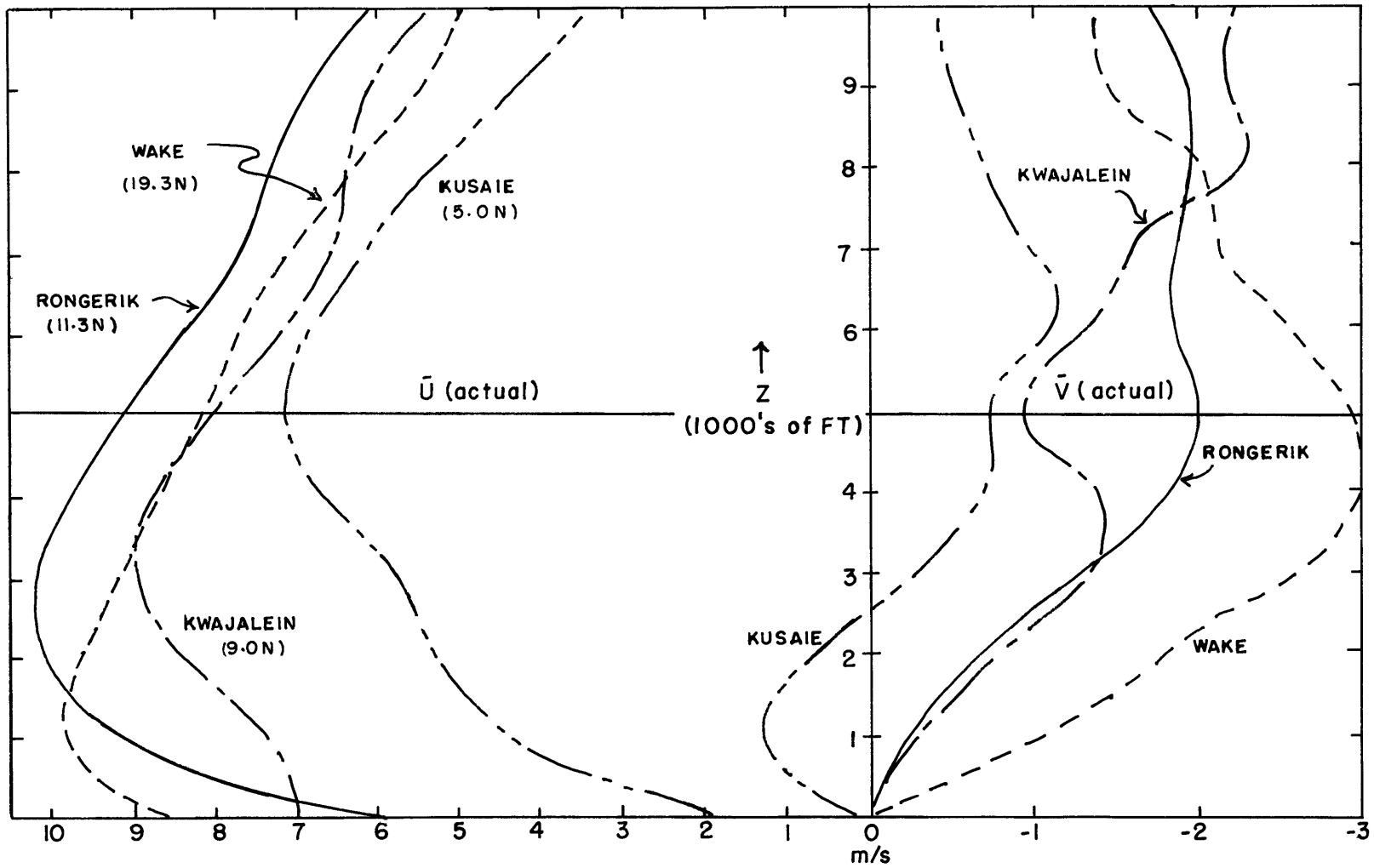

Fig. 3.32. Mean wind profiles from four stations in the Redwing area for 0300Z, May 1956 in natural coordinates with x-axis along u_o.

The backing from the surface to 1000 feet at Kusaie may be related to the terrain since there is at least one peak over 2000 feet high on the island.

These similarities are not sufficient to prove the existence of a true Ekman layer in the region, but they are necessary in that the lack of such characteristics would enable us to reject Ekman theory.

Thus, this rather detailed look at wind data from Rongerik and the other stations shows that, at least for the period 1-30 May 1956 in a particular region of the tropics, Ekman theory provided a reasonable explanation for the mean boundary layer behavior down to nearly 4^{o}N. It also appears that Ekman-like behavior showed up in most of the daily cases as well (Tables 3.12 and 3.13).

3.6. Significance of the Transition at 4^{o}North Latitude

Throughout this chapter, it has been noted that the flow changed character near 4^{o}N. In particular, the significance of non-geostrophic terms in the y-equation of motion increased there, and the Ekman character of the boundary layer vanished south of this point. An examination of various cross-sections and analyses reveals that the mean axis of the ITC position for May 1956 was also near this latitude at the surface, and sloped toward the north with increasing altitude.

Certainly, the divergence cross-section, Fig. 3.2 is most suggestive. The convergence axis is shown near 4^{o}N at the surface, and crosses 6^{o}N at 24,000 feet. The cell of strongest positive divergence near 37,000 feet is also centered near 4^{o}N, and this would logically be the compensation for the low-level convergence maximum. Below 500 mb, there is a belt of predominantly low pressure near 4^{o}N which was independently analyzed (Figs. 2.6 through 2.8) which supports the low-level convergence. Above 500 mb, there is a transition to high pressure cells at the lower latitudes, but the structure is not well aligned with the divergence maxima. This poor agreement at high levels may be due to the difficulties inherent in pressure analysis in this region.

Figure 3.18 shows that, in addition to the pronounced steadiness minimum near the level of zonal wind reversal, there is also a secondary minimum which dips down to the surface near 4^{o}N. This corresponds to the increased activity in minor disturbances which populate the ITC. The same feature shows up in the R_K cross-section depicting the relative kinetic energy of the mean flow, Fig. 3.19.

Figures 3.33 and 3.34 are vertical sections through Wake, Eniwetok, Ponape, and Kapingamarangi showing thermodynamic and moisture parameters for May 1956 at 0300Z. The atmosphere is hydrostatically stable to dry perturbations since the potential temperature (Θ_d) is seen to increase with height at all levels. Conditional instability prevails below about 20,000 feet where the wet-bulb potential temperature (Θ_W) decreases with height.

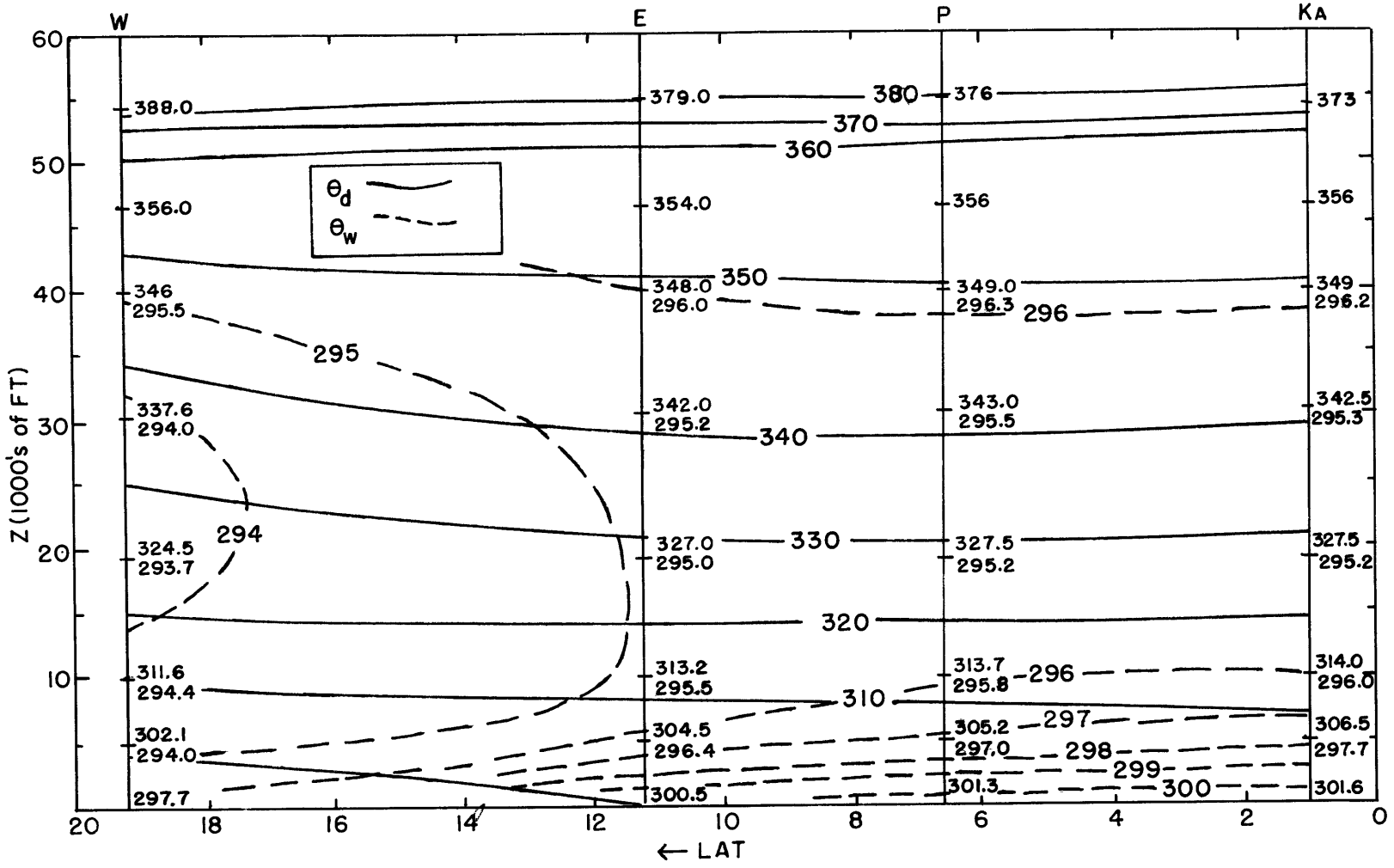

Fig. 3.33. Mean cross-section of potential temperature (θ_d) and wetbulb potential temperature (θ_w) for 0300Z, May 1956.

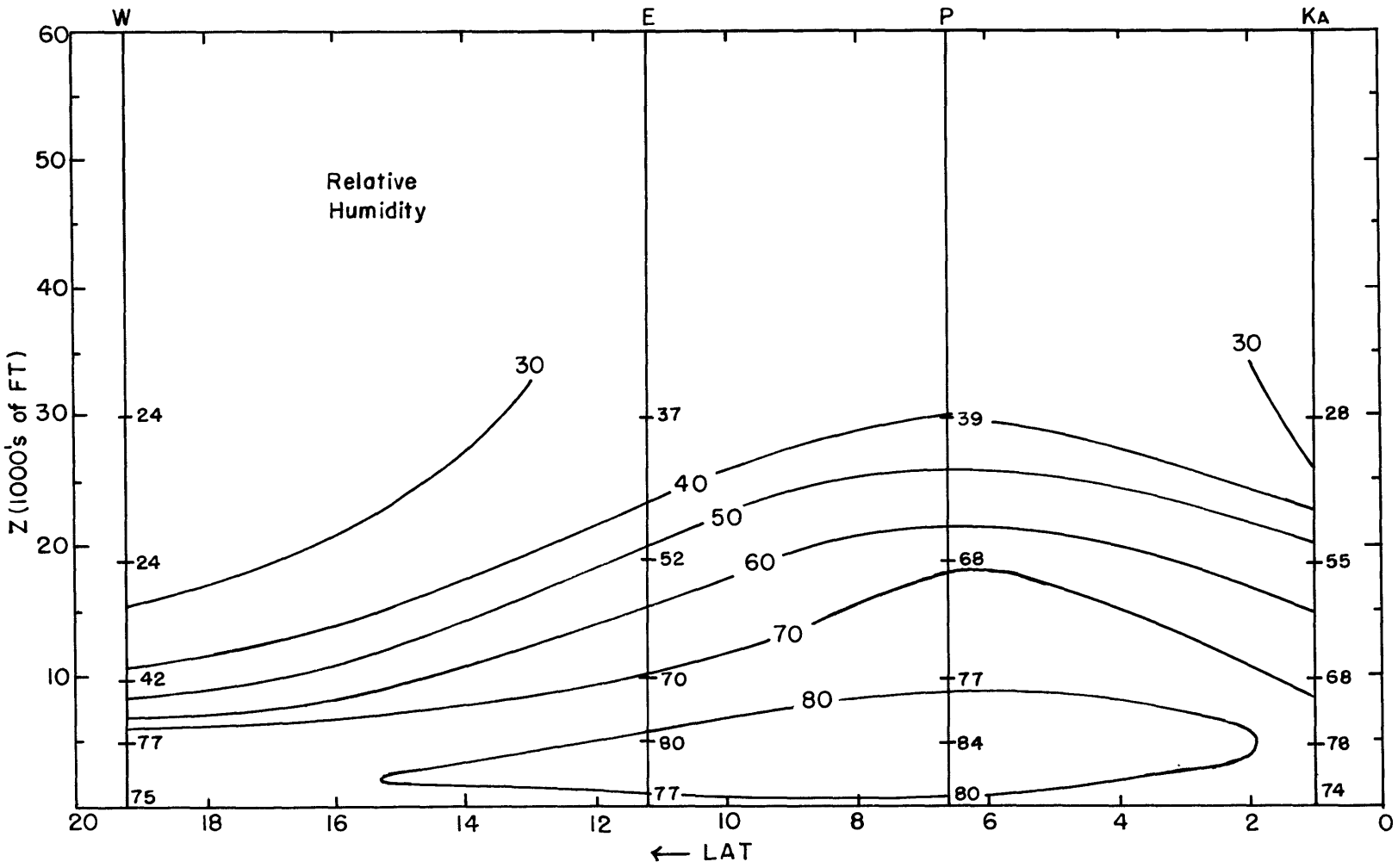

Fig. 3.34. Mean cross-section of relative humidity (RH) in percent for 0300Z, May 1956.

The auxilliary parameter having the most bearing on the position of the ITC is the relative humidity field (RH). The strong vertical gradient of RH above 6000 feet at Wake is characteristic of a true trade regime with subsidence aloft. In fact the subsidence may be verified by checking the vertical motion structure in Fig. 3.3. The RH gradient maximum weakens and slopes upward toward the south until it reaches Ponape near $6.6^{o}N$ where the slope reverses. The RH maximum at Ponape is correlated with, but not coincident upon the convergence maximum of Fig. 3.2 . The fact that the RH maximum is centered on Ponape and not further south is due in part to the natural tendency to draw for the data when so few stations are involved; also, this is not a longitudinally averaged field as is the divergence cross-section. Even though time- and space-mean data have been used, the ITC in both the wind (divergence and steadiness) and moisture analyses shows up rather clearly as a zone with its most likely mean position at or just north of $4^{o}N$. Although the convergence axis slopes northward with height, if we consider the upper-air divergence maximum to be part of the ITC, then the zone favoring the development of deep cumulus must be essentially vertical.

It seems quite significant that the southern boundary of the region of zonal quasi-balance and a possible Ekman layer is essentially the central axis of the mean ITC position. These two observations may be related in the following simple manner. It has already been noted that if the flow at very low latitudes is relatively unsteady, then the geostrophic relationship is easily invalidated by

local and inertial accelerations which are at least of order fu and fv . Since the ITC is disturbed, one should not expect geostrophy to prevail through the zone.

3.7 South to the Equator

Here no simple picture emerges. In the x-equation, both U_x and P_x are significant, especially in the zonal wind extrema near the surface and below the tropopause. Yet, these are terms which would not appear in an idealized, axially-symmetric model designed to explain equatorial motion. Also, the mean local time derivatives, which were omitted from the scale analysis due to their assumed upper limit of 4×10^{-6} ms^{-2}, would need to be considered near the equator, which reflects the non-steady behavior noted in the cross-sections of S and $1 - R_K$ at $1^{o}N$ above 10,000 feet (Figs. 3.18 and 3.19).

Computations of all terms were not made on the equator, but they are available at $2^{o}N$. Tables 3.14 and 3.15 indicate the variations with height of the orders of magnitude of the terms in the equations of motion for this latitude. Each term has been rounded to the nearest power of ten in order to simplify the comparisons. In the x-direction, the measured mean terms at $2^{o}N$ which are consistently most important are: U_x, U_z, -FV, P_x, and S_4. In the y-direction, the most important measured terms are: FU, P_y, and T_4 up to an including 300 mb, and are: V_x, FU, P_y, and T_4 at 200 mb and above. The local time derivatives are estimates, and F_x and F_y are unmeasured residues computed from the other measured terms. Except for near the

surface, these "friction" terms are likely to be spurious due to possible pressure gradient errors.

z	$\frac{\partial u}{\partial t}$*	U_x	U_y	U_z	-FV	JW	P_x	S_1	S_2	S_3	S_4	F_x**
SFC	-6	-6	-6	--	-5	--	-5	-6	--	-7	--	-5
850	-6	-5	-6	-5	-5	-6	-5	-6	-6	-6	-5	-5
700	-6	-5	-5	-5	-5	-6	-5	-6	-5	-7	-7	-5
500	-6	-7	-6	-5	-5	-6	-5	-7	-6	-7	-5	-5
300	-6	-7	-6	-5	-6	-6	-5	-5	-5	-6	-5	-4
200	-6	-5	-7	-5	-5	-6	-5	-6	-6	-6	-5	-4
150	-6	-5	-6	-6	-6	-7	-4	-6	-5	-6	-5	-4
100	-6	-5	-7	--	-5	--	-4	-6	-6	-6	--	-4

Table 3.14. Orders of magnitude of the mean forces per unit mass in the x-equation of motion for 0300Z, May 1956 at 2^{o}N in rounded power of 10 units of ms^{-2}. (*) means these are estimates since they were not computed during the scale analysis phase. (**) means these are residues computed after all other terms were summed.

z	$\frac{\partial v}{\partial t}$*	V_x	V_y	V_z	FU	P_y	T_1	T_2	T_3	T_4	F_y**
SFC	-6	--	-6	--	-5	-5	-6	--	-7	--	-4
850	-6	-5	-6	-6	-5	-4	-7	--	-7	-6	-4
700	-6	-6	-6	-6	-5	-4	-6	-6	--	-5	-4
500	-6	-7	-6	-6	-5	-4	-7	--	--	-5	-4
300	-6	-7	-6	-5	-6	-4	-6	-6	-7	-5	-4
200	-6	-5	-5	-7	-5	-4	-6	-5	-6	-5	-4
150	-6	-5	-6	-6	-5	-4	-6	-6	-7	-5	-4
100	-6	-5	-6	--	-5	-5	-6	--	-6	-5	-4

Table 3.15. Same as Table 3.14 in the y-direction

The flow at 2°N (and probably at the equator) reflects the increased complexity and non-linearity of the horizontal equations of motion when Coriolis terms are small. The only natural simplification that remains is that of quasi-hydrostatic equilibrium in the vertical.

Indirectly, we can see that the equatorial flow, though complex, is not as actively disturbed during the period as that of the ITC region. Note the relative humidity cross-section, Fig. 3.34 and the comparison of "convective events" in Table 3.16. Since moisture was certainly available at the equator, the lower values of RH and the diminished precipitation at Kapingamarangi (near 1°N) further indicate that the convergence axis derived from the wind field is properly placed north of the equator.

STATION	PRECIP		TOTAL
	0300Z	PAST 3HRS	
Eniwetok (11°N)	4	8	12
Ponape (6.6°N)	5	13	18
Kapingamarangi (1°N)	2	2	4

Table 3.16. Occurrences of precipitation at 0300Z or during 0000Z to 0300Z at selected stations in May 1956.

In regard to meridional motions, whereas the equatorward flow at the surface was accomplished primarily in a thin boundary layer north of the mean ITC, the cross-equatorial flow consisted of a deep poleward branch which switched to an equatorward branch above 30,000 feet (eg. see Figs. 3.7 and 3.8). The boundary layer within 2° of

the equator shows up as shear in the direction of the mean flow, i.e., the effect of earth rotation appears to be negligible. This latter observation will also show up in the BOMEX and LIE studies in the next chapter. The presence of strong shear in the first kilometer or two forces us to ask why the flow has a boundary layer on the equator at all. Further north the boundary layer depth is proportional to $f^{-\frac{1}{2}}$ since it is seen to have the characteristics of an Ekman layer, but on the equator this constraint does not apply. One alternative is the possibility that the equatorial troposphere may undergo subsidence and be more stable above a few thousand feet. This would tend to inhibit mixing and not allow turbulent exchange of momentum through a deep layer. Another possibility stems from the fact that low level flow south of the ITC is from across the equator in Redwing and BOMEX data. Since it takes a day or two to generate (or destroy) the boundary layer (time constant proportional to $\bar{f}^{-1}$), it is very possible that the low latitude stations have characteristics of a southern hemisphere Ekman layer advected on trajectories from the south. The vertical profiles would show speed shear and the winds would either back with height or have very little pronounced turning. The winds at Tarawa and Kapingamarangi (Fig. 3.20) have these characteristics.

3.8 Vertical Motion

One final comparison may be made which concerns the vertical velocities. In May, vertical integration of the divergence values led to a maximum upward value for $\left[\bar{w}\right]$ of 2.58 cm/s at 30,000 feet

and 6^{o}N. In June, P.C. Sinclair (Ballif et al., 1958) used the kinematic method and found a maximum upward velocity of 2.5 $\pm$ 0.2 cm/s located between 30,000 and 35,000 feet between 7^{o}N and 8^{o}N. This is both an excellent agreement and an indication of the probable northward migration of the ITC with the approach of summer.

Chapter 4

BOUNDARY LAYER CHARACTERISTICS DURING BOMEX AND THE LINE ISLANDS EXPERIMENT AND A COMPARISON WITH REDWING

4.1. Introduction

As noted in Chapter 3, the Fourth Phase BOMEX period of record is 13-28 July, 1969. Climatology indicates that we should expect a low level confluence zone in the Trades between 5° and 10°N surmounted by a semi-permanent 200 mb ridge (Atkinson (1971), pp 4-12 and 4-19). The mean Mid-Atlantic Trough position at 200 mb is generally north of 20°N in July (Frank and Trumbower (1971) reference in Atkinson (1971), p 4-22). The low level confluence is associated with a broader zone of maximum cloudiness representing the ITC coupled with the frequent traveling disturbances near 15°N which sometimes emanate from Africa (Atkinson (1971), p 6-4 and Frank (1969)). It was observed that this was indeed the general situation during BOMEX Fourth Phase; however, the mean ITC was somewhat closer to 10°N. Thus, the three ships Discoverer (13°N), Mt. Mitchell (10.5°N) and Oceanographer (7.5°N) effectively straddled the ITC except for disruptive periods. Relevant data will be taken primarily from these ships in this chapter.

The LIE was carried out in February, March and April 1967. Wind data used in this paper covered the periods 25 February-21 April at Palmyra (5.9°N), 2 March-21 April at Fanning (3.9°N), and 5 March-21 April at Christmas (1.9°N). Low level climatology data puts a

confluence axis and an east-west band of enhanced cloudiness in the vicinity of 5°N (Atkinson and Sadler, 1970). As in the Marshalls, the zonal winds reversed with height at each location. The reversal level was 600 mb which is much lower than in the Redwing study. The thermal wind is a complication when one attempts to locate the boundary layer using wind data.

4.1.1. Objective

In a sense, our approach in this chapter will resemble the Marshall Islands study in that the accent will be on composited results. We shall look for thermodynamic and kinematic descriptors that will specify the boundary layer (sometimes referred to as B. L.) and determine whether or not it can play an active role in organizing the ITC cloud bands and the structure of traveling disturbances in the trades.

Experience with the Redwing data (Chapter 3) has shown that geostrophic theory could be applied as far south as the mean ITC position and that the monthly mean wind profiles could be modeled with an Ekman solution modified to account for a simple thermal wind regime. It was further noted that south of the ITC, the winds did not veer with height, rather the converging, southerly flow extended through a deeper layer ($\sim$ 20,000 feet) than did the flow from the north. The geostrophic departure model for Rongerik (13°N) and hodographs from stations with similar wind profiles, showed that north of the mean ITC, the main cross-isobaric mass transport was below

2 km which is one way defines the dynamically important boundary layer depth. The Redwing data provide a conceptual framework for the BOMEX study and we will look for comparable characteristics in other parts of the world. Ultimately, results from Redwing, BOMEX, and LIE. will be compared and synthesized to form model relationships between the boundary layer and the ITC.

4.1.2. Limitations

The author, with an assist from Prof. F. Sanders of M.I.T., has regretfully concluded that ship surface barometry errors in the BOMEX data are large enough in the ITC region to preclude the successful use of the geostrophic departure technique attempted with partial success in the Marshalls. Pressure data will not be used in the LIE study. Also, this chapter focuses attention on only the lowest 4500 m ($\sim$ 600 mb). It seemed safe to assume that if boundary layering could not be found below this level then, from scale considerations, certain suspected flow characteristics could no longer be termed boundary layer phenomena.

4.2. Stratification of the BOMEX Data

Time-height cross-sections of potential temperature, relative humidity (corrected for diurnal bias) and wind components were constructed for each of the key ships. Parameters were displayed at 250 m increments from the surface to 2000 m and at 500 m increments to 4500 m. The state parameters for all ships and the winds at Oceanographer and Mt. Mitchell came from the A_o data, winds for

Discoverer were from her teletype messages. The plotting interval was 3 hours and missing points that were no further from their neighbors than ±6 hours were linearly interpolated for ease of analysis. Appendix II shows a cross-section set for the Mt. Mitchell.

Experience with Redwing data and recent work with LIE time sections (Madden and Zipser, 1970) prepared the author for highly structured wind component cross-sections and this was borne out in the ship data. In attempting to specify the boundary layer from wind components we look for exaggerated vertical gradients of speed and/or direction. Directional shear is important since for the boundary layer to actively participate in the organization of cloud bands through the mechanism of CISK, there must be cross contour transport of mass and water vapor. In general the large speed gradients were predominantly below 500-1000 m while the large changes in direction often extended to 2 km or beyond. The sections showed that time and height variability of the winds increased with decreasing latitude (as the ITC was approached and penetrated). The greater number of showers and CB's at Mt. Mitchell and Oceanographer contributed to the increased variability and helped produce several ephemeral anomalies. With the exception of the last five days (24-28 July) the v-component structure at Discoverer (13^{o}N) was reasonably simple due to its trade wind environment and the use of 6-hourly rather than the frequent 3-hourly wind data. Below 2 km v was normally toward the south with either reversal or weakening above. At the other two ships such a simple summary could not be made; however, further study suggested that

the data should be stratified to bring out the fact that the boundary layer appeared to change character across the ITC.

From the daily ESSA-9 and ATS-III pictures it was noted that an effective (but not perfect) stratifier was the 500 m wind. It was not possible to simply use the pictures because even with ATS-III images available, more than one-half of the soundings occurred either at night or without satellite coverage. The average u,v components, potential temperature and relative humidity profiles, along with their variances were stratified into "northerly" and "southerly" regimes. A 500 m v-component less than zero put the entire sounding into the first stratum, all others went into the second.

4.2.1. The Wind as a Boundary Layer Descriptor

Figures 4.1-4.3 are the stratified wind profiles from Discoverer, Mt. Mitchell and Oceanographer and the numbers of real (not interpolated) soundings used. Figures 4.4-4.6 are stratified hodographs of direction and speed from the same data. The southerly regime at Discoverer (13^{o}N) is not representative of quiescent ITC conditions in that her southerly components came during essentially three periods, 17-18, 25 and 28 July which were characterized by two waves in the trades and an ITC depression (on the 25th).

Discoverer (Figs. 4.1 and 4.4) shows distinct Ekman boundary layers in both strata depicted most dramatically in the directional shear which reflects the impact of the Coriolis "force" at 13^{o}N. Recall the success of using a modified Ekman solution at Rongerik

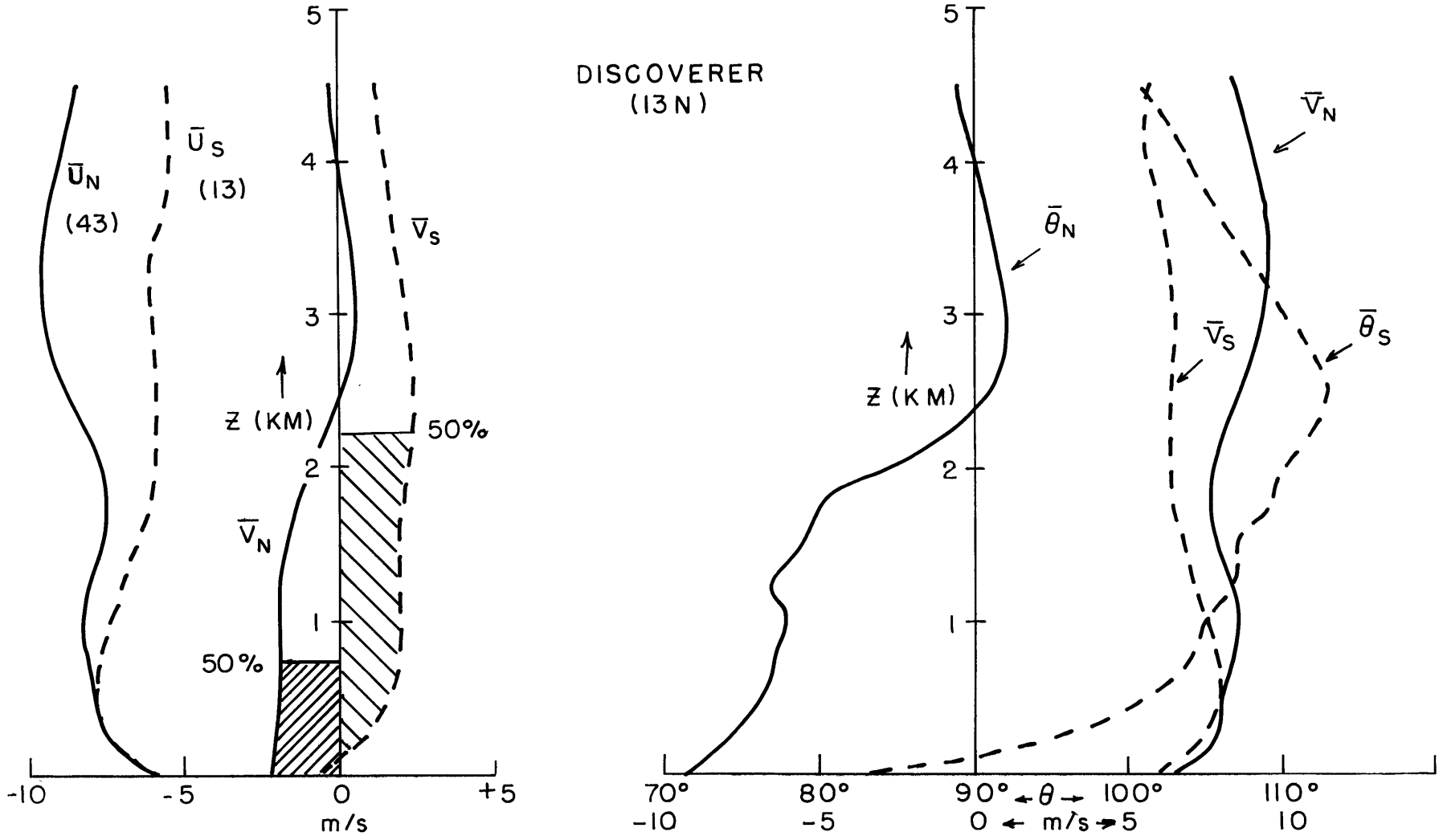

Fig. 4.1a,b. Stratified $\bar{u},\bar{v}$ components (a), and direction ($\bar{\Theta}$) and speed ($\bar{V}$) (b) for ship Discoverer during BOMEX, 13-28 July 1969. Subscript "N" means northerly wind at 500 m ("s" means southerly). Number of cases in parentheses. Shaded regions contain 50 percent of meridional flux.

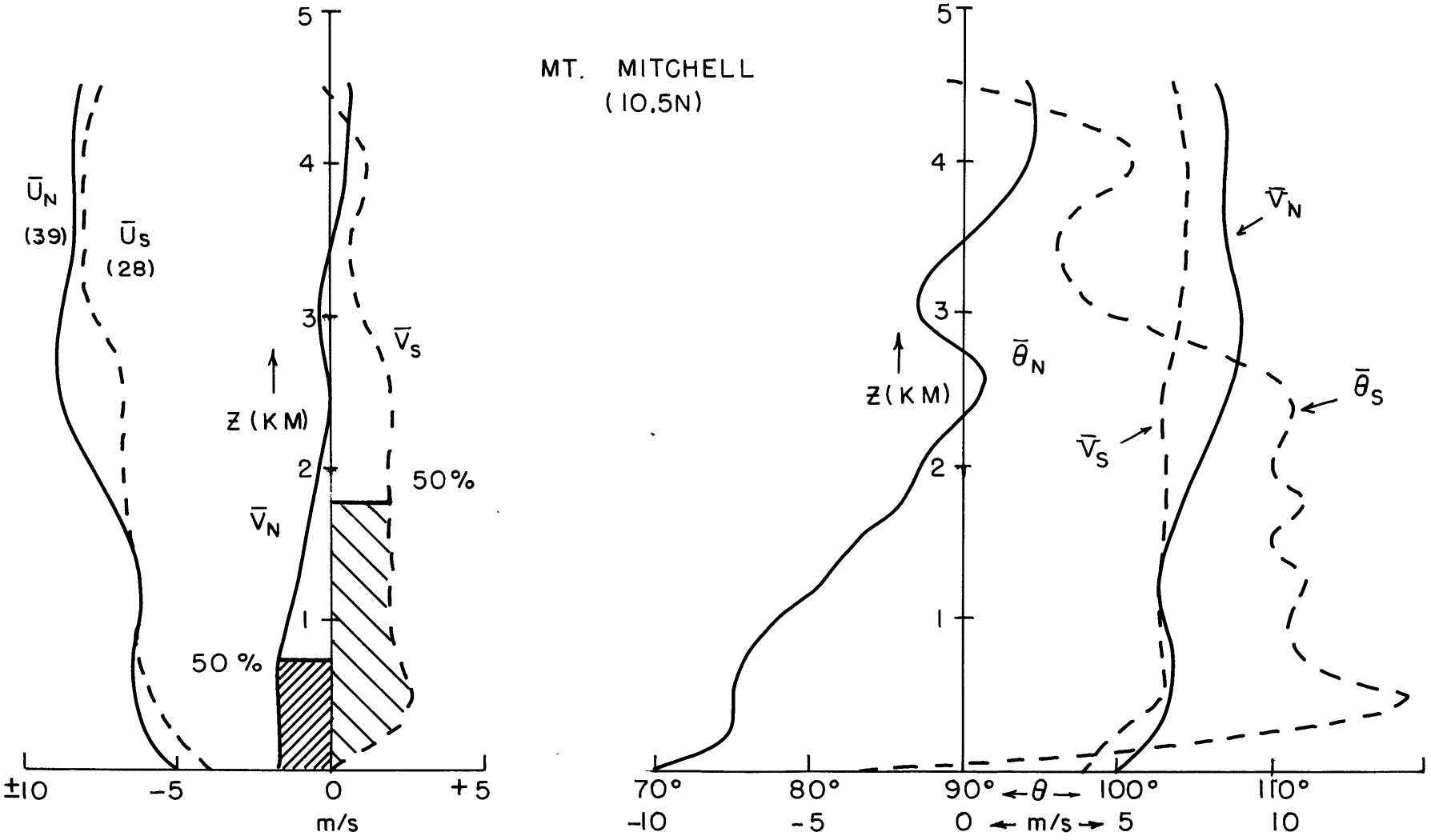

Fig. 4.2a,b. Same as Fig. 4.1 for Mt. Mitchell.

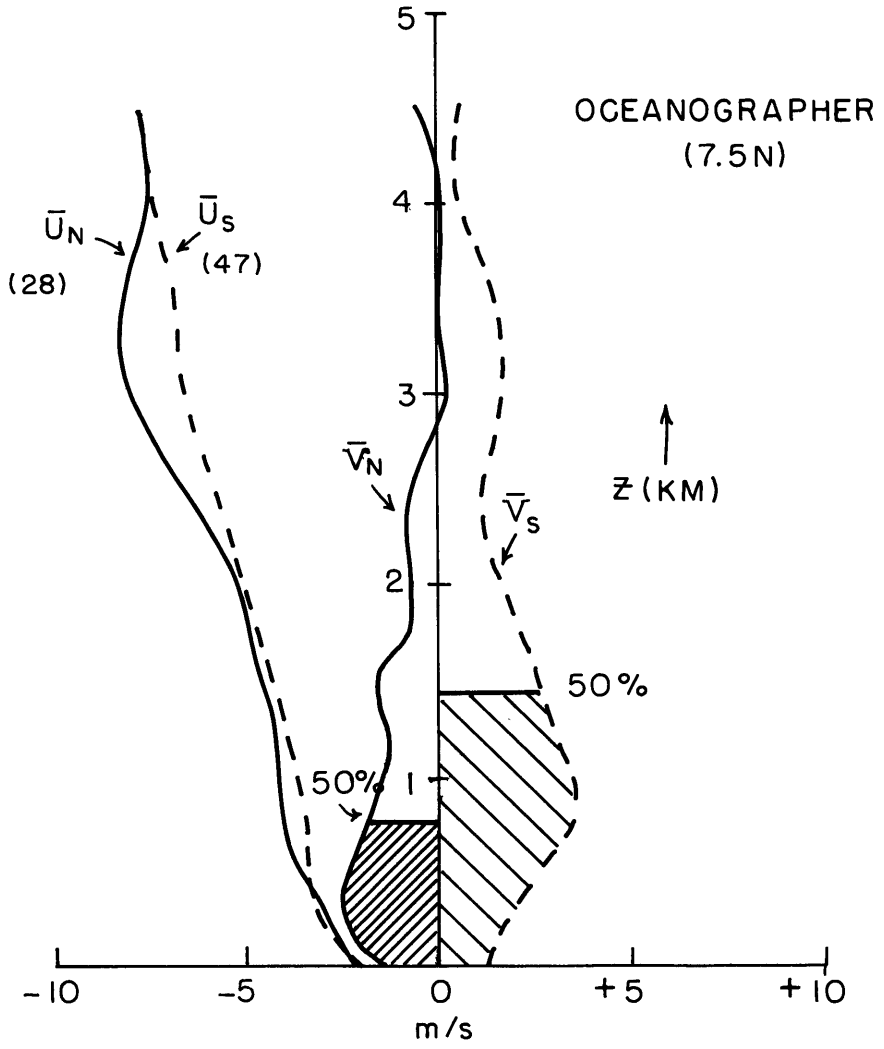

Fig. 4.3a. Same as Fig. 4.1a for Oceanographer.

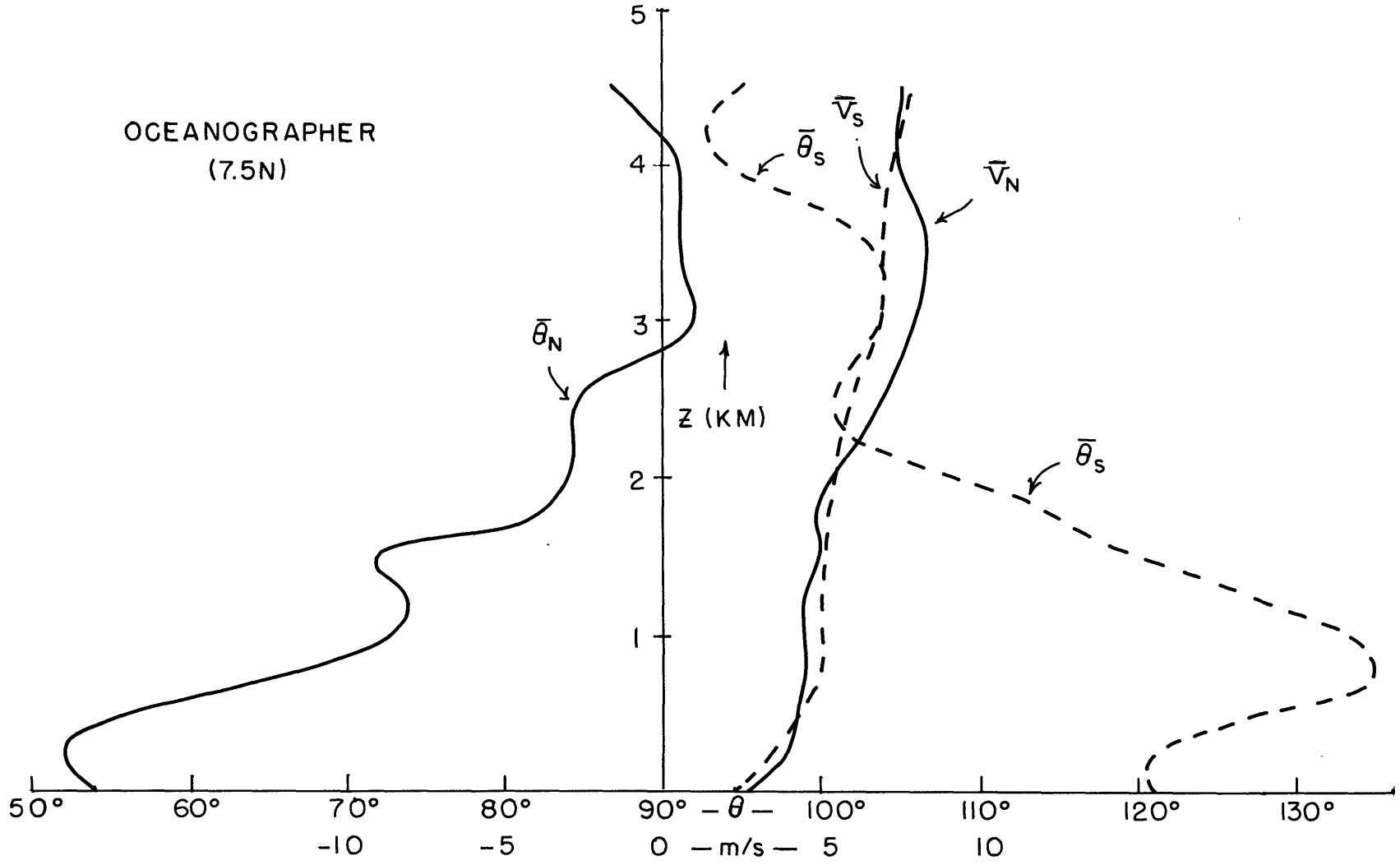

Fig. 4.3b. Same as Fig. 4.1b for Oceanographer.

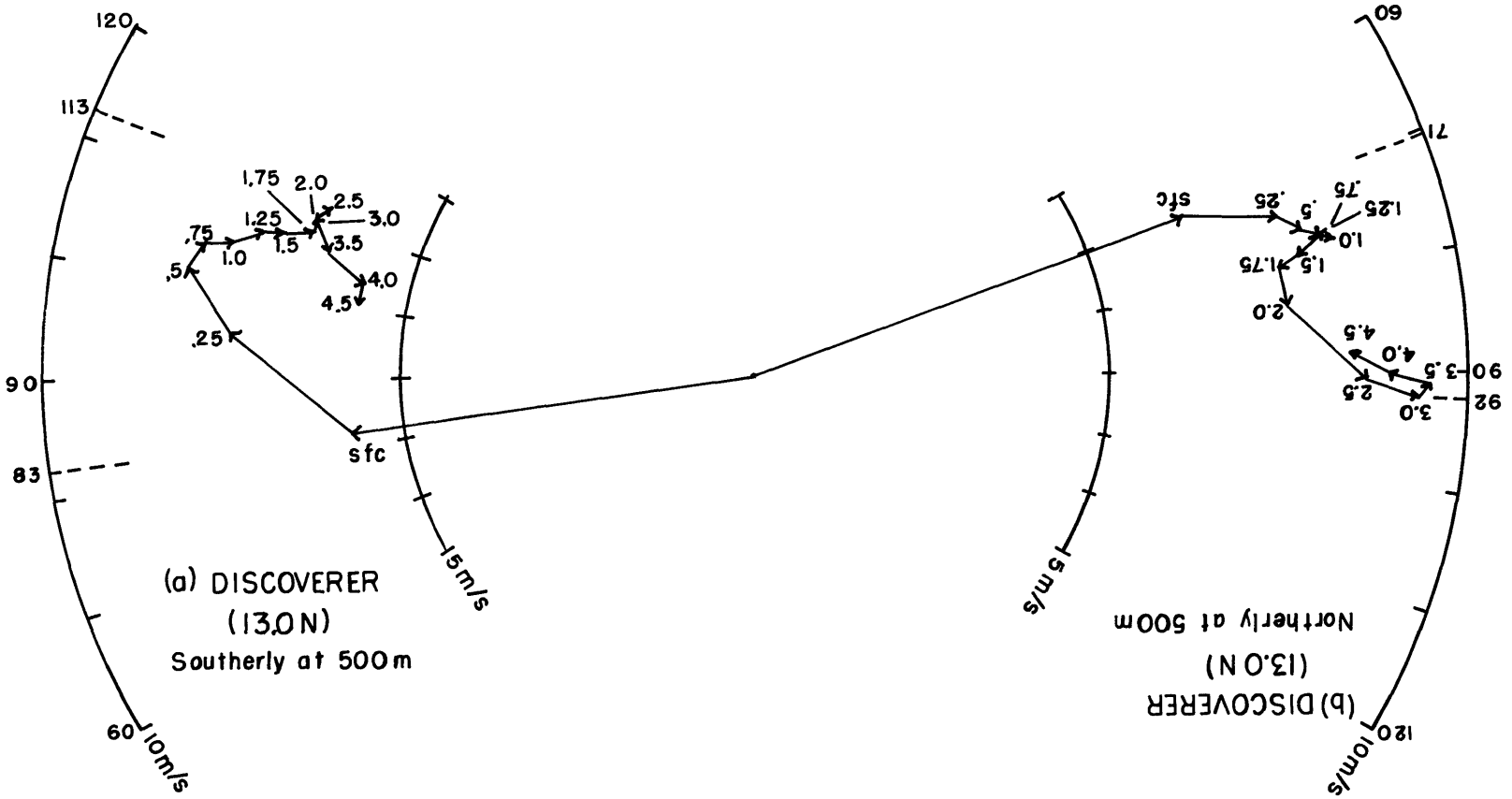

Fig. 4.4a,b. Stratified hodographs from BOMEX 13-28 July 1969. Heights are in kilometers.

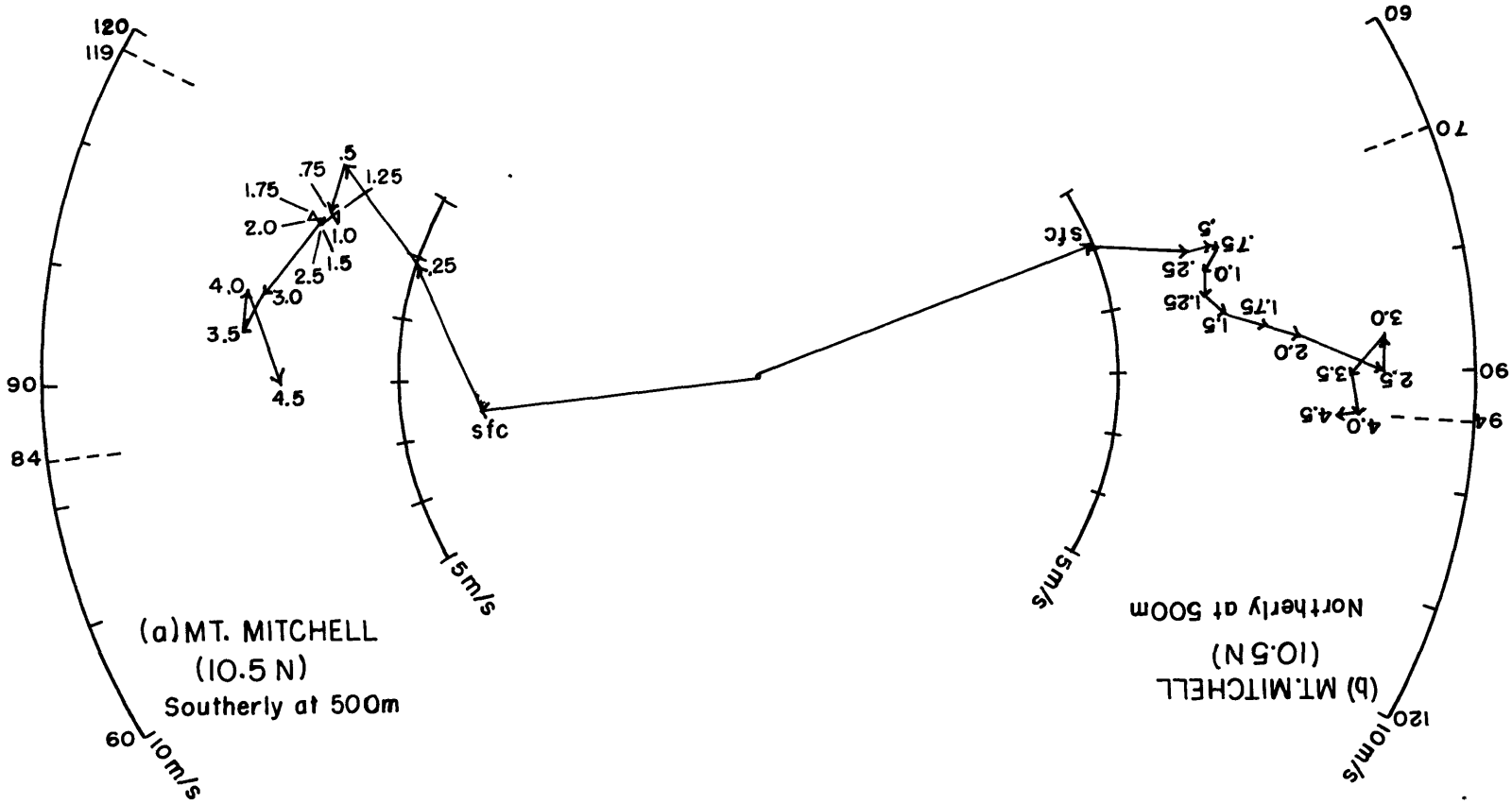

Fig. 4,5a.b. Stratified hodographs from BOMEX 13-28 July 1969. Heights are in kilometers.

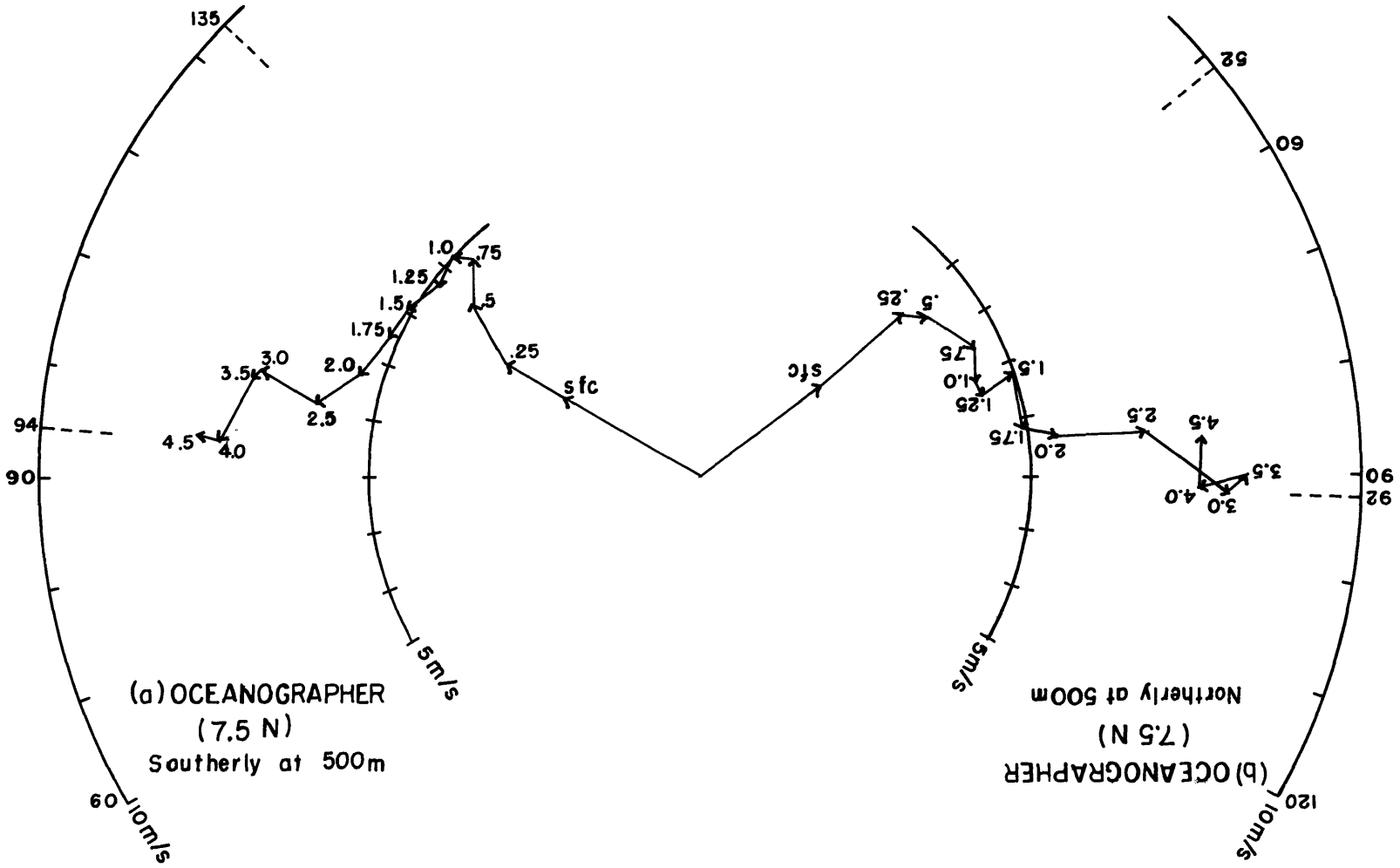

Fig. 4.6a,b. Stratified hodographs from BOMEX 13-28 July 1969. Heights are in kilometers.

(11.3°N) (Chapter 3, Fig. 3.32). The Θ_S and Θ_N profiles are similar but rotated which simply reflects an absolute rotation of the mean geostrophic wind of perhaps 25°. The geostrophic wind implied by the more reliable northerly regime is virtually zonal which puts the top of Discoverer's boundary layer at 2.4 km; from Fig. 4.1 it is easy to show that 50 percent of the southward mass transport is below 750 m.

Stratified wind data from Mt. Mitchell (10.5°N) (Figs. 4.2 and 4.5) and Oceanographer (7.5°N) (Figs. 4.3 and 4.6) reveal the existence of two quite different regimes, marked rather well in the Θ_S and Θ_N profiles again. The northerly strata at the two ships are clearly similar to Discoverer's northerly regime except that the veering with height at Oceanographer is through about 40° rather than the 20° observed further north.

At Mt. Mitchell, the stratification more closely correlates to simple ITC displacement than at Oceanographer. The latter vessel experienced a northerly regime mainly in disturbed conditions on the 14th (cloud cluster and possible vortex to the east), 22-33rd (developing ITC depression to the east), and on the 28th (Africa wave and possible vortex to the east). Thus enhanced convergence in the boundary layer into these nearby disturbances due to the release of latent heat combined with the Ekman effect could have caused the larger veering through Oceanographer's northerly regime B.L.

At these two southern ships, the veering ceases near 90°. On the assumption that the geostrophic wind is nearly zonal, the depth of the northerly regime B.L. would be 2.3 km at Mt. Mitchell (10.5°N)

and 2.8 km at Oceanographer (7.5°N). As at 13°N, the most significant speed shear is below 500 m in the sub-cloud layer. Fifty percent of the equatorward mass transport is below 750 m at both Mt. Mitchell and Oceanographer.

The southerly regime at Oceanographer occurred two-thirds of the time and represents a reasonable mix of quiescent and disturbed ITC conditions. The southerly component is seen at all levels and undoubtedly extends to at least 5.5 km because the non-stratified mean $\bar{v}$-component becomes small negative at this level as shown in the summary report by Fernandez-Partagas and Estoque (1970). In the same report, $\bar{v}$ again approaches +2.5 m/s between 7 and 11 km in the poleward branch of the Northern Hemisphere Hadley cell. The veering/backing θ_S profile (Fig. 4.3b) may be the signature of an Ekman layer which is overcome by a backing of the thickness fields with height above 800 m. This is consistent with advection of cooler air in trajectories approaching a warm ITC from the southeast. Estoque (1971) found that the rotation of the winds at Christmas Island (2°N) could be controlled by the thermal wind.

The Mt. Mitchell southerly regime also shows weaker backing with height above a 500 m layer of veering from 84° to 119°. The surface winds in A_o records are from the Ship Surface Synoptic reports and, considering the large veering of 35° in the first 500 m one might suspect an error has created an inconsistency with the Mt. Mitchell sounding at low levels; however, the northerly stratum profile should also show extreme low level veering if such an error factor exists

but the profile is well behaved. The author therefore accepts strong veering in the lowest levels as a real feature of the southerly regimes at the two southernmost ships. The backing above cloud base level was not as severe as it was at Oceanographer; the possible significance of this will be discussed in Section 4.2.2. The depth of the veering is seen to be equal to the depth of maximum speed shear at both locations which supports the assertion that frictionally induced Ekman characteristics dominate in the sub-cloud layer.

Clearly, the simple stratification scheme defined different boundary layer regimes on either side of the ITC. North of the ITC the Ekman characteristic is unmistakable even at 7.5°N. The top of the layer is between 2 and 3 km. South of the ITC the regime is more complex showing poleward flow through at least 4.5 km and backing of the wind above a shallow (500-800 m) veering layer. Note that a deep poleward drift was characteristic of the Marshall Islands also. It will be shown in Section 4.3 that stratified Line Island data for Palmyra further substantiate the two-regime argument.

The low level v-profile maxima at Oceanographer and Mt. Mitchell (Figs. 4.2 and 4.3) are partly due to the choice of the 500 m wind as the descriptor as opposed to, say the 1500 m wind. Inspection of the author's v-component time section showed, for example, that if 1500 m had been used, the same stratification choices would have been made for 78 percent of the soundings. However, 1500 m would not have been quite as reliable as a descriptor of the position of the ITC relative to the ship in question. In the case studies shown in Chapter 5, it

will be apparent to the reader that the 500 m flow patterns, when seen as map analyses, correlate with satellite images of ITC cloud bands in a most satisfactory manner.

4.2.2. Relative Humidity as a Boundary Layer Descriptor

Over oceans in the tropics, relative humidity (RH) is nearly conservative in the horizontal because of the warm and nearly flat temperature fields. Significant variations in RH at some level are virtually always due to specific humidity variations except as a result of temperature drops in an occasional thunderstorm accompanied by downdrafts cooled by evaporation.

Relative humidity in oceanic tropical regions should be a useful boundary layer specifier and can be used to corroborate or refute conclusions drawn from the wind data. The magnitude of RH should drop with altitude at the top of a well defined boundary layer which separates a well mixed layer below from a more stable, basically decoupled region above. We might expect this to be more applicable north of the ITC in a true trade environment. Large bursts of moisture will occasionally be pumped out of the B. L. in the form of large cumuliform clouds; hence, another possible specifier would be a rapid increase in the variance of RH with altitude. In Appendix II, the RH time section for Mt. Mitchell has the characteristics just described. Note too how the moisture intrusions or "spikes" are nearly always accompanied by a precipitation event. In several cases the intrusion has vanished in six hours or less. Drying out aloft

occurs and evolves on a synoptic time scale, moisture intrusions are on a meso-time scale or less.

Figures 4.7-4.9 are stratified RH and standard deviation of RH (σ(RH)) profiles for the three key ships. An attempt was made to identify inflection points which represent the tightest gradients and hence the "top" of the B. L. in each profile. These are marked on the profiles unless the position was too ambiguous to locate meaningfully. The climatological cloud base is marked at 600 m which is the value separating base 4 from base 5 in Synoptic code*.

The increase of RH with height below cloud base level is consistent with a well-mixed, unsaturated layer that cools with height. RH and σ(RH) are obvious not independent specifiers due to the boundedness of RH. As RH decreases from its upper bound, a wider variation is permitted. This dependence can be seen as a "mirror image" effect (e.g. the Mt. Mitchell northerly regime, Fig. 4.8). The northerly regime B. L.'s at 10.5° and 13°N are clearly near 2 km using either specifier and the low RH values aloft are quite consistent with a subsident Trade wind climatology. At 7.5°N, the northerly regime has a different character: $\sigma(RH_N)$ indicates a 2km depth but RH_N suggests a diffuse or "soft" top. These latter data were generated in disturbed conditions not in the vicinity of a

*During BOMEX Fourth Phase, Discoverer reported base 5, Mt. Mitchell base 4 and Oceanographer base 3 ! During Phases 2 and 3, Oceanographer reported base 3 69% of the time while stationed near 17.5°N in distinct contrast to her neighbors. This suggests a procedural error in cloud base reporting on the Oceanographer.

quiescent ITC. The general impression from RH data is that the northerly B. L. deepens with decreasing latitude. A depth of 2 km is suggested at 10.5° and 13°N which is only 3-400 m lower than the estimates using wind components. Because of RH_N and the wind structure (Fig. 4.3) the author concludes that the evidence favors a deeper (2.8 km) northerly B. L. at 7.5°N.

Although tops are marked on some of the profiles, the southern regime B.L.'s are less sharply defined in the RH data. This suggestion of "softness" is especially apparent at 10.5° and 7.5°N (Figs. 4.8 and 4.9). It seems quite logical that this can be understood from the statistics in Table 4.1 showing "precipitation events" at the three ships.

Ship	Northerly	Southerly
a Disco (13N)	1/43 = 2.3%	6/13 = 46%
b Mt. Mit. (10.5N)	7/39 = 18%	19/28 = 68%
c Oceanog. (7.5N)	5/28 = 18%	12/47 = 25%
Totals, b and c only	12/67 = 18%	31/75 = 41%

Table 4.1. Ratio of wind soundings with "precipitation events" to total soundings in each stratum.

Precipitation events are shower, thundershower or lightning observations taken from the Ship Surface Synoptic records and compared to soundings having actual (not interpolated) wind reports. Table 4.1 shows that deeper, more frequent coupling in the vertical must have occurred in the southerly regimes especially at Mt. Mitchell.

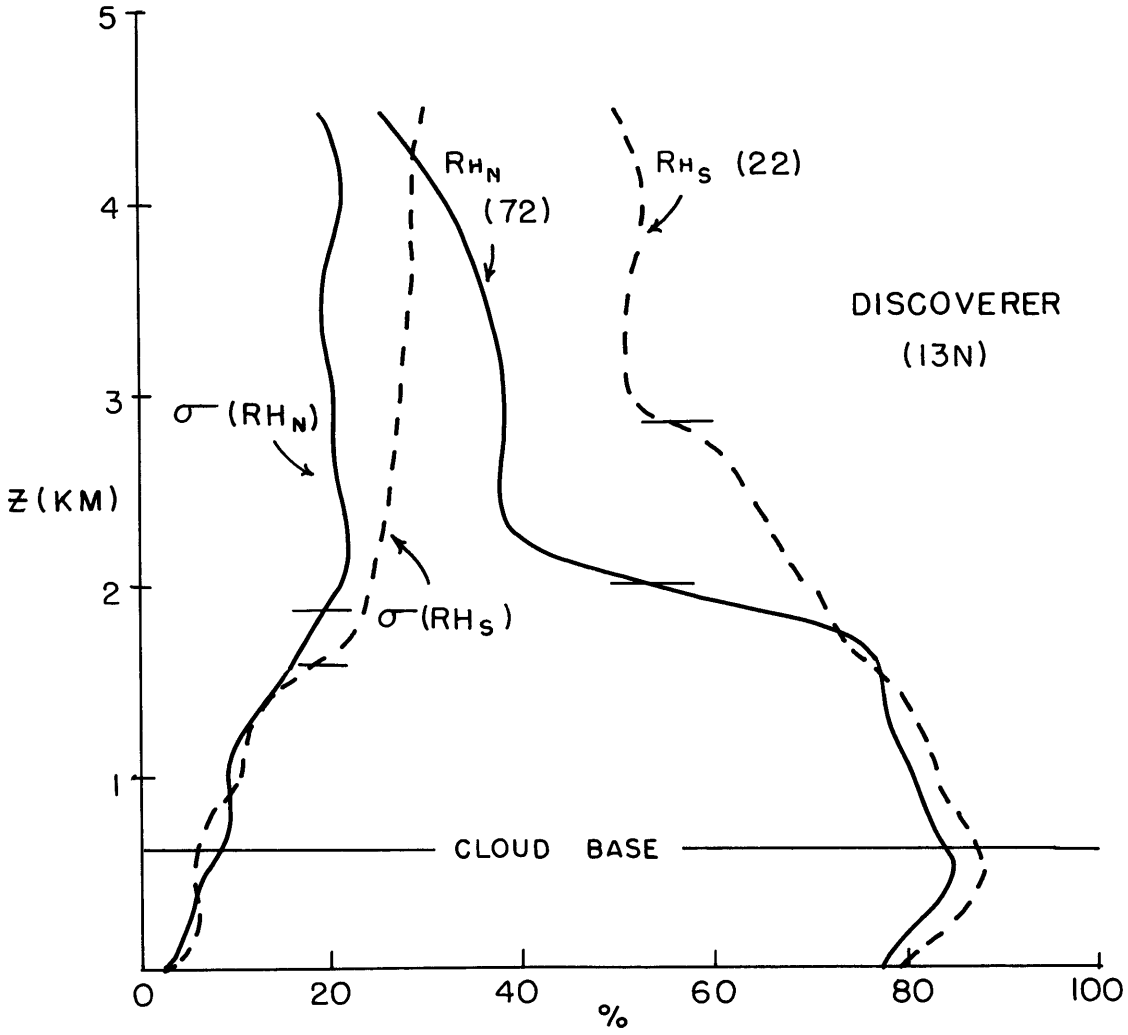

Fig. 4.7. Stratified relative humidity (RH) and standard deviation of RH (σ(RH)) from ship Discoverer during BOMEX, 13-28 July 1969. Short hack marks denote inflection points and one definition of top of boundary layer. Subscripts S and N denote southerly or northerly regime.

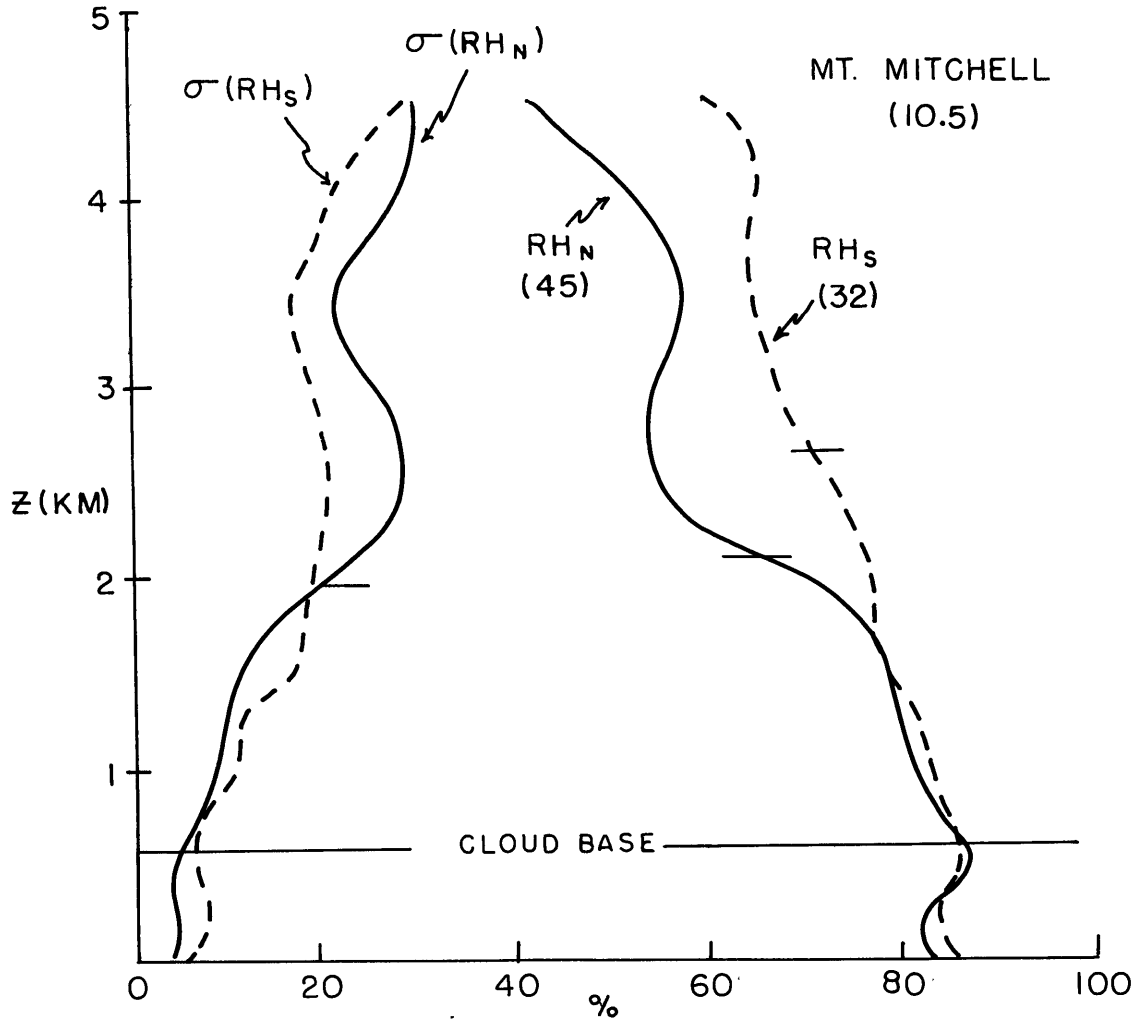

Fig. 4.8. Stratified relative humidity (RH) and standard deviation of RH (σ(RH)) from ship Mt. Mitchell during BOMEX, 13-28 July 1969. Short hack marks denote inflection points and one definition of top of boundary layer. Subscripts S and N denote southerly or northerly regime.

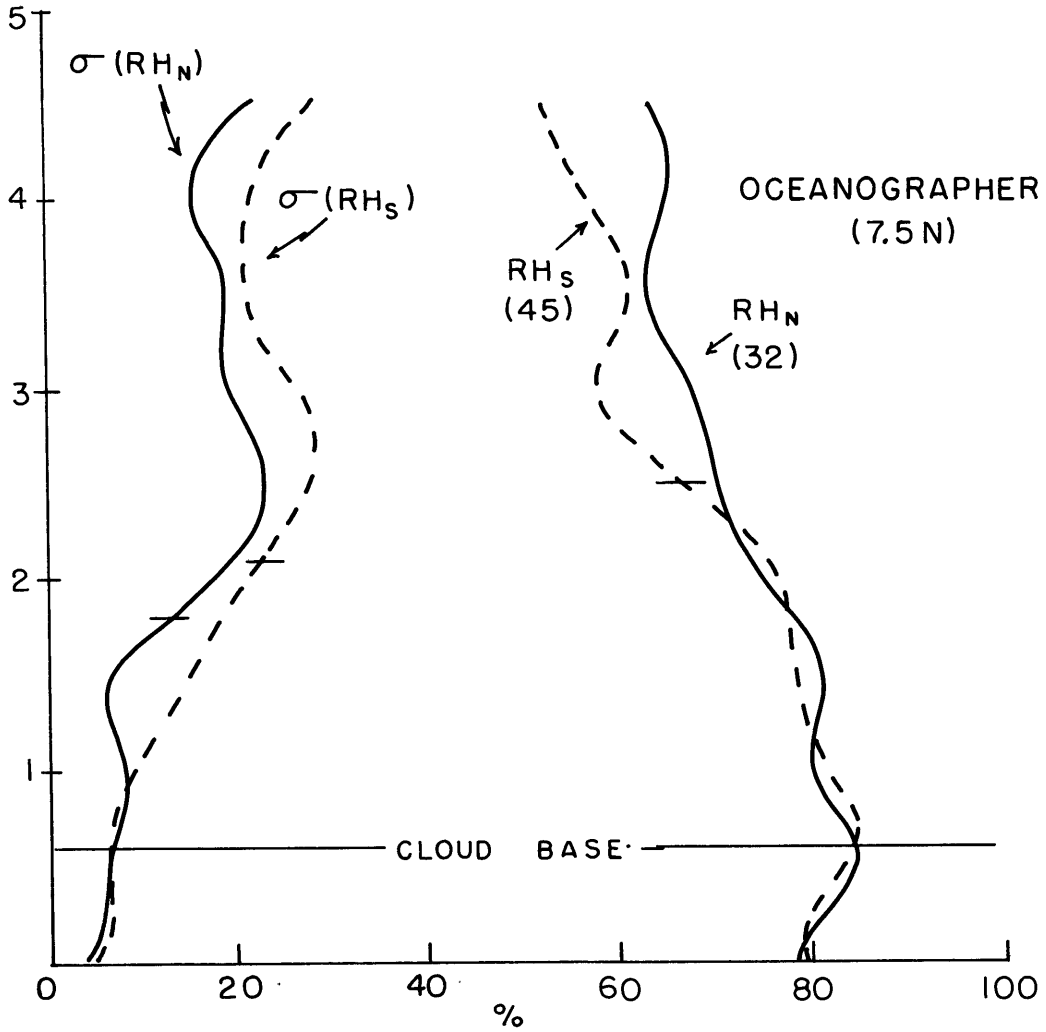

Fig. 4.9. Stratified relative humidity (RH) and standard deviation of RH (σ(RH)) from ship Oceanographer during BOMEX, 13-28 July 1969. Short hack marks denote inflection points and one definition of top of boundary layer. Subscripts S and N denote southerly or northerly regime.

From the table it is apparent that Mt. Mitchell's shower activity favored the southerly regime by a wide margin. Also, Mt. Mitchell's southerly regime winds veered strongly in the sub-cloud layer but turned little or backed above. It is suggested that the excessive cumulus convection acted to homogenize the wind profile above cloud base level through enhanced turbulent exchange with the deep tropospheric flow. Further to the south, Oceanographer's precipitation events did not significantly favor her southerly regime and above cloud base, there is strong backing of the winds rather than a homogeneous profile.

4.2.3. Temperature as a Boundary Layer Specifier

Appendix II shows the time height section of Mt. Mitchell's potential temperature (θ_d) soundings. The standard deviation of θ_d is a degree or less at all levels. Occasional short period fluctuations (usually cooling due to shower drafts) are seen as well as two persistent intrusions of nearly dry adiabatic, low humidity air near 3 km on 24 and 28 July. Both of these intrusions were from air just north or northwest of bright cloud clusters associated with first, a disturbance in the trades and second, an ITC depression. Since this air is north of the ITC and at the correct level it is probably of African origin (Carlson, 1971). The strong easterly jet on the u-component cross-section on 23 July descends with time as does the dryness and, to a minor degree the nearly dry adiabatic layer. Jets on the southern periphery of warm African air masses will be seen in more detail in the case studies of Chapter 5 and are discussed in Appendix V.

In the boundary layer, the most persistent signature is the nearly adiabatic lapse rate from the surface to between 5-750 m in the sub-cloud layer. This was a common trait at the other two key ships as well which indicates thorough mixing without saturation. Since turbulent stirring without the aid of convective cloud towers occupies most of the first kilometer, and persistent, scattered tradewind cumulus occupy the next kilometer or two, the Fourth Phase boundary layer, defined as a region of small scale turbulent exchange, must be deeper than $\sim$1 km. Furthermore the wind and humidity profiles show that the top of the dynamically relevant boundary layer in the northerly regime can be found between two and three kilometers. In Chapter 3 we found this same depth scale using geostrophic departures whereas in this chapter the evidence is more circumstantial.

4.3. Stratified Boundary Layer Regimes from LIE Winds

NCAR kindly stratified the winds from the three islands by using the 950 mb v-component in a manner completely analogous to the BOMEX technique. Stratified state parameters were not available.

Based on examination of the ESSA-3 and ATS-I satellite pictures for the period it was possible to subjectively locate the ITC on 42 out of the 50 days of available pictures. Table 4.2 is a summary of the ITC's position near 00Z with respect to the three Line Islands.

ITC LOCATION	NORTH PALMYRA	SOUTH PALMYRA	SOUTH FANNING	SOUTH CHRIST.	NO ITC	NO DECISION
Number	27	14	1	0	2	6
Percent	54	28	2	0	4	12

Table 4.2. Distribution of location of ITC with respect to the LIE Observing sites from ESSA-3 and ATS-I Pictures.

Table 4.2 shows that the stratification scheme used in BOMEX is only meaningful in its original context at Palmyra. In theory Fanning should have southerly winds at 950 mb about 97 percent of the time and Christmas always, but this was not the case.

Table 4.3 is a contingency table for Palmyra showing the relation between ITC position and the 950 mb wind for 00Z ($\pm$ 6 hr if missing).

WINDS / SATELLITE	SOUTHERLY $V_{950} \geq 0$	NORTHERLY $V_{950} < 0$	TOTALS
NORTH PALMYRA	24	3	27
SOUTH PALMYRA	5	9	14
TOTALS	29	12	41

Table 4.3. Contingent distribution of ITC position derived from satellites relative to 00Z 950 mb wind at Palmyra.

The ITC was rarely completely south of Palmyra in the satellite pictures which probably accounts for the fact that only 64 percent (9/14) of the satellite-derived northerly regime specifications worked.

However, when the northerly wind regime was specified it was a correct decision 75 percent (9/12) of the time.

Although there were some differences between wind strata at Fanning and Christmas, the only distinctive change in regimes occurred at Palmyra as shown in Fig. 4.10. The latter's northerly boundary layer looks to be a cooperation between friction and thermal wind while the southerly regime (as with BOMEX) is characterized by a shallow veering layer ($\sim$300 m) capped by a 3 km backing layer. The new feature is the return to veering above 3 km. The southerly regime winds have a weaker zonal component which implies cyclonic vorticity across the ITC.

Poleward transport in Palmyra's southerly regime is through at least 4.5 km while the equatorward branch is only 1.6 km deep. The only reasonable signature in the wind components that indicates the "top" of the boundary layer is the switch from backing to veering at 3 km in the southerly regime at Palmyra.

Figure 4.11 shows the unstratified direction and speed profiles for the southernmost islands Fanning and Christmas. The speed shear is well marked below 1500 which indicates boundary layering. The low level backing with height again suggests the possibility that a southern hemisphere B. L. has been transported across the equator. However, the mean v-component above 500 m at Christmas is northerly which would destroy the above argument were it not for the uncertainty in the Christmas wind direction as discussed in Section 2.3. If Estoque's

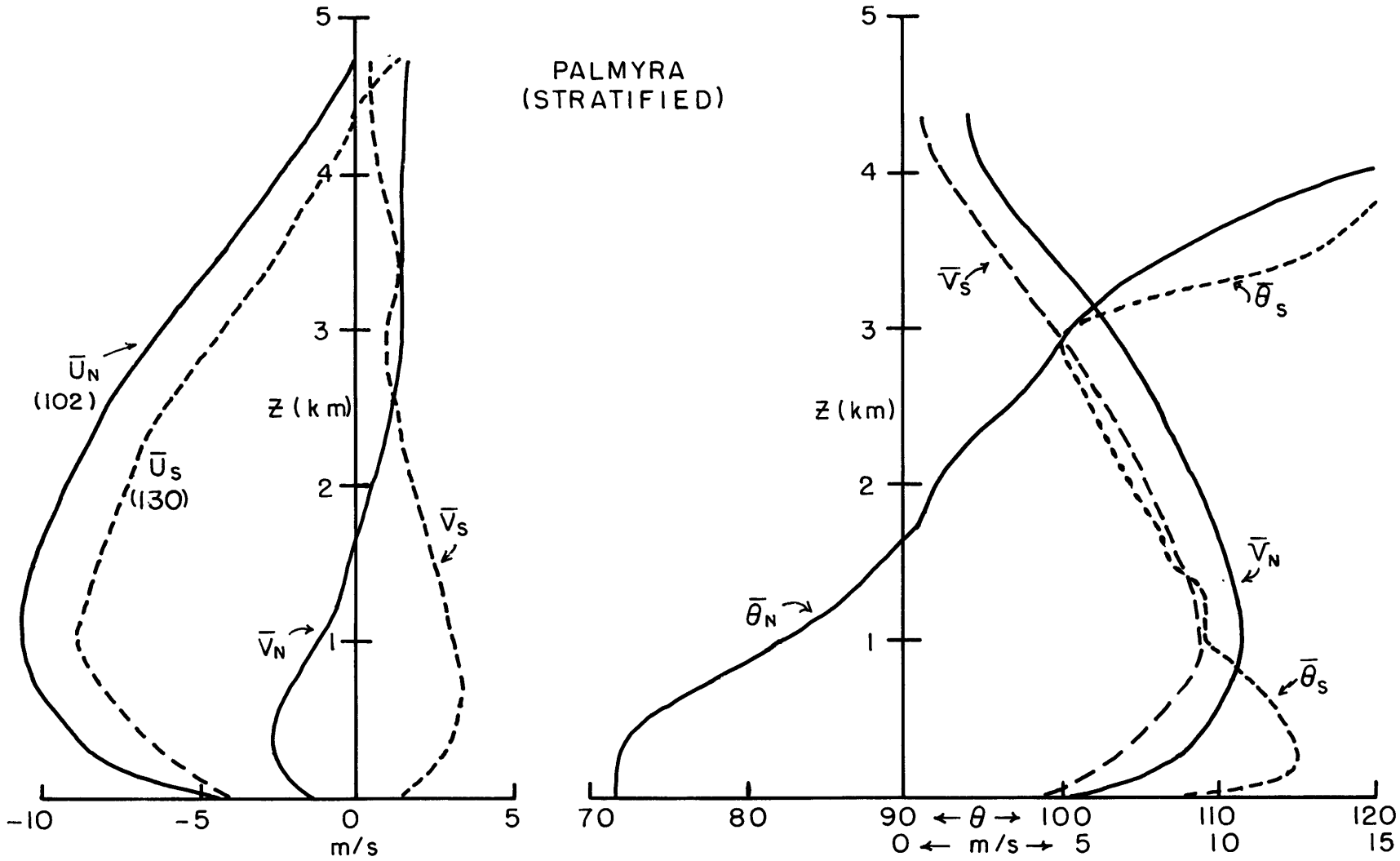

Fig. 4.10a,b. Stratified $\bar{u},\bar{v}$ wind components (a), and direction ($\bar{\Theta}$) and speed ($\bar{V}$) (b) for Palmyra in the Line Islands, Feb.-Apr. 1967. Subscripts N and S denote northerly and southerly regimes. Number of soundings shown in parentheses.

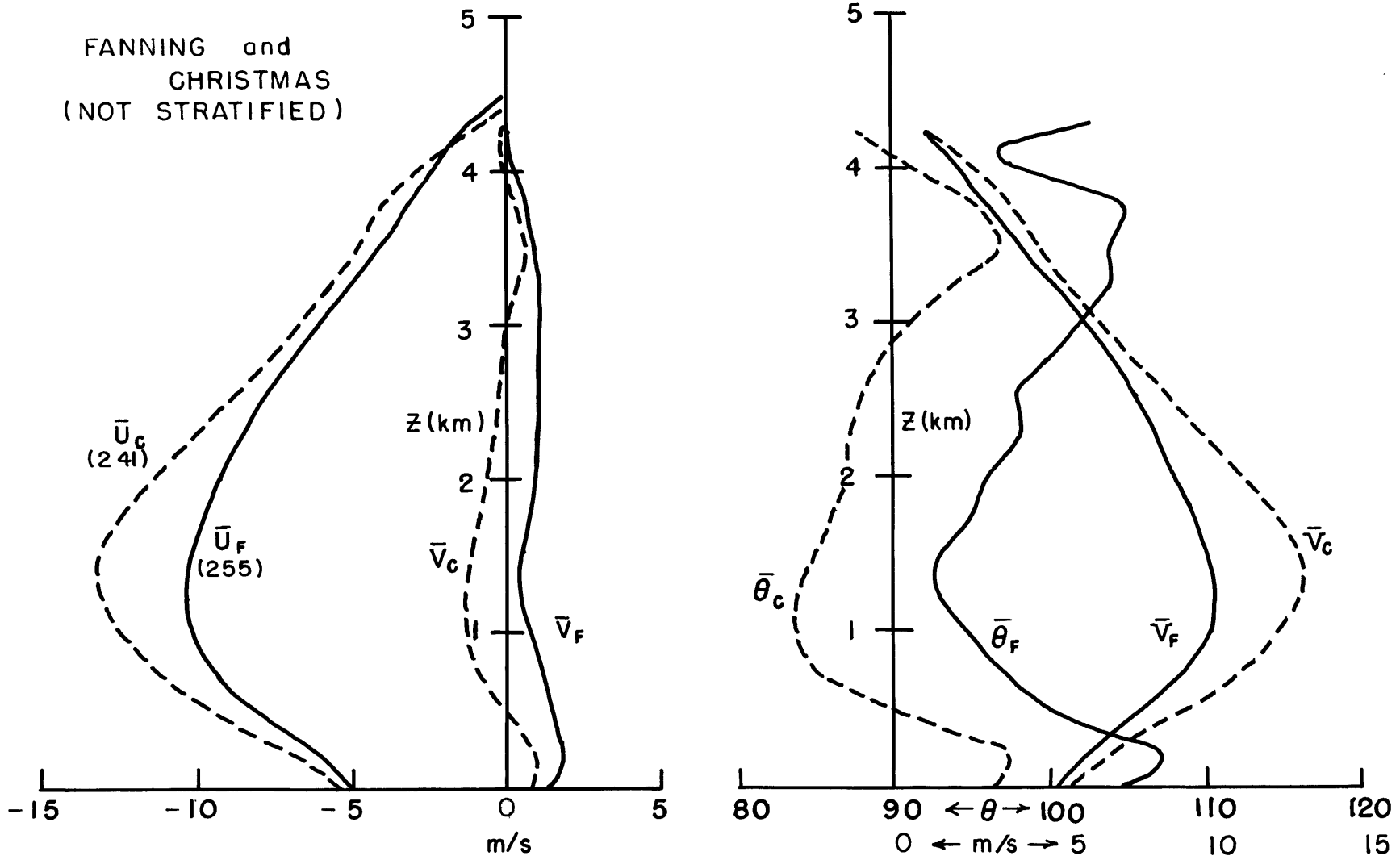

Fig. 4.11a,b. Unstratified $\bar{u},\bar{v}$ wind components (a) and direction ($\bar{\Theta}$) and speed ($\bar{V}$) (b) at Fanning (sub-F) and Christmas (sub-C) in the Line Islands, Feb.-Apr. 1967. Numbers of soundings in parentheses.

PIBAL directions are correct, then the mean B. L. flow at Christmas would indeed be from the Southern Hemisphere and would support the idea that the backing layer is the remnant of an Ekman layer which has crossed the equator. Otherwise we might wish to accept Estoque's conclusion that control of the Christmas (and hence Fanning) wind profile is from the thermal wind. Clearly this problem is far from solution.

Unstratified relative humidities for the three islands are shown in Fig. 4.11 and, using the inflection point as a criterion, the depth of the moist layer decreases with decreasing latitude from 2.4 km at Palmyra to 1.6 km at Christmas which is in keeping with subsidence south of the ITC and with the precipitation rates shown in Table 4.4. Boundary layers at the three islands are probably less than 3 km in depth and greater than 1.5 km.

	Palmyra (Army Site)	Fanning (Army Site)	Christmas (N.E. Point)
Precip. mm/day	83	29	4.8

Table 4.4. Precipitation rates during March and April 1967 in mm/day.

In the ITC synthesis that follows, stratified data will be used at Palmyra to describe its northerly regime which is reasonably well correlated with ITC displacement. At Fanning and Christmas, only unstratified mean data will be used.

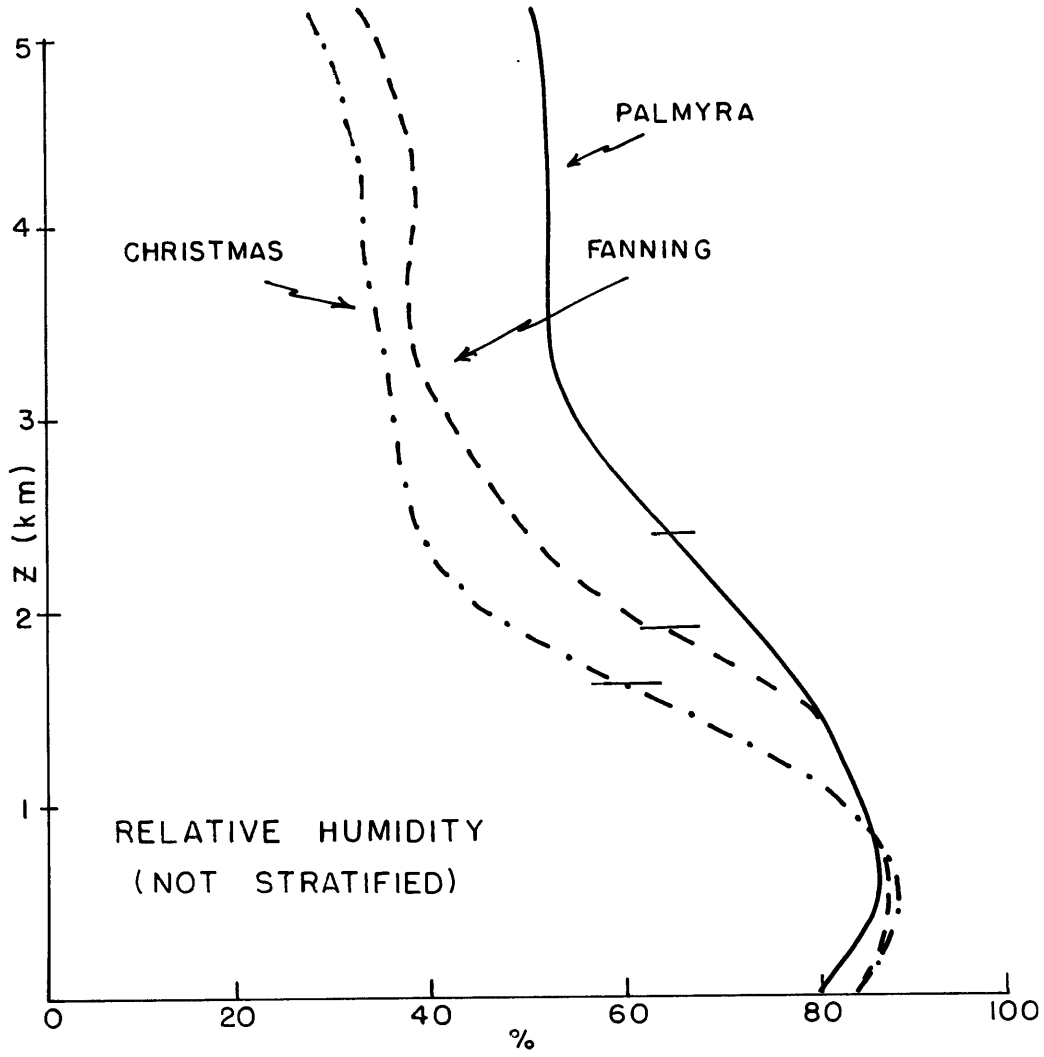

Fig. 4.12. Unstratified relative humidity profiles for the Line Islands, Feb.-Apr. 1967. Only night-time humidities were used. Hack marks show inflection points which are one definition of top of boundary layer.

4.4. Composite Cross-Sections of Wind through the ITC Boundary Layer

In each data source region, an attempt was made to develop realistic latitude vs. height cross-sections of $\bar{u}$ and $\bar{v}$ wind components, $-\partial\bar{u}/\partial y$, and $\partial\bar{v}/\partial y$ through the ITC. The idea was to preserve the ITC without either artificially smoothing or sharpening its kinematic features. Because of the manner in which each data set was originally prepared, each composite required a different technique.

4.4.1. Redwing Composite

Redwing data were not stratified. Longitudinal averaging acted as a smoother in the basic study in Chapter 3. Two cross-sections were constructed using mean station data. The western section was through Wake-Eniwetok-Ponape-Kapingamarangi, the eastern through Wake-Rongerik-Kwajalein-Majuro-Tarawa. The $\bar{u},\bar{v}$ component sections were graphically averaged after choosing as a common origin the point where the $\bar{v} = o$ contour intersected the surface. This puts the winds into a relative y-coordinate system; however, it should represent an ITC situation south of 10^{o}N. Fig. 4.13 a and b show the sections of $\bar{u}$, $\bar{v}$, $-\partial\bar{u}/\partial y$, and $\partial\bar{v}/\partial y$ for May 1956 03Z during Redwing.

4.4.2. BOMEX Composite

BOMEX data were re-stratified based on the sign of the 500 m v-component at Mt. Mitchell only. For example, all Discoverer winds that were conditional on Mt. Mitchell's southerly component were averaged. This was also done for Oceanographer conditional on Mt. Mitchell's northerly component. By knowing from ESSA-9 and ATS-III that

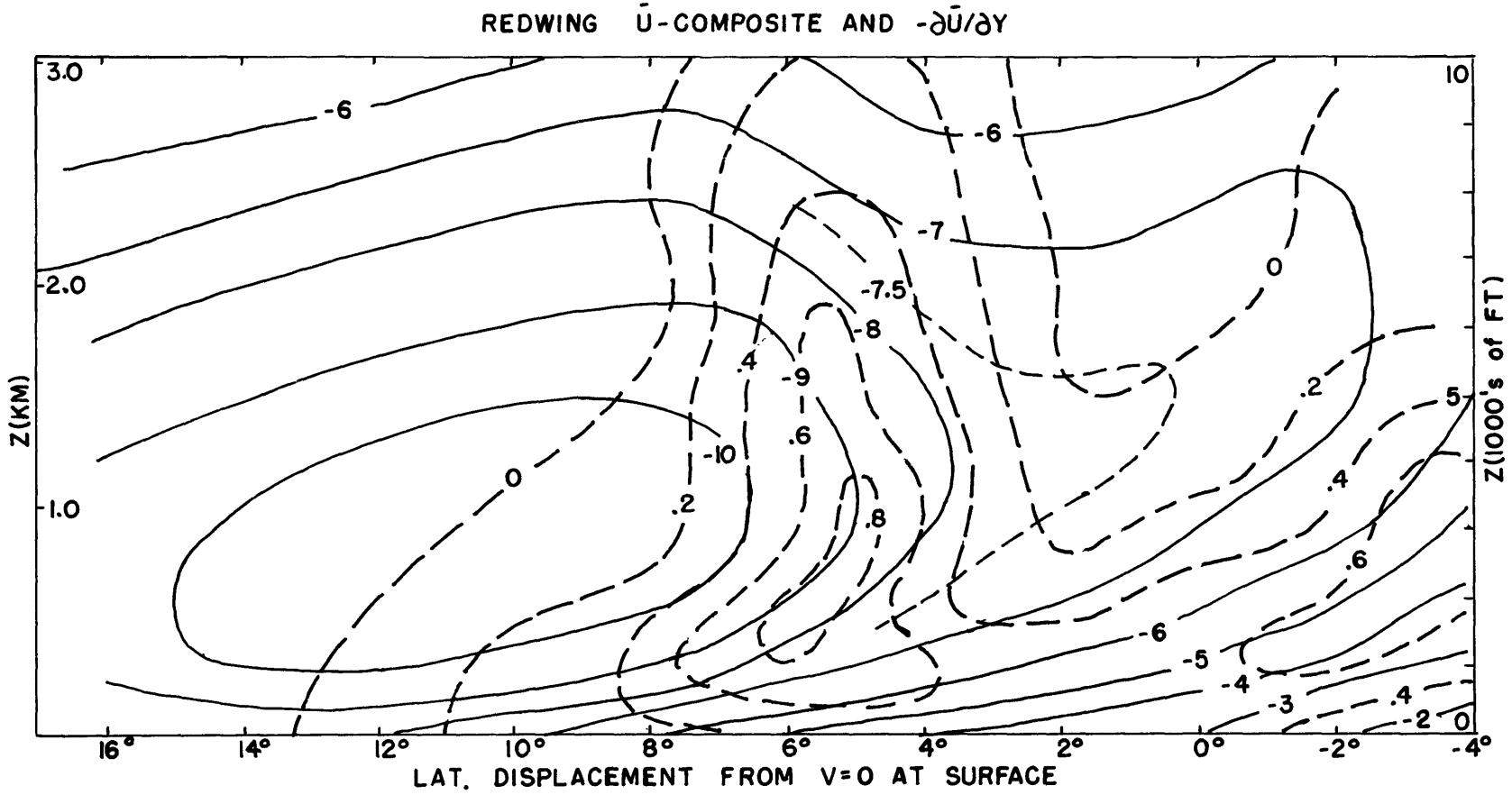

Fig. 4.13a. Mean zonal wind (solid, ms^{-1}) and shear vorticity (dashed, 10^{-5} s^{-1}) from two north-south cross-sections in the Marshall Islands, 0300Z, May 1956.

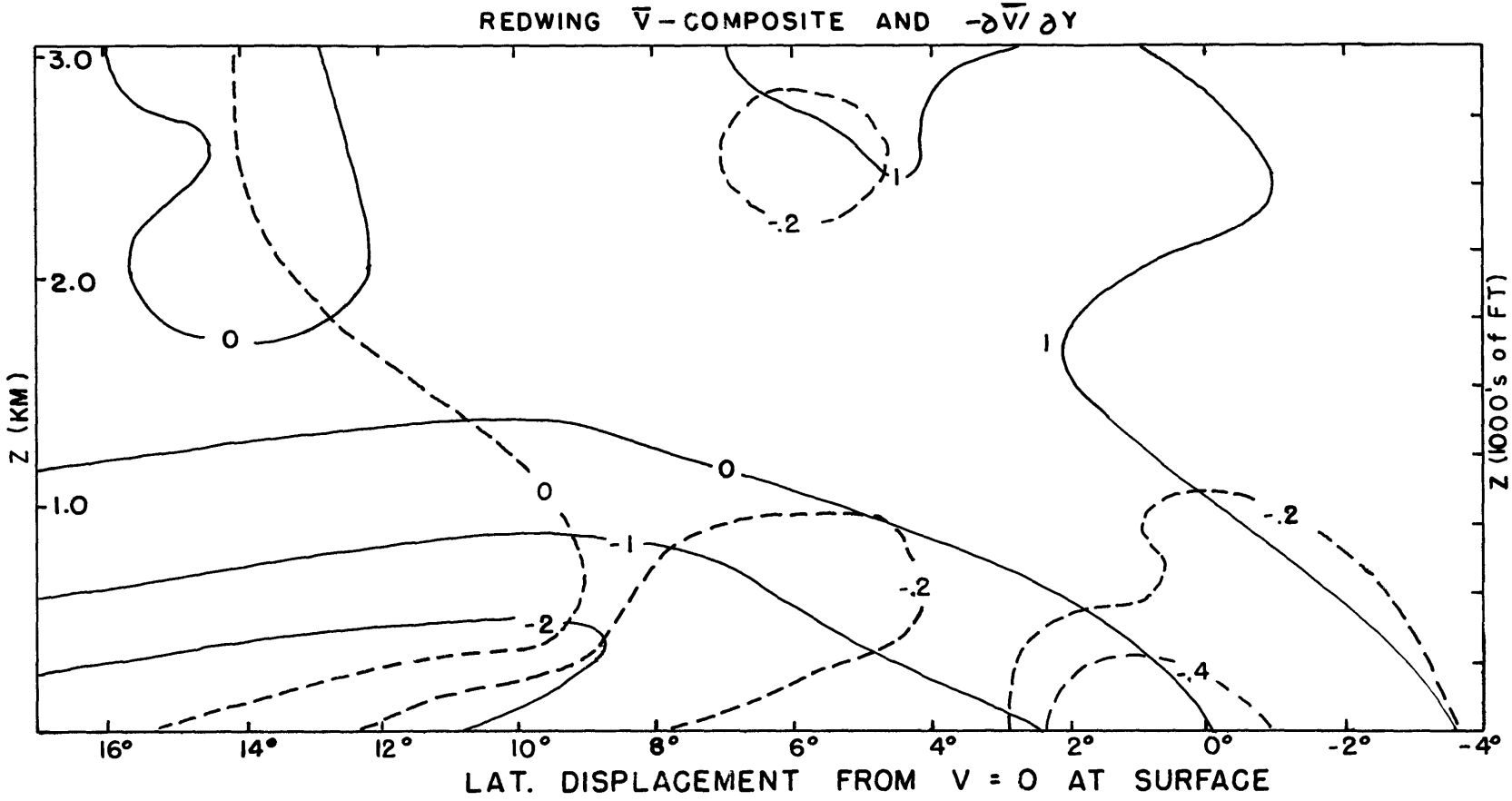

Fig. 4.13b. Mean meridional wind (solid, ms^{-1}) and meridional horizontal divergence (dashed, 10^{-5} s^{-1}) from two north-south cross-sections in the Marshall Islands, 0300Z, May 1956.

the ITC was mainly between Oceanographer and Discoverer during Fourth Phase, these two stratifications 'trapped' the ITC first between Mt. Mitchell and Discoverer then between Mt. Mitchell and Oceanographer. The resulting sections were then averaged by aligning them with reference to the intersection of the $\overline{v} = o$ contour at the surface. The effect was to expand the latitude spread and create a more interesting display. These composites are shown as Figs. 4.14a, b.

4.4.3. LIE Composites

It was decided to "trap" the ITC only between Palmyra and Fanning since Palmyra had the only justifiable regime change. Data had been independently stratified by NCAR but no conditional strata were available. A complete manual check of the wind reports from Palmyra and Fanning showed that when Palmyra's 500 m wind was northerly, Fanning had southerly only 60 percent of the time which is not overwhelming. Thus unstratified means were used at Fanning and Christmas along with Palmyra's northerly regime in order to produce Figs. 4.15a, b with the model ITC between 4^{o}-6^{o}N.

4.4.4. Discussion

Redwing data (Fig. 4.13) were not stratified into regimes and it is evident by comparing the three figure sets that this region had the most diffuse convergence pattern. Vorticity maxima are well within the boundary layer but above the surface near 2000 feet. The convergence maxima are well correlated with vorticity in support of a frictional mechanism. The equatorward flow seems to undercut the air

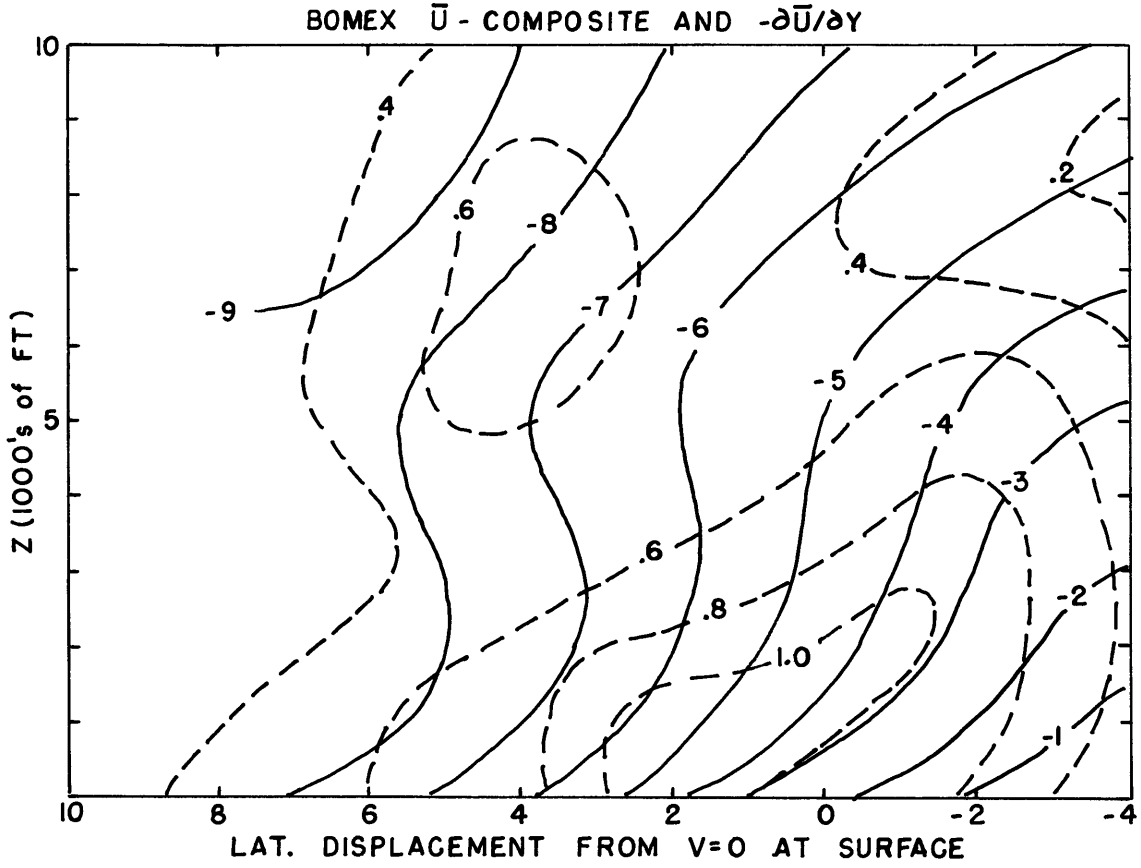

Fig. 4.14a. Mean zonal wind (solid, ms^{-1}) and shear vorticity (dashed, 10^{-5} s^{-1}) from stratified ship data during BOMEX, 13-28 July 1969.

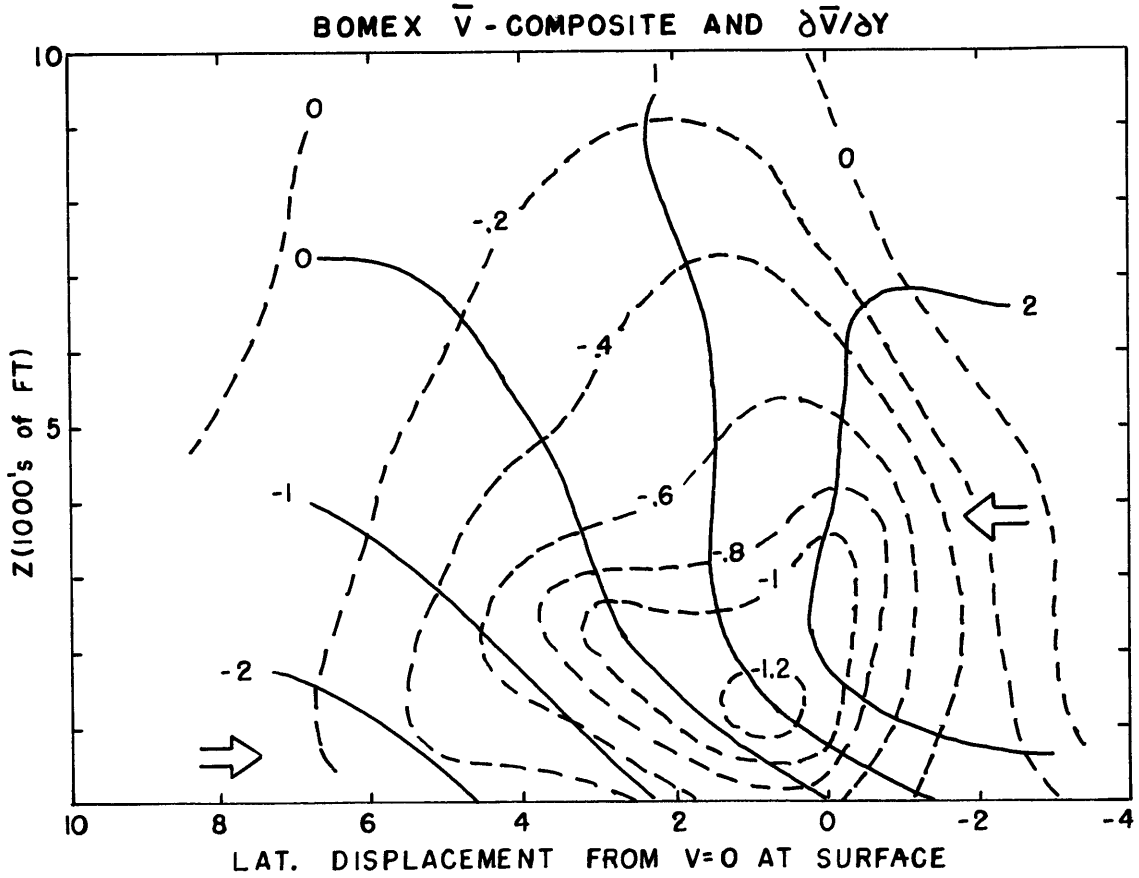

Fig. 4.14b. Mean meridional wind (solid, ms^{-1}) and meridional divergence (dashed, 10^{-5} s^{-1}) from stratified ship data during BOMEX, 13-28 July 1969.

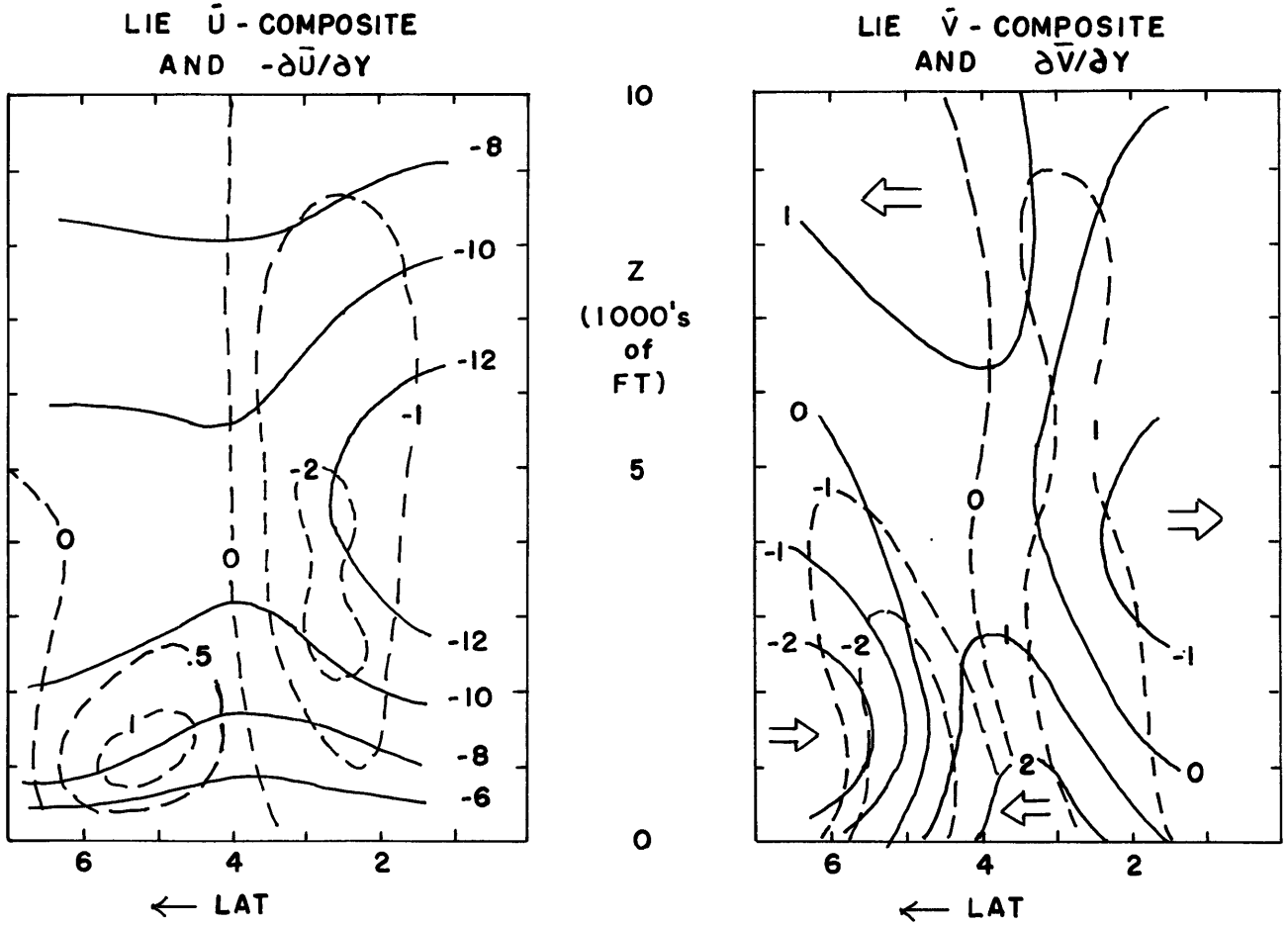

Fig. 4.15a,b. Mean zonal wind and shear vorticity (a) and mean meridional wind and meridional divergence (b) from LIE data using northerly regime data at Palmyra (6°N) and grand averages from Fanning (4°N) and Christmas (2°N). Units the same as Figs. 4.13,14.

from the south which can be seen in the shallow northward slope of the $\overline{v} = o$ isotach. Vorticity values approach $10^{-5} s^{-1}$ whereas convergences are one-fourth to one-half this magnitude.

The stratified BOMEX data (Fig. 4.14) formed a sharper composite. Cyclonic vorticity and convergence maxima are tightly correlated, with both having magnitudes near 10^{-5} just below cloud base. Again, the $\overline{v} = o$ isotach slopes toward the north as the poleward moving air overruns the boundary layer flow from the north.

The LIE behavior in Fig. 4.15 is sharper still, and more complicated. Vorticity changes sign at Fanning ($4^{o}N$). To the north, cyclonic vorticity and convergence are correlated in the sub-cloud layer. The convergence magnitude is double that of the vorticity ($-2x10^{-5} s^{-1}$ vs. $10^{-5} s^{-1}$). To the south, the anticyclonic vorticity and divergence extend through 3 km which supports the general dryness in the region south of the ITC but north of the equator. The $\overline{v} = o$ isotach still shows a slope of about 1/100. The reader must realize that these sections are stretched so much in the vertical that even a small tilt is actually quite horizontal in the real world. The extreme of this is in the Redwing data which shows the slope of the $\overline{v} = o$ isotach to be $\sim 2x10^{-3}$.

The more complex circulation observed in the LIE data has been previously documented (e.g. see review article by Zipser, 1970). Robitaille and Zipser (1970) found the surface divergence near the equator which shows up in Fig. 4.15. Zipser (1970) also notes that

Christmas had the most backing with height and that this vanishes at Palmyra. However, in the stratified Palmyra data, there is 15° of backing in the southerly regime between 500 and 3000 m. Thus, the lack of backing in the total mean wind profile is due to the cancellation of the v-components north and south of the ITC as it moves back and forth across Palmyra.

4.5. Summary

Mean wind, humidity and temperature data were used to specify the B.L. in the BOMEX Fourth Phase data and from the Line Islands Experiment. As in the Redwing study, the depth of the B. L. is 2-3 km based on wind shear (mainly turning with height) and the humidities.

We consistently find veering with height and equatorward transport north of the ITC in a B. L, with Ekman layer characteristics. Fifty percent of the equatorward flux is below 750 m. Poleward flow is through a deeper layer as shown in stratified profiles from Mt. Mitchell (10.5°N), Oceanographer (7.5°N) and Palmyra (6°N). Winds back with height after veering in the sub-cloud layer at these locations. A boundary layer 1.5 to 2 km deep also may be found within two degrees of the equator at Kapingamarangi (1°N), Tarawa (1.5°N) and Christmas (2°N). This layer shows slight backing of the wind at the first two islands and backing through about 15° at the latter. The profile at Fanning (4°N) looks similar to that of Christmas except that the former is more from the southeast. The backing with height cannot be explained with northern hemisphere Ekman theory but may represent

the effect of advection of a southern hemisphere Ekman layer across the equator. A similar effect was observed by Swallow and Bruce (1966) in the Somali current as far north as 3^{o}N. In these observations the ocean current was directed to the left of a southerly monsoon wind.

The stratified humidity and standard deviation of humidity profiles identified the tops of the moist layers near 2 km in northerly regimes at Mt. Mitchell and Discoverer. The southerly regimes showed "soft" tops, especially at Mt. Mitchell which also had most of its precipitation when south of the ITC. This indicates much greater coupling with the higher troposphere which may account for the more homogeneous southerly regime wind profile at Mt. Mitchell above a sharply marked veering layer below the clouds. In the LIE data and in the Marshalls, the top of the moist layer became shallower toward the equator and was about twice as deep in the Marshalls. In the LIE the variation was from 2.4 km at Palmyra to about 1.6 km at Christmas.

The Marshalls are further west and therefore in a less stable portion of the Trades with mean upward vertical motion, while in the LIE, the region south of the ITC was divergent indicating subsidence. Because there often was a southern hemisphere ITC during the LIE, the subsidence in the center produces a linear analogy to the eye of a typhoon.

Due to the characteristics of the profiles from the stratified data we see that the winds north of the ITC tend to undercut the deeper

layer of poleward moving air. The positive vorticity and convergence correlated very well (especially when data could be stratified and composited) and maxima on the order of $1\text{-}2\text{x}10^{-5}\ s^{-1}$ were observed for both quantities near cloud base level. Case studies in the next chapter from BOMEX will show that clouds are indeed confined to such zones and that the kinematical extremes are often packed into zonal bands only a degree or two wide.

The necessary conditions for CISK are supported by these findings; however, the dynamics of the boundary layer south of the ITC are not explained by quasi-geostrophic reasoning. More theoretical work is needed in this area.

CHAPTER 5

A BOMEX CASE STUDY ON THE DECAY AND REGENERATION OF THE ITC

5.1. Background

In Chapters 3 and 4 it was shown in various composites that a reasonably shallow (2-3km) boundary layer (B.L.) can be found at ITC latitudes. North of the ITC in air with a nearly zonal or ENE history, the B.L. has Ekman characteristics. At intermediate latitudes between the ITC and the Equator (e.g. Oceanographer at 7.5°N or Palmyra at 6°N) the B.L. shows veering and pronounced speed shear below 500-750m with backing and reduced speed shear above. Near the Equator, the most consistent feature is the speed shear to about 1500m (e.g. Kapingamarangi at 1°N or Christmas at 2°N). Composite north-south vertical cross-sections showed that cyclonic vorticity and convergence are strongly correlated with maximum values of convergence occurring near the cloud base level.

Time cross-sections from Mt. Mitchell showed that the B.L. is more difficult to specify on a day-to-day basis, specifically, the transition to the free atmosphere is frequently not clear cut. The composite cross-sections, which are time averages, tend the smear the ITC over latitude and mask the true dimensions of the convergence field and the implied zone of cumulus and showers. In general, the composited results support the notion that the ITC is organized by the boundary layer flow and that necessary conditions for CISK are present. But on a day to day basis, it is still possible to argue that relationships between wind and cloud structure are not really in phase, and we have not seen which organized pattern (wind or cloud) precedes

the other if they are related.

5.2. Objectives

The objectives of this case study are limited and are natural extensions of the ideas suggested by Chapters 3 and 4. We will look at the 1800 GMT ($\pm$ 6 hr) subsynoptic scale kinematics at 500m and 700mb (3-3.5km), and compare the wind, vorticity and divergence patterns with the cloud and weather depictions taken from ESSA-9 images and aircraft reconnaissance records. In a semi-quantitative fashion this will enable us to determine:

(a) the size of organized kinematical features and whether or not these can be associated with significant cloud patterns;

(b) the level at which the flow patterns are best organized to support the weather features;

(c) the approximate time scale of the meso-scale ITC cloud bands; and

(d) whether organized motion fields precede the cloud bands or vice versa.

Ultimately we will comment on the validity of CISK as a viable rationale for the generation and maintenence of the ITC.

Thermodynamic factors and the energy budget are not discussed except in an occasional speculative fashion. It is logical that a more quantitative follow-on to this study should include such elements.

An unsuspected bonus feature which is not directly related to the ITC problem will also be illustrated and discussed. From 14-20

July, an easterly jet with maximum speed >20mps was more or less evident at 700mb north of 10°N. This jet has been built up quasi-geostrophically on the southern periphery of a warm, nearly dry-adiabatic tongue of African air. It will be shown in Appendix V that this jet has the necessary condition for instability of an "internal jet" and may have undergone an unstable oscillation during the study period.

5.3. General Situation

During the period 13-21 July, 1969, the ITC in the BOMEX array passed from a mature state (13,14,15 July) to a state of complete disruption and virtual disappearance (16,17 July) through a period of regeneration (18,19,20 July) and partial disruption on 21 July. Starting on or about 22 July, a warm core disturbance formed in the ITC and dominated the region until late on 26 July; hence, because this thesis is concerned primarily with quiescent ITC characteristics, the case study was terminated on the 21st. However, the ITC can hardly be considered undisturbed during the study days due to the passage of traveling disturbances further to the north that show up best at 700mb. On the 13th and 14th, a disturbance of African origin appeared to cause a fracture in the ITC south of the wave's position. The disintegration on 16,17 July actually began further upstream on 15 July and advected into the BOMEX region. An arc-shaped band of cumulus and strato-cumulus formed the leading edge of the clear area and extended to the northeast north of 15°N. At 700mb, an easterly jet in excess of 40 knots progressed westward and northward (12°N to 16°N) on 14, 15 and 16 July. On the 17th, a distinct trough appeared

near 56°W at 700mb and simultaneously there was a major intensification of cloudiness and showers near 60°W and north of 17°N. On the 19th and 20th, another strong 700mb trough passed through the region north of 15°N.

At low levels (∿500) the flow was relatively simple only during 15-18 July; otherwise there were quite complicated deformations at the meso-scale mainly in the form of cusps and small enclosed cyclonic circulations. One cusp or possible closed circulation in the ITC could be followed for three days from the 19th through the 21st.

5.4 Analysis Technique and Limitations

Surface and upper-air data from the islands formed the basic, synoptic scale data base. At the 500m level it was possible to justify analyses at the meso-scale (∿100km) in regions of the map having ATS-III or aircraft-derived wind data. At 700mb (3-3.5km) data density also varied, especially south of 13°N, depending on the daily flight schedule. Because ATS-III vectors are not available, the 700mb analyses are essentially at the subsynoptic scale (∿3-500km) except in the vicinity of the RFF or WC-130 aircraft. See Appendix IV for discussion of daily data.

Isogons and isotachs were drawn and then converted to streamlines and isotachs. Standard analysis models were used (Atkinson, 1971 pp 10-18 to 10-25) unless data demanded a departure from the model. Vorticity and divergence fields were differenced using a 200km grid unless the flow was complex, then a 100km grid was used. Divergence values are more reliable at 500m than at 700mb and are suspect when

the magnitudes are less than $\sim 2 \times 10^{-5}$ s^{-1}. At 500m, the significant divergence patterns were usually associated with sharp directional shear as well as speed variation ; whereas, at 700mb, the patterns showed much more compensation between direction and speed gradients.

5.5 Case Study Format

There are six figures for each of the nine days. The first two in each set show the ESSA-9 photo and a cloud and weather depiction. The latter was drawn from the ESSA-9 photo by a projection technique and was supplemented by synoptic and flight observations. On the cloud depictions, the brightest and/or hardest looking targets have been drawn in bold outline. The other four figures show the streamline and isotach analyses at 500m and 700mb (3-3.5km), and the vorticity and divergence analyses at each level. Selected data bases and short discussions are provided in Appendix IV.

A synoptic time of 1800 GMT $\pm$ 6 hr was chosen as a convenient compromise to accommodate the off-time aircraft and satellite data. Data earlier (later) than 1800 GMT were displaced and plotted west (east) of their actual position at a distance concomitant with an east-west speed of 15 knots. This was a very workable technique, especially north of the ITC, in the zone of the travelling disturbances. This method is recommended in Atkinson (1971) and was used with considerable success by Zipser (1969) in the Line Island between 2° and 6°N.

The discussions will be oriented toward the four periods described in 5.2 and will cover the general situation and specific details

at each level relevant to the objectives of this paper.

5.6. Discussion of Figures

5.6.1. Mature ITC and Africa Wave, 13-15 July

On the 13th and 14th, the ITC was aligned in two east-west bands along 6° and 9°N (Fig. 5.1a and 5.2a). A fracture in these bands was seen to occur on both 13 and 14 July just to the south and east of a travelling disturbance of African origin. This fracture was also visible on the 12th outside the BOMEX grid which indicates its persistence, and, because it traveled with the Africa wave, it is safe to assume that the fracture is a manifestation of an interaction between the wave and the ITC. By the 15th, the wave had intensified and moved to 60°W (Fig. 5.3a), and a single ITC band remained in its wake at 9°N. Throughout the period, organized shower activity with considerable cirrus and probable middle cloud debris showed up in the ITC (and the storm), thus the designation as a "mature" ITC.

The reader is referred to Fig. 1.1 as a reminder that the ITC cloud bands as seen from even the ESSA-9 with its one mile resolution, are much narrower than the pictures indicate. Yet the wind perturbations in the B.L. associated with these bands are broad enough to be detected in a meso-scale ($\sim$ 100km) analysis. Thus it is possible to relate cloud scale patterns of organization to meso scale wind analyses in a manner that is not misleading.

13 July 1969: Figs. 5.1 a-f

On the 13th (Figs. 5.1 c,d), a low level cusp and west-east shear line support the bright cloud masses at A and C (Fig. 5.1 b) in the

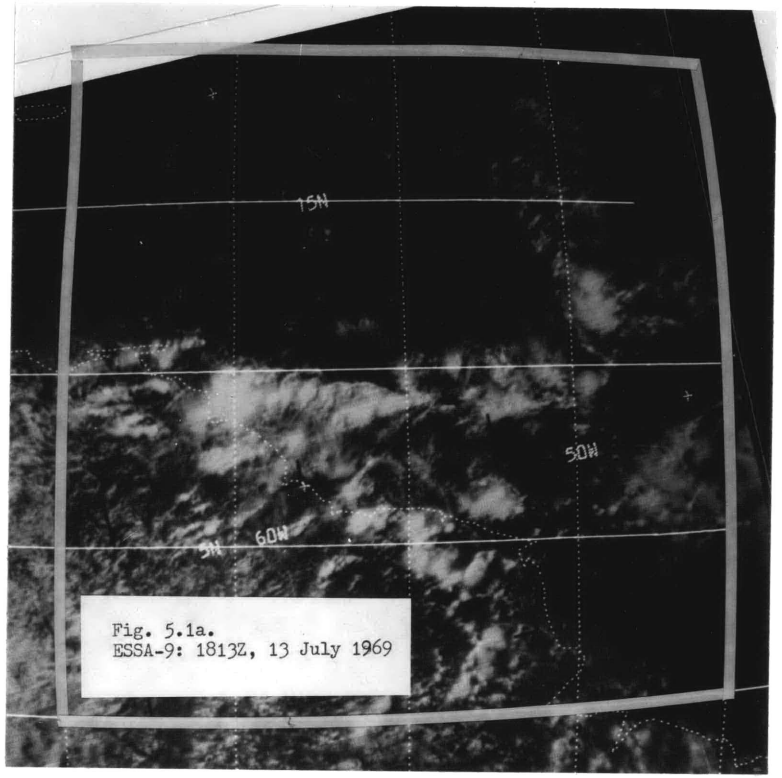

Fig. 5.1a.
ESSA-9: 1813Z, 13 July 1969

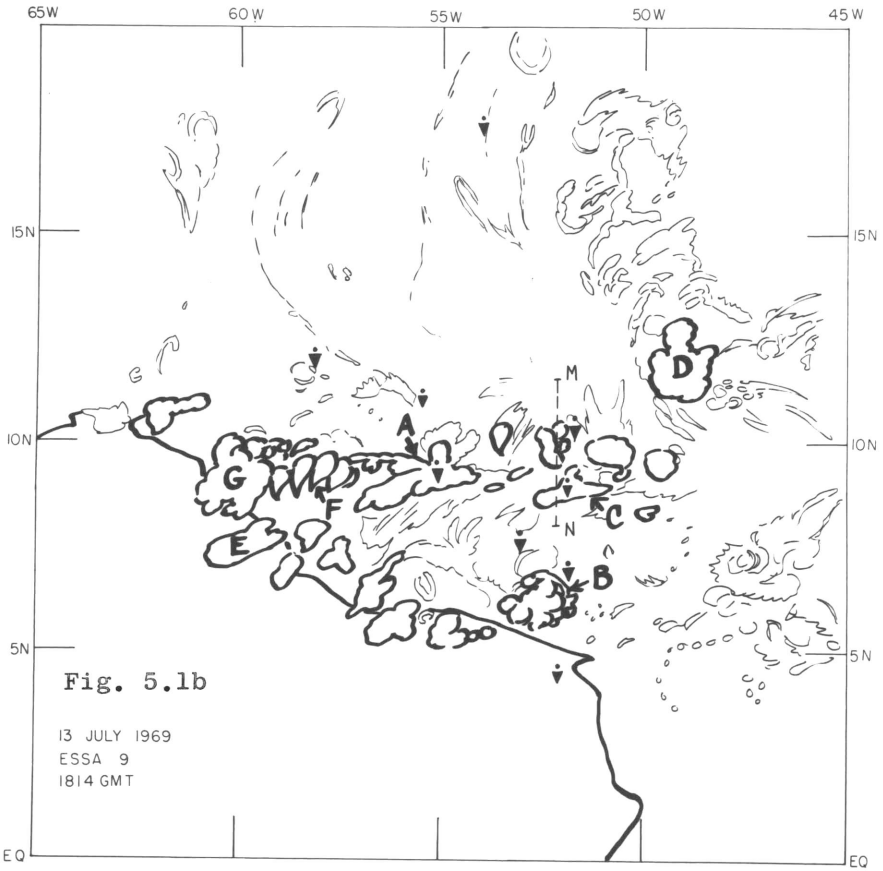

Fig. 5.1b

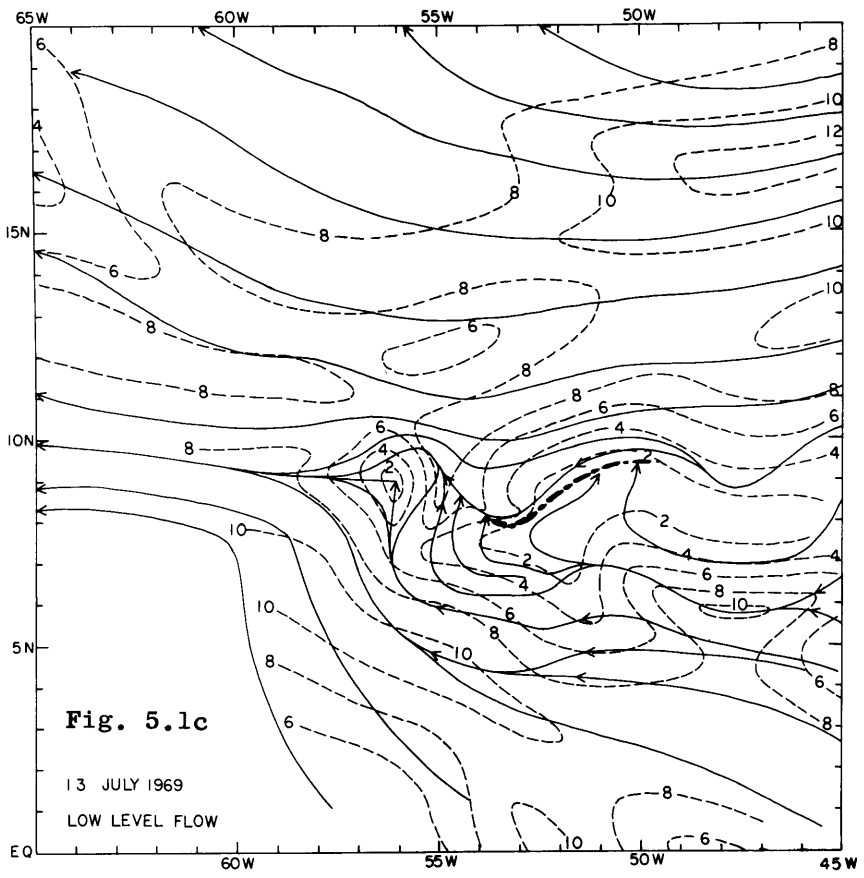
65W
60W
55W
50W
15N
10N
5N
EQ
45W
Fig. 5.1c
13 JULY 1969
LOW LEVEL FLOW

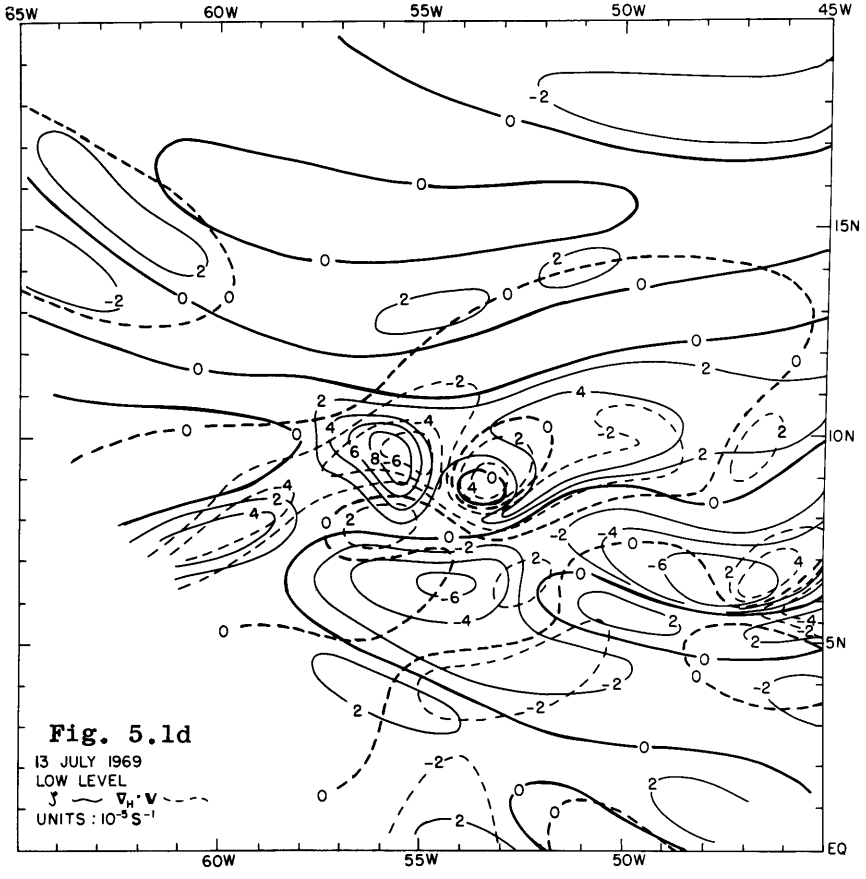
65W
60W
55W
50W
45W
15N
10N
5N
EQ
Fig. 5.1d
13 JULY 1969
LOW LEVEL
UNITS : $10^{-5} S^{-1}$

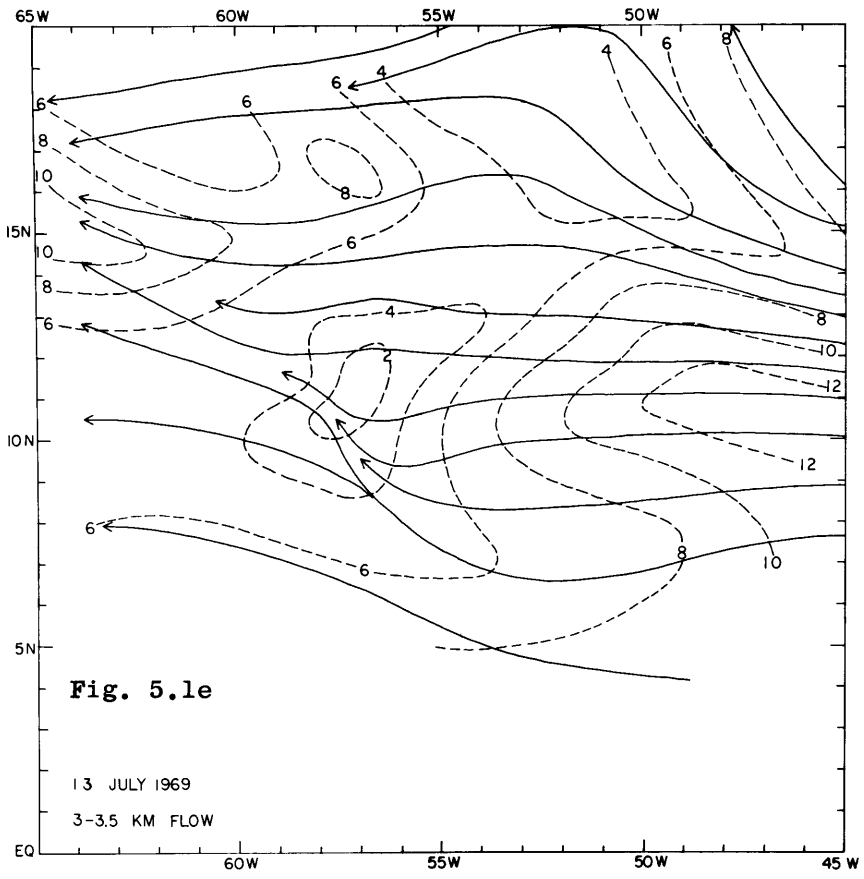

Fig. 5.1e

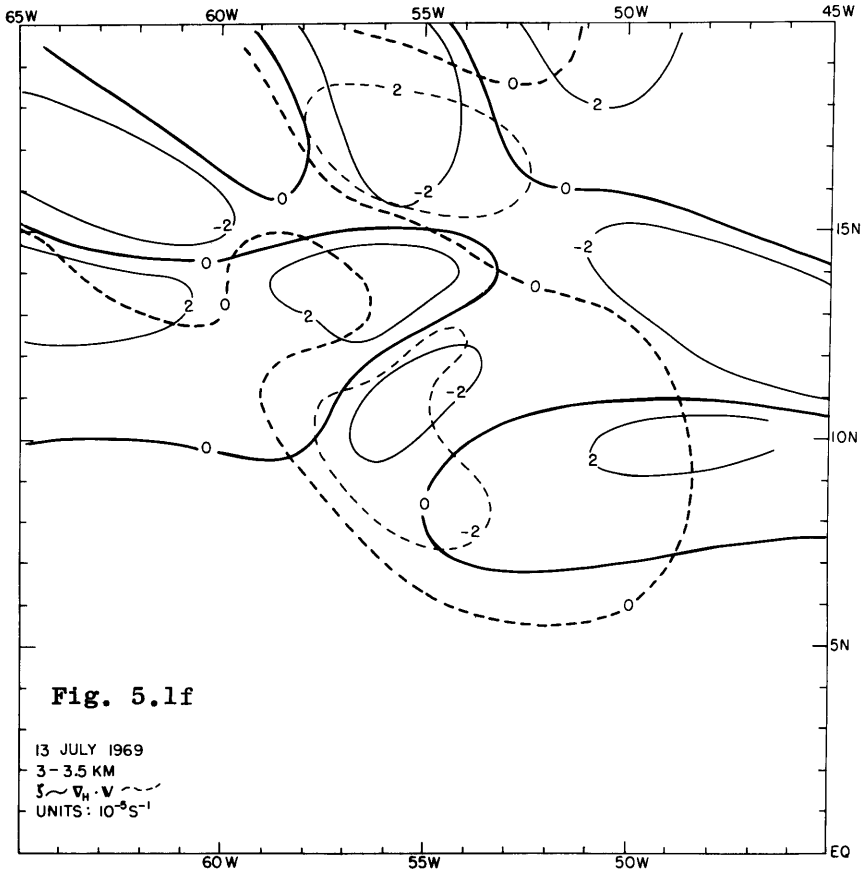

Fig. 5.1f

northern ITC band. Large vorticity (order $4\text{-}8\times10^{-5}\ s^{-1}$) and convergence (order -2 to $-6\times10^{-5}\ s^{-1}$) are well correlated in these regions. The zone of weak activity between these two areas has weak positive vorticity and strong divergence. The southern band is dissipating (can be shown in the ATS-III sequence) and, indeed, the cloud cluster at B is in a region of anticyclonic flow and divergence. The bright cloud families at E and F are well supported by the vorticity and convergence analysis while the cloud cluster at G has little support and cannot be found on the 14th (Fig. 5.2 a,b). The bright portion of the disturbance (area D) has little low level support but does intensify by the 14th and can be found in the low level on this date. In general, the Africa disturbance is not reflected at 500m on the 13th. The fracture south of the disturbance occurs in anticyclonic flow with negative vorticity and divergent winds.

At 700 mb on the 13th (Fig. 5.1 e,f) the Africa wave trough at 53°W leads the cloud mass in a mannger suggestive of a classical easterly wave. The northern ITC cloud band is in a broad zone of convergence, but in general, there are no correlated vorticity-convergence patterns to support the organized cloudiness. The pocket of 700mb convergence centered near 10°N, 56°W is most likely related to the 500m trough and cusp and may reflect coupling between layers due to the vigorous convection in this part of the ITC. In contrast, to the low level flow, there is no 700mb support for the fracture in the ITC.

14 July 1969: Figs. 5.2 a-f

On the 14th, the ITC is also in two bands east of 52°W. The fracture south and east of the African disturbance is accentuated by a pair of cloud clusters. The one to the north has a diameter of about 130km while the other's is close to 200km. Between 6° and 9°N and 55° and 60°W there appears the remnants of the ITC bands that preceded the Africa wave on the 13th. The African disturbance has intensified considerably on the 14th which is seen on the ESSA-9 image as a better organized pattern of middle and high cloud. Showers and thundershowers accompanied the passage of this storm at locations such as Discoverer and Barbados. For more details on this African disturbance see, for example, Fernandez-Partagas and Estoque (1970) or Carlson and Prospero (1971).

RECCO data from the WC-121 and WC-130 indicate that bright regions in the northern ITC band near 47°W are Cb's with tops to 25-30,000 ft. There was also considerable shower activity along the return leg from 8°N, 50°W to 10.5°N, 55°W. The northern cloud cluster on this leg contained at least one Cb but appeared to be a mix of cumulus and alto cumulus as well. The bright cloud near 10°N, 55°W was also at least one Cb.

At the low level, each major ITC band can be identified with an appropriate feature in the flow field. The rudimentary band at point A in 5.2 is along a confluence axis (convergence as intense as $-4 \times 10^{-5}\ s^{-1}$) in a field of strong anticyclonic vorticity associated with the ridging just to the north. In the ridge the flow becomes divergent which probably accounts for the sharply defined clear zone.

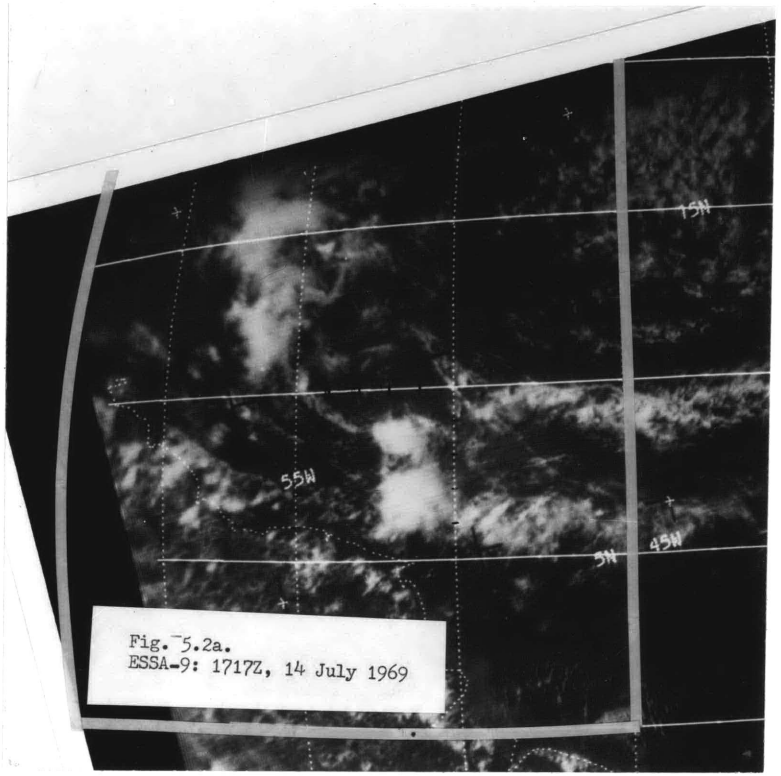

Fig. 5.2a.
ESSA-9: 1717Z, 14 July 1969

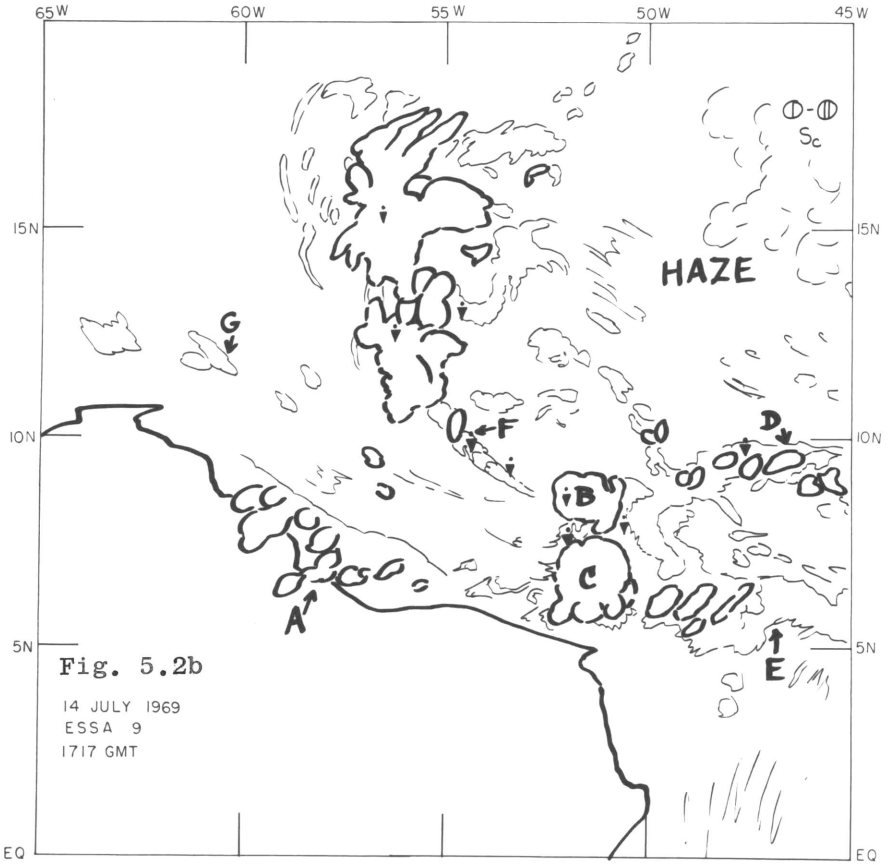

Fig. 5.2b

14 JULY 1969
ESSA 9
1717 GMT

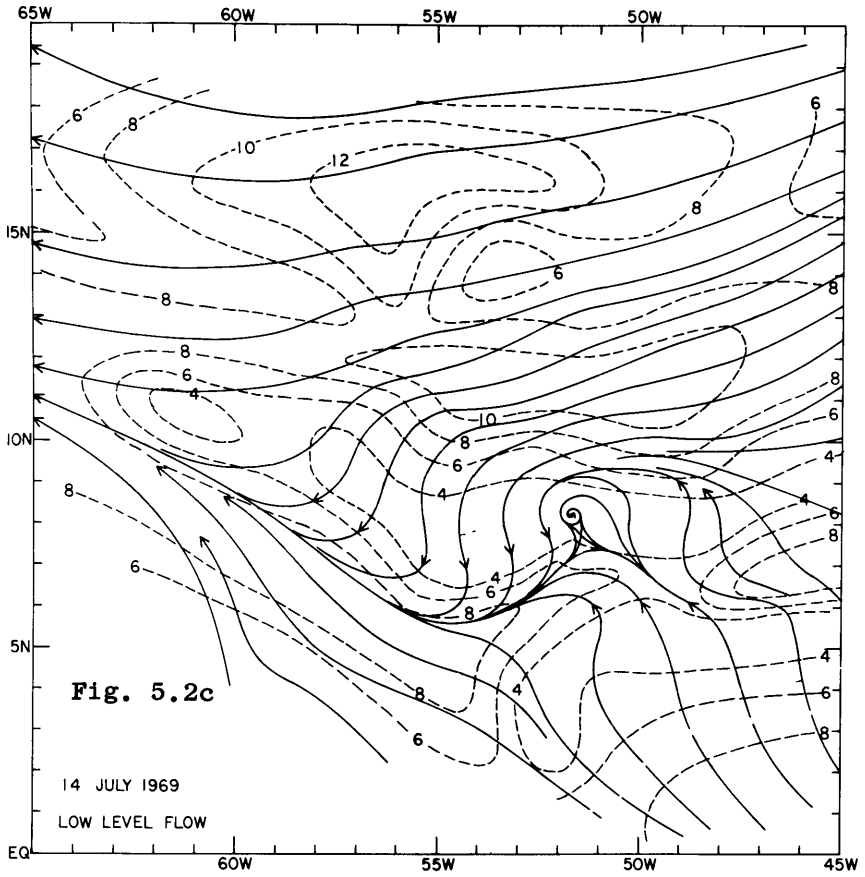

Fig. 5.2c

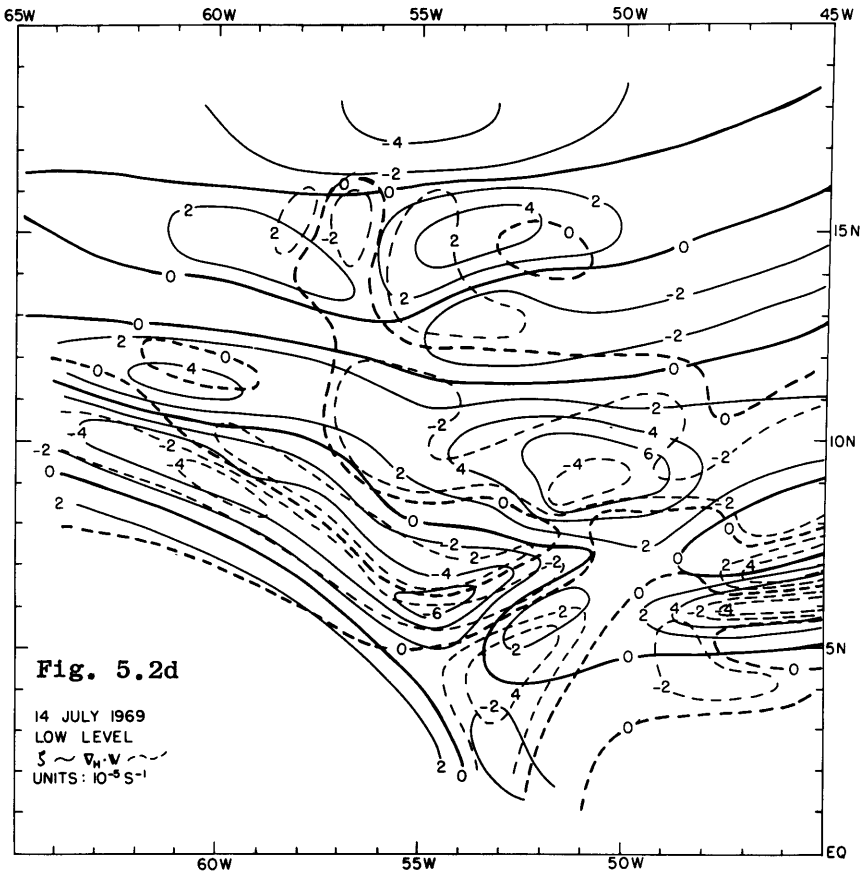

Fig. 5.2d

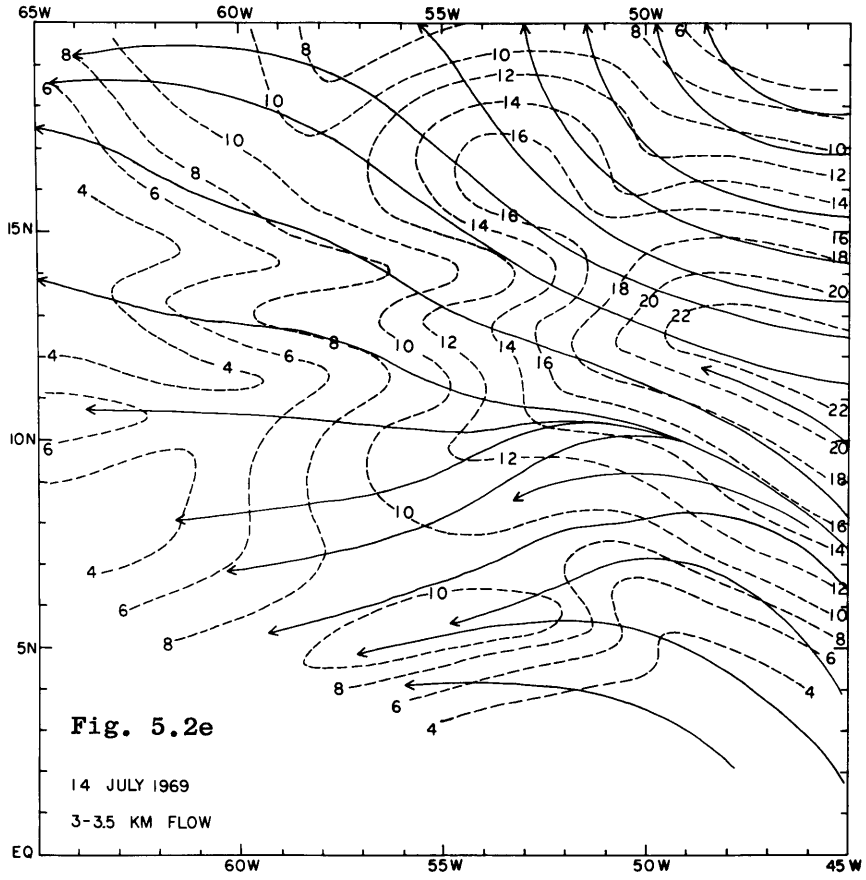

Fig. 5.2e

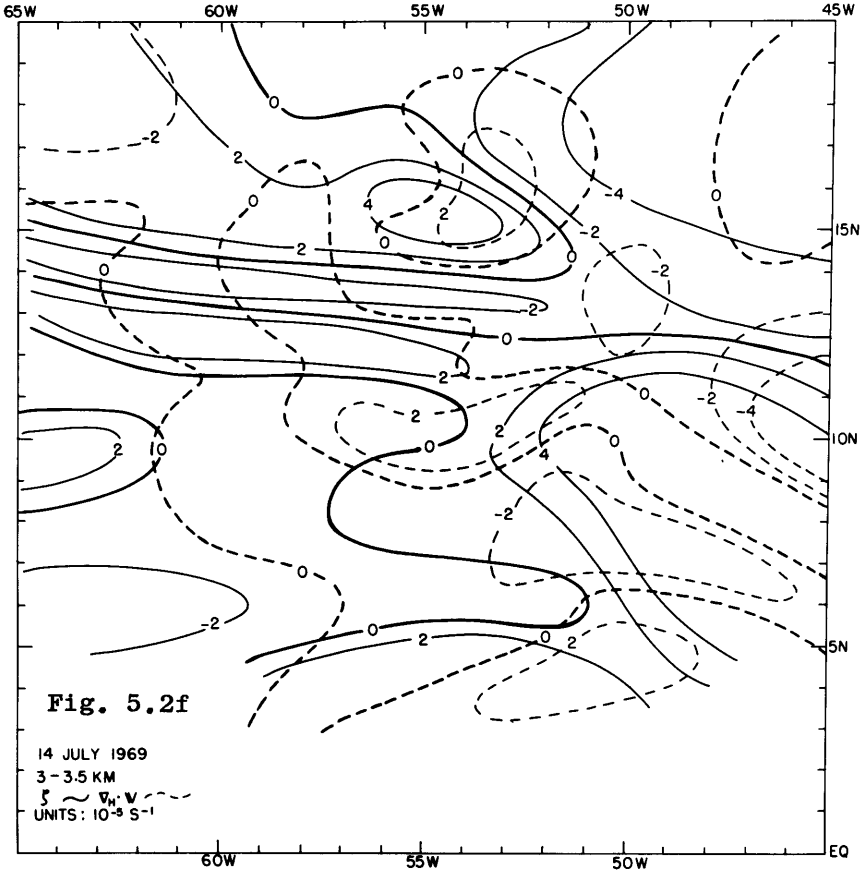

Fig. 5.2f

Cloud clusters B and C are in a trough and closed circulation system with cyclonic vorticity as large as $6 \times 10^{-5}\ s^{-1}$ and convergence as intense as $-4 \times 10^{-5}\ s^{-1}$. Both bands D and E lie in east-west correlated streaks of cyclonic vorticity and convergence. Band E lies in a trough in the southerly flow while band D is in a confluence axis. Weak anti-cyclonic flow and divergence characterizes the clear area between the two bands. Showers and Cb's in the cloud streak at F lie in a trough in the trade wind air stream representing a broader zone of cyclonic vorticity and convergence. The cloud patches at G also may be part of the ITC from the 13th and we note that the entire sequence G,F,B,D lies in a strip of cyclonic vorticity and convergence, the significant width of which varies from 200-300km.

The African disturbance at the low level is characterized by two streaks of positive vorticity and two associated pockets of convergence. In general, it appears that the storm, which has intensified from the 13th, is now in the boundary layer and is tapping the moisture source, in contrast to the previous day.

In the 700mb flow field (Figs. 5.2 e,f) there are two troughs, one has tracked westward as part of the African disturbance at about 16 knots. The other trough at low latitudes may be associated with the cloud cluster trough at low levels. Another important feature is the 22 m/s jet from the southeast which fans out into at least three branches across the array. At 700mb as well as the low level there are two streaks of positive vorticity passing through the Africa wave, but the divergence fields show little relation to clouds and poor continuity

from the 13th. The anticyclonic strip at 13° - 14°N intersects the storm at a point where it later fractures and begins to disintegrate on the 15th. The ITC region east of 55°W is in a broad zone of positive vorticity at 700mb. Clusters B and C and band E show a modest correlation with an elongated patch of -2×10^{-5} s^{-1} convergence; otherwise there is little resemblance between the organized 700mb convergence patterns and the ITC clouds.

15 July 1969: Figs. 5.3 a-f

Cloud clusters B and C and southern band E from Fig. 5.2b on the 14th have vanished by 15 July. Instead of the double band, a single ITC band 100km wide stretches eastward along 9°-10°N in the wake of the Africa wave. Since the lower portion of the Africa wave moved only 500km in the 24 hour period, it is unlikely that the 15 July ITC band moved west from B and/or D on the 14th (Fig. 5.2b). Rather this is somewhat younger cloud material (note lack of cirrus east of 55°W) which began to show up as the small band F containing showers and a few Cb's on the 14th. The Mt. Mitchell, which is close to the new band, had Cb's showers and thunderstorms from 15/0000 GMT to 15/1800 GMT (which was the last report until the 17th). The "nose" of an arc-like band of cumulus and strato-cumulus shows at A near 12°N and 57°W (Fig. 5.3b). This will accompany the clearing of the ITC on 16 and 17 July and may also be of African origin. Many large shower cells in the old Africa wave are visible through a diminished cirrus canopy.

The 500m flow pattern is extremely simple with an east-west confluence zone directly in the ITC cloud band and the southern part of the old Africa wave cloud cluster B. Although the flow is weak

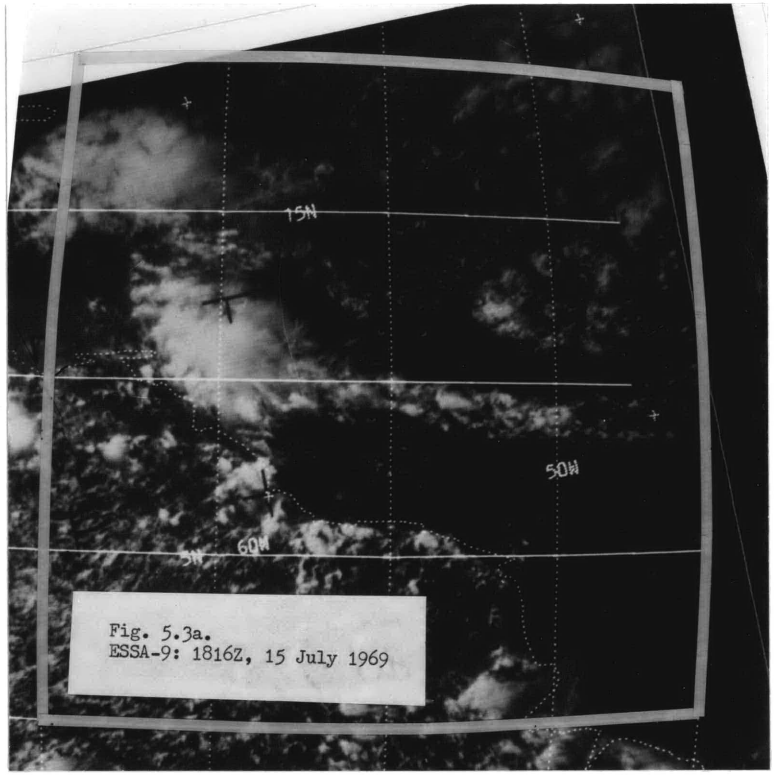

Fig. 5.3a.
ESSA-9: 1816Z, 15 July 1969

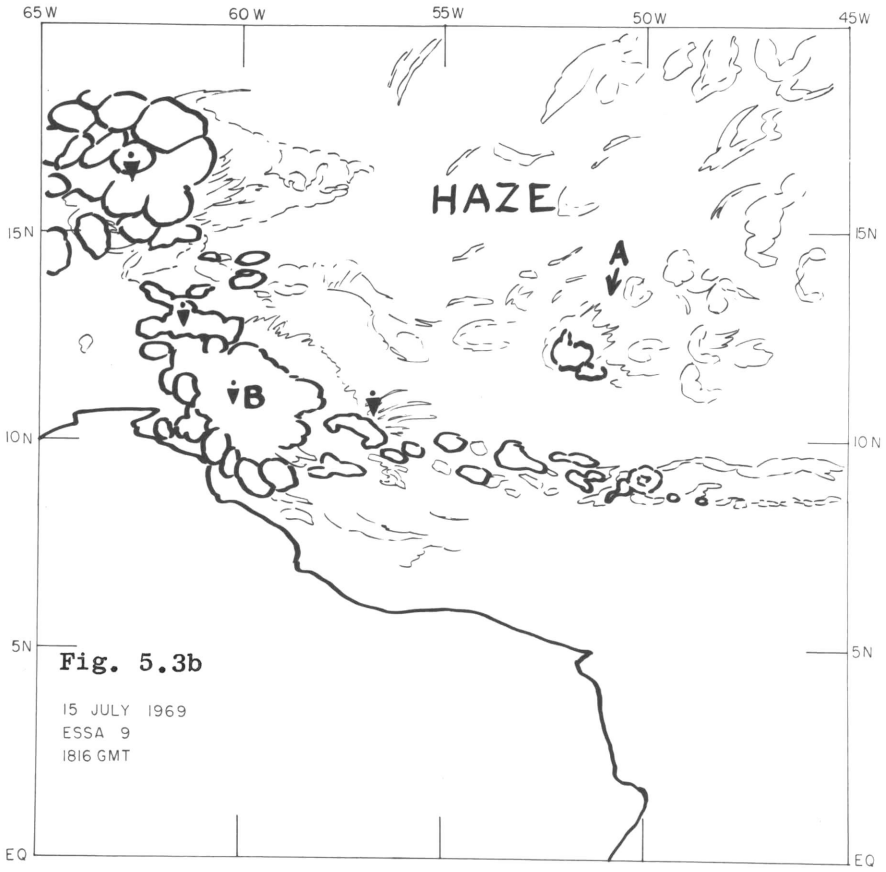

Fig. 5.3b

15 JULY 1969
ESSA 9
1816 GMT

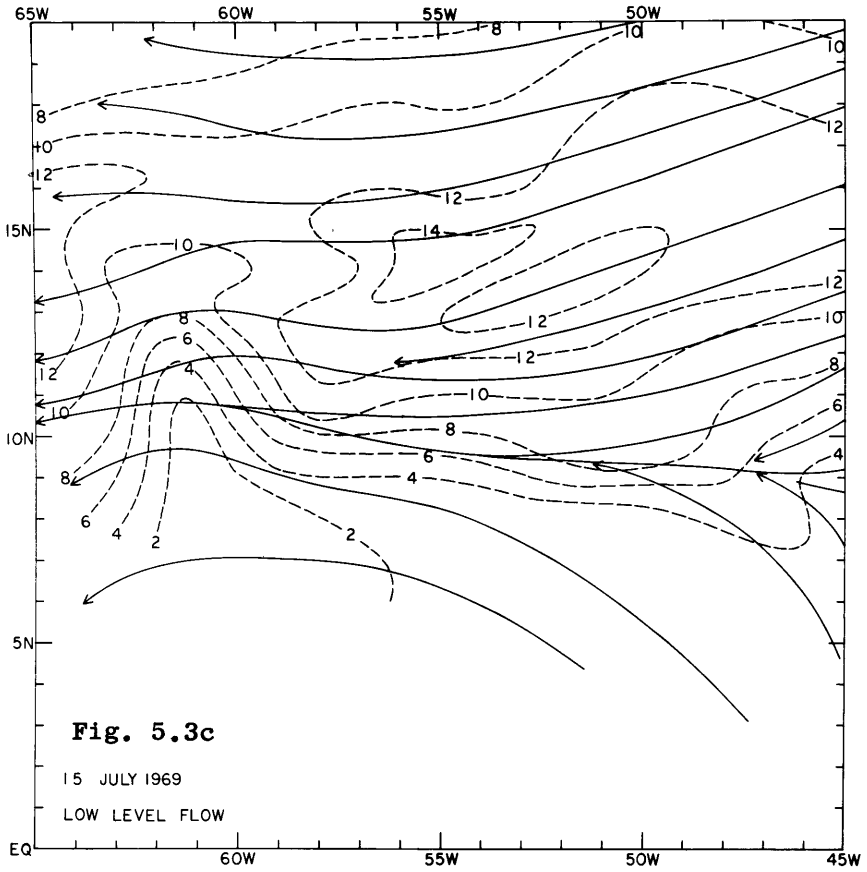

Fig. 5.3c

15 JULY 1969

LOW LEVEL FLOW

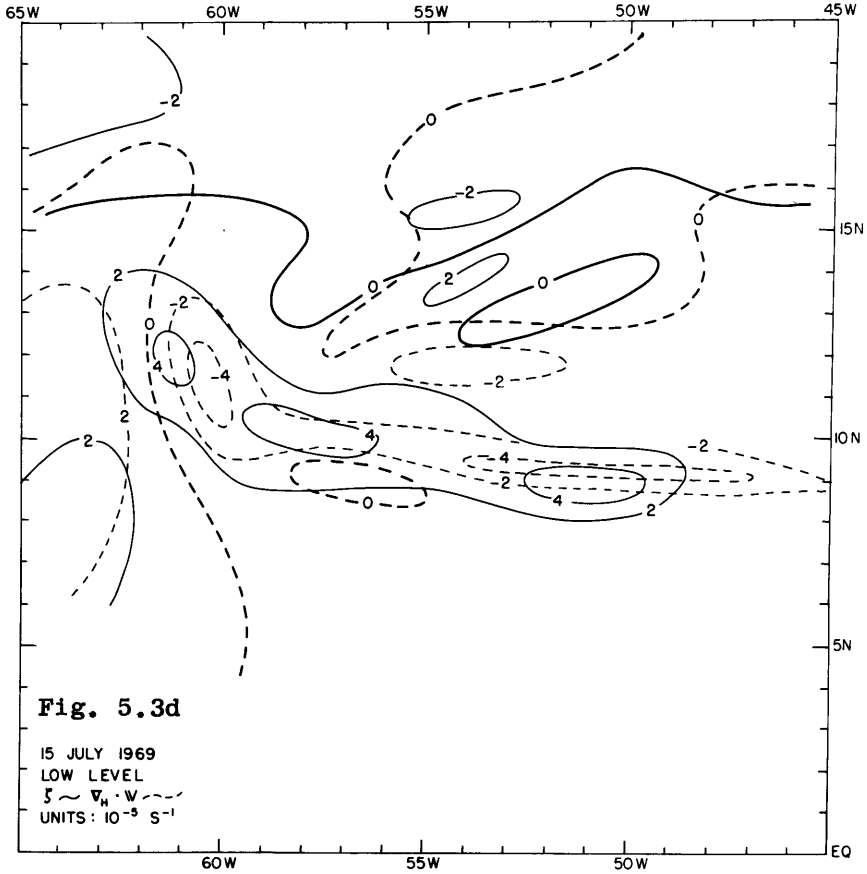

Fig. 5.3d

15 JULY 1969
LOW LEVEL
$\zeta \sim \nabla_H \cdot W$
UNITS: 10^{-5} S^{-1}

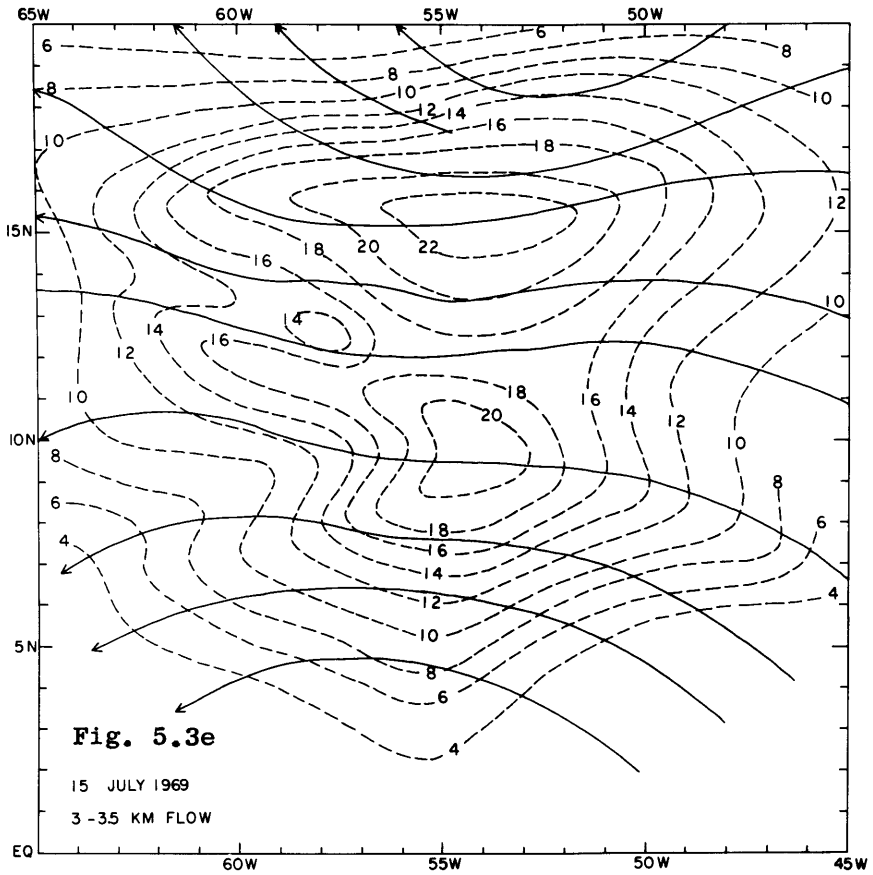
65W
60W
55W
50W
15N
10N
5N
EQ
45W
Fig. 5.3e
15 JULY 1969
3-3.5 KM FLOW

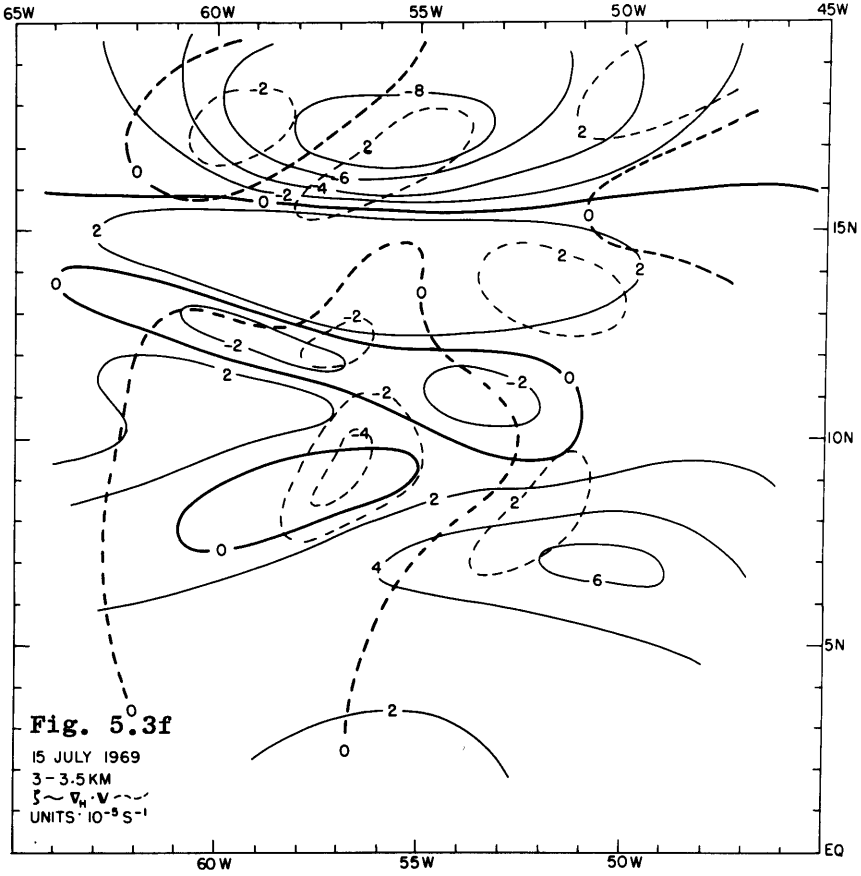
65W
60W
55W
50W
45W
15N
10N
5N
EQ
Fig. 5.3f
15 JULY 1969
3-3.5KM
$\zeta \sim \nabla_H \cdot V$
UNITS: $10^{-5} S^{-1}$

cyclonic over much of the grid, the major zone of significant positive vorticity and convergence is essentially packed into the ITC band and cluster B. It should be noted that this confluence zone could not have been placed without the MSL wind data derived from ATS-III imagery.

The 700mb flow (Fig. 5.3 e,f) is relatively simple as the low and high latitude troughs leave the western edge of the array. The dominant features are the substantial easterly wind maxima near 15° and 10°N. The one to the north is likely due to advection of strong easterlies present on the 14th further to the east. The patch of strong winds at 10°N had little continuity with the 14th and is impossible to find on the 16th. The Mt. Mitchell u-component time-height section (Appendix II) shows the passage of two maxima between 3000-4500m at 15/0600 GMT and at 15/1800 GMT. A similar isotach pattern does not appear at the low level. Since the isotach max occurs directly over the ITC in a band of showers and thundershowers, the ephemeral nature of this feature may be related to vertical exchange of momentum due to large cloud drafts. Both jet maxima are near 4000m with a rapid drop with height above: for example at Rockaway, the 15/12Z winds changed from 105/39k at 16,000 ft. to 060/13K at 20,000 ft. No sound explanation is offered to account for the southernmost wind max; however, the more persistent jet to the north is probably quasi-geostrophically related to the horizontal temperature gradient at the interface between intrusions of dry hot African air and the cooler, more humid maritime air (see Carlson and Prospero, 1971,and Appendix V). These easterly jets are frequently observed to form in a dry baroclinic zone over Africa and they probably represent the source

of Africa wave energy through an instability mechanism not unlike that suggested by Charney and Stern (1962) for an "internal jet" (see Burpee, 1971). However, these jets have apparently not been considered in this context in the Caribbean. It may be that this very narrow jet is quite common during the summer when the Africa waves and their attendent hot air intrusions across the Atlantic every three or four days. In this instance, the Gull Hotel flight reported haze during the entire 700mb leg which is a distinct attribute of the African source region. This type of intensification of the 700mb easterlies may be the cause of what is often termed a "surge in the Trades". The terminology in its classical context is due to Deppermann (see ref. in Riehl, 1954, P. 273), and it formerly represented a dynamic adjustment to pressure rises due to intrusions of extratropical high pressure cells. However, today it seems to be used with any sudden increase in the easterlies.*

As before, there is little structure at 700mb to suggest that the ITC cloud bands were organized by flow above the boundary layer.

5.6.2 Disruption of the ITC, 16-17 July

An arc-shaped band of cumuliform clouds dominated the BOMEX array north of 10°N on the 16th. The leading edge was composed of cumulus congestus ($C_L 2$) at Rainier (17.5°N) followed later by middle cloud at 17/12Z and no shower activity. Further south, the leading edge brought $C_L 2$ and showers to Rockaway, (15.3°N), at 17/05-06Z followed by showers from C_L 3 and $C_L 9$ at 17/12Z and 17/18Z with middle

* Dr. R.L. Burpee, NHRL and G.D. Atkinson, Hq. Air Weather Service, personal communications .

cloud beginning at 17/12Z. ESSA-9 reveals that only a disorganized patch of cumuliform clouds can be found south of the system and north of 9°N. Remnants of the ITC from the 15th may still exist near 10°N but this is speculative. The integrity of the arc-shaped band and the destruction of the ITC were clearly established in ATS-III pictures on 15 July; the disruption extended east of 47°W to a bright cloud mass off the coast of Africa. It is difficult to find this specific system earlier than the 15th; however, haze was reported by the Gull Hotel flights on 16 and 17 July on both sides of the cloud band meaning it may have been triggered over the African continent. Evidence against this hypothesis also exists in that there is only a very minor suggestion of a 700mb wave on the 16th and the strong surface winds (17-24 knots at Rainier and Rockaway on the 17th) suggest that formation and maintenance were somehow related to the low level flow.

The 17th is very interesting because of: the appearance of a 700mb wave near 56°W where nearly unperturbed flow was present on the 16th; the breakup of the easterly jet into two distinct maxima with a minimum in the wave trough; and a rapid intensification of the arc-cloud convective system in the vicinity of 60°W. Also, it is clear that the ITC has not yet returned except perhaps near 10°N east of 50°W.

The 700mb wave deserves special attention even though it is not directly relevant to the present thesis. Fernandez-Partagas and Estoque (1970)(hereafter referred to as FPE) in their preliminary BOMEX work correctly analyze this feature at the 8000 foot level and term it a weakening disturbance. They also state that no attempt was made to trace its early history. In addition, it is not found in their low

level or 20,000 foot analyses (although it shows up in my low level streamlines as a weak perturbation). Thus, this wave either formed in situ or advected into the array at about 30 knots which is twice the normal wave speed and twice the speed of the disturbance that moved through the array. By 18Z on the 18th, a wave axis may be found west of 65°W in my 700mb analysis (Fig. 5.6 f) which is again consistent with the FPE depiction. We might conclude that whether or not the wave on the 17th formed in situ, it appears to have left the array at about 30 knots. FPE offer a different interpretation which is that the wave of the 17th decayed and a new one formed from above on the 18th near 65°W. This is supported by their 20,000 ft analyses on the 17th and 18th which show a slow moving trough already established west of 60°W at this higher level. Time series of island winds are inconclusive because they can be made to fit both interpretations. Raizet, the only northerly station with 12-hourly observations, slightly favors FPE's theory. They get a 700mb wind shift from 087/17 m/s to 097/17 m/s between 17/12Z and 18/00Z which is 6-12 hours too early. My wave would have passed them at 18/06Z. However, between 18/00Z and 18/12Z there is a massive shift from 097/17 m/s to 147/8 m/s which contributes to the confusion.

Because a 30 knot wave speed is the least acceptable piece of evidence, this author suggest that the 700mb wave on the 17th formed in situ as a moderate perturbation on the easterly jet and disappeared within a few hours after 17/18Z.

On the 17th, the leading edge of the arc cloud at 15°N is at 62°W. On the 16th, the arc cloud intersected 15°N at 56°W thus implying

a speed of 15 knots. Since this system could also be seen in ATS-III imagery on the 15th near 50°W at 15°N it is clear that the cloud blow-up on the 17th was an intensification of a travelling disturbance that most likely has an African history.

16 July 1969: Figs. 5.4 a-f

At low levels (Fig. 5.4 c,d) confluent flow is nearly compensated by speed divergence, especially south of the cloud arc. Data shortcoming make the entire divergence pattern quite suspect. The more reliable 500m vorticity pattern supports the position of the cloud arc, but the divergence field is distinctly out of phase. At 10°N, where the ITC would normally lie. there is a broad region of weak cyclonic vorticity. If the CISK mechanism plays a role in the formation of the ITC, then the regeneration of the convergence zone and associated cloud bands should occur sequentially in this zone of cyclonic vorticity.

The dominant 700mb feature on the 16th (Figs. 5.4 e,f) is a nearly unperturbed easterly jet. The travelling disturbance is not associated with a wave on the 16th. To the south, the flow becomes more southerly, and, in direction and speed, looks quite similar to the flow at low levels. The winds at Kourou, Fr. Guiana have a southeast orientation to 300mb. At Oceanographer, the 17/00Z are southeast to at least 500mb. The latter data were from Oceanographer's teletype message because the A_o winds looked bad. Presumably, the shipboard observer knew a means of correcting this since the message winds made sense and were consistent with Kourou to the south. In other words, south of 10°N there is a gentle drift of air to the north

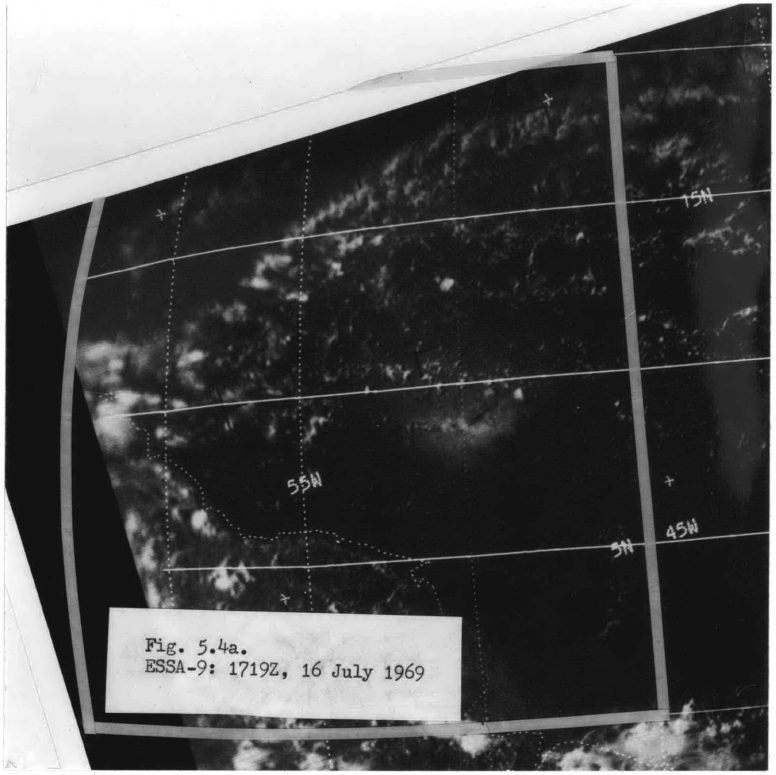

Fig. 5.4a.
ESSA-9: 1719Z, 16 July 1969

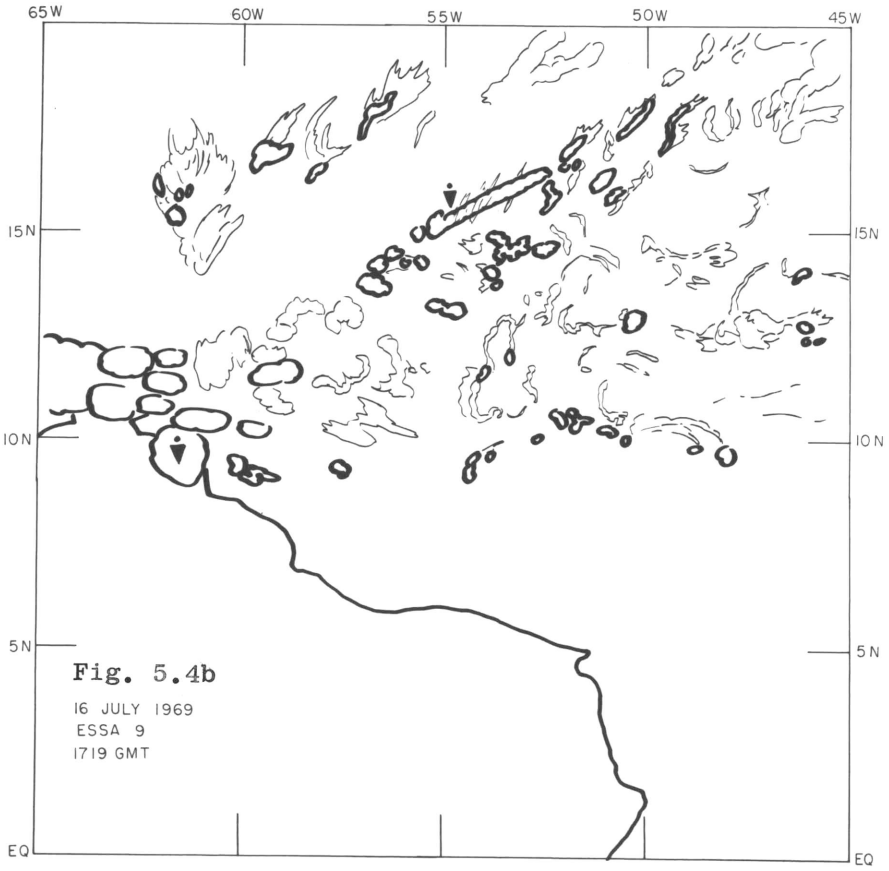

Fig. 5.4b
16 JULY 1969
ESSA 9
1719 GMT

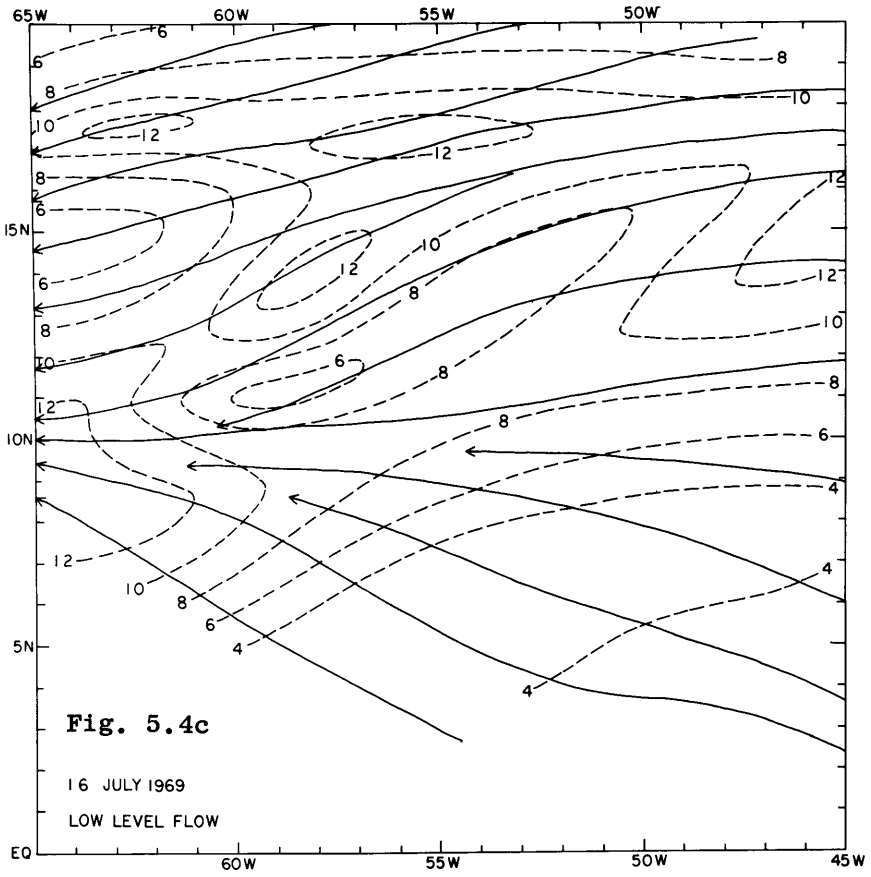

Fig. 5.4c

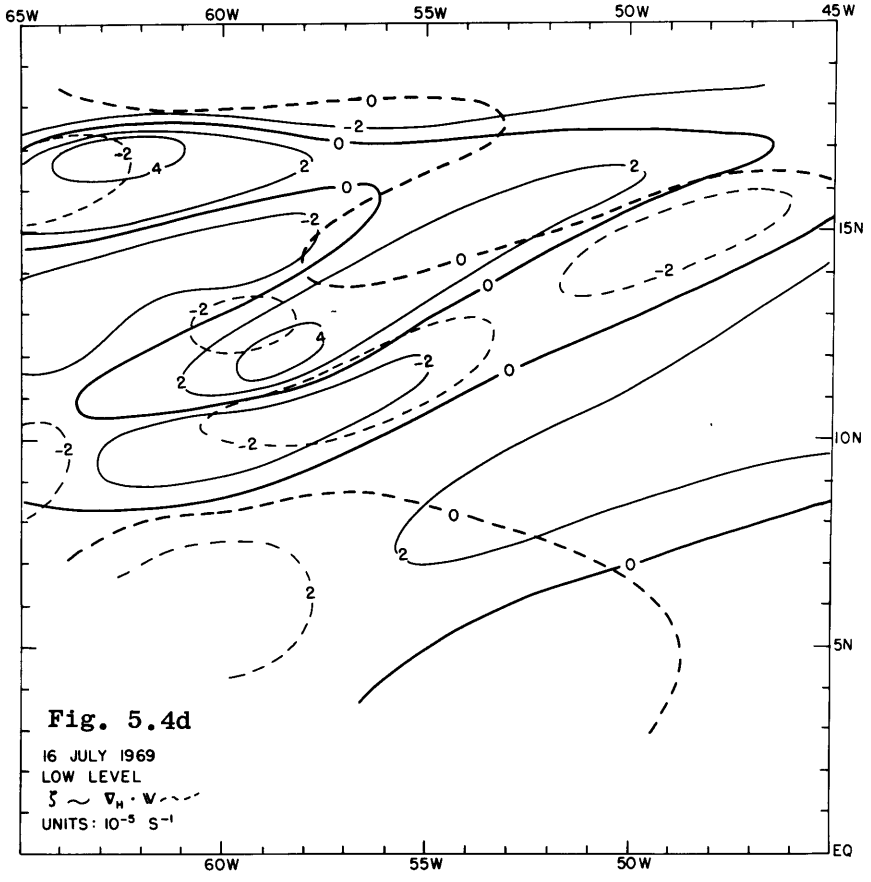

Fig. 5.4d

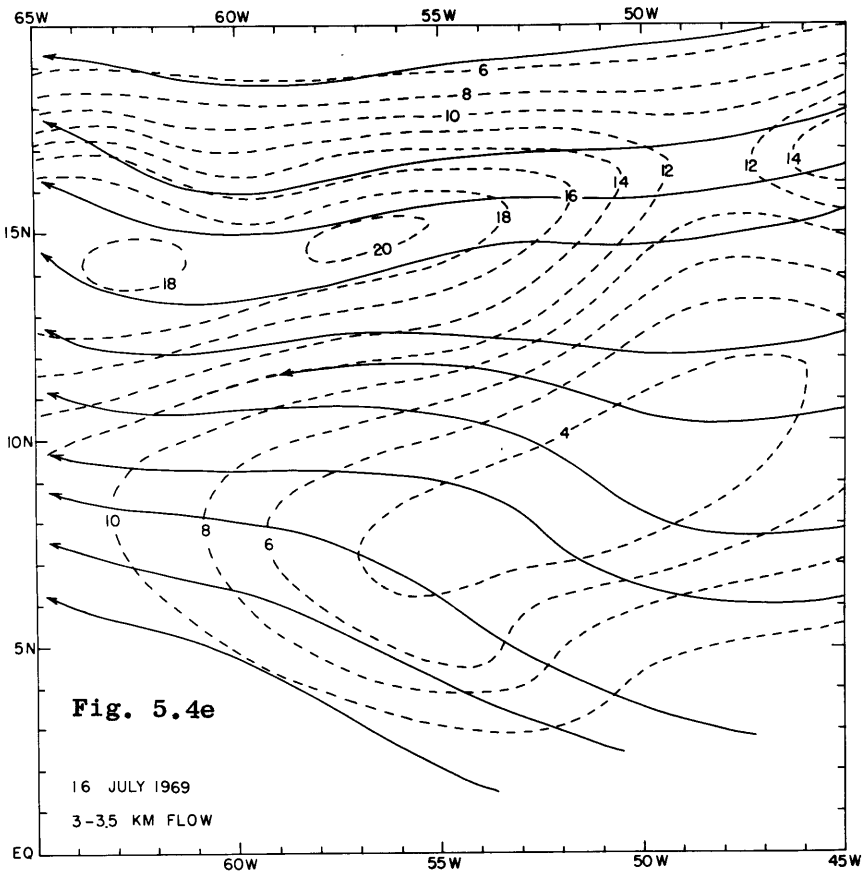

Fig. 5.4e

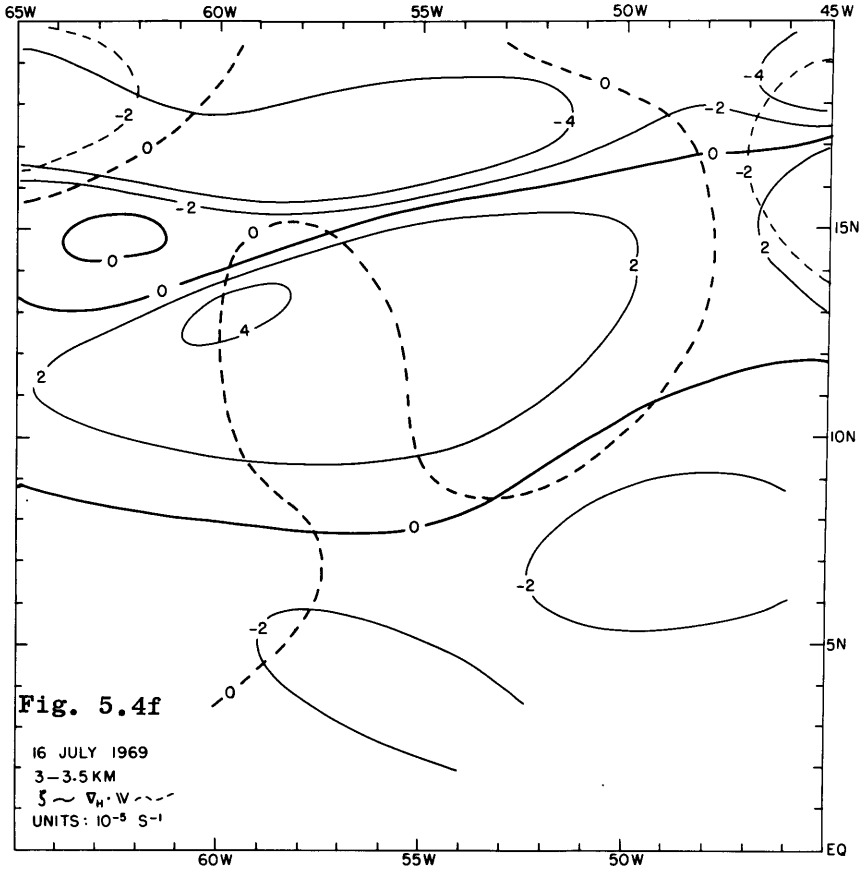

Fig. 5.4f

through a fairly deep layer. North of 10°N on the 16th, the 700mb flow is virtually zonal; since the 500m winds are ENE, there is a veering with height in the region. Thus this particular day displays both of the "stratified regimes" described statistically in the previous chapter and is noteworthy because no distinct ITC begins to show up until 17 July.

17 July 1969: Figs. 5.5 a-f

In Figs. 5.5 c,d a minor 500m trough reflecting the system at 700mb lies to the east of the major cloud system which is in a distinct,well correlated region of low level cyclonic vorticity ($\sim 4 \times 10^{-5}\ s^{-1}$) and convergence ($\sim -4 \times 10^{-5}\ s^{-1}$). The clearing south and east of the system north of 10°N is partly in a region of divergence, but the vorticity is cyclonic due to shear which is only partially compensated by diffluent ridging in the stream lines. The bulk of the convective cloudiness can be supported by the following hypothesis: This disturbance was accompanied by an easterly jet which could be seen on both 16 and 17 July. The jet was also reflected at low levels on these days and the dominant clouds were found in a cyclonic vorticity maximum induced by horizontal shear south of the jet. Frictionally induced convergence in the positive vorticity field became better organized on the 17th and allowed the storm to tap the high moisture content in the boundary layer which would account for the rapid increase in cloud content. Further intensification may have been supported by the upper level trough under which the storm moved on the 18th as noted in FPE.

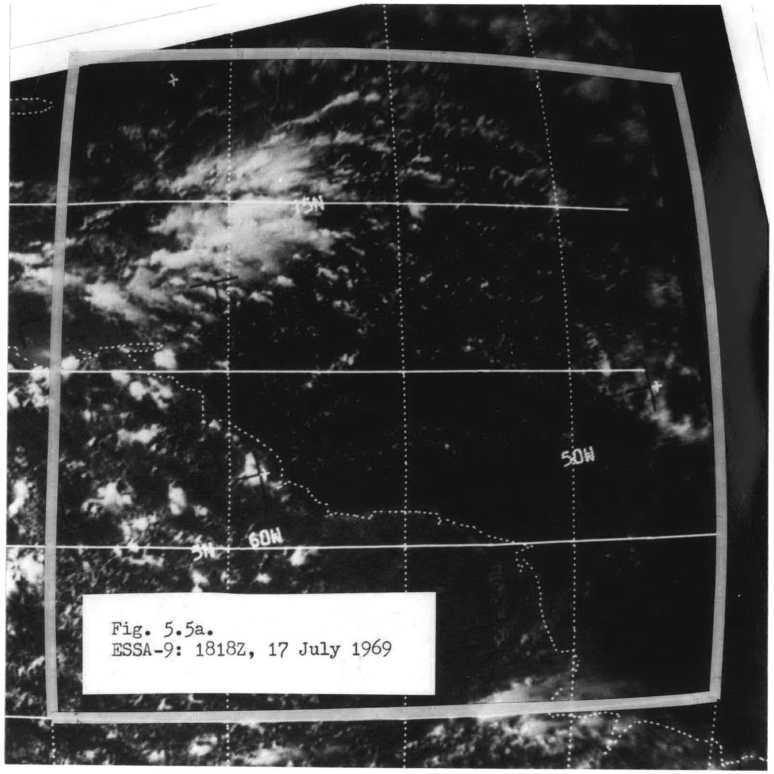

Fig. 5.5a.
ESSA-9: 1818Z, 17 July 1969

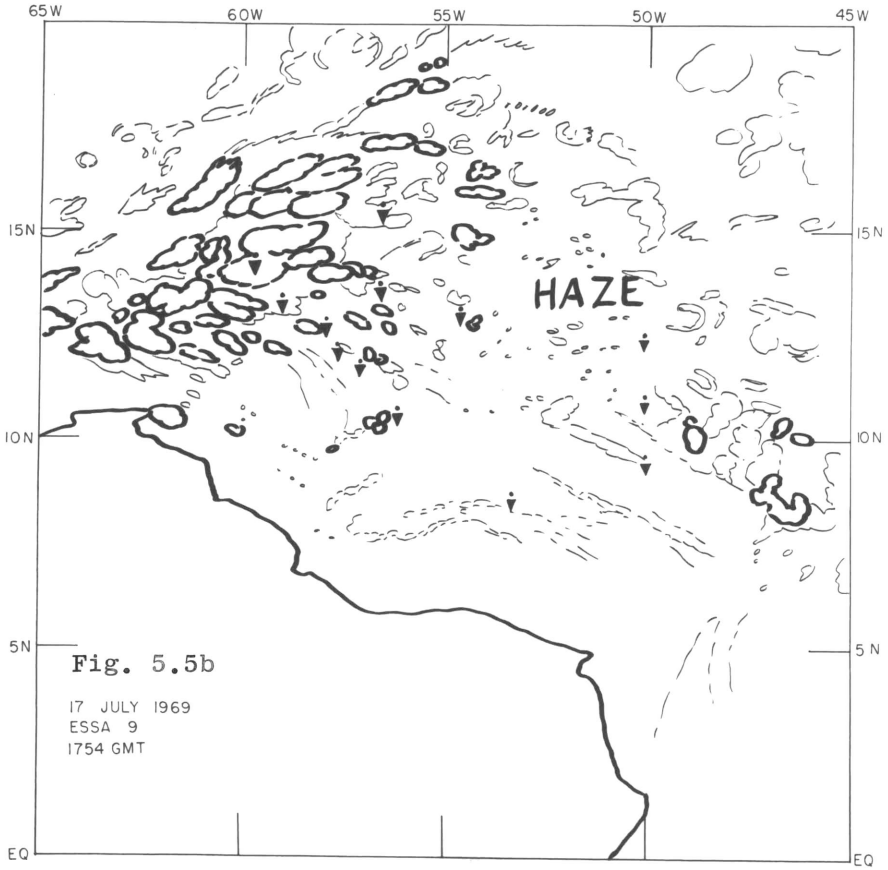

Fig. 5.5b

17 JULY 1969
ESSA 9
1754 GMT

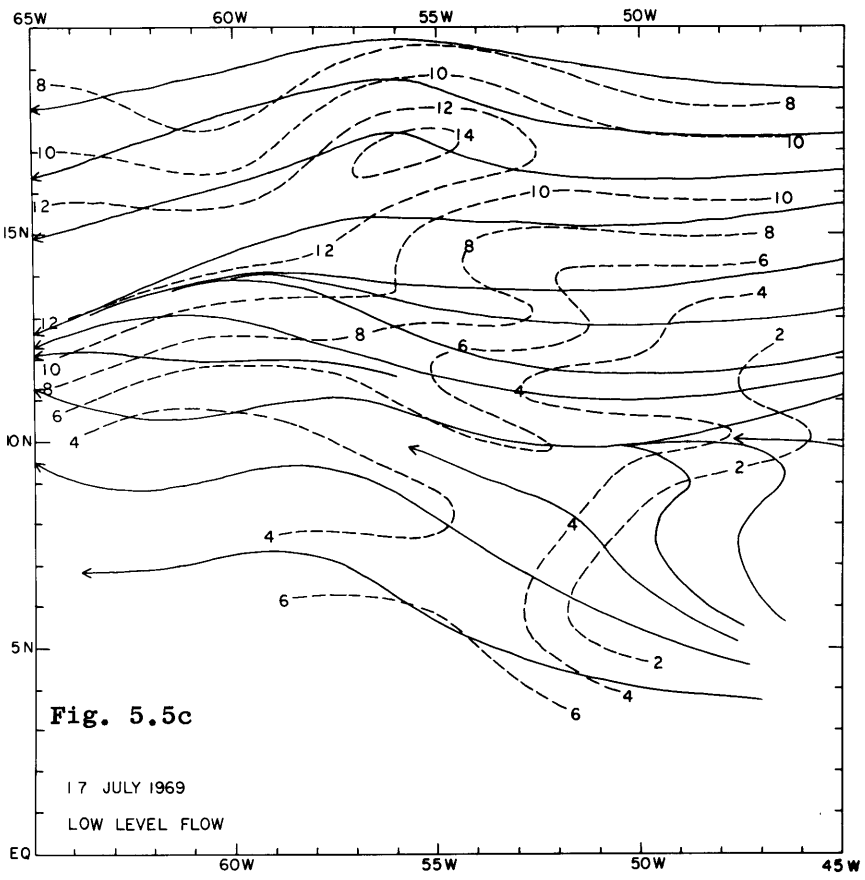

Fig. 5.5c

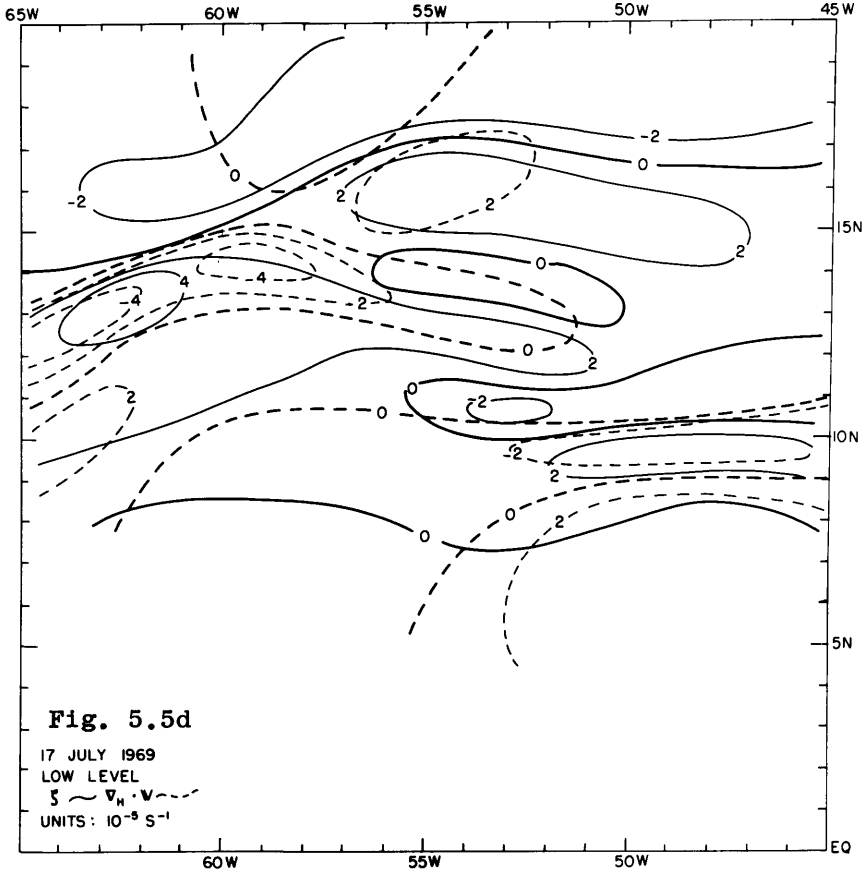

Fig. 5.5d

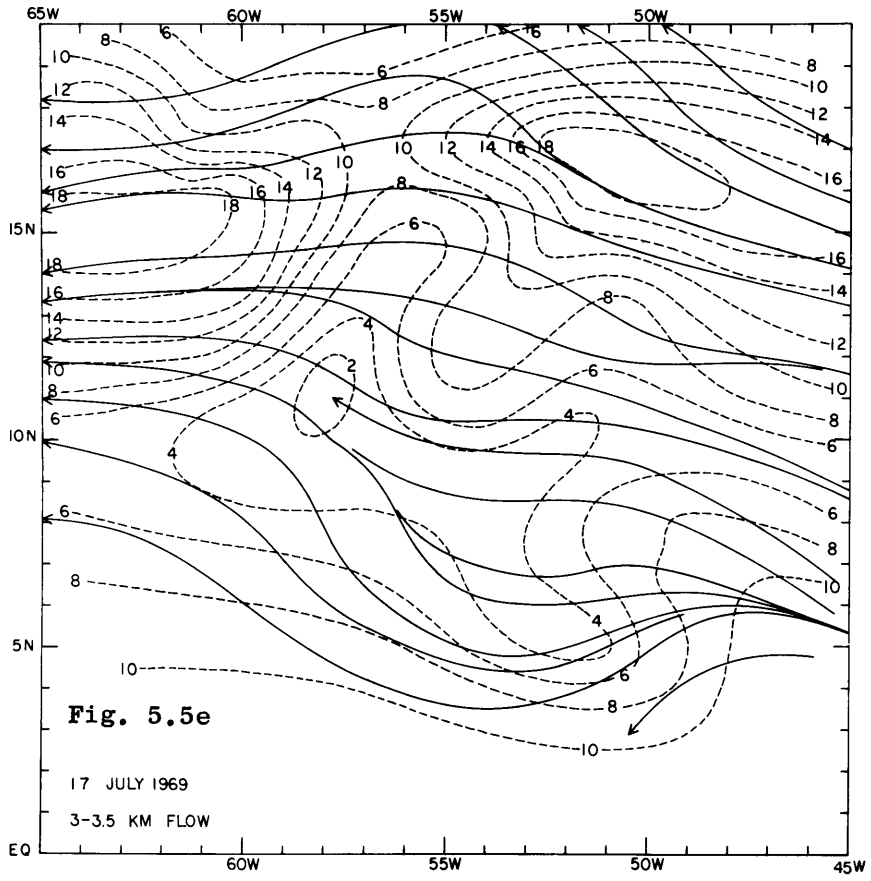

Fig. 5.5e

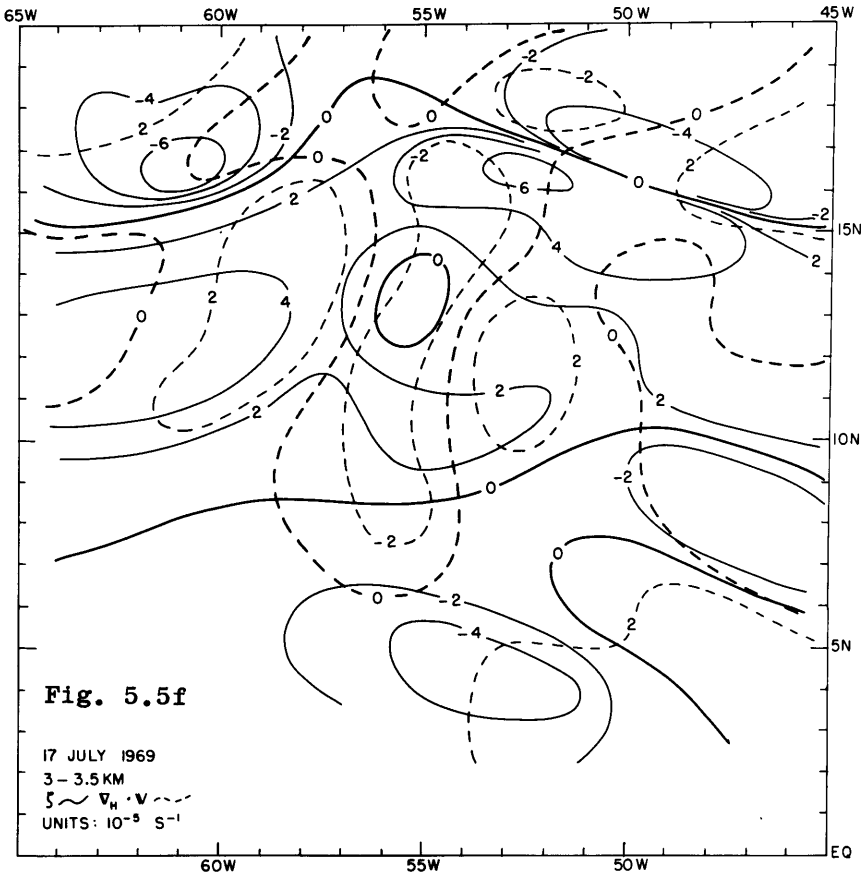

Fig. 5.5f

The shape of the cloud bands or streaks as well as the vorticity maximum resemble the "Inverted V" cloud patterns described by Frank (1969). This is a subsynoptic mass of convective clouds with dimensions on the order of 300 x 600km; thus it fits into the class of disturbances related to the CISK hypothesis.

There was widely distributed shower activity reported on the WC-121 RECCO reports (see symbols on the satellite depiction Fig. 5.5 b). Although Mt. Mitchell at 17/18Z and Discoverer at 17/15Z reported $C_L 9$ (cumulonimbus cappilatus), the WC-121 and WC-130 reported tops to a maximum of only 15,000 feet and $C_L 3$ as the principal shower cloud. The shower clouds near the two ships were both visible on ESSA-9 as isolated bright targets so there may have been a few unorganized $C_L 9$ in the generally open area to the rear of the storm.

Note the narrow streak of cyclonic vorticity and convergence along 10°N forming in a confluence of weak southerly flow and stronger trades to the north. RECCO reports along 50°W show that the cloud population in this streak has tops below 10,000 feet even in showers. East of 49°W there are brighter clouds which may be Cb's but west of 49°W, the convergence appears in the motion field without the support of a well organized thermo dynamic forcing. The evolution of the ITC over the next few days can be traced to this weak feature on the 17th.

The 700 mb flow (Figs. 5.5 e,f) is characterized by the wave perturbation already discussed. Across the map there are a series of alternating convergence and divergence patches which are not particularly correlated to either the vorticity or cloud fields. There is no sign of the weak convergence zone near 10°N that is observed in

the boundary layer. As on the 16th, the low level flow tends to undercut the 700mb flow (winds veer with height) north of 10°N. East of 58°W and north of 5°N, winds at both levels show a weak drift toward the north.

Comments on the Breakup of the ITC

ATS-III photos showed that the arc cloud and attendant disruption of the ITC were initially obvious on 15 July east of the BOMEX grid, therefore it is difficult to determine the real cause of the rapid decay. The decay and virtual disappearance of the ITC on 16 and 17 July occurred as the arc cloud system entered the array; thus, this was an advective phenomenon moving at essentially the speed of the disturbance to the north. On the 16th there was low level cyclonic vorticity behind the disturbance but it did not show signs of correlation with convergence in the boundary layer near 10°N until the 17th.

The air south of 10°N was unusually dry above 2km and the assertion that this air was subsiding, at least below 3km can be defended by studying the moisture and temperature time sections at Oceanographer and its divergent environment on the 17th.

Because Discoverer and Mt. Mitchell did not show extreme dryness aloft, the dry air at Oceanographer probably came from the south as part of a temporary northward migration of the equatorial dry zone.

5.6.3 Regeneration of the ITC, 18-20 July

This period is characterized by the rapid development of a low level convergence zone near 11°N and the growth of ITC cloud bands in the regions of maximum positive vorticity and convergence. Continuity

from the 17th shows that the motion field was becoming organized at least simultaneously with and possibly ahead of the principal cloud lines. On the 19th we will see the appearance of a meso-scale vortex which can then be followed westward as a member of the ITC, although it appears to weaken to a cusp stage on the 20th and 21st.

At the 700mb level another wave passes through the BOMEX array accompanied by a weakening easterly jet.

18 July 1969: Figs. 5.6 a-f

The 500mb level (Figs. 5.6 c,d) clearly shows a major confluence axis curving across the grid from 12.5°N, 60°W to 11°N, 45°W which is also an axis of positive vorticity. In contrast to the 17th, there are distinct bright cloud lines beginning to form from the chaotic distribution of the previous day. The line from A to A' in Fig. 5.6b is in the main confluence zone and appears to be composed of young cumulus or Cb's since there is so little evidence of widespread anvil development. Except for the diffuse region near 50°W, the northern line forms the southern border of a clear swath about three degrees wide which probably indicates subsidence and is indeed in a region of weak anticyclonic vorticity at 500m. By the 19th, this zone is even better defined (Figs. 5.7 a,b). To the south, bands B and C are poorly correlated with the wind field, but by the 19th, band C is gone, which is consistent with its lack of support.

The strong convergence pocket near 12°N, 56°W contains few clouds; however, on the 19th (Figs. 5.7 a,b) there is a new blowup of cirrus debris about 5-6 degrees to the west which might reflect Cb development in this pocket after westward advection at a typical

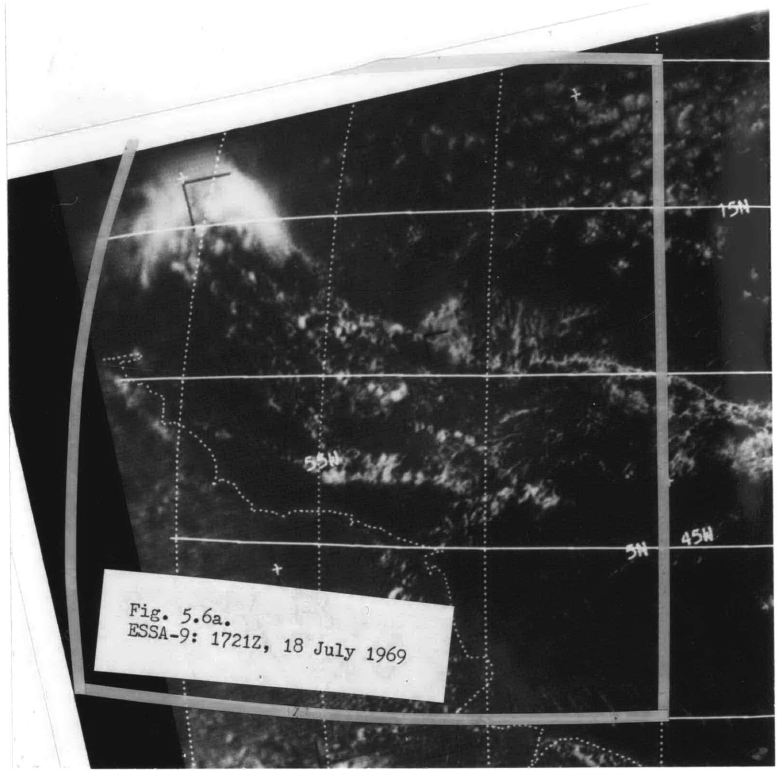

Fig. 5.6a.
ESSA-9: 1721Z, 18 July 1969

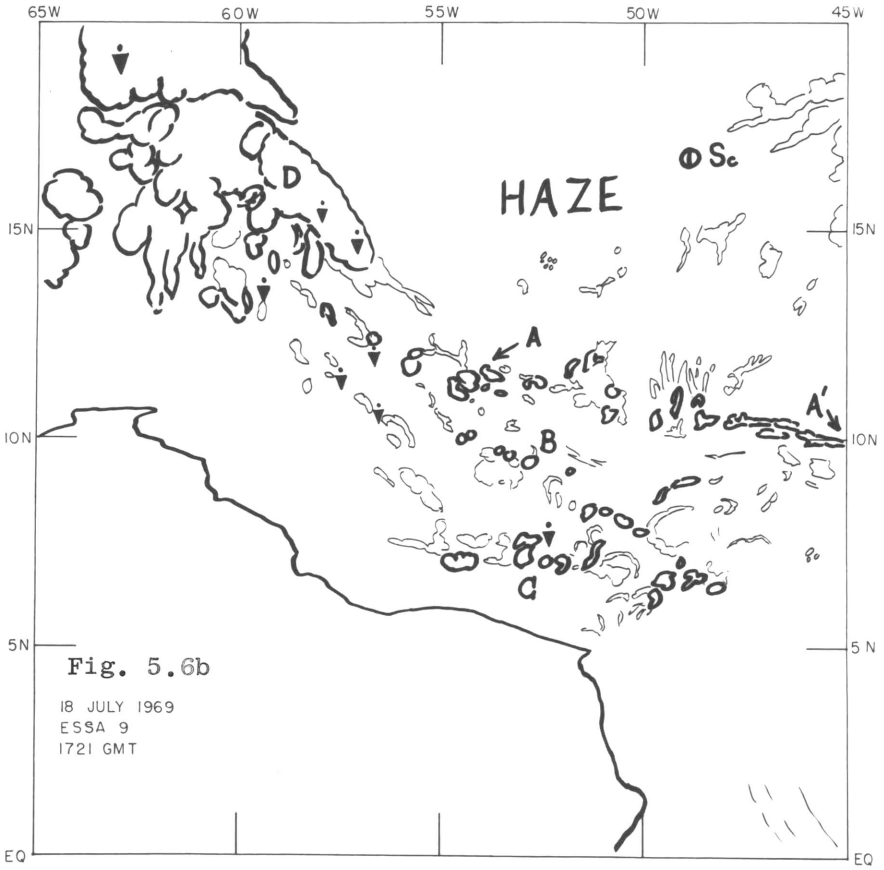

Fig. 5.6b

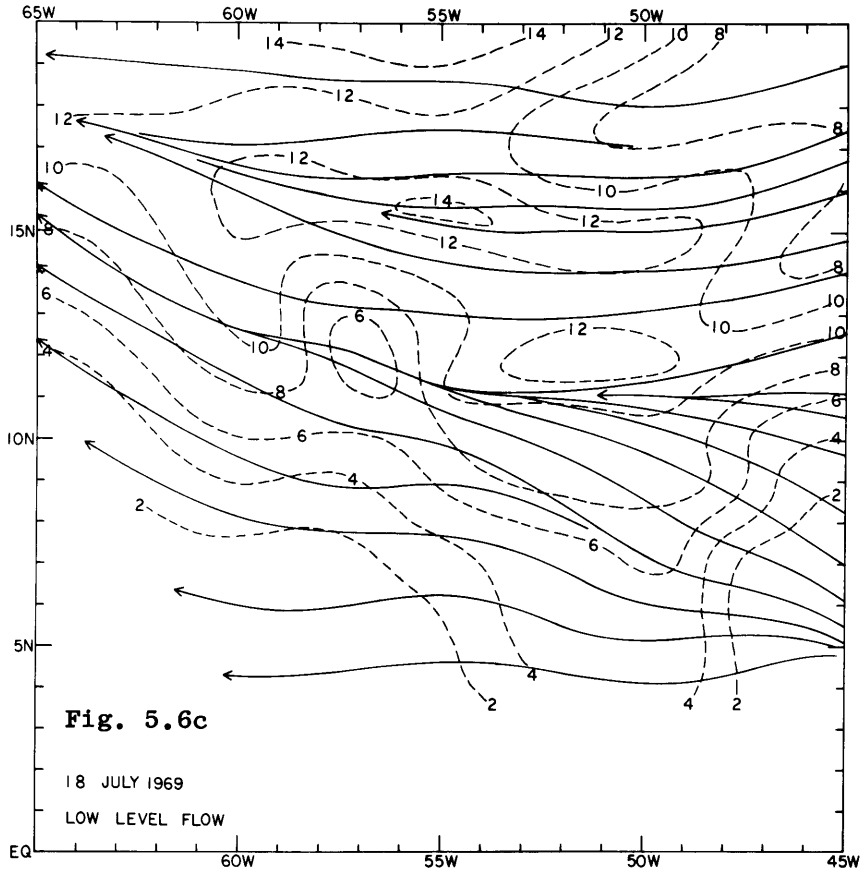

Fig. 5.6c

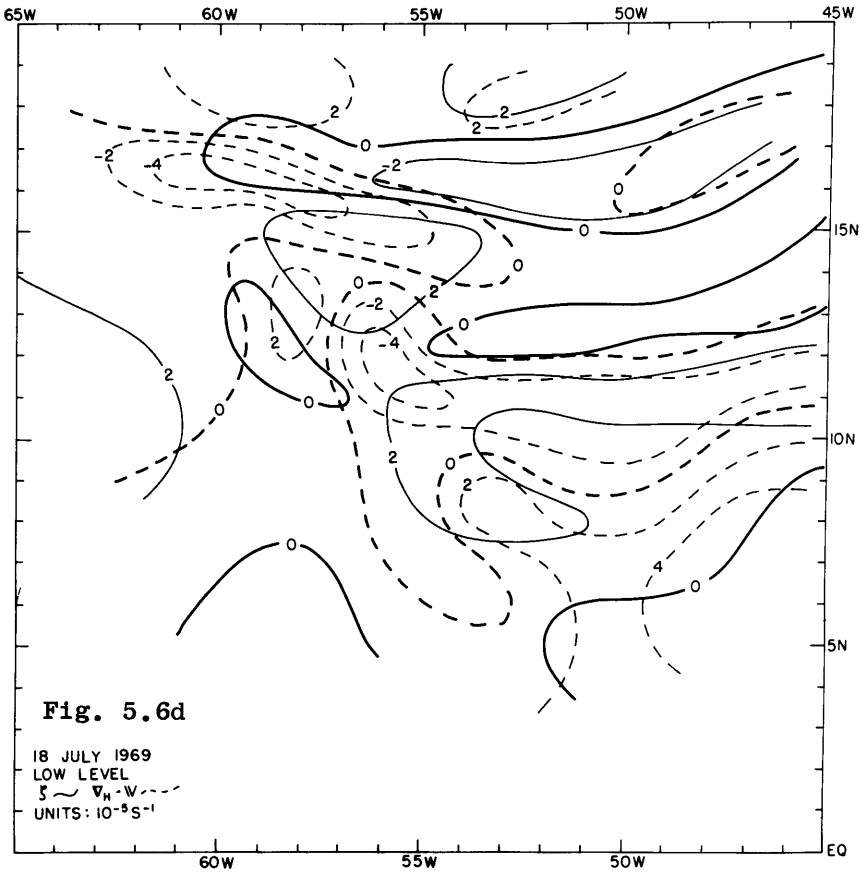

Fig. 5.6d

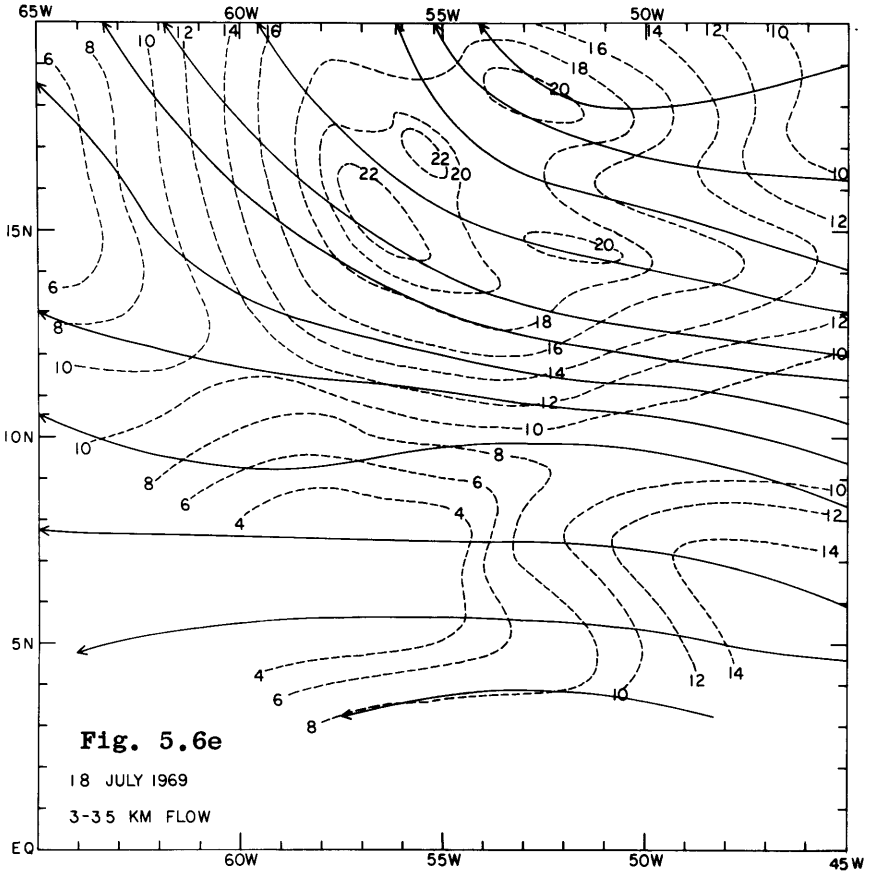
65W
60W
55W
50W
15N
10N
5N
EQ
45W
Fig. 5.6e
18 JULY 1969
3-35 KM FLOW

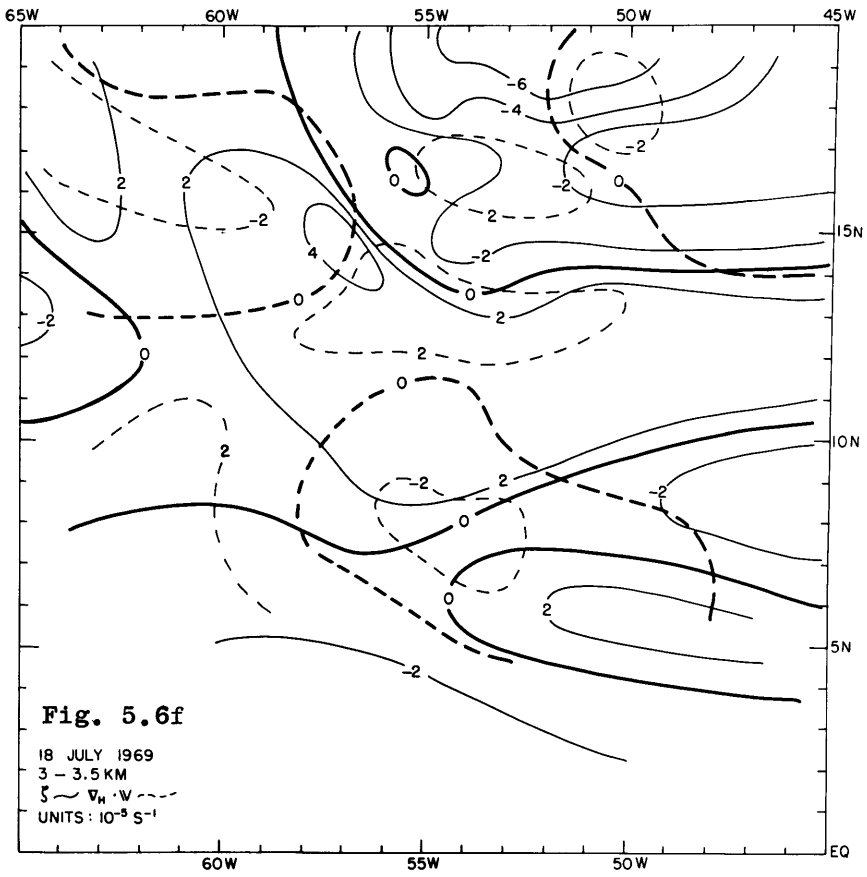
65W
60W
55W
50W
45W
15N
10N
5N
EQ
Fig. 5.6f
18 JULY 1969
3 - 3.5 KM
UNITS : 10^{-5} S^{-1}

speed of about 15 knots.

The low level convergence near 16°N, 60°W strongly supports a bright portion of the travelling disturbance at D which is leaving the BOMEX grid. This can also be seen as a confluence in the streamlines in Fig. 5.6c.

In the 700mb flow (Figs. 5.6 e,f) the dominant feature is the loosely organized easterly jet on the back side of the departing wave trough. Cloud bands B and C and the disturbance D are in broad convergence areas, but the main band A-A' is not.

The flow generally veers with height north of the ITC bands and backs with height south of the main bands near 11°N, which is consistent with the stratified composites of the previous chapter.

19 and 20 July 1969: Figs. 5.7 and 8, a-f

During this period we observe the consolidation of a single, well-developed band of ITC cloud lines along 10°N. On the 19th the low level confluence axis is more clearly defined due to the considerable veering with time of the flow south of 10°N. The persistent cloud band A (Figs. 5.7 a,b) still appears young due to the lack of cirrus blowoff and the clear strip just north of the ITC is especially well defined on the 19th. The closed vortex at B is supported by WC-121 winds, and RECCO reports showed this region to contain many layers of cloud and considerable showers out of Cb's with tops to 30,000 ft.

Cloud band A and the cluster at B are in intense regions of positive vorticity and convergence at 500m (Figs. 5.7 c,d) while at 700mb the support is virtually non-existent (Figs. 5.7 e,f).

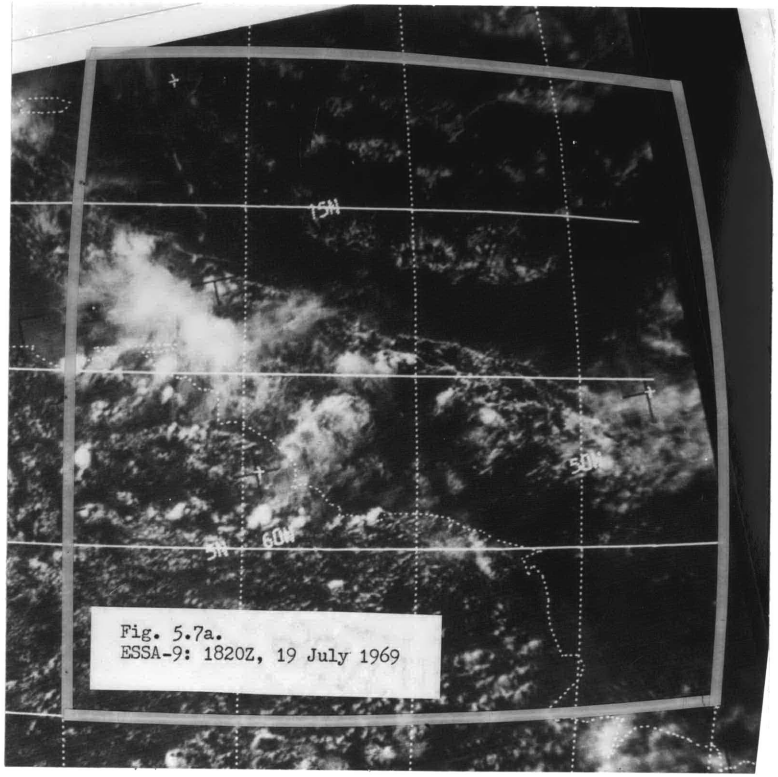

Fig. 5.7a.
ESSA-9: 1820Z, 19 July 1969

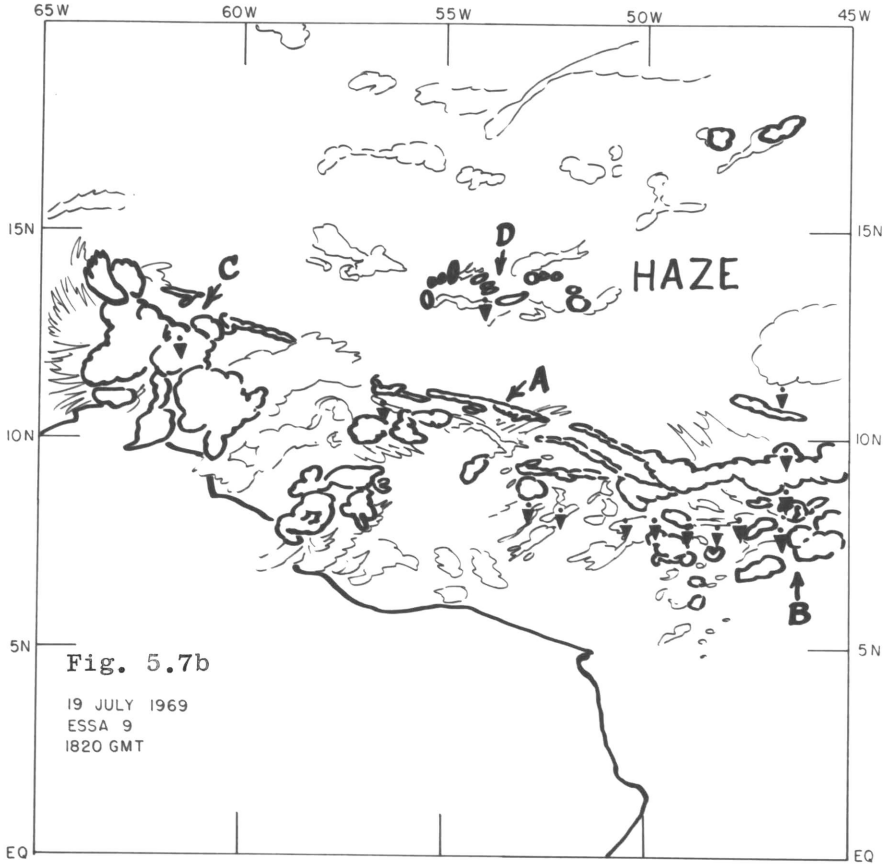

Fig. 5.7b

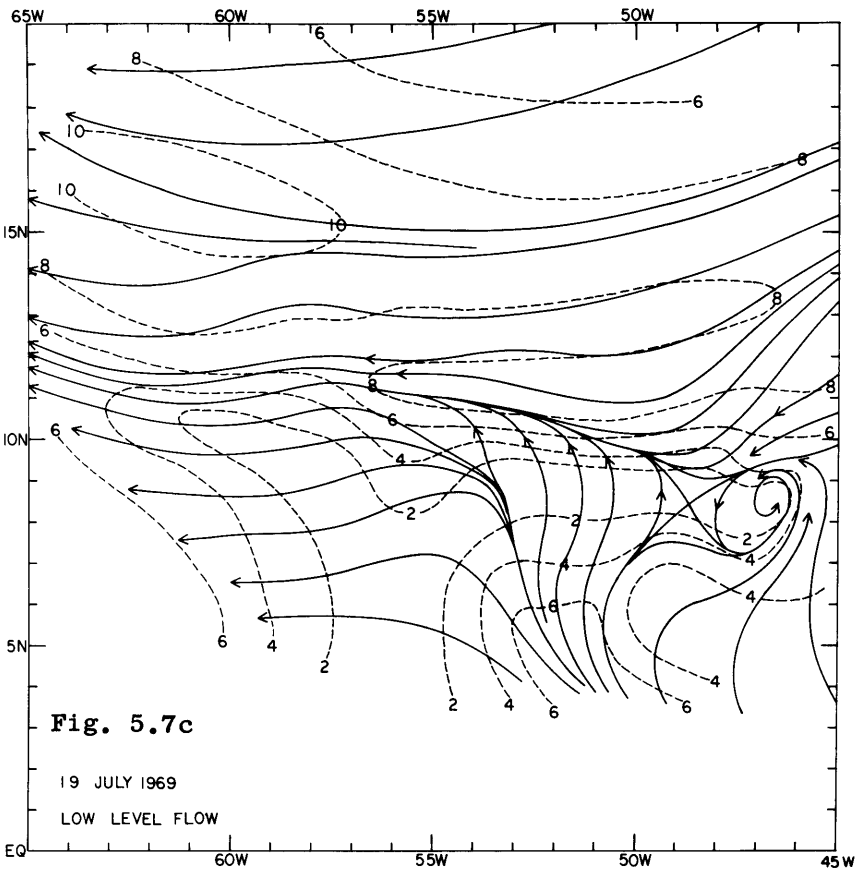
65W
60W
55W
50W
15N
10N
5N
EQ
45W
Fig. 5.7c
19 JULY 1969
LOW LEVEL FLOW

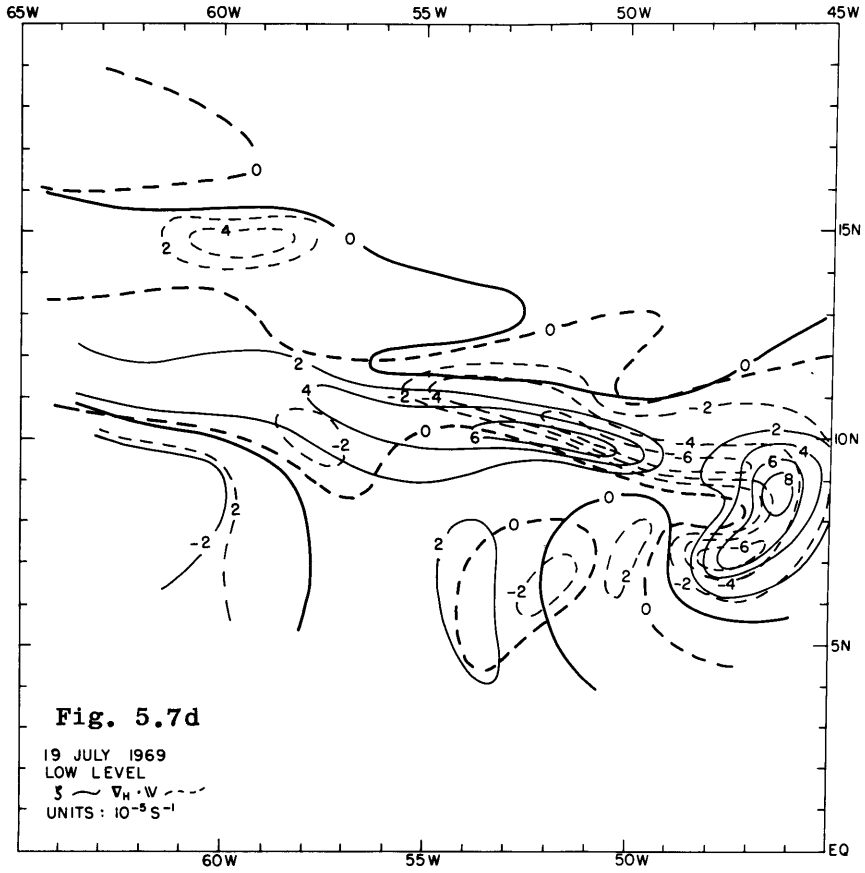
65W
60W
55 W
50W
45W
15N
10N
5N
EQ
Fig. 5.7d
19 JULY 1969
LOW LEVEL
UNITS : $10^{-5} S^{-1}$

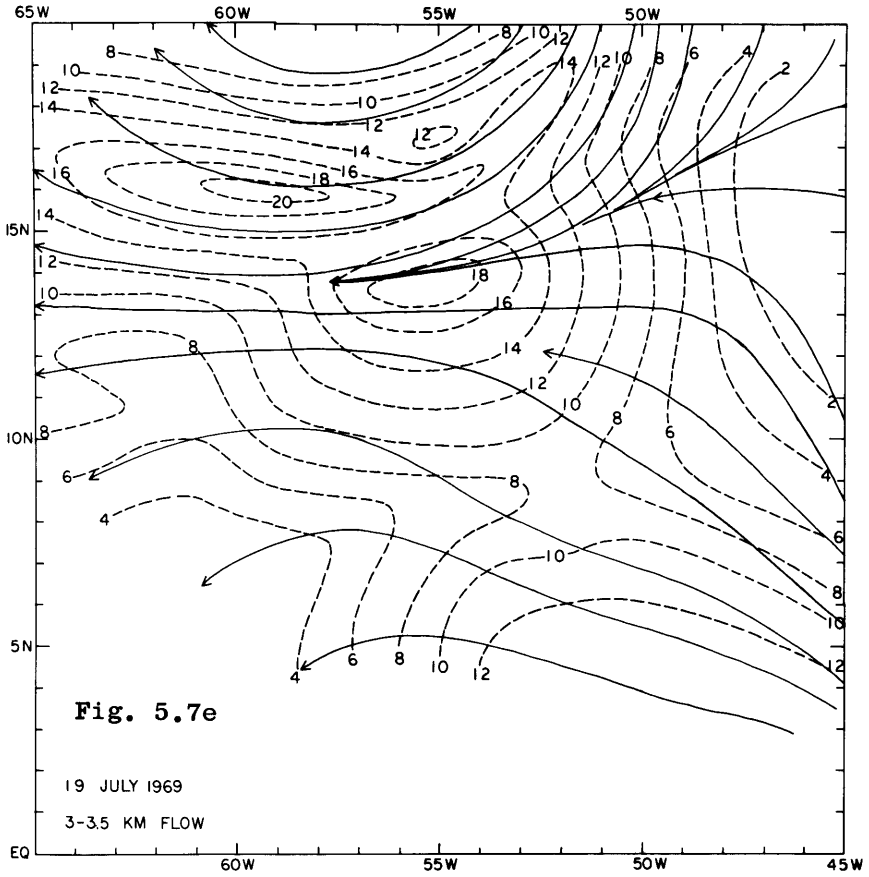

Fig. 5.7e

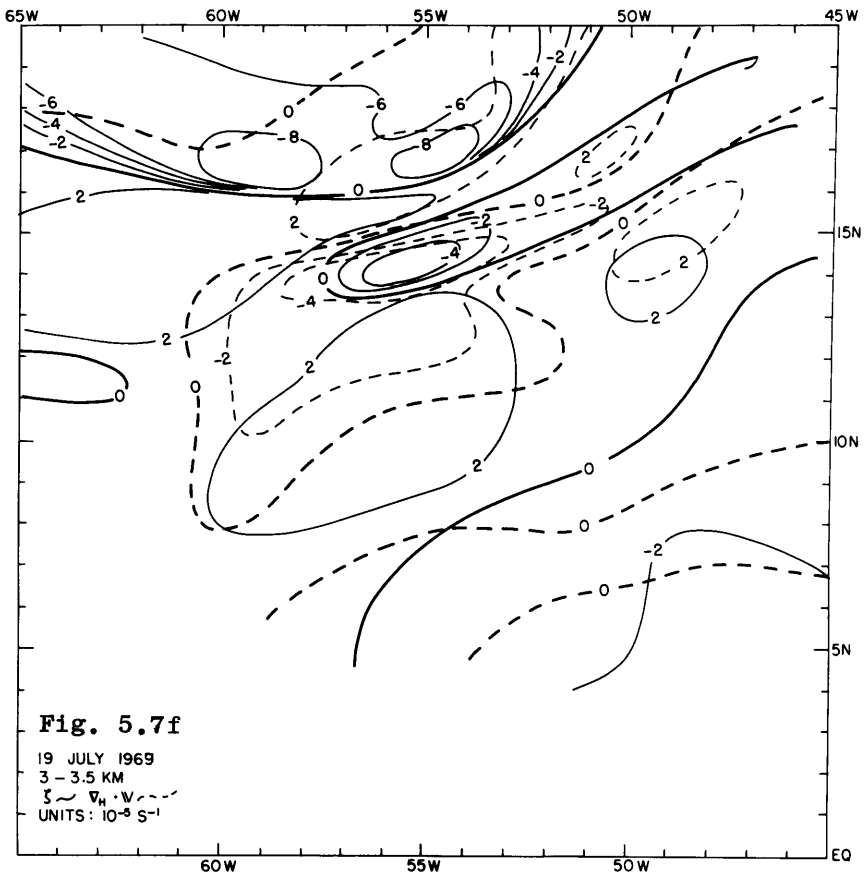

Fig. 5.7f

Since cloud band A became organized on the 18th, the 500m vorticity and convergence values increased by a factor of 3 mainly due to the directional veering in the southern regime wind field. This wind structure is possibly the lower branch of a direct circulation in the vertical induced by the release of latent heat in the cloud line.

Cloud cluster C formed between 18/1800 GMT and 19/1800 GMT and only has weak support on the 19th. Significantly, this cluster is gone by the 20th.

At 700mb on the 19th (Figs. 5.7 e,f), the dominant feature is the appearance of another wave at the eastern edge of the grid. Also, the easterly jet is sharply defined and north of its axis the relative vorticity approaches -8×10^{-5} which means that the absolute vorticity is $\sim -4 \times 10^{-5}$. This type of situation can be unstable and is further discussed in Appendix V. The 700mb convergence zone with a divergence minimum of $-4 \times 10^{-5}\ s^{-1}$ is essentially unrelated to significant cloudiness except for the showers at D. The latter were observed as $C_L 9$ at Discoverer at 19/2100 Z. But essentially the 700mb convergence is decoupled from the moist layer below.

By the 20th, the low level confluence zone is no longer dominant (Figs. 5.8 c,d). Evidence for a closed vortex was lacking in the wind data but a strong trough and cusp formed satisfactory continuity with the 19th. The cumulus band has thickened and many anvils are evident (Figs. 5.8 a,b). The intense kinematical features are north of the cusp and correlate quite well with the ITC. Although the cells are well developed on the 20th, the ITC's continuity is decaying as will be seen on the 21st. The clear air north of the cloud band is well

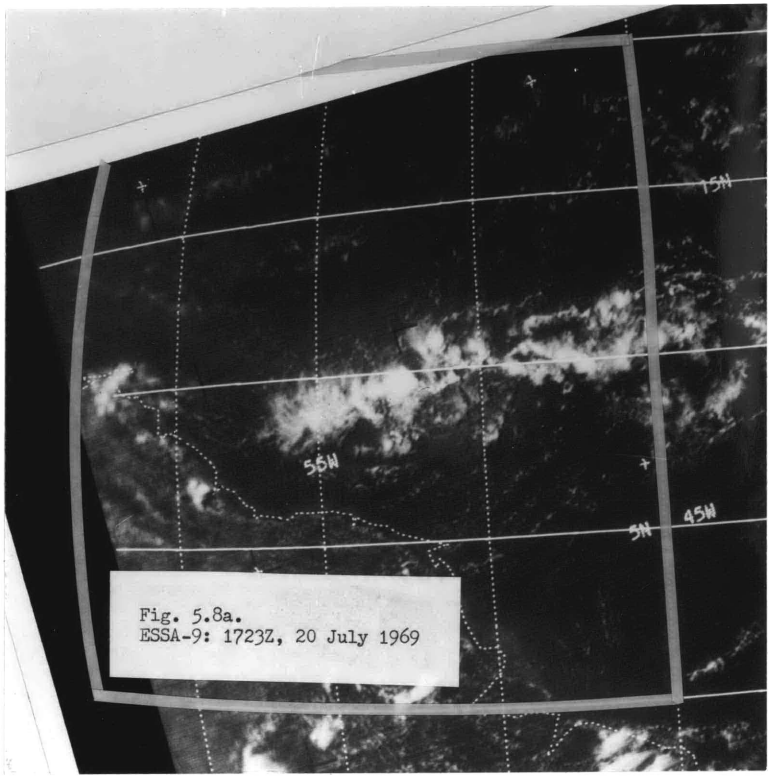

Fig. 5.8a.
ESSA-9: 1723Z, 20 July 1969

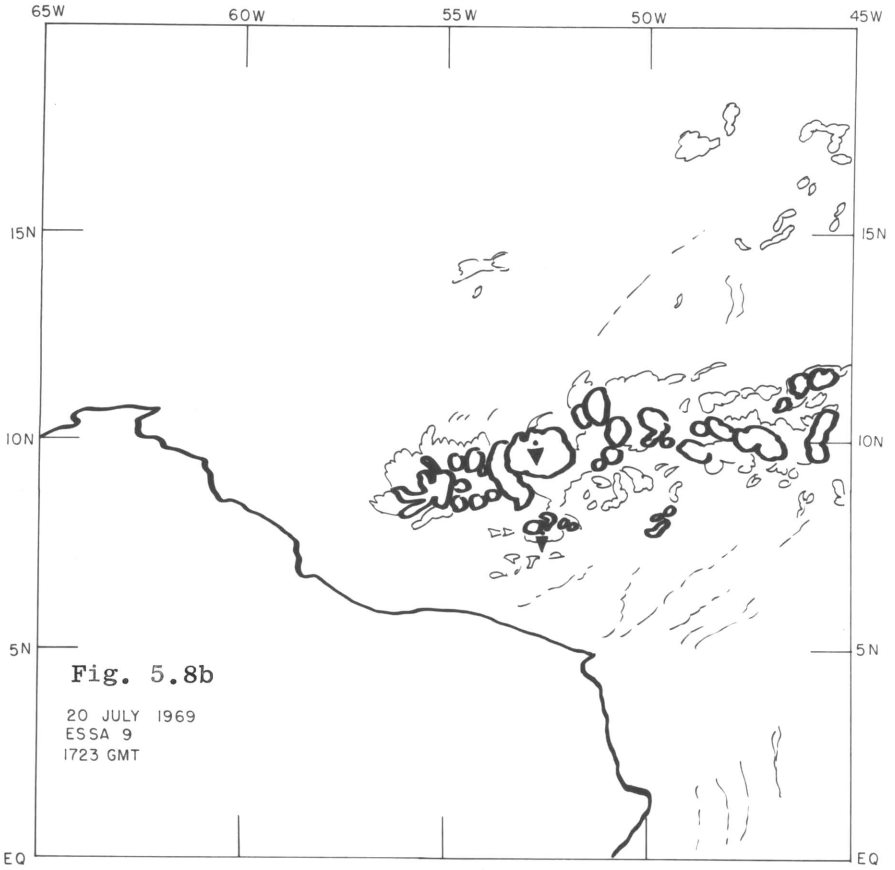

Fig. 5.8b

20 JULY 1969
ESSA 9
1723 GMT

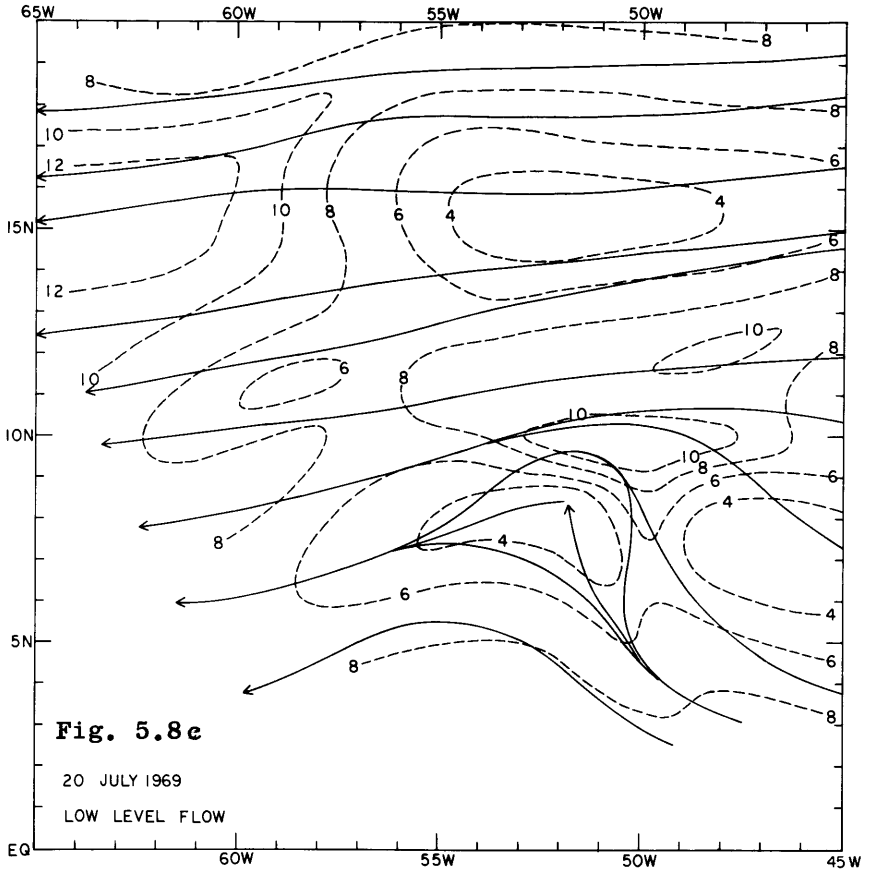

Fig. 5.8c

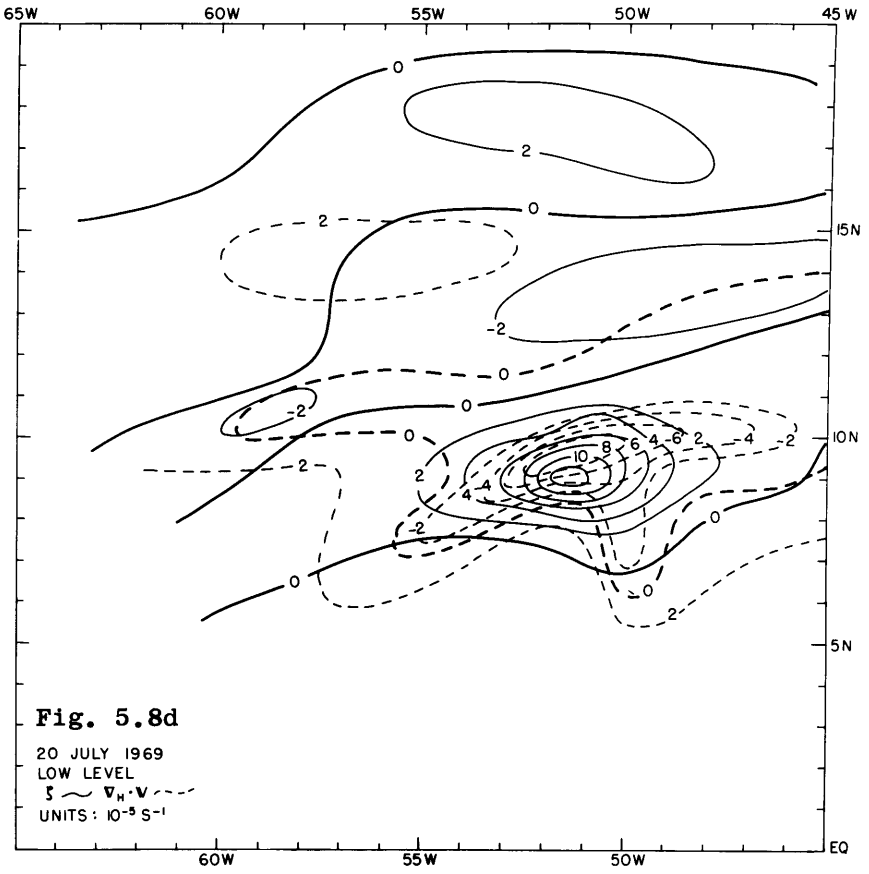

Fig. 5.8d

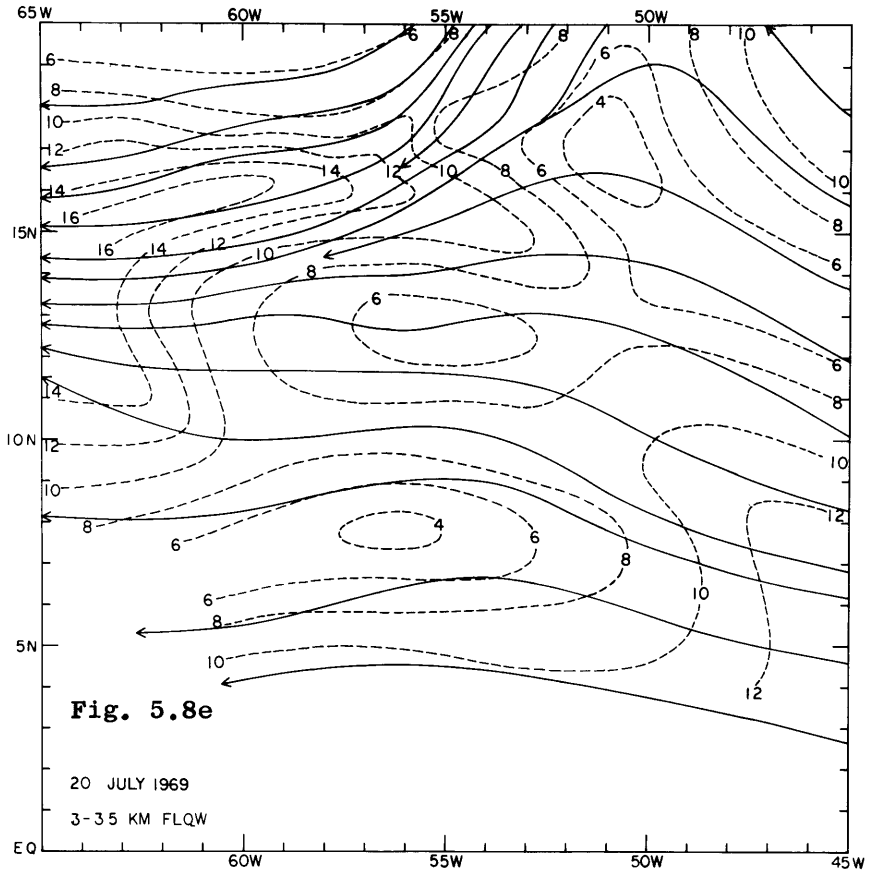

Fig. 5.8e

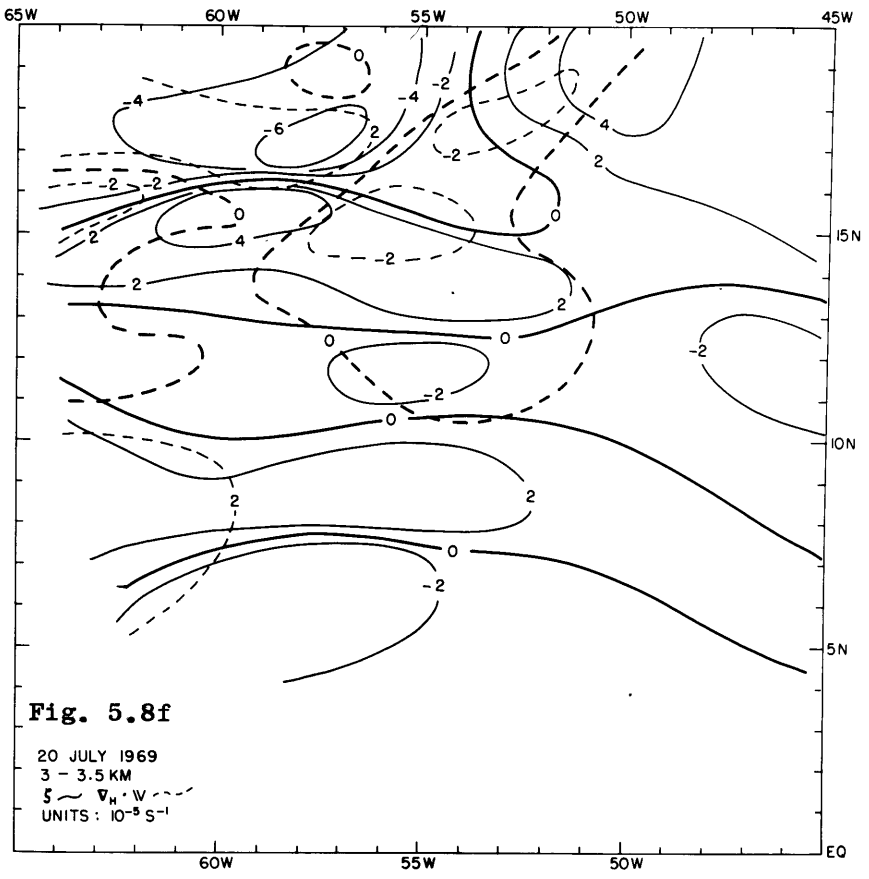

Fig. 5.8f

aligned with anticyclonic vorticity and divergence at 500m.

At 700mb the latest wave axis is now at 50°W and the jet maximum is weaker than on the 19th. There are no significant cloud masses associated with what appears to be a very strong wave except for the weak north south bands between 45° and 50°W. It is significant, however, that as this wave passes through the grid, the 500m flow will become less favorable for ITC support and it will break down as on previous occurrences of wave passage. Although the mechanism is not clear from this study, interaction between these waves and the ITC is clearly suggested.

5.6.4 Disruption of the ITC, 21 July

The low level cusp is still in evidence and has moved northwest at about 10K (Fig. 5.9 c). As on the 20th, vorticity and convergence are concentrated north of the cusp and a correlated but more diffuse cloud cluster has tracked northward with the trough. On both the 20th and 21st, vorticity and convergence approach magnitudes of $10^{-4}\ s^{-1}$.

South and east of the low level trough, the fracture in the ITC is again related to anticyclonic flow with a probable trajectory from north of 10°N. The shower activity near 7.5°N is definitely from $C_L 9$ and the anvils are visible in Fig. 5.9a. Neither analysis level supports this cloud band. However, since nearly all previous shower areas could be related to at least the vorticity field, it is assumed that there is a wind perturbation, probably in the B.L. that is not seen due to a lack of data.

The strong northeasterly winds at 500m near the southeastern

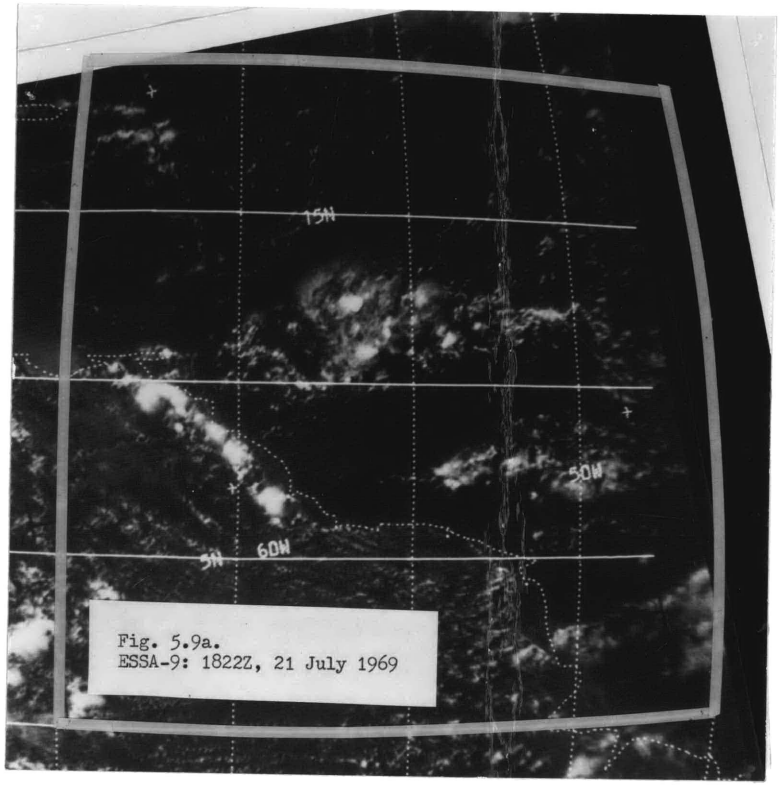

Fig. 5.9a.
ESSA-9: 1822Z, 21 July 1969

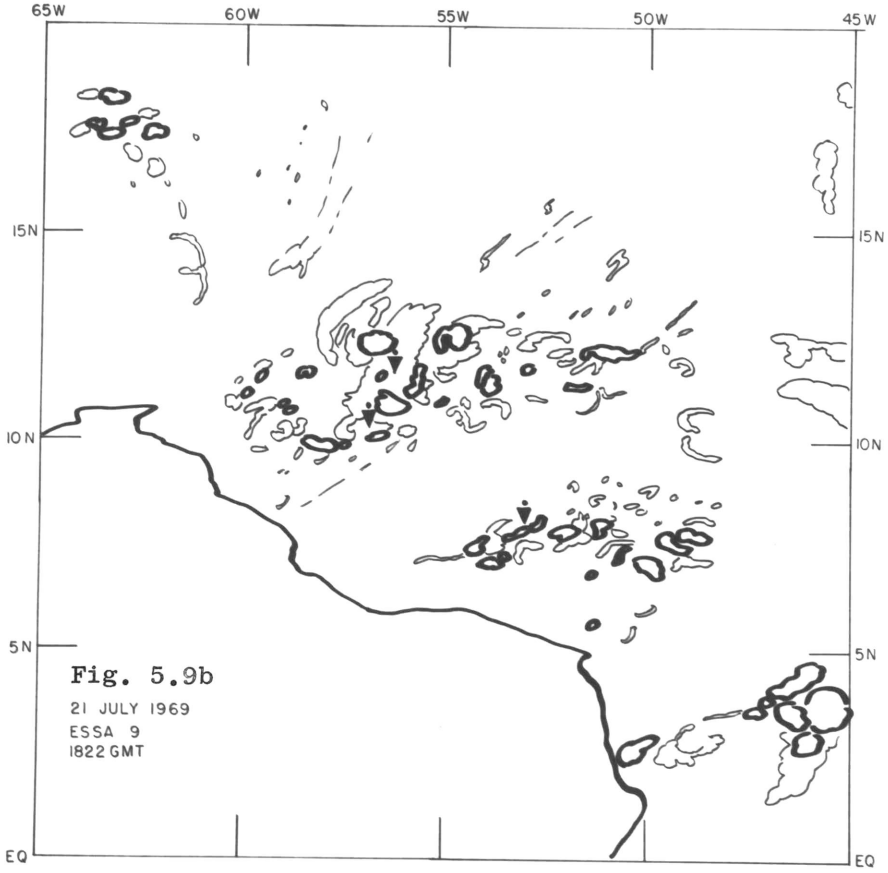

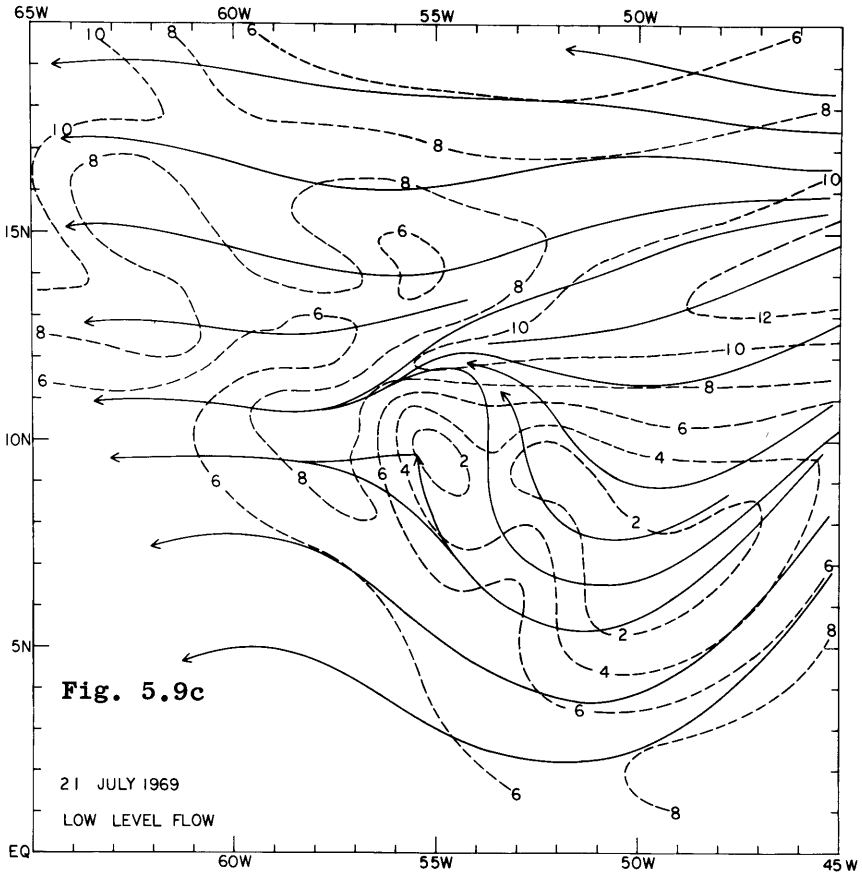

Fig. 5.9c

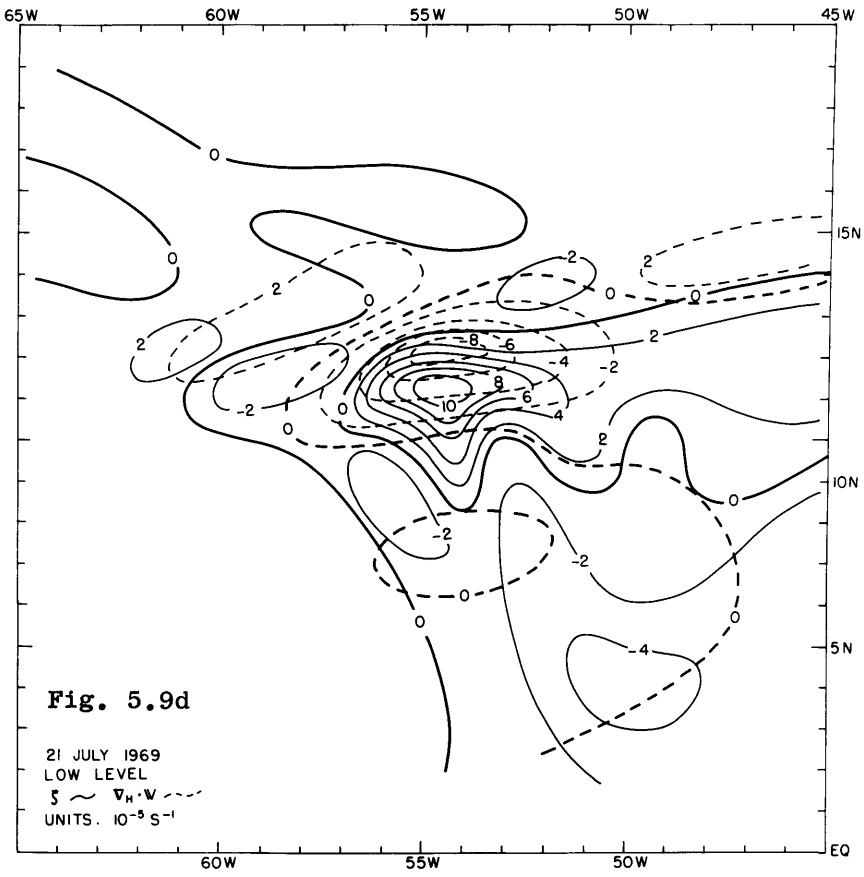

Fig. 5.9d

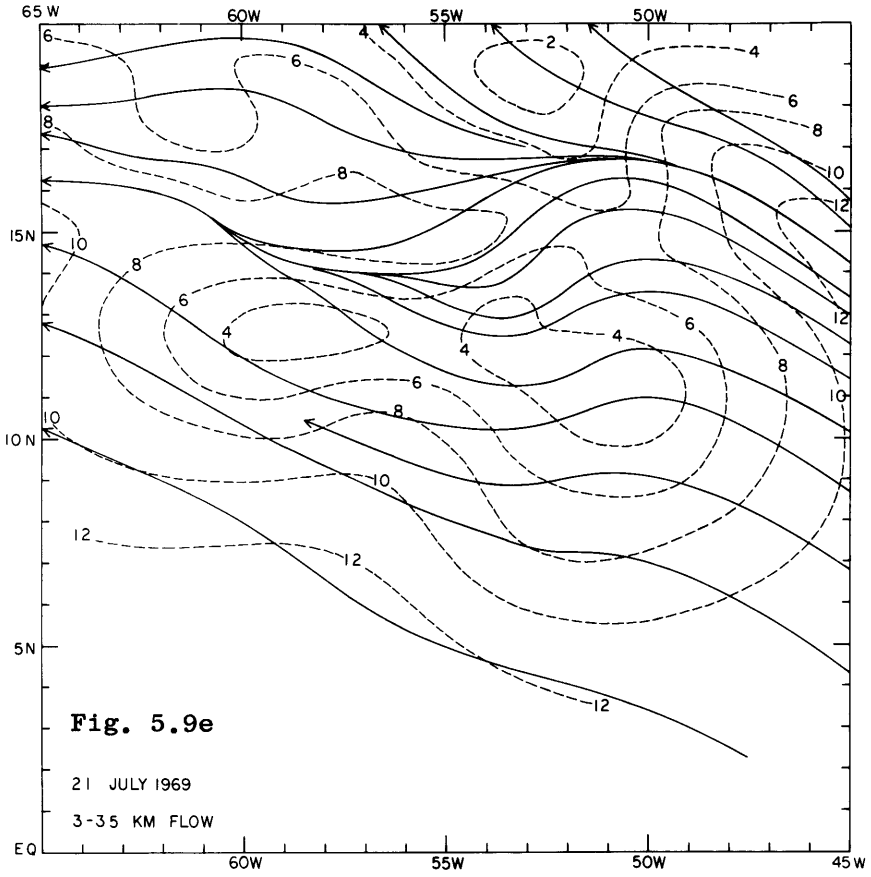
65 W
60W
55W
50W
45 W
15N
10 N
5N
EQ
Fig. 5.9e
21 JULY 1969
3-35 KM FLOW

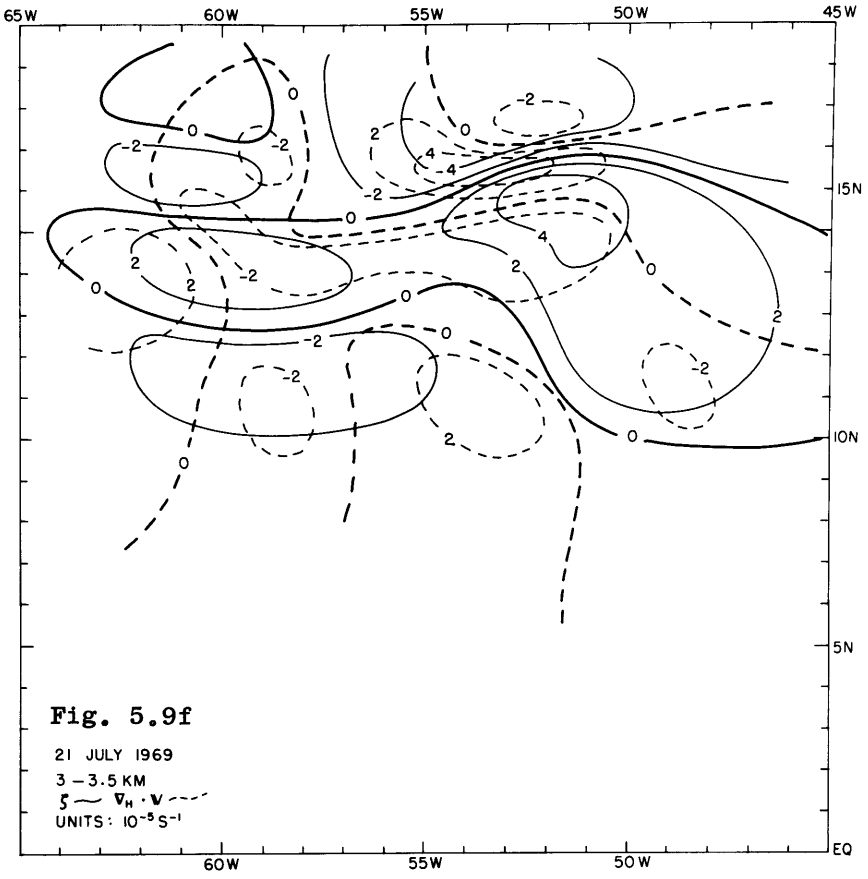
65W
60W
55W
50W
45W
15N
10N
5N
EQ
Fig. 5.9f
21 JULY 1969
3 – 3.5 KM
ζ ~ $\nabla_H \cdot \mathbf{v}$ ~
UNITS: $10^{-5} S^{-1}$

corner of the grid are associated with a deepening circulation in the ITC which evolved into a tropical depression that entered the BOMEX grid late on the 22nd.

5.7 Summary

This case study has shown that ITC cloud bands are virtually always situated in a well correlated strip of boundary layer positive vorticity and convergence having orders of magnitude like $4 \times 10^{-5}\ s^{-1}$. The kinematical patterns are mesoscale features with widths of ∿100-200km. The cloud scale vorticities and divergences must be of a higher order and would be more detailed however, as shown in Fig. 1.1.

We observed the regeneration of the ITC cloud bands as an intensification of the shear and convergence which required about 48 hours. Modest evidence suggests that the initiation of the growth cycle occurred in the field of boundary layer motion without strong support from organized cumulus convection.

If more cases such as this could be analyzed, they might suggest that the initial perturbation is some form of linear instability in the boundary layer flow* followed by the CISK cycle.

Cloud blowups in waves to the north of the ITC were seen to occur when they could be detected in the low level flow indicating that the moisture layer had been tapped. In-phase patterns of low level vorticity and convergence again suggest the CISK mechanism.

Except for the disruption on the 16th and 17th, fractures in the ITC occurred in regions of low level, anticyclonic, divergent flow.

---

* suggested during a discussion with Prof. J.G. Charney, M.I.T.

In such instances, frictional divergence is probably a major factor. During the 16th and 17th, the disruption was more extensive, and a more complete, synoptic scale interaction is suggested. One clue might lie in the fact that extreme low latitude dryness apparently advected northward as far as 7.5°N in a subsident zone. Perturbations in some form occurred on the ITC with each wave passage.

From the 19th through the 21st the ITC contained a sharp 500m trough or cusp, yet the major cloud bands were essentially zonal and this mesoscale circulation did not appear to intensify. However, the warm core disturbance after 21 July was a major storm and appeared to have a broader circulation regime than the cusp. Perhaps this indicates that the initial size of the disturbance was related to further development.

An easterly jet at 700mb was observed for most of the study period. It is shown in Appendix V that such features can be geostrophic and are related to hot African air intrusions. The case of 17/00Z had the necessary conditions for instability of an "internal jet".

There were three distinct periods of 700mb wave occurrence: 13, 14 July, 17 July and 19-21 July. The common feature was a wave length on the order of 2000km, a familiar value; otherwise, each was unique. The first had its trough ahead of the cloud system; the second was behind (and may not have been related to the clouds at all); the third had little or no cloudiness associated. The first moved at 16 knots; the second may have moved at 30 knots or simply dissipated; while the third may have accelerated to about 25 knots. The first was well ahead of a 22 m/s easterly jet while the others showed jet winds in the

anticyclonic ridges on both sides of the trough; these may be related to the higher apparent speeds of the latter waves. The V-component cross section at Discoverer (13°N) indicates a wave speed of ∿ 26 knots for the third case which is consistent with the 24 hour map continuity. We should also add that each wave passage was accompanied by some form of break in the ITC. Convergence patterns generally had poor time continuity, but dipolar vorticity patterns could easily be followed, especially in the latter two cases.

Because reconnaissance flights observed haze east of the three wave troughs (not until the 22nd in the last case), each was either triggered over the African continent (the first case) or possibly nurtured by interaction with a jet built by the airmass contrast.

CHAPTER 6

SUMMARY, CONCLUSIONS AND RECOMMENDATIONS

6.1 Summary

This paper had one major objective, namely: to describe the wind structure in the lowest few kilometers in the vicinity of the ITC. It was not explicitly assumed that a planetary boundary layer would be found at these latitudes, yet it rapidly became apparant that one did exist in each of the regions studied.

Data from the Marshall Islands were used to evaluate the balance of forces and to determine the utility of geostrophic balance and Ekman theory in the boundary layer. The Marshall data plus additional data from LIE and BOMEX were used to form composites of average wind and humidity profiles and cross-sections, which enabled us to examine latitudinal and longitudinal variations in the tropical boundary layer.

A nine-day case study using a variety of meso-scale data sources was then discussed in detail comparing boundary layer flow (500m) with basically free-atmosphere flow (700mb). The relationships between clouds and kinematics were analyzed, and some interesting 700mb features were noted.

6.2 Conclusions

Detailed reviews may be found at the end of each chapter; thus only main points are included here.

6.2.1 Balance of Forces

Marshall Island data (Chapter 3) showed that where the mean winds were not light and variable, the zonal wind was quasi-geostrophic to at least the latitude of the ITC (4-5°N) and probably further south. An Ekman balance was suggested at 850mb and below, north of the ITC. South to the equator a variety of inertial and fluctuation terms are alternatively important (including zonal derivatives such as which would vanish in a global study), and the impression is that these are principally generated in the Hadley cell and travelling disturbances. Surface friction is also important at 850mb and below. Judging from the cross-sections of $[\ \bar{v}\ ]$ (Fig. 3.1) and $[\ \bar{w}\ ]$ (Fig. 3.3), the winter hemisphere Hadley cell extended across the equator in agreement with the data gathered by Newell et al (1969).

Wind profiles north of the ITC could be successfully modeled with an Ekman equation modified to include a linear thermal wind. Fifty percent of the equatorward boundary layer transport occurred below 750m although the "top" of the B.L. was about 2.5_{km} near the ITC based on geostrophic departures.

In the work by Ballif et al (1958), C.E. Palmer states that "within the observational error of $\pm$ 10°, the mean wind direction does not change with height from the anemometer level to 6000 feet". Thus he concludes that the Ekman layer did not exist in the Marshalls in June 1956, the month following my study. However, the round-off direction error in daily data is only $\pm$ 5° and the June mean would reduce this further. In the Ballif paper the time-and-space-mean wind components for June

1956 were tabulated by latitude to the nearest tenth of a meter per second at PIBAL levels to 60,000 ft. This author solved for wind direction from these data and the resulting cross-section is shown in Fig. 6.1. Clearly, little deep turning existed; however, veering as large as 31° (at 7°N) occurred in the subcloud layer. One can see that a deeper layer of flow from the southeast surmounts the equatorward flow. It seems clear that a friction layer with Ekman characteristics was also present in the June 1956 Marshall Islands data north of 4°-5°N.

6.2.2 Detailed Boundary Layer Structure and Composite Cross-Sections

Unstratified data from the Marshall Islands and data from BOMEX and the Line Islands Experiment that had been stratified relative to the displacement of the ITC were composited and discussed in Chapter 4. Characteristics of the wind, humidity and temperature profiles were used to specify the boundary layer in the BOMEX and LIE data guided, in part, by the results from Redwing which involved geostrophic departures.

Fig. 6.2 attempts to summarize many of the results from Chapter 4 by blending B.L. characteristics from the three areas studied with subjective inference from satellite photos and precipitation data. Explicit reference to the possibility of strong west-east shear (as in the Redwing and LIE data) is not made, nor does this figure incorporate the details of the northerly winds at Christmas Island (Fig. 4.11a).

The placement of the $\bar{v} = o$ intersection with the surface at 6°N is somewhat arbitrary but is only a degree south of the mean position of the ITC from the three study regions. The mean ITC position

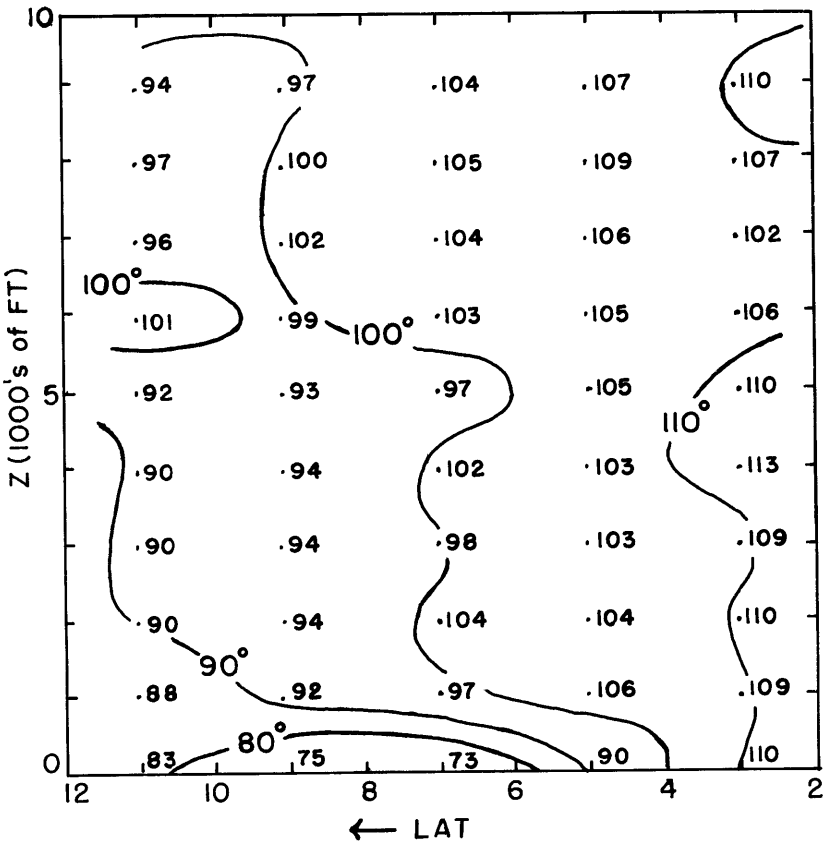

Fig. 6.1. Cross-section of time- and space-averaged wind directions taken from Ballif's Redwing data for 0300Z, June 1956.

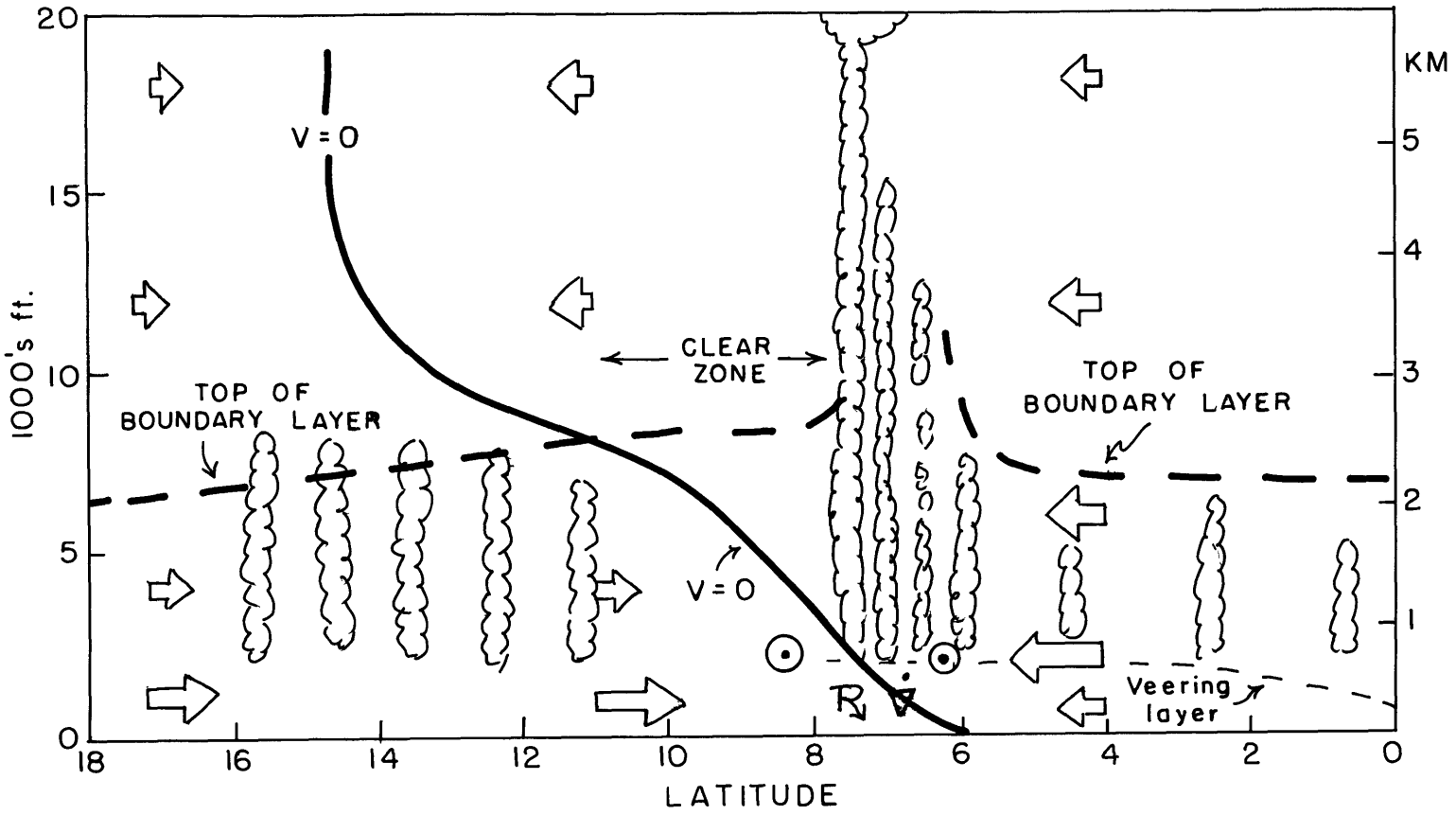

Fig. 6.2. Cross-section through a simulated ITC. Bold arrows are meridional velocities; largest arrow represents 5 knots. Circles with dots represent low level easterlies (showing positive shear vorticity). Data synthesized from Redwing, BOMEX and LIE data.

(7°N) was used to place the center of the cloud bands. The $\bar{v} = o$ curve has been based primarily on Redwing and BOMEX cross-sections (Figs. 3.1, 4.13b and 4.14b). The top of the B.L. north of the ITC has been adjusted to fit the Rongerik (11.3°N) Ekman result (Chapter 3) and the estimated heights from the BOMEX profiles of stratified wind and humidity (Figs. 4.1, 4.2, 4.7, 4.8). North of Rongerik, the height is determined proportional to $f^{-1/2}$.

South of the ITC, finding the top of the B.L. is more difficult, and may depend somewhat on the large scale vertical motion. The u-component velocity shear at low latitudes and the height of the moist layer from Redwing data suggests a depth near 3km (Figs. 3.7, 3.8, 3.9, 3.34), while the LIE data argue for a shallower layer (Figs. 4.11, 4.12). Near-equatorial mean vertical motion was upward during Redwing (Fig. 3.3), but probably subsident in a strong divergence field during the LIE (Fig. 4.15b). A subsident air mass can increase the static stability and inhibit the vertical turbulent flux of momentum and water vapor; whereas the opposite will occur in large scale rising motion. The depth chosen near the equator is a compromise of the two sets of results.

The Mt. Mitchell southerly regime showed a "soft" top in the humidity data (Fig. 4.8) and rather homogeneous wind profiles (Fig. 4.2b) above a shallow veering layer. Also, this ship had most of its precipitation in southerly flow. Thus, these data suggest coupling through a deep layer due to penetrative cumulus activity in and south of the main convergence zone. This aspect is indicated as a break in the top of the B.L. in Fig. 6.2.

The bold arrows indicate the meridional wind component and the longest arrow is scaled to 5 knots. The dotted circles indicate the relative strength of the easterlies and are drawn such that cyclonic shear accompanies the strongest convergence near the cloud bases. Trade cumulus with tops 6-8000 ft are well within the boundary layer and contribute to turbulent exchange of momentum, heat and moisture.

The "clear zone" indicated in Fig. 6.2 may be seen in satellite photography. When the ITC cloud bands are sharp and free from cirrus overcast, it is frequently noted that a 2-3° wide strip having very few cumuli separates the suppressed cumulus families in trades from the ITC further south. In Chapter 5, such a zone shows up on the depictions of the 18th, 19th and 20th (Figs. 5.6-8, a and b). Since extensive trade cumulus persist quite well in the face of the subsident branch of the Hadley cell and weak boundary layer divergence further north, the clearing of the area north of the ITC evidently requires a more intense subsidence.

The mean low level dynamics south of the ITC are not explained by Ekman theory (Northern Hemisphere) nor by a model which forces a symmetry condition at the equator. In this region there is some evidence (Chapter 4) that a southern hemisphere Ekman layer has been advected across the equator in the southeast flow. Given that boundary layer adjustment requires a few days (say 72 hours), then with a 5 knot southerly component southern hemisphere structure might still be found in the wind as far north as 5° or 6°N.

A sharp veering layer below cloud base showed up well in only

stratified BOMEX profiles (Figs. 4.2b, 3b); however, a weaker version is also in each of the LIE profiles (Figs. 4.10b, 11b). This layer has northern hemisphere Ekman characteristics but is quite shallow. It may be that this is simply how northern hemisphere rotational control first appears in the northward moving boundary layer air.

6.2.3 BOMEX Case Studies

Winds at 500m and 700mb at 18Z$\pm$6hr from 13-21 July 1969 were analyzed using conventional, aircraft and ATS-III wind data.

It was shown that convective elements in the ITC were nearly always organized within meso-scale regions of 500m positive vorticity in phase with convergence. Cloud lines were in narrow (100-300km) kinematical streaks; while cloud clusters often had small troughs or vortices associated with them. At 700mb the flow was usually decoupled from below except for a few cases, when the coupling mechanism was probably the organized cumulus penetration.

Boundary layer pumping due to frictional convergence in regions of cyclonic vorticity is the key to CISK and, in theory, requires an Ekman boundary layer. Although an Ekman layer can be justified only north of the ITC, the daily analyses showed that the principal mechanism -- that of correlated positive vorticity and convergence -- was a property of the low level flow in both the ITC cloud bands and in passing disturbances that tapped the boundary layer moisture supply and intensified.

At 500m, the vorticity and convergence are of the same order of magnitude in the intense zones with values $\sim 5 \times 10^{-5}\ s^{-1}$ in several instances. No doubt a cloud-scale analysis would show values as much

as an order of magnitude higher (see Fig. 1.1).

We can assume that the depth of the well organized vorticity and divergence patterns was $\sim 2_{km}$ based on the composites discussed previously, the fact that the 700mb flow lacked supporting patterns of flow, and also on recent work by Anawalt (1971) who looked at the kinematical structure of the troposphere using BOMEX Fourth Phase data. Anawalt used the Bellamy triangle method to evaluate vorticity and divergence and stratified these data by estimates of cloud cover in each triangle. His study depended solely on ship and island data; therefore, it is sub-synoptic not meso-scale and his triangles are north of 10°N. His mean stratified results showed positive vorticity and convergence from the surface to 800mb during disturbed conditions with a marked drop in the mean convergence above 800mb. In undisturbed conditions, boundary layer vorticity was negative with insignificant divergence values. At least in disturbed conditions, the B.L. is 2-3km deep in his study, and CISK is supported by his findings.

We can observe rapid decay of major ITC bands having a time scale of several hours. For example, the sequence 14-16 July (Figs. 5.2-4) shows little day to day persistence. Regeneration of organized bands may require 24 to 48 hours if the sequence 16-18 July is representative. In the latter case, an east-west band of positive vorticity was apparently beginning to organize prior to the outbreak of penetrative cumulus by at least several hours.

Sub-synoptic 700mb analyses showed little evidence of organized flow to support the ITC. On the other hand, the higher latitude flow was highly perturbed during the period and was characterized by a

prominent easterly jet (Appendix V). Disruptions of the ITC bands occurred to the rear of the wave troughs on 14 and 21 July, while the disruption on the 16th preceded the wave on the 17th. However, in the latter case the breakup formed on the previous day (15 July) and advected into the region. Most fractures of a few hundred kilometers or more were related to low level anticyclonic flow and apparent frictionally induced subsidence.

The easterly jet occurs in confluence zones on the southern periphery of ridges. Anticyclonic vorticities $\sim -6 \times 10^{-5}\ s^{-1}$ or less were frequently found. This is an "internal jet" (Charney and Stern, 1962) and is probably geostrophic (Appendix V). The necessary condition for this type of jet to be unstable is similar to the necessary condition for barotropic instability and can be found on most days. This wind system is built in the baroclinic zone between warm, dry African air and ambient tropical air to the south. It may be one major source for so-called "surges in the Trades" during the summer tropical wave season.

6.3 Recommendations

6.3.1 Data Acquisition

The author has used or attempted to use much of the BOMEX meso-scale data base and makes the following comments which are hopefully relevant to the planning of future experiments in tropical exploration.

a. Continue to sample in the boundary layer and at 700mb with a meso-scale orientation;

b. Surface barometry must be more precise. A common calibration should be maintained among sites;

c. The Rawindonde schedule should be maintained with great determination, especially with respect to wind data;

d. RECCO code has many virtues; therefore, all participating aircraft should provide RECCO records every 15 minutes even if they carry a wide variety of sophisticated recording gear. Winds should be 1-3 minute averages;

e. An improved temperature sonde should be developed for the tropics;

f. The array of permanent sites should provide for separation in longitude as well as latitude since we have much to learn from good quality synoptic analyses. At least one site should be on the equator;

g. Establish a program for conveniently supplying satellite-derived cloud motion vectors to interested investigators;

h. In general the emphasis should be on the collection and refinement of conventional parameters. Quality should take priority over quantity, especially in the tropics where the tolerance for error is so small.

6.3.2 Suggestions for Further Research

This paper has provided empirical guidelines for a variety of possible empirical or theoretical studies. Among these are:

a. To investigate the boundary layer dynamics south of the ITC where the general circulation is assymetric with respect to the equator;

b. To study the stability of linear perturbations imposed on viscous planetary flows with horizontal shear;

c. To extend the case studies of the ITC by including a more thorough analysis of the upper atmosphere and/or the heat and moisture budgets during periods of growth and decay;

d. To determine the mechanism of interaction between tropical waves and the ITC;

e. To determine the structure and global climatology of the easterly jet at 700mb.

APPENDIX I

Errors in Geostrophic Wind due to Sounding Errors

This discussion applies primarily to the analysis in Chapter 3 where geostrophic departures were studied.

An error in the zonal geostrophic wind due to the gradient of height errors on a constant pressure surface is:

$$\delta u_G = -\frac{g}{f}\delta\left(\frac{\partial z}{\partial y}\right) = -\frac{g}{f}\frac{\partial}{\partial y}(\delta z) \qquad \text{(I-1)}$$

The height of a constant pressure surface is derived by integrating the hydrostatic equation:

$$z(p) = \frac{R\bar{T}^*}{g}\ln\left(\frac{p_0}{p}\right) \qquad \text{(I-2)}$$

The height error from (I-2) is:

$$\delta z(p) = \frac{R}{g}\left[\bar{T}^*\frac{\delta p_0}{p_0} + \ln\left(\frac{p_0}{p}\right)\delta\bar{T}^*\right] \qquad \text{(I-3)}$$

Where it has been assumed that the sonde's barometer correctly records p. The two terms in brackets represent an error in surface barometry and a thickness error. The former decreases slowly with height; the latter increases with height unless $\delta\bar{T}^*$ decreases.

Assuming that height errors between sounding stations are uncorrelated, then the horizontal difference in height error between two stations (or grid points) is on the order of the error itself. This is somewhat conservative since a contour analysis will tend to remove the obvious errors.

Based on the previous remarks, the error gradient will be a function of the differencing increment which was four degrees in Chapter 3.

Considering the profiles of $[\bar{u}]$ and $[\bar{u}_G]$ in Figs. 3.1 to 3.16 it appears that north of about 6°N the main difference between the profiles is due to an initial error in surface barometry (the first term in [I-3]) whereas both terms become increasingly important south to the equator. Assume that $\delta p_o \sim .5$mb and $\delta\bar{T}^* \sim .1$°K; then with a differencing increment of 4° lat, we can illustrate the sensitivity of $[\bar{u}_G]$ to the two terms in (I-3) in Table I-1.

p	δp_o – term		$\delta\bar{T}^*$ – term		Total	δu_G	δu_G
(mb)	δZ	%	δZ	%	δZ	5°N	10°N
100	3.4	33	6.8	67	10.2	19.6 m/s	9.9
200	3.7	44	4.8	56	8.5	16.3	8.2
300	3.9	51	3.7	49	7.6	14.6	7.4
500	4.1	66	2.1	34	6.2	11.9	6.0
700	4.2	79	1.1	21	5.3	10.2	5.2
850	4.2	88	.5	12	4.7	9.2	4.6
SFC	4.3	100	0	0	4.3	8.2	4.2

Table I-1. Contribution to δZ by the surface barometry error (δp_o – term) and the thickness error ($\delta\bar{T}^*$ – term) from expression (I-1). Percent of total δZ is shown and the error in $[\bar{u}_G]$ at 5° and 10°N.

The height errors in Table I-1 are in general smaller than those from Table 2.2 especially at high altitudes. This is due to the use of a fixed estimate of $\delta\bar{T}^{*}$ = .1°K in Table I-1. Since the values above compare favorably with the observed differences in Figs. 3.2 through 3.16, it is assumed that the thickness measurements during Redwing were better than one would expect from Table 2.2. Another interpretation would be that all temperature measurements are biased in a correlated fashion meaning thickness gradient errors are significantly less than the errors themselves.

Table I-1 supports the idea that surface barometry errors dominate from the surface to 300mb. It should be easier to correct this problem in future tropical experiments than to improve the rawinsonde sensors.

APPENDIX II

Mt. Mitchell Time-Height Cross-Sections

Time-height cross-sections of u, v wind components, relative humidity and potential temperature are shown in Figs. II-1 through II-4 respectively for the ship Mt. Mitchell. Winds are in units of m s^{-1}, relative humidities are corrected for diurnal bias and frequency doubling (see Chapter 2), and potential temperatures are in degrees centigrade. Data points that were missing have been linearly interpolated if they were no more than plus or minus six hours from points with real data. Data were missing on the 16th and 24th due to the scheduling of rest breaks.

In Fig. II-3, shaded regions represent relative humidities $\geq$ 90 percent. Weather symbols along the top were taken from the Ship Surface Synoptic records. Note the strong correlation of precipitation with the pumping of high relative humidities into the region above 2km and with southerly winds.

Marked high frequency anomalies in u and v below 2km have a southerly component and occur with shower activity. For example, 14/00Z, 19/18Z and 25/09Z will illustrate such cases. Each of these is also accompanied by a drop in potential temperature; hence these wind shifts are probably due to down drafts from the shower clouds.

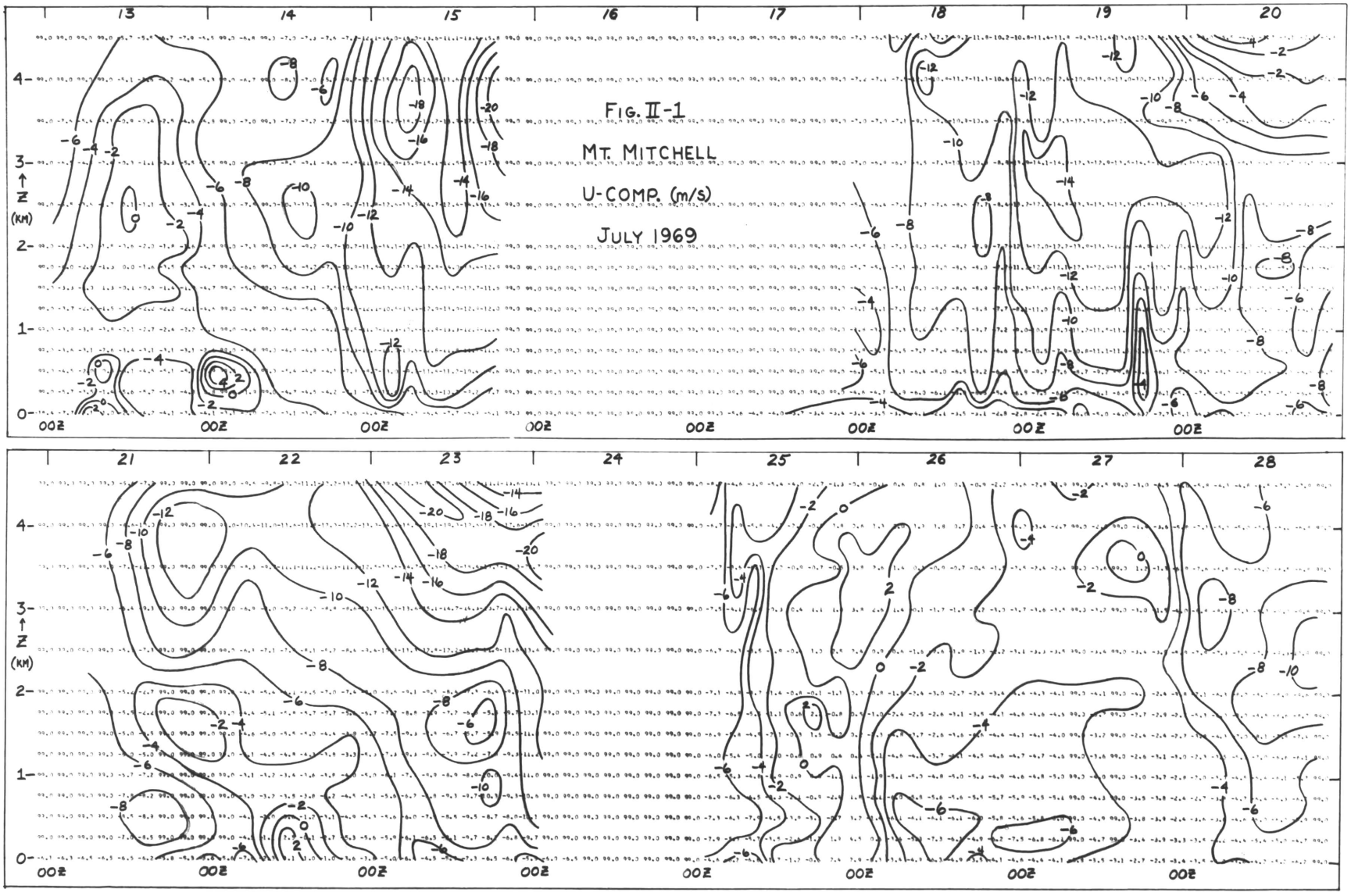

FIG. II-1

MT. MITCHELL

U-COMP. (m/s)

JULY 1969

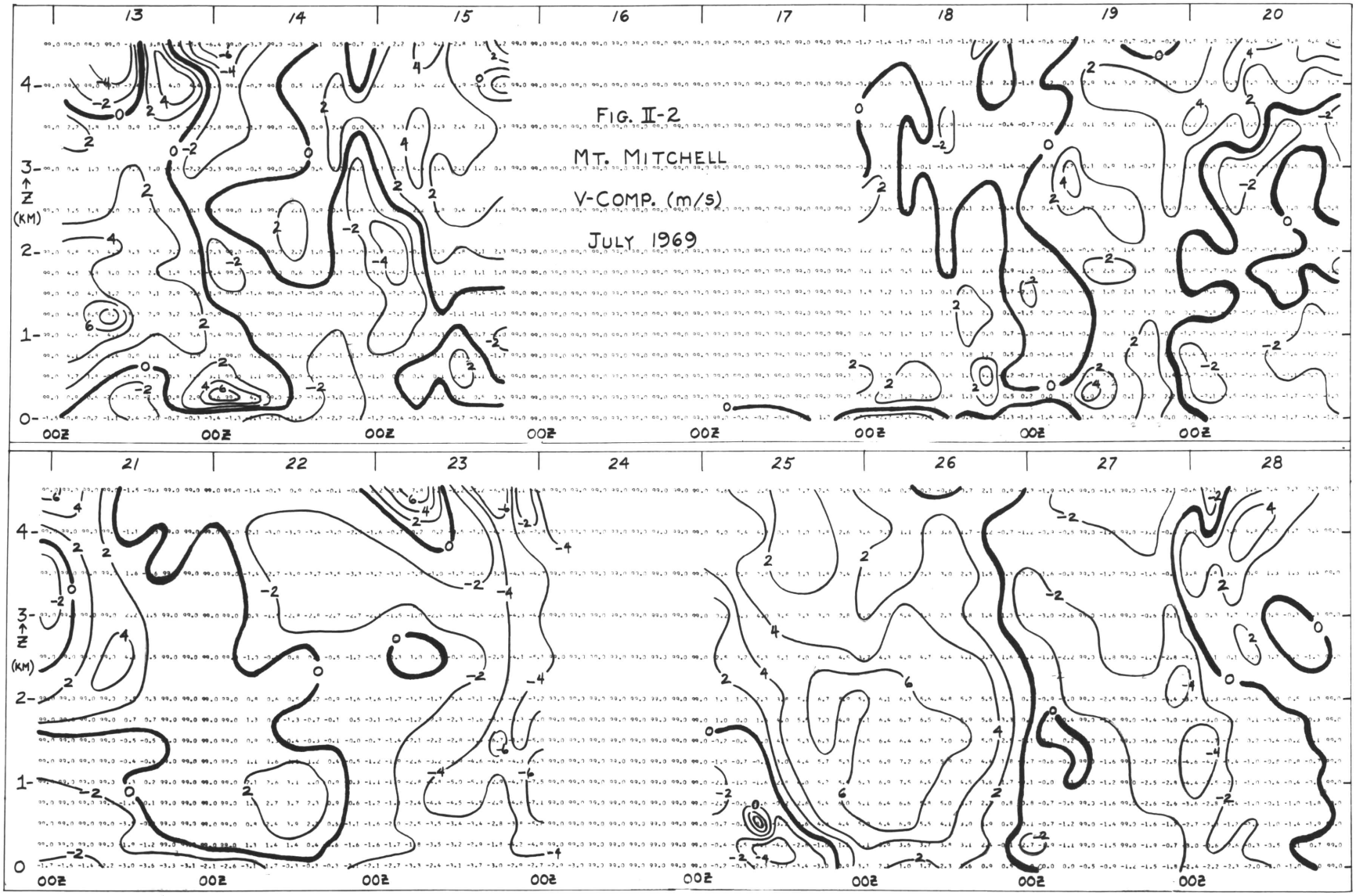

FIG. II-2

MT. MITCHELL

V-COMP. (m/s)

JULY 1969

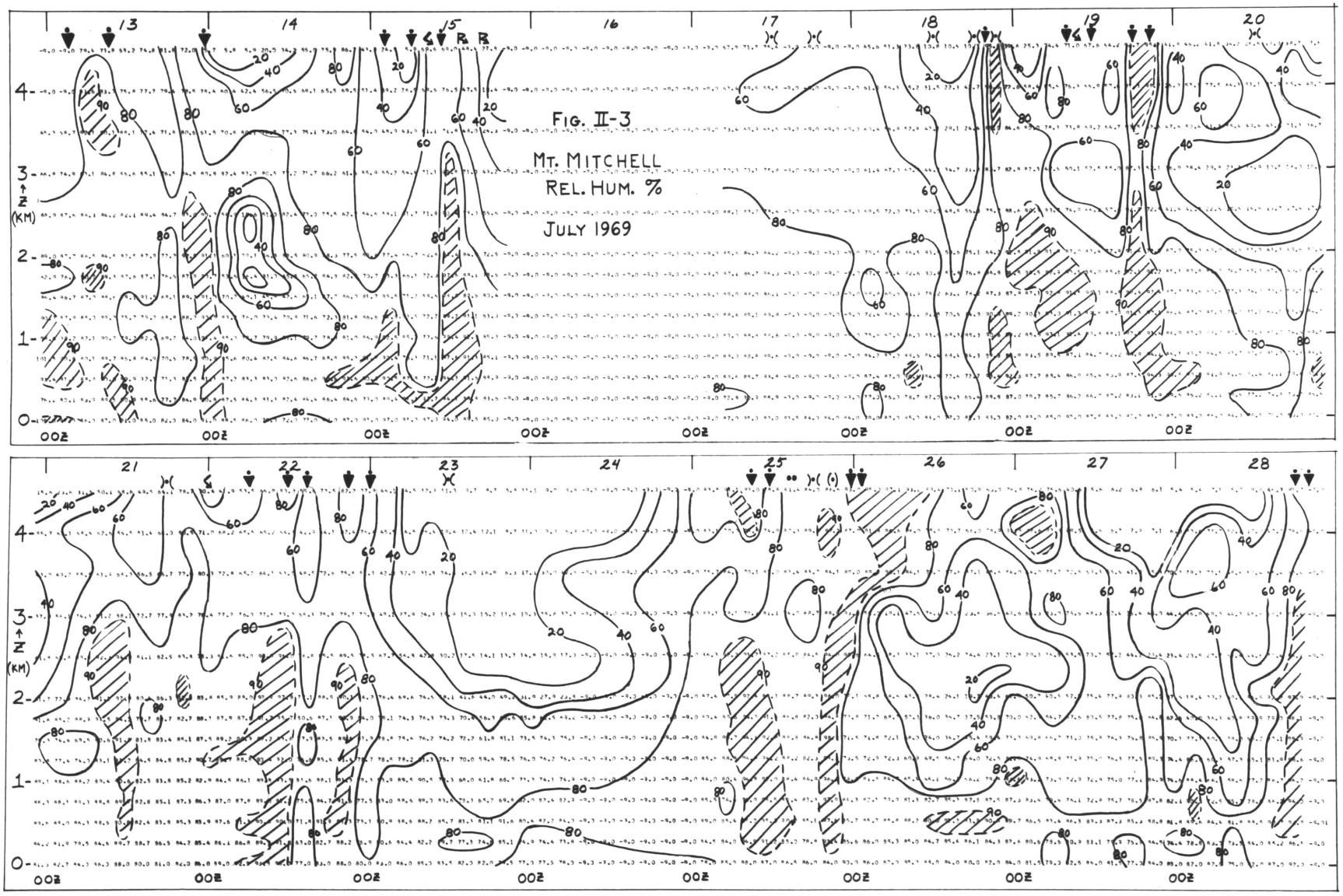

FIG. II-3

MT. MITCHELL
REL. HUM. %
JULY 1969

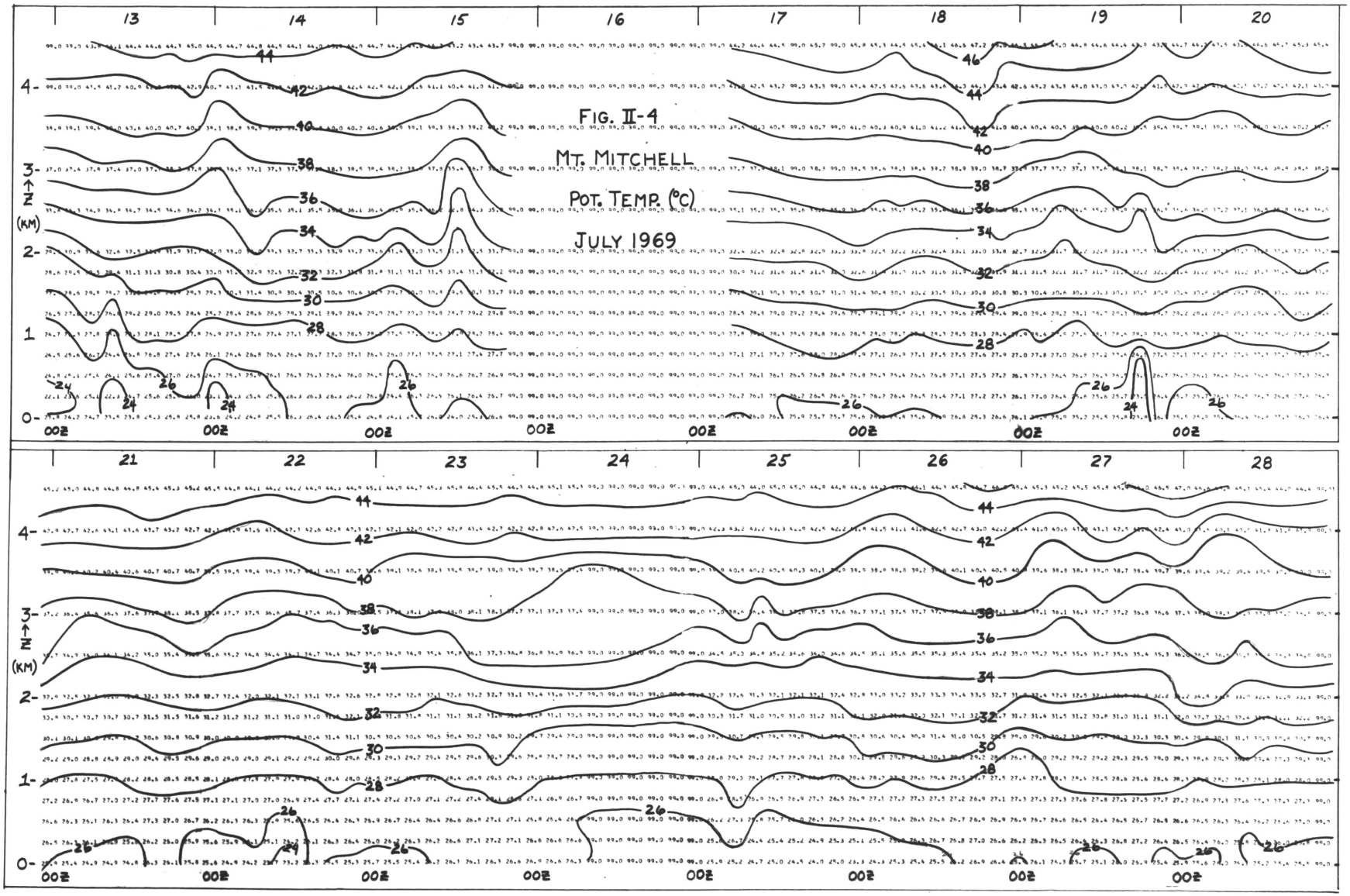

FIG. II-4

MT. MITCHELL

POT. TEMP. (°C)

JULY 1969

APPENDIX III

Data Card Format

Sounding data for Discoverer, Mt. Mitchell and Oceanographer were extracted from A_o soundings and punched at the following levels:

(a) every 250m from the surface to 2000m

(b) every 500m from 2500m to 4500m.

Soundings are assumed to exist every 3 hours.

At Discoverer, winds were interpolated from 6-hourly teletype messages.

A specific sounding requires either one card or 15 cards depending on whether or not it was missing.

First card in a set:

Column	Data	Format
1 - 4	Day Number	I4 (or A4)
5 -12	Ship Name	2A4
13, 14	G.M. Time	I2
15	Test digit	I1

If the test digit is 0, no sounding follows.

If the test digit is 1, 14 cards follow.

Next 14 cards:

Column	Data	Format
1 - 4	Day Number	I4 (or A4)
5 -12	Ship Name	2A4
13 -18	Temp (°C)	F6.2

Column	Data	Format
19 -24	Relative Hum. (%)	F 6.2
25 -32	Pressure (mb)	F 8.2
33 -40	Height (m)	F 8.2
41 -47	Do not use	7X
48 -54	u-comp (m/s)*	F 7.2
55 -61	v-comp (m/s)*	F 7.2
62 -64	Blank	3X
65,66	G.M. Time	I2
67 -80	Do not use	14X

Missing values are indicated with the following numbers:

Temperature	-	99.
Rel. Hum.	-	-1.00
Pressure	-	0.00
Height		-1.00
u-comp	-	999.00
v-comp	-	999.00

If an entire level is missing, the card will have the day number, ship name and G.M. Time but the rest of the card will be blank.

Relative Humidity is not corrected for diurnal error except at the surface where ship's instrument is used.

---

* At Discoverer u-comp and v-comp are replaced by direction and speed in the same format.

APPENDIX IV

Discussion of Data for BOMEX Case Study

Data distribution and special problems are discussed below. Figures are not displayed for all dates; however, selected examples are shown to give the range of data that was available. So that the reader may develop a standard for comparison, the selected figures are discussed first. In the figures, not all data used is necessarily shown. Complete weather models were plotted for the WC-121 and WC-130 flights using the RECCO code. Partial weather models were plotted for the Discoverer, Mt. Mitchell and Oceanographer and often for the other stations depending upon the ITC's position or the data's general value to this thesis. RFF data (A,B, and E planes) were generally plotted every half degree although data were available every 10 seconds. Rawinsonde data are shown zonally displaced in space from their true locations at a rate of 15 knots. Aircraft and satellite data were plotted in their true locations;then the time adjustments were made during the analyses. The "low level" is 500m in A_o data and 950mb at the islands.

Fig. IV-1 shows the low level data base for 14 July 1969. It is one of the two most densely covered maps due to the Fujita ATS-III winds. (The other is the 13th). The A and B planes traded low altitudes to the northeast of Barbados and the Navy WC-121 flew a route into the ITC. The pattern is quite coherent and there were few analysis problems. North of 15°N between 50° and 55°W, ATS-III winds must have been from middle clouds, hence they were ignored in this region.

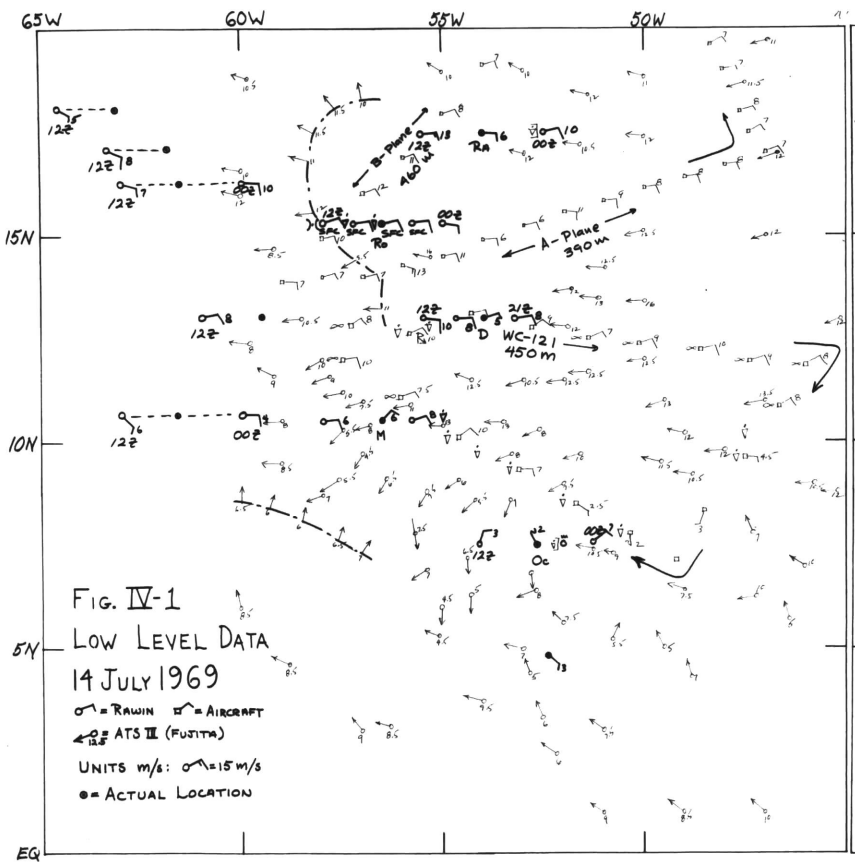

FIG. IV-1
LOW LEVEL DATA
14 JULY 1969
= RAWIN = AIRCRAFT
= ATS III (FUJITA)
UNITS m/s: = 15 m/s
= ACTUAL LOCATION

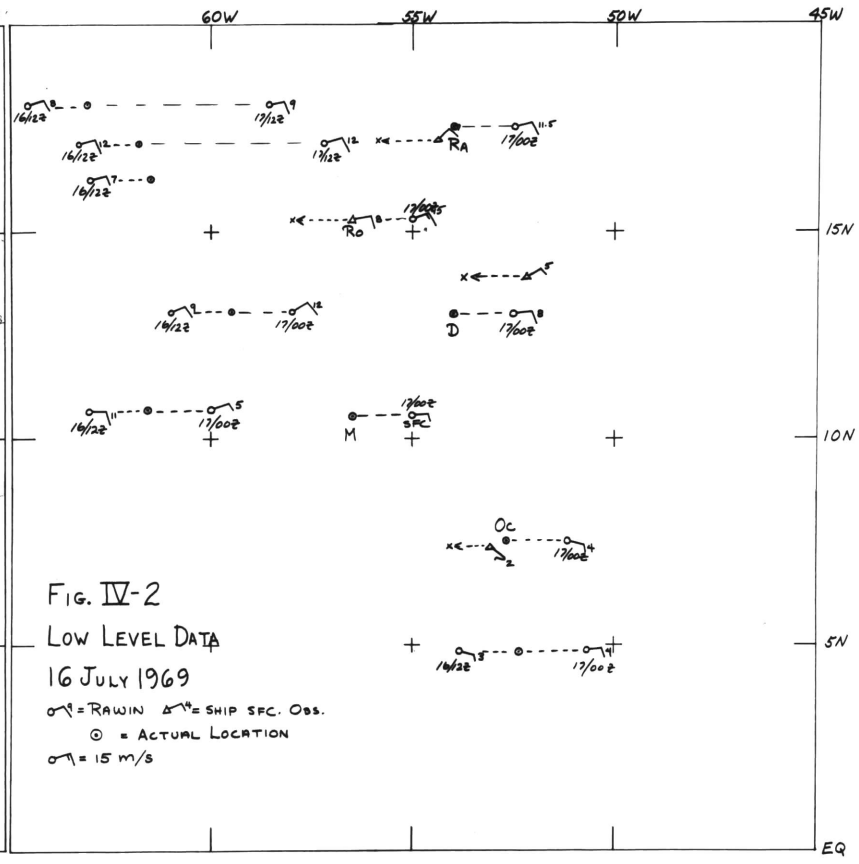

FIG. IV-2
LOW LEVEL DATA
16 JULY 1969
= RAWIN = SHIP SFC. OBS.
= ACTUAL LOCATION
= 15 m/s

Figure IV-2 shows the other extreme at the low level on 16 July. There are no aircraft or ATS-III data and BOMEX rawinsondes are for 17/00Z. Four commercial ships in the area provided surface winds. This is a worst case, yet the analysis (Fig. 5.4c) seems reasonable if not very detailed.

Figure IV-3 is shown because it illustrates how a well placed aircraft can compensate for the lack of satellite data. On 17 July the ITC was quite broken up behind a travelling disturbance. This flight picked up the vorticity and convergence field beginning to form along 10°N and showed that the shower activity is from small cumulus with tops below 10,000 ft except west of 57°W. Even the Cb's at Discoverer and Mt. Mitchell may have had tops to no more than 15,000 ft according to the WC-130 flying the same route at 700mb.

Figure IV-4 shows the low level data for 20 July. This is an example of typical coverage using ATS-III data generated by the author at MSL/NOAA. The A and B planes remained in the vicinity of Barbados and contributed little to this type of analysis. The MSL data in the southeast quadrant of the array supports the cusp that was carried near the Oceanographer (Fig. 5.8c). There was considerable directional shear at Oceanographer from 500 to 1000m and 1000m winds were ultimately used because of their better time history. Local showers may have confused the picture below 1000m.

Figure IV-5 is the 700mb data base for 17 July which shows the winds supporting the wave that may have developed as a result of instability in the easterly jet. The Gull Hotel USAF reconnaissance flight is identical each day and was missing only on 14 July. As on

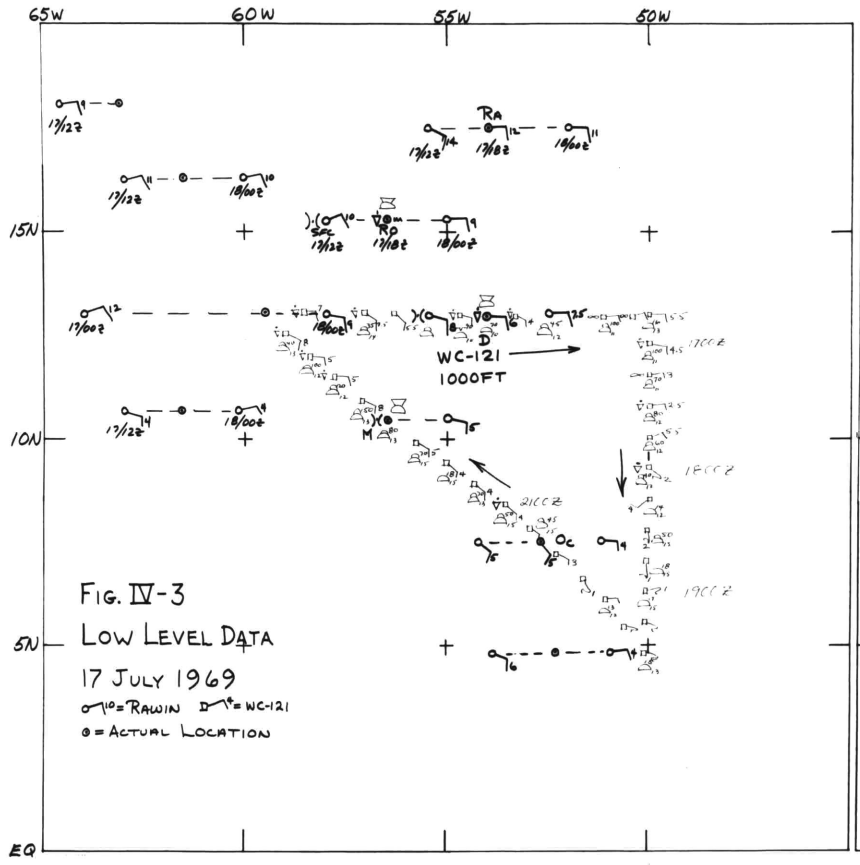

FIG. IV-3

LOW LEVEL DATA

17 JULY 1969

○10 = RAWIN D9 = WC-121

⊙ = ACTUAL LOCATION

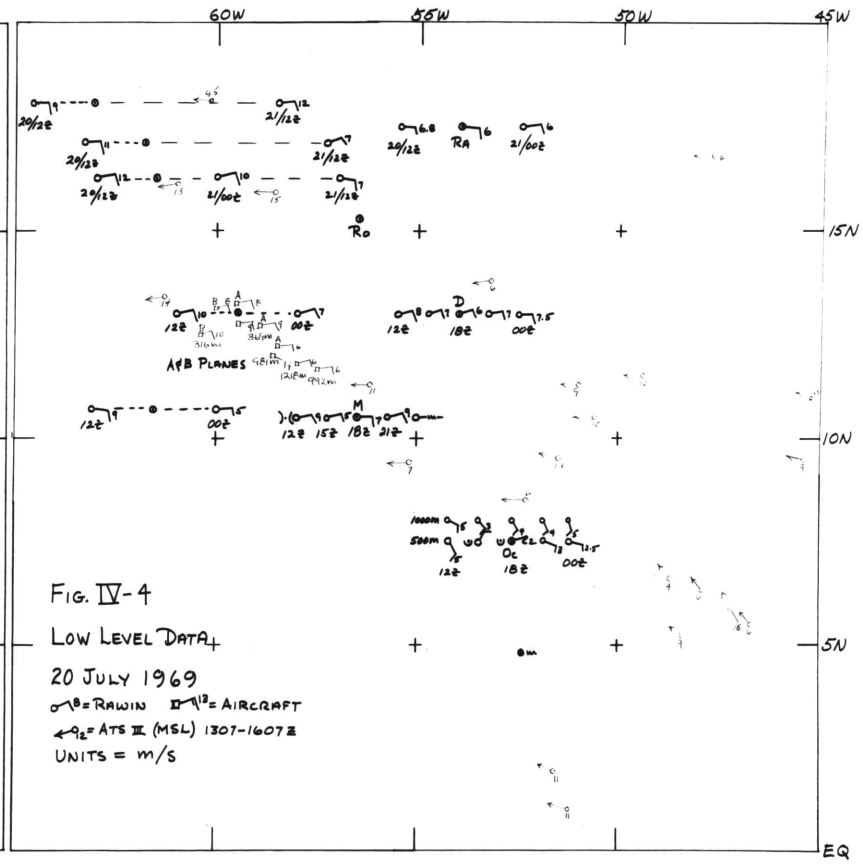

FIG. IV-4

LOW LEVEL DATA

20 JULY 1969

○8 = RAWIN D12 = AIRCRAFT

←92 = ATS III (MSL) 1307-1607Z

UNITS = m/s

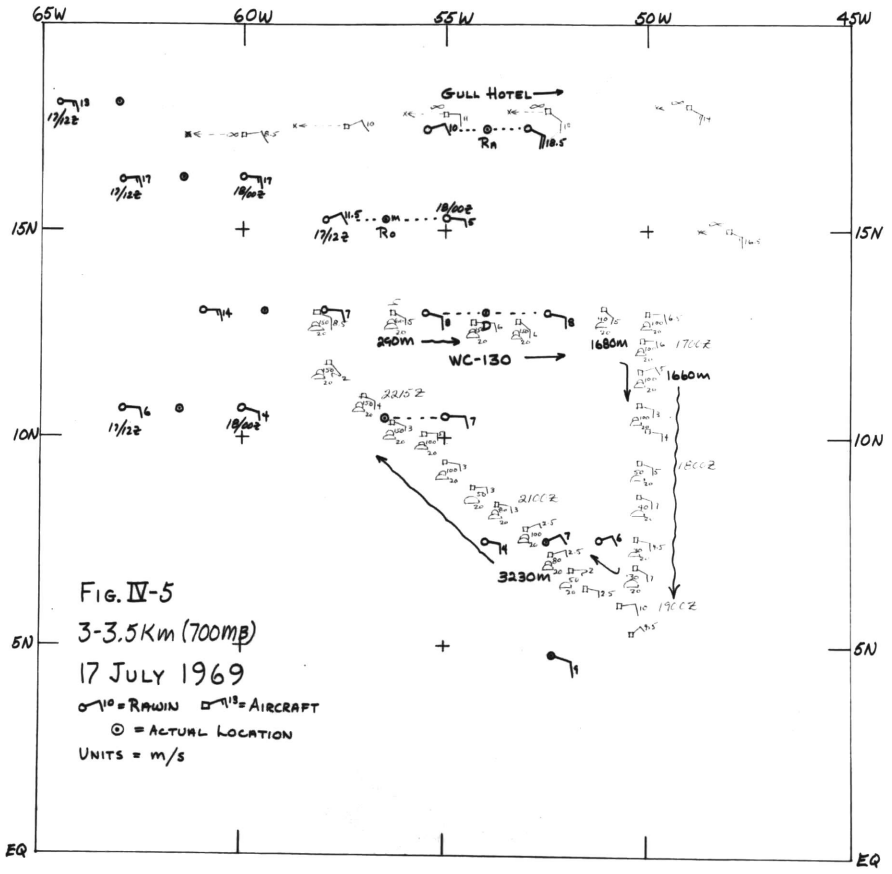
65W
60W
55W
50W
45W
15N
10N
5N
EQ
GULL HOTEL
Ra
Ro
290m
WC-130
1680m
1660m
3230m
17CCZ
18CCZ
19CCZ
21CCZ
22ISZ
FIG. IV-5
3-3.5Km (700mb)
17 JULY 1969
= RAWIN = AIRCRAFT
= ACTUAL LOCATION
UNITS = m/s

14 and 19 July, the WC-130 is shown flying as companion to the WC-121 below on a route typical of their flights. This was the only WC-130 flight exhibiting such large altitude variations. The 290m data were not used, and the 1660m data were only really used for direction. At 3230m, the WC-130 winds were too light but the directions made sense so they were kept for continuity. The typical 700mb data base consists of Gull Hotel plus the island and ship rawinsondes. The WC-130 was flown only on 14, 17 and 19 July during my study period.

The data bases for the remaining days are discussed in the following paragraphs.

13 July 1969: There was no low latitude flight at 700mb; otherwise the distribution at this level was normal. The RFF A and B-planes flew identical routes to the east and south similar to that shown for the WC-121 in Fig. IV-3, and alternately provided 300m winds. The RFF E-plane aborted after providing three hours of 150-300m data to the southeast of Barbados. The WHOI C-54Q flew a low level route from Barbados to the Oceanographer and return. There was some conflict between the C-54 winds and those of the A and B-planes which may have been due to meso-scale gustiness. About one hour's worth of the C-54 data was ignored near 8°N.

ATS-III winds were available from both Dr. Fujita and MSL/NOAA with a data density comparable to that of Fig. IV-1.

14 July 1969: Low level shown in Fig. IV-1. At 700mb the Gull Hotel flight was missing; however, the RFF A and B-planes shown at the low level alternated between the boundary layer and 700mb. The WC-130 flew above the WC-121 to the south and east at 700mb.

15 July 1969: At the low level the RFF E-plane and the WHOI C-54Q flew short legs north and south of Barbados. ATS-III winds from MSL/NOAA were excellent with better density than those shown in Fig. IV-4. There was fair coverage at 700mb especially south of 10°N since only the 06Z sounding from Oceanographer and 00Z sounding from Kourou were available. The Gull Hotel flight to the north made up for rather poor coverage at Rockaway and Rainier.

16 July 1969: This was a BOMEX rest period and data were very sparse (see Fig. IV-2). The Gull Hotel flight at 700mb gave this level better coverage than at 500m. ATS-III imagery was unusable. Time displaced soundings for 17/00Z were used at the BOMEX ships. Continuity with the 15th and 17th suggests that the flow on 16 July was reasonably simple so the sub-synoptic analyses are reasonable under the restrictive circumstances.

17 July 1969: Both data bases shown as Figures IV-3 and 5 are described earlier in this appendix.

18 July 1969: Low level flights were made in a restricted triangular region extending east of Barbados to about 56°W and between 9° and 17°N. Participants were the RFF A, B and E planes and the WHOI C-54Q . An excellent set of ATS-III winds was computed by the author at MSL which covered the array except in South America. Ship RAWIN density was above average.

At 700mb, the Gull Hotel flight compensated for apparent directional errors at Rainier. The RFF B-plane flew a northeast leg at 700mb to 16°N, 51°W. Other normal coverage from ships and islands was excellent.

19 July 1969: No satellite winds available. However, the WC-121 and WC-130 flew a low level and 700mb formation on a path similar to that of the 17th which extended to 47°W and encircled the young ITC that was forming. Gull Hotel flew its normal leg, but its winds had to be recalibrated based on Rainier's 700mb continuity which resulted in a reduction of 4 m/s. Extensive recomputation was also required of the WC-121 data using logs that were available to the author.

20 July 1969: Low level data is illustrated in Fig. IV-4 and was previously discussed. Only Gull Hotel supplemented a good set of conventional data at 700mb.

21 July 1969: At the low level, the WC-121, WHOI C-54Q and RFF E-plane flew an overlapping pattern in a small region east of Barbados to 54°W. A well distributed but sparse set of ATS-III winds were generated by the author at MSL and were the basis for the pronounced northeasterly flow east of the ships. The 700mb coverage was identical to that of the 20th.

APPENDIX V

The Easterly Jet at 700mb during BOMEX

The belt of strong easterly winds at 700mb observed during the period of the BOMEX case study (Chapter 5) has the character of an "internal jet"; that is, the baroclinic zone in which such a jet forms does not extend vertically to intersect horizontal boundaries (Charney and Stern, 1962). For example, note the 700mb chart for 16 July 1969 (actually based on 17/00Z data) which shows a jet axis near 15°N (Fig. 5.4e). The axis is over ship Rockaway and is straddled by Rainier (17.5°N) and Discoverer (13°N). Figure V-1 below shows the 17/00Z temperature soundings for these three ships and distinctly supports the internal jet specification. The baroclinic zone lies between 870 and 650 mb while at the surface (and above 500mb) the horizontal temperature gradient is virtually flat. The temperature gradient is almost certainly due to an intrusion of warm African air. Rockaway's maximum wind occurred at 680mb, quite close to the thermal wind reversal near 650mb. The geostrophic zonal component derived from the 700mb heights at Rainier and Discoverer is 16 m/s which is precisely the value of the isotach on Fig. 5.4e that intersects 15°N between these two ships. The geostrophic zonal component derived from 700mb heights at Raizet and Barbados is 18 m/s compared to about 19 m/s from the isotach field at 15°N between these two islands. Thus it is clear that this jet is quasi-geostrophic.

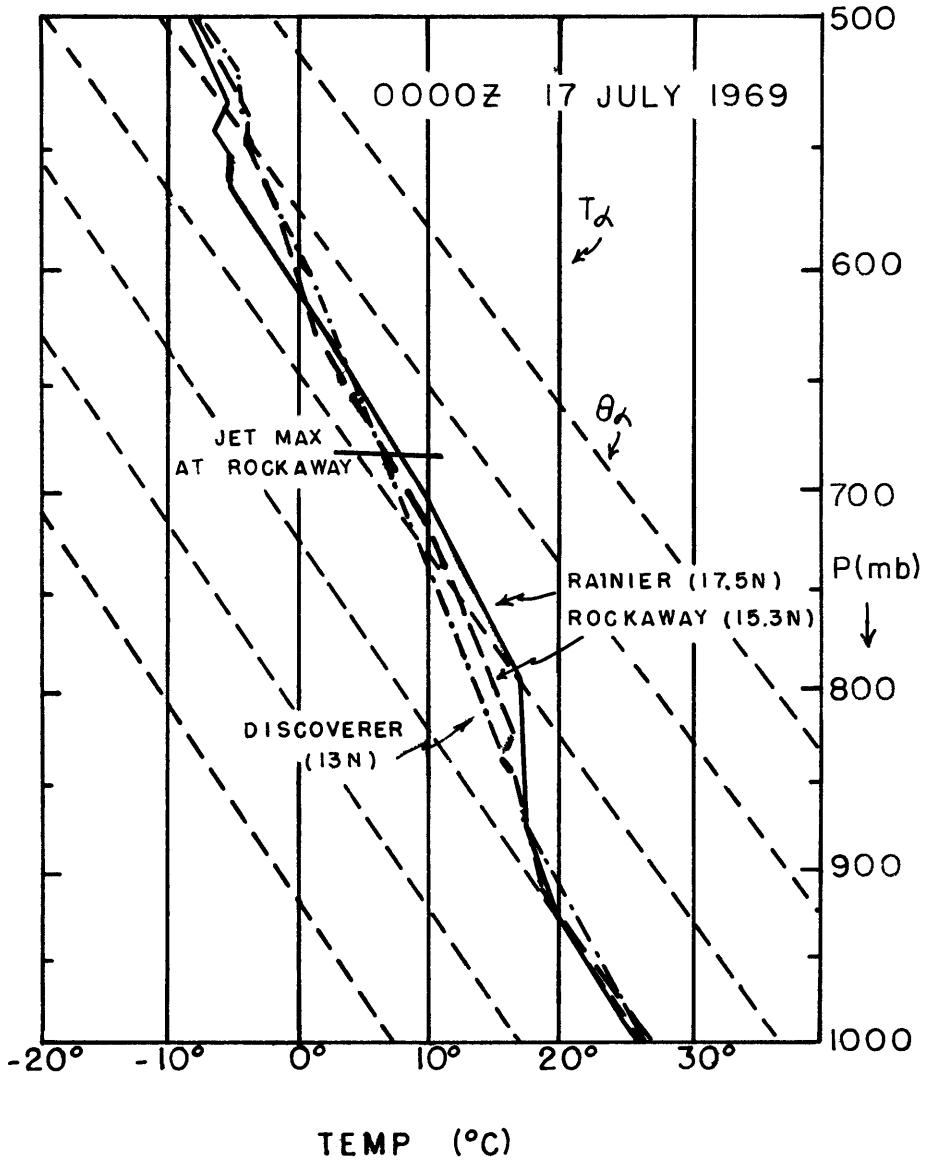

Fig. V-1. Soundings for 00Z, 17 July 1969 at three BOMEX ships which straddled a 700 mb easterly jet.

From the Charney and Stern theory, the necessary condition for instability of an internal jet is that the meridional gradient of the potential vorticity (Q) must vanish in an isentropic surface. An approximate expression for Q is:

$$Q = -\left[f - \frac{\partial u}{\partial y} + \frac{u \tan\phi}{a}\right] g \frac{\partial \theta}{\partial p} \qquad \text{(V-1)}$$

where conventional symbols have been used. Fig. V-2a shows a vertical cross-section through Rainier, Rockaway and Discoverer of the isotachs and potential temperatures for 17/00Z; units are m/s and °C respectively. Expression (V-1) was evaluated along the Θ =40°C isotherm and is shown as Fig. V-2b. The gradient of Q vanishes at 16.5°N; thus, the necessary condition for instability of this jet has been met. Eighteen hours after these soundings, a well developed wave was found on the 700mb chart in the center of the BOMEX array. As discussed in Chapter 5, it is more likely that this wave formed in situ and not as the result of advection from the east; therefore, this case is probably an example of an unstable breakdown of the jet.

In Fig. V-2a, the zonal wind minimum near 800mb is due to Rockaway's sounding, and may be unreal. It is known that this ship had difficulty acquiring the sounding balloon during approximately the first six minutes of each flight or to nearly the 800mb level. Fortunately, the jet maximum is higher, and therefore measurable at Rockaway, and the height gradient supports the jet geostrophically; therefore, there is sufficient evidence to support the existence of the jet of 17/00Z. There are other examples such as 15/00Z (not displayed) which show that the wind speed decreases with height to 800mb at both Rockaway

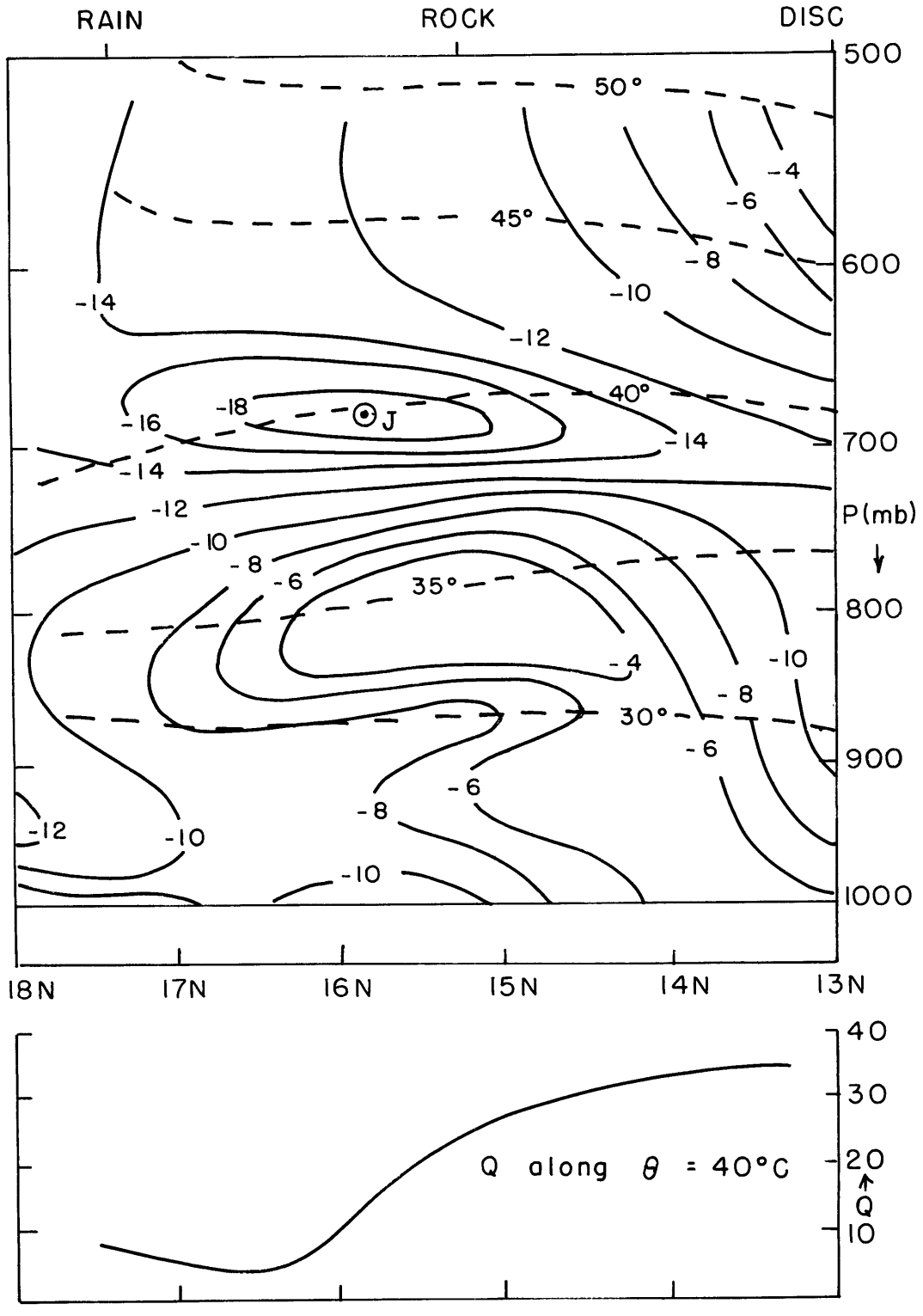

Fig. V-2a,b. Top, isotach and potential temperature cross-section for 00Z, 17 July 1969. Bottom, potential vorticity trace along 40°C isotherm showing Q-minimum at 16.5°N.

and Rainier and then increases to form a 30 knot maximum above 700mb. In the latter example, the minimum is again much more pronounced at Rockaway, probably due to sounding errors.

BIBLIOGRAPHY

Air Weather Service Technical Report 105-133, 1955: Accuracies of Radiosonde Data. Hq. AWS(MATS), USAF, Wash. 25, D.C., Sept. 1955. (Note: Hq. AWS now at Scott AFB, Ill.)

Anawalt, R. A., 1971: Kinematic Studies of BOMEX - Phase IV. S.M. Thesis, MIT Department of Meteorology, June 1971.

Atkinson, G. D. and J. C. Sadler, 1970: Mean Cloudiness and Gradient Level Wind Charts over the Tropics. Vol. I and II, AWSTR 215, Air Weather Service (MAC), United States Air Force, August 1970.

Atkinson, G. D., 1971: Forecasters' Guide to Tropical Meteorology, Air Weather Service (MAC), Tech. Rept. 240, 1 April 1971. (357 refs.)

ATS-III, 1969: The Applications Technology Satellites Meteorological Data Catalog, Vol. IV, 1 January through 31 July 1969, ATS Project, Goddard Space Flight Center, Greenbelt, Maryland, December 1969.

Ballif, J. R. et al., 1958: An empirical study of air movement near the Equator. Final Report under Contract Number AF 19(604)-2134. Sponsored by GRD of the AF Cambridge Research Center, ARDC, University of California Institute of Geophysics, Los Angeles, California, August 1958.

Bates, J. R., 1969: Dynamics of Disturbances on the Intertropical Convergence Zone. Ph.D. Thesis, MIT Department of Meteorology, 203 pp.

BOMAP, 1971: Temporary BOMEX Data Archive Documentation, Doc.-1, (on microfilm). See p. 44 of BOMEX Bulletin no. 9 for availability.

BOMEX Bulletin no. 9, 1971: Prepared by the BOMAP Office, U.S. Dept. of Commerce, NOAA, Rockville, Maryland 20852.

Bunker, A. F. and M. A. Chaffee, 1970: BOMEX Meteorological Data. Unpublished Manuscript, WHOI Ref. No. 70-49, September 1970. 18 pages and 46 figures.

Burpee, R. W., 1971: The Origin and Structure of Easterly Waves in the Lower Troposphere of North Africa. Ph.D. Thesis, MIT Department of Meteorology, January 1971.

Byers, H. R., 1944: General Meteorology. New York, McGraw-Hill.

Carlson, T. N., 1969: Synoptic histories of three African disturbances that developed into Atlantic hurricanes. Mon. Wea. Rev. 97, 256-276.

Carlson, T. N., 1971: A detailed analysis of some African disturbances. NOAA Tech. Memo. ERL NHRL-90, U.S. Dept. of Commerce, NOAA, ERL, April 1971.

Carlson, T. N. and J. M. Prospero, 1971: The large-scale movement of Saharan air impulses over the Western Tropical Atlantic. Manuscript received from the National Hurricane Research Laboratory, NOAA, Miami, Fla. in July 1971. Paper to be published.

Charney, J. G., 1963: A note on the large-scale motions in the Tropics. J. Atmos. Sci. 20, 607-609.

_____, 1968: The Intertropical Convergence Zone and the Hadley circulation of the atmosphere. Proc. of the WMO-IUGG Symposium on Numerical Weather Prediction, Tokyo, Japan, Nov-Dec. 1968. Published by Japanese Meteorological Agency, March 1969.

_____, 1969: A further note on large-scale motions in the Tropics. J. Atmos. Sci. 26, 182-185.

Charney, J. G. and A. Eliassen, 1949: A numerical method for predicting the perturbations of the middle latitude westerlies. Tellus, 1, 1949.

_____, 1964: On the growth of the hurricane depression. J. Atmos. Sci. 21, 68-75.

Charney, J. G. and M. E. Stern, 1962: On the stability of internal baroclinic jets in a rotating atmosphere. J. Atmos. Sci. 19, 159-172.

Charnock, H. et al. 1956: An investigation of wind structure in the Trades, Anegada 1953. Phil. Trans. Roy. Soc. Lon., A, Mathematical and Physical Sciences, 249(963), 18 October 1956.

Estoque, M. A., 1971: The planetary boundary layer wind over Christmas Island. Mon. Wea. Rev. 99, 193-201.

Faller, A. J., 1963: An experimental study of the instability of the laminar Ekman boundary layer. J. Fluid Mech. 15, 560-576.

Fernandez-Partagas, J.J. and M. A. Estoque, 1970: A preliminary report on meteorological conditions during BOMEX, fourth phase (July 11-28, 1969). Report prepared for National Science Foundation under Grant no. NSF GA 10201. Rosentiel School of Marine and Atmospheric Sciences, Division of Atmospheric Science, University of Miami, Coral Gables, Fla. 95 pp.

Frank, N. L., 1969: The 'inverted V' cloud pattern - an easterly wave? Mon. Wea. Rev. 97, 130-140.

Friedman, H. A. and J. D. McFadden, 1970: Essa Research Flight Facility aircraft participation in the Barbados Oceanographic and Meteorological Experiment. Bull. Amer. Meteor. Soc. 51, 822-834.

Fujita, T. T., 1969: Present status of cloud velocity computations from ATS-I and ATS-III satellites. Proc. Eleventh Plenary Meeting of COSPAR, Tokyo, 1968, 557-570.

_____ , 1970: Application of ATS-III photographs for determination of dust and cloud velocities over the Northern Tropical Atlantic. SMRP Research Paper no. 90. Univ. Chicago, December 1970.

Fujita, T. T., K. Wantanabe and T. Izawa, 1969: Formation and structure of equatorial anticyclones caused by large-scale cross-equatorial flows determined by ATS-I photographs. J. Appl. Met. 8, 649-667.

Gray, W. M., 1968: Global view of the origin of tropical disturbances and storms. Mon. Wea. Rev. 96, 669-700.

Hide, R., 1963: The viscous boundary layer at the free surface of a rotating baroclinic fluid. Scientific Report HRF/SR4, Hydrodynamics of Rotating Fluids Project, MIT.

Holton, J. R., 1965: The influence of viscous boundary layers on transient motions in a stratified rotating fluid: part I. J. Atmos. Sci. 22(4), 402-411.

Hubert, L. F. and L. F. Whitney, Jr., 1971: Wind estimation from geostationary satellite pictures. Mon. Wea. Rev. 99.

Joint Task Force Seven, 1956: Meteorological Report on Operation Redwing, Part I -- Meteorological Data, Vol. 1-12; Part II -- Meteorological Analyses.

Kornfield, J. and A. F. Hasler, 1969: A photographic summary of the earth's cloud cover for the year 1967. J. Appl. Meteor. 8, 687-700.

Kuo, H. L., 1965: On formation and intensification of tropical cyclones through latent heat release by cumulus convection. J. Atmos. Sci. 22, 40-63.

Madden, R. A. and E. J. Zipser, 1970: Multi-layered structure of the wind over the Equatorial Pacific during the Line Islands Experiment. J. Atmos. Sci. 27, 336-342.

Madden, R., E. Zipser, E. Danielsen, D. Joseph, and R. Gall, 1971: Rawinsonde Data Obtained during the Line Islands Experiment, Volume I: Data Reduction Procedures and Thermodynamic Data, National Center for Atmospheric Research NCAR-TN/STR-55.

Malkus, J. S., 1956: On the maintenance of the Trade Winds. Tellus, VIII.

Manabe, S., J. Smagorinsky and R. F. Strickler, 1965: Simulated climatology of a general circulation model with a hydrologic cycle. Mon. Wea. Rev. 93, 769-798.

Newell, R. E., D. G. Vincent, T. G. Dopplick, D. Ferruzza and J. Kidson, 1969: The energy balance of the global atmosphere. The Global Circulation of the Atmosphere, ed. G. A. Corby, Roy. Met. Soc., 1970, 257 pp.

Nitta, T. and M. Yanai, 1969: A note on the barotropic instability of the tropical easterly current. J. Meteor. Soc. Japan. 47, 127-130.

Palmen, E. et al., 1958: On the meridional circulation and release of kinetic energy in the Tropics. J. Met. 15(3), 271-277.

Palmer, C. E., 1951: Tropical meteorology. Compendium of Meteorology. Amer. Met. Soc. 859-880.

Petterssen, S., 1956: Weather Analysis and Forecasting, Vol. I. New York, McGraw-Hill.

Priestly, C. H. B., 1959: Turbulent Transfer in the Lower Atmosphere. Univ. of Chicago Press.

Riehl, H., 1945: Waves in the easterlies and the polar front in the Tropics. Misc. Rept. No. 17, University of Chicago.

Riehl, H., 1947: Diurnal variation of pressure and temperature aloft in the Eastern Caribbean. Bull. Amer. Met. Soc. 28, 311-315.

Riehl, H., 1954: Tropical Meteorology. New York, McGraw-Hill. 392 pp.

Riehl, H., T. C. Yeh, J. S. Malkus, and N. E. LaSeur, 1951: The north-east trade of the Pacific Ocean. Quart. J. Roy. Meteor. Soc. 77, 598-626.

Riehl, H. and J. S. Malkus, 1957: On the heat balance and maintenance of circulation in the Trades. Quart. J. Roy. Meteor. Soc. 83, 21-29.

Riehl, H. and J. S. Malkus, 1958: On the heat balance in the equatorial trough zone. Geophysica. 6, 503-538.

Robitaille, F. E. and E. J. Zipser, 1970: Atmospheric boundary layer circulations equatorward of the Intertropical Convergence Zone. Symposium on Tropical Meteorology, Honolulu, Hawaii, June, 1970.

Sadler, J. C, and B, E, Harris, 1970: The Mean Tropospheric Circulation and Cloudiness over Southeast Asia and Neighboring Areas, HIG-70-26 Scientific Report No. 1 or AFCRL-70-0489, Hawaii Institute of Geophysics, U. of Hawaii, August 1970, 37 pp.

Sheppard, P. A. et al, 1952: Observations of the wind stress over the sea. Quart. J. Roy. Meteor. Soc. 78,

Sutton, O. G., 1960: Atmospheric Turbulence. London, Methuen and Co. Ltd. New York, John Wiley and Sons Inc.

Swallow, J. C. and J. G. Bruce, 1966: Current measurements off the Somali coast during the Southwest Monsoon of 1964. Deep Sea Res. 13, 861-888.

Taylor, G. I., 1915: Eddy motions in the atmosphere. Phil. Trans. Roy. Soc, A. 215, 1-26.

Teweles, S., 1970: A spurious diurnal variation in radiosonde humidity reports. Bull. Amer. Meteor. Soc. 51(9), 836-840.

Warnecke, G. and W. S. Sunderlin, 1968: The first color picture of the earth taken from the ATS-3 Satellite. Bull. Amer. Meteor. Soc. 49, 75-83.

Williams, K. T., 1970: A statistical analysis of satellite-observed trade wind cloud clusters in the Western North Pacific. Atmos. Sci. Paper no. 161, Colorado State Univ. 80 pp.

Zipser, E. J., 1969: The role of organized unsaturated convective downdrafts in the structure and rapid decay of an equatorial disturbance. J. Appl. Meteor. 8, 799-814.

_____, 1970: The Line Islands Experiment, its place in tropical meteorology and the rise of the fourth school of thought. GARP Topics No. 15. Bull. Amer. Meteor. Soc. 51, 1136-1146.

Zipser, E. J. and R. C. Taylor, 1968: A Catalogue of Meteorological Data Obtained during the Line Islands Experiment, February - April 1967, LIE Report No. 1. National Center for Atmospheric Research NCAR-TN-35, Hawaii Institute of Geophysics HIG-67-19, 362 pp.

ACKNOWLEDGEMENTS

The author is greatly indebted to many people and organizations who have supported his work on this paper for the past several years. He is especially grateful for the inspiration and friendship of Professor Jule G. Charney whose patience and optimism enabled the author to return to the task on numerous occasions. Thanks are also extended to Professor Frederick Sanders for his many hours of constructive guidance, to Professor James M. Austin and Dr. Robert Burpee for their friendly, positive support, and to James S. Kennedy, Lt. Col., USAF, who is an expert in the theory and practice of true friendship.

The author thanks the Air Weather Service for providing the opportunity for his temporary return to M.I.T. and for providing data and satellite photographs through the Environmental Technical Applications Center at Washington, D.C.

Personnel at other organizations also took time from their normal duties to extend a helping hand. The author received data and valuable advice during several visits and telephone calls to the Barbados Oceanographic and Meteorological Analysis Project Office, Rockville, Md. The author gained considerable insight into the descriptive aspects of tropical meteorology and valuable wind data at NOAA's Meteorological Satellite Laboratory in Maryland. Personal support also came from the National Center for Atmospheric Research at Boulder, Colorado in the form of specially processed wind data from the Line Islands. Dr. T. T. Fujita of the University of Chicago supplied ATS-III

wind vectors in response to a personal request.

Numerical computations were made at the M.I.T. Information Processing Center and the research was partially assisted by NSF Grants GA 402 X3 and GA 28724, and NOAA Grant E 22-37-71G.

Special thanks to Miss Isabelle Kole, Mrs. Terry Berker and Miss Diana Lees for drafting figures, and to Mrs. Marie Gabbe and Miss Kate Higgins for typing the manuscript.

BIOGRAPHICAL SKETCH

The author was born on October 25, 1935 in Chicago Heights, Illinois, but spent his later public school years in Shaker Heights, Ohio. He received his A.B. in Mathematics and a commission in the Air Force in June, 1957 at Butler University, Indianapolis, Indiana. The author's first assignment as a Second Lieutenant was to St. Louis University where he received his S. M. in Meteorology in February, 1959 under the USAF Institute of Technology program. After three years of duty as a forecaster at McGuire AFB, New Jersey, the author was privileged to enter the doctorate program at M.I.T. in June, 1962, again under USAFIT.

Duty commitments terminated the author's academic endeavors in March 1965, prior to the completion of his thesis. However, these years were profitable and the research based on the Marshall Islands data was completed during this period under Professor Charney's guidance.

From 1965 through 1967 the author was assigned to the USAF Global Weather Central in Nebraska where he did exploratory work on automated analysis techniques, and on a fine-mesh, diagnostic model of the planetary boundary layer. His most recent tour of duty prior to his temporary stay at M.I.T. was in Washington, D.C., where he developed analytical decision making algorithms for certain aerospace systems that are sensitive to meteorological constraints.

The author was married in June, 1959 to Carol Stebbings of Park Ridge, Illinois, and has five children: Jim, Dan, Dave, Mike and Mollie.